An integrated furnace co-simulation methodology based on a reduced order CFD approach

by

Brad Travis Rawlins

Thesis presented for the degree of
Doctor of Philosophy
in the
Faculty of Engineering and the Built Environment
at the
University of Cape Town

Supervisor: Prof. R. Laubscher
Co-supervisor: Prof. P.G. Rousseau

November 2022

Declaration

I, **Brad Travis Rawlins**, hereby declare that the work on which this thesis is based is my original work (except where acknowledgements indicate otherwise) and that neither the whole work nor any part of it has been, is being, or is to be submitted for another degree in this or any other university. I authorise the University to reproduce for the purpose of research either the whole or any portion of the contents in any manner whatsoever.

Signature: .....

Date: November 2022

Declaration on the Inclusion of Publications in a PhD Thesis

I, **Brad Travis Rawlins**, confirm that I have been granted permission by the University of Cape Town's Doctoral Degrees Board to include the following publication(s) in my PhD thesis, and where co-authorships are involved, my co-authors have agreed that I may include the publication(s):

Conference articles

1. **Title:** "Validation of a thermal non-equilibrium Eulerian-Eulerian multiphase model of a 620 MW_e pulverized fuel power boiler"
Authors: B.T. Rawlins, R. Laubscher, and P.G. Rousseau
Conference: 12th South African Conference on Computational and Applied Mechanics, (SACAM2020)
Reference number: [115]

2. **Title:** "A fast thermal non-equilibrium Eulerian-Eulerian numerical simulation methodology of a pulverized fuel combustor"
Authors: B.T. Rawlins, R. Laubscher, and P.G. Rousseau
Conference: Proceedings of the 13$^{\text{th}}$ European Conference on Industrial Furnaces and Boilers, (INFUB-13)
Reference number: [111]

Journal article

1. **Title:** "Application of Computational Fluid Dynamics and Process Modeling to Investigate Low-Load Operation of a Subcritical Utility-Scale Boiler"
Authors: B.T. Rawlins, R. Laubscher, and P.G. Rousseau
Journal: ASME Journal of Thermal Science and Engineering Applications
Reference number: [104]

Journal article published since submission of the thesis

1. **Title:** "An integrated data-driven surrogate model and thermofluid network-based model of a 620 MW_e utility-scale boiler"
Authors: B.T. Rawlins, R. Laubscher, and P.G. Rousseau
Journal: Proceedings of the Institution of Mechanical Engineers, Part A: Journal of Power and Energy

Publications that are under peer review

Journal article

1. **Title:** "A fast thermal non-equilibrium Eulerian-Eulerian numerical simulation methodology of a pulverized fuel combustor"
Authors: B.T. Rawlins, R. Laubscher, and P.G. Rousseau
Journal: Proceedings of the 13$^{\text{th}}$ European Conference on Industrial Furnaces and Boilers, Special issue of *Thermal Science and Engineering Progress*

Abstract

An integrated furnace co-simulation methodology based on a reduced order CFD approach

B.T.Rawlins
University of Cape Town
Department of Mechanical Engineering

An integrated thermofluid modelling methodology for pulverised fuel fired utility-scale boilers that is computationally inexpensive, fast, and sufficiently accurate would be valuable in an industrial setting. Such a model would enable boiler operators to investigate a range of off-design operating conditions, which includes flexible operation. The aims of this study was: to develop a reduced order computational fluid dynamics (CFD) model of the furnace and radiative heat exchangers that captures all the important particulate effects while using a Eulerian-Eulerian (EE) approach; using the reduced order CFD model to generate a database of results that covers a wide range of operating conditions; to develop a data-driven surrogate model using machine learning techniques; to integrate the surrogate model with a 1-D process model of the complete boiler; and finally to demonstrate the use of the integrated model to investigate flexible operation and off-design operating conditions. The validity of the CFD modelling approach was demonstrated via application to a 2.165 $[MW_{th}]$ lab-scale swirl pulverised fuel burner, as well as to a 620 $[MW_e]$ utility-scale subcritical two-pass boiler, both operating at various loads. The results were compared to measured data and a detailed CFD model using the conventional Eulerian-Lagrangian (EL) approach. A computational speed enhancement of 30% was achieved. The data-driven surrogate model uses a mixture density network (MDN) to predict the heat transfer in the furnace and radiative heat exchangers, together with the uncertainty in the predicted values. The integrated model was validated against applicable measured data and then applied to a utility-scale case study boiler to investigate the optimal burner firing positions for low-load operation, as well as to investigate the effects of fuel quality on the overall boiler performance. It was shown that the integrated data-driven surrogate model and 1-D process model can predict the overall thermofluid response of the boiler and the uncertainties associated with it with good accuracy, whilst maintaining a low computational effort when compared to a conventional CFD model coupled to 1-D process model.

Key words: Computational fluid dynamics, Coupled simulation, Machine learning, Surrogate modelling, Utility-scale boiler

Acknowledgements

I would like to acknowledge and express my sincere gratitude to the following people:

- My mother for her constant support and motivation for the entirety of my studies.
- My supervisors Prof. Ryno Laubscher and Prof. Pieter Rousseau for the technical advice and their constant motivation in my project over the past three years.
- My siblings, Lauren, Caitlin and Dean, my permanent best friends who always had my back.
- To my fellow research associates at the Applied Thermofluid and Process Modelling research unit, your participation in the countless card games and lunchtime discussions kept the days interesting.
- To Nerine, an exquisite lady, the love of my life, whose supply of blueberries and thoughtful gestures kept me on track during the final stages of completing this academic milestone.
- And finally to my best friend, Dane Grobler and his family, for your few words of encouragement and countless weekend activities kept me focussed on what is important in life.

Dedication

In loving memory of my father,
Brendon Ross Rawlins
1963 - 2016

Table of contents

List of figures

List of tables

Nomenclature

Constants

σ_{SB}	Stefan-Boltzmanns constant	5.67×10^{-8} W/m^2K^4
g	Gravitational constant	9.81 m/s
Pr_t	Turbulent Prandtl number	0.85
R_u	Universal gas constant	8314.47 $J/kmolK$
Sc_t	Turbulent Schmidt number	0.7

Variables

$\bar{h}_l$	Output signal of a single neuron	–
$\bar{P}_r$	Surrogate model predicted value/s	–
$\bar{P}_{per}$	Perturbated surrogate model predicted value/s	–
$\bar{X}$	Neural network input vector	–
$\bar{Y}$	Neural network output vector	–
$\bar{z}_l$	Summed signal in a single neuron	–
$\tilde{h}$	Heat transfer coefficient	W/m^2K
$\tilde{P}$	Partial pressure	Pa
$\vec{D}$	Binary diffusion coefficient	m^2/s
$\vec{J}$	Mass diffusion flux	kg/m^2s
A	Area	m^2
A_c	Char pre-exponential factor	1/s
A_{vol}	Volatile pre-exponential factor	$1/s$
c_p	Constant pressure specific heat	J/kgK
d	Diameter	m
E	Energy	J/kg
E_a	Activation energy	$J/kmol$
E_p	Emission power of the particle	$J/kmol$
f	Scattering factor	–
G	Incident radiative flux	W/m^2
h	Enthalpy	J/kg
I	Radiation intensity	W/m^2sr
k	Turbulent kinetic energy	m^2/s^2
L	Length	m
L_p	Particle loading	kg/m^3
M	Molecular weight	$kg/kmol$
m	Mass	kg
P	Pressure	Pa
p	Perimeter	m

R	Arrhenius rate	$1/s$
S_{con}	Continuity source term	kg/m^3s
S_h	Energy source term	W/m^3
S_{mom}	Momentum source term	kg/m^3s
S_{rad}	Radiation source term	W/m^3s
T	Temperature	K
u	Velocity	m/s
V	Volume	m^3
X	Mole fraction	$kmol/kmol$
x	Fluid quality	$(0, 1)$
Y	Mass fraction	kg/kg

Greek variables

α	Absorption coefficient	$1/m$
$\bar{\mu}$	Mean value	$-$
$\bar{\pi}$	Mixing coefficient	$-$
$\bar{\sigma}$	Standard deviation value	$-$
$\dot{\omega}$	Volumetric generation rate	m^3/s
ϵ	Emissivity	$-$
Γ	Radiation diffusion term	m
κ	Gray gas absorption coefficient	$1/mPa$
λ	Thermal conductivity	W/mK
μ	Viscosity	kg/ms
ϕ	Generalised scalar variable	$-$
ψ	Mixture fraction	$-$
ρ	Density	kg/m^3
σ	Scattering coefficient	$1/m$
ε	Turbulent dissipation rate	m^2/s^3
ζ	Normally distributed random number	$(0, 1)$

Subscripts

ASH	Ash content
c	Char
$cnst$	Constant
$cond$	Conduction
$conv$	Convection
eff	Effective
$evap$	Evaporation
ext	External
FC	Fixed carbon
fg	Flue gas
G	Gas-phase in 1-D process models (steam)
g	Continuous gas-phase
H_2O	Moisture content
hp	Enthalpy of pseudo particle
int	Internal
k	Species designation (Part I), Normal distribution designation (Part II)

L	Liquid phase in 1-D process models (water)
l	Laminar
M	Mixture in 1-D process models
m	Mixture
mb	Mean beam length
$mp0$	Initial mass of pseudo particle
o	Stagnation point
p	Particulate phase
$proj$	Projected
rad	Radiation
ref	Reference
s	Surface
t	Turbulent
VM	Volatile matter
vol	Volatiles
x, y, z	Cartesian coordinates

Abbreviations

ANN	Artificial Neural Network
ATT	Attemperator
CFD	Computational Fluid Dynamics
CFPP	Coal Fired Power Plant
DAF	Dry Ash Free
DOE	Design of Experiments
DPM	Discrete Phase Modelling
EC	Economiser
EE	Eulerian-Eulerian
EL	Eulerian-Lagrangian
EV	Evaporator
HHV	Higher Heating Value
IFRF	International Flame and Research Foundation
MAE	Mean Absolute Error
MCR	Maximum Continuous Rating
MDN	Mixture Density Network
MLP	Multilayer Perceptron
MSE	Mean Square Error
NIST	National Institute of Standards and Technology
RANS	Reynolds Averaged Navier-Stokes
RH	Reheater
RMSE	Root Mean Square Error
RTE	Radiation Transport Equation
SH	Superheater
WSGGM	Weighted Sum of Gray Gas Model

Chapter 1

Introduction

1.1 Background

Conventional thermal power plants, such as coal-fired power plants (CFPP's), nuclear power plants and biomass power plants, typically use steam as the working fluid which expands through a series of turbines connected to a generator, to produce electrical energy. The Rankine cycle, developed by the Scottish engineer William J.M. Rankine [1], is considered the ideal cycle for conventional thermal power plants. A basic schematic and temperature versus entropy (T-s) diagram illustrating the ideal reheat Rankine cycle is given in Figure 1.1.

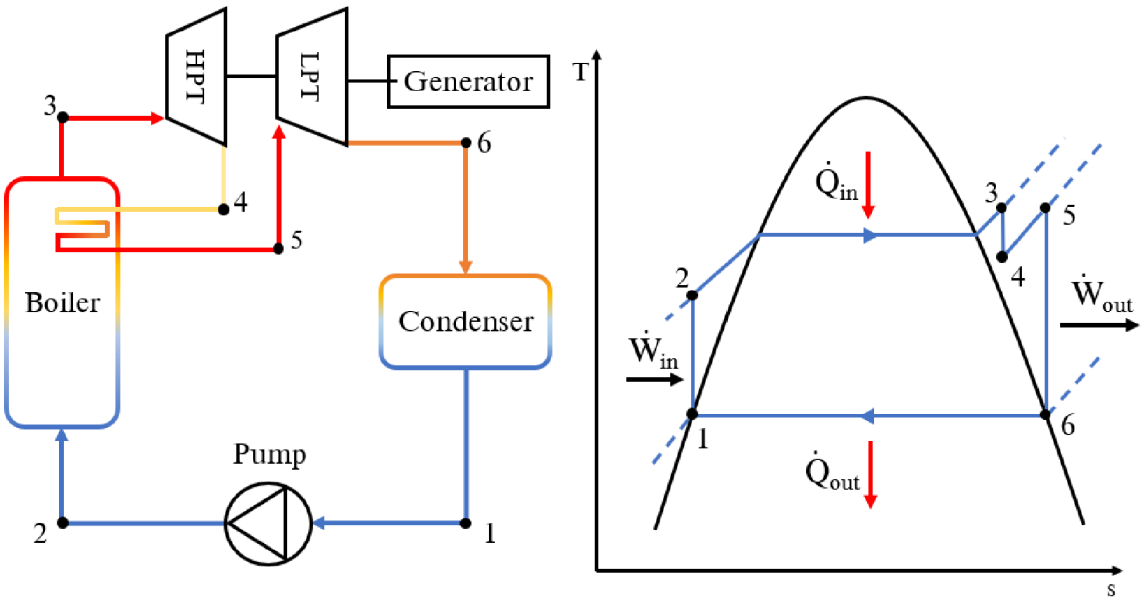

Figure 1.1: Ideal reheat Rankine cycle schematic and temperature versus entropy diagram.

The cycle comprises of an isentropic compression (process 1-2), a constant pressure heat addition (process 2-3), isentropic expansion in the high-pressure turbine (process 3-4), constant heat addition (process 4-5), isentropic expansion in the low-pressure turbine (process 5-6), and constant pressure heat rejection (process 6-1).

Utility-scale thermal power plants, such as large solid fuel boilers, are typically designed to operate as base load units, meaning they would operate for extended periods of time at near full load. Therefore, they are not designed for major shifts in operational outputs [2]. The South African energy sector, at present, is highly dependent on the use of CFPP's to generate electricity, with 70% of the country's primary energy needs being provided by CFPP's [3]. The current global trend in environmental policies are mainly focused on reducing the effects of climate change with the focal drive for renewable energy implementation [4]. However, the main contributors to renewable sources, namely solar and wind, are highly variable in nature, which results in an intermittent supply of energy for power generation.

What this means for the future operation of CFPP's, in the South African context, is the switch from a base load to a mid-merit/flexible operational protocol. A mid-merit plant is classified as a power plant that can adjust its output as the demand fluctuates throughout the day [5]. Since CFPP's are primarily designed as base-load plants, research into flexible/mid-merit operation is required to better understand the flexible operation and subsequent operating limits arising from these off-design conditions. Operating at low-loads for continuous periods of time could result in insufficient heat being extracted by the working fluid present in the heat exchanger tubes. This can lead to elevated metal temperatures that are higher than the design temperatures. Researchers such as Modlinski et al. [6] as well as Laubscher and Rousseau [7] show that the most susceptible component to this phenomenon is that of the radiant superheaters, especially the reheaters.

Physical experimentation is not a feasible option to investigate the thermal operating limits of the heat exchanger materials due to the scale of the plants and the associated risks and costs. Thus, numerical simulation is the only practical solution that can be used to obtain further insight into various dynamic operating scenarios, such as start-up, load following and low-load ramp down.

1.2 Motivation

Numerical simulation of CFPP's has been done successfully using a variety of simulation approaches. Computational fluid dynamics (CFD) simulation of CFPP's offers the most accurate and information rich approach for determining the combustion characteristics, the radiative and convective heat transfer as well as the gas-solid flow interactions [8]. These simulations are usually conducted for separate steady-state load cases due to the computational demand of the simulations. Therefore, using CFD to study plant dynamics or the integrated operation of the flue gas- and water-sides is not currently computationally feasible.

A model that is computationally inexpensive, fast, and relatively accurate would be advantageous in an industrial setting. Such a model would enable boiler operators and engineers to investigate off-design operating conditions, which include the control protocols needed when considering flexible load operations and unexpected natural phenomena affecting operations (e.g., a change in the weather conditions or a drop in fuel quality).

Furthermore, such a model can provide a fast and efficient way for recommendations to be made on a variety of what-if scenarios in near real-time, such as the best protocols to mitigate burner mill failure and to counter overheating of critical heat exchanging components.

Recent developments in data-driven techniques to reduce the inference time of high-fidelity computational models have proven to be a useful tool. This shift in simulation complexity has led to the development of rudimentary digital twins, that can be used for real-time process monitoring applications. The digitalisation and the use of digital twins, along with reduced order modelling techniques, can bring new possibilities for energy-intensive industries. One potential scenario is the use of digital twins to optimise the performance. For example, by creating a digital twin of an industrial plant or a process, it's possible to simulate the performance of the system under different conditions, such as varying process parameters, loads, or environmental conditions. This can be used to identify the optimal operating conditions for the system, which can lead to improved energy efficiency and reduced energy costs. Such a model would be highly beneficial in the operation of CFPPs in the context of reducing the computational requirements of the flue gas side heat transfer calculations, especially during flexible operation. Currently no such model exists for a subcritical CFPP that incorporates data-driven techniques to reduce the computational burden of the flue gas side spatial and heat transfer effects.

The use of 1-D process models can efficiently and accurately capture the steam side flow phenomena, heat transfer and phase change characteristics [9, 10]. The coupling of 3-D CFD models and 1-D process models is a promising development in the field of simulation techniques. However, the main limitation is the simulation time required for the CFD component. Replacing the conventional CFD model with a data-driven model of the furnace and other radiation-dominated heat exchangers can therefore lead to a promising integrated model that is both fast and suitably accurate for the application in condition monitoring and what-if analysis. The development of a co-simulation modelling methodology that employs a data-driven reduced order CFD surrogate for a CFPP furnace is, therefore, seen as a necessary step to create a computationally efficient integrated model that can be used to investigate power plant flexibility, while capturing the 3-D spatial effects of combustion, fluid flow and heat transfer.

1.3 Research statement

The mid-merit operation of CFPP's, needed to compensate for the intermittent power generated by renewable sources, requires research into the operational limits and procedures that would reduce the risk damage to existing infrastructure. This requirement highlights the need for a better understanding of the dynamic response of such plants. Numerical modelling techniques are proven to be more feasible and better suited for flexibility studies than costly experiments, due to the size of these plants and the associated risks and costs.

The traditional dynamic modelling of CFPP furnaces, using a 1-D network modelling approach, rely on semi-empirical relations that were developed from tests carried out on pilot and utility boilers. These empirical relations are not always accurate in determining the temperature profiles and wall heat fluxes of boiler furnace components. This is due to the spatial nature of combustion and radiation heat transfer, which empirical models fail to capture adequately. The use of CFD modelling can capture these effects with a greater degree of accuracy. However, it remains a computationally expensive approach, especially for dynamic simulations.

The current development of coupled simulation models combines the benefits of both modelling approaches. One such approach are quasi transient simulations that utilise a steady-state CFD and 1-D process model to study the phenomena that change slowly when compared to the time step. An example would be the thermal response of the water/steam side components of a typical subcritical CFPP boiler when the fuel flow rate is increased, since the residence time of the fuel combustion products and subsequent traversal through the system is very small. However, these approaches remain computationally expensive since the coupled models solve independently and transfer data between iterations. The use of data-driven surrogate models, based off a CFD simulated database, have been shown to lessen the computational burden whilst maintaining an adequate degree of accuracy [11].

Therefore, a need exists for a co-simulation methodology that combines the use of a data-driven surrogate and a 1-D process model to investigate the flexible and low-load operating conditions of a subcritical CFPP boiler.

1.4 Hypothesis

The hypothesis for the current research is that an efficient and fast integrated boiler co-simulation model can be developed based on a data-driven reduced order CFD surrogate model of a CFPP furnace to investigate power plant flexibility, while adequately capturing the 3-D spatial effects of combustion, fluid flow and heat transfer.

1.5 Research aim and objectives

The primary aim for the current project is to develop a co-simulation modelling methodology to study the thermofluid behaviour of a CFPP furnace and radiant superheater over a range of operating conditions, using a reduced order CFD approach. The overall aim will be fulfilled through several specific objectives stated below:

1. Investigate the level of complexity reduction that can be achieved via a Eulerian-Eulerian (EE) CFD approach which does not rely on discrete phase modelling (DPM) of the fuel particles. Such a CFD model will reduce the computational requirements for machine learning purposes.
2. Validate the EE approach against experimental results in the form of case studies, which include a lab-scale burner and a utility-scale boiler.
3. Using the developed reduced order CFD generate a database of simulation results for a pulverised fuel furnace.
4. Using the simulated database, develop a data-driven surrogate model for the furnace that can produce the necessary heat fluxes and temperature profiles based on boiler load inputs.
5. Integrate the surrogate model with a 1-D process model, using open-source software, to investigate the effects of continuous low-load operation and fuel quality variations.

1.6 Thesis structure

The thesis is made up of two parts. The first part focusses on the development of a reduced order numerical model. The second part incorporates the development of an integrated model that combines a 1-D process model and a data-driven surrogate model of a utility-scale boiler that is developed using machine learning techniques. The surrogate model utilises the reduced order numerical model of Part I in the generation of a suitable training dataset. Figure 1.2 provides a schematic of the thesis structure accordingly.

Chapter 2 provides a discussion of the available literature pertaining to physics-based modelling approaches and machine learning based modelling of thermofluid systems.

Part I begins with Chapter 3 and provides the theoretical background of 3-D CFD modelling techniques used in simulating thermofluid systems and the theory behind 1-D process modelling techniques. Attention is centred on the discussion of the numerical modelling of the conservation equations, combustion, and heat transfer. The traditional method of particle modelling in a Lagrangian framework is also discussed with emphasis provided on the interactions with the continuous phase.

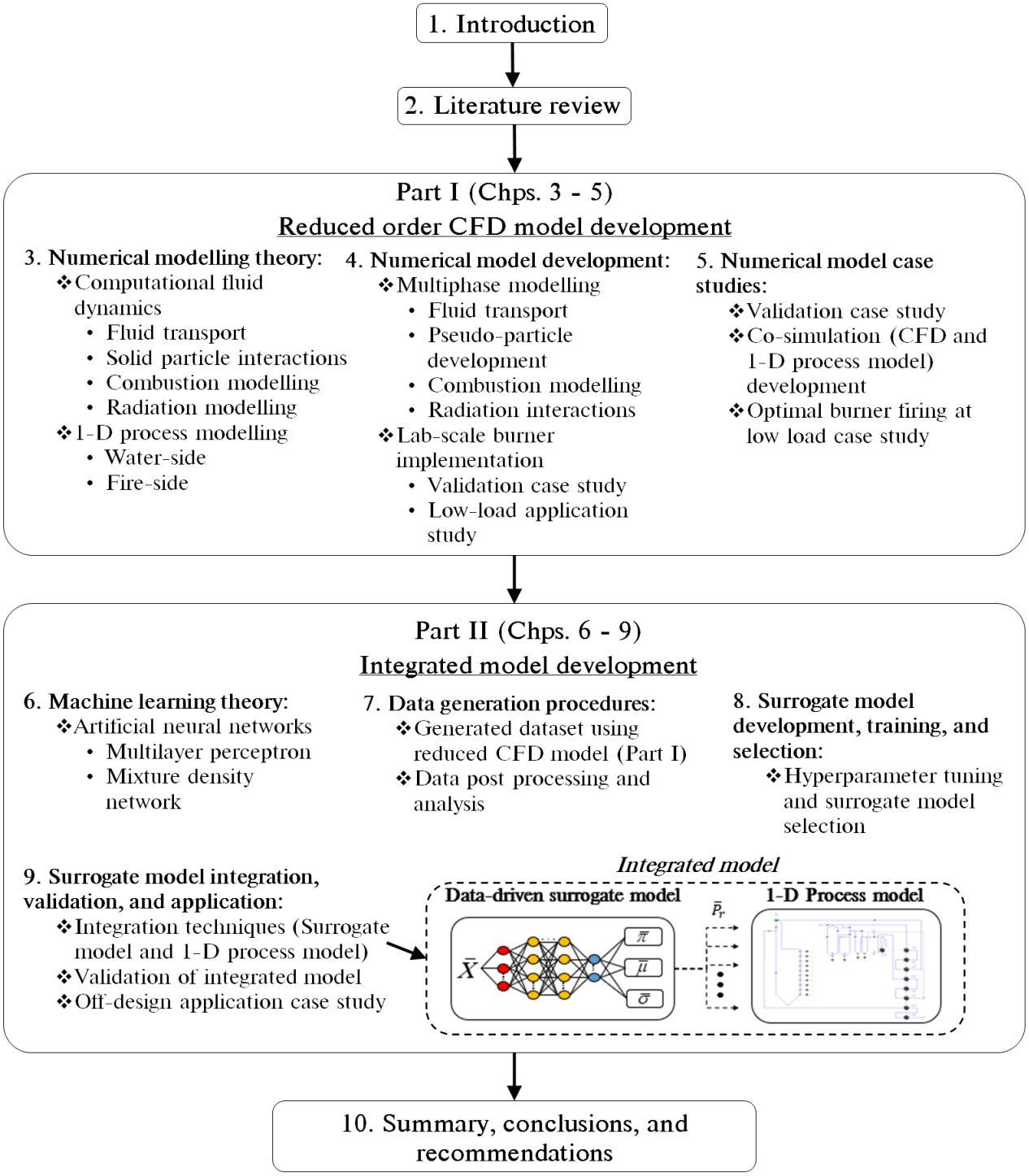

Figure 1.2: Schematic of the thesis structure

The EE numerical model development is examined in Chapter 4. The similarities and differences between the conventional modelling techniques of solid fuel systems are evaluated. Validation and verification of the EE model is provided in the context of a case study conducted on the well-documented international flame and research foundation's (IFRF) Furnace No. 1 burner.

The developed modelling methodology of Chapter 4 is applied in the form of case studies which are discussed in Chapter 5. The validated model is subsequently used in the modelling of a full-scale utility boiler. Validation results for the full-scale utility boiler are provided for multiple loads against numerical and measured data. A further low-load case study was conducted to establish the optimum firing configuration.

Part II starts with Chapter 6, which provides the theoretical background of the machine learning theory. The most common and applicable machine learning approaches are discussed, with emphasis on linear regression, deep learning, and mixture density networks (MDNs).

Chapter 7 provides a summary of the data generation process. A design of experiments (DOE) is discussed in terms of the inputs and generated outputs. Furthermore, an exploratory data analysis is performed to investigate the distributions and common trends of the output data. Subsequently, Chapter 8 considers the surrogate model development in terms of establishing the best machine learning modelling approach. The final architecture and best performing machine learning model were selected based on the results of a hyperparameter search using both training and testing data. The surrogate model integration and application are discussed in Chapter 9. The model was validated for various operational loads. Using the integrated surrogate model, a case study exploring the importance of fuel quality was conducted illustrating the model's robust and efficient solving times.

A summary and conclusion of the findings are provided in Chapter 10 and includes recommendations for future work. In addition, three appendices have been provided that present the relevant derivations, sample calculations and fluid property polynomials used throughout the work.

Chapter 2

Literature study

This section will present literature pertaining to the use and application of physics-based modelling approaches and machine learning techniques. Physics-based modelling includes discussing 3-D CFD techniques in relation to the complexity of modelling CFPPs and solid fuel combustion. In addition, advances in process modelling and coupled simulations are explored. Finally, the conventional machine learning applications are examined, culminating with a review of data-driven approaches applicable to thermofluid systems.

2.1 Physics-based modelling of CFPPs

2.1.1 3-D modelling of CFPPs

CFPPs are considered complex chemical reactors comprised of many interrelated processes such as the three modes of heat transfer, turbulent flow regimes, non-premixed combustion, and two-phase flow, which occur simultaneously [12]. While full-scale testing or experimentation on CFPPs are deemed too expensive to pursue, mathematical models can accurately capture the thermal response of boilers at varying loads and can be used to determine the safe and efficient operating limits [7]. CFD allows for the steady-state resolution of full-scale CFPP boilers, provided sufficient boundary conditions, and computational resources are available. CFD simulations have been successfully used to model a variety of CFPP boiler types [13, 14] and cover various operational aspects such as pollution control [15–17], gas-solid flow effects [18] and boiler retrofitting [14, 19].

The conventional CFD approach for modelling solid fuel combustion systems is acknowledged as the Eulerian-Lagrangian (EL) approach [12]. This approach uses an Eulerian description of the gaseous phase, with the governing equations being derived using a finite volume approach in a stationary frame of reference [20]. The solid fuel particles are modelled using a Lagrangian frame of reference by tracking the trajectories of the particle parcels as it moves through the domain. The source terms are calculated by averaging over a multitude of particle trajectories (discussed in [21]), typically leading to instability of the continuous phase source terms. This requires significant under-relaxation of the solid-phase source terms in the continuous phase equations, resulting in extended computation times.

The use of ANSYS Fluent® by Wang et al. [22] aided the researchers in developing a set of 3-D heat transfer calculation methods that incorporates the essential physics of the combustion and heat transfer processes in a CFPP boiler furnace. Since the furnace walls directly affect the overall furnace temperature level, subsequently affecting the combustion and emission formation characteristics, analysing the furnace thermal performance forms a crucial part of condition monitoring. The methods used by the aforementioned researchers were validated on a 330 $[MW_e]$ tangentially fired boiler. The study also shows the highly non-uniform nature of the furnace wall heat and temperature distribution. Using similar modelling approaches Dugum and Hanjalić [23] investigated the believed cause of high-temperature corrosion in the membrane walls of a 230 $[MW_e]$ utility boiler furnace. The numerical analysis used ANSYS Fluent® to examine the inflow conditions for sub-optimal coal combustion. The study found that the burner exits near field concentrations of CO and O_2 were in the region that can lead to high-temperature corrosion.

As alluded to, the furnace of a CFPP is a critical component in its design and operation since all furnaces must provide sufficient residence time for the coal particles to completely burn and allow the fly-ash to cool below the softening temperature [24]. This is to limit ash deposition on downstream components. Ash plays a significant part in the attenuation radiative heat transfer of solid fuel fired systems, especially in furnaces and radiative heat exchangers [8].

Rousseau and Laubscher [25] investigated the heat transfer characteristics using a co-simulation of a subcritical boiler firing coal with a significant increase in ash content. The work used 3-D CFD and 1-D process modelling to capture the flue gas and thermofluid effects, respectively. The numerical CFD study considered two case studies, one with the design ash content and the other with higher ash content. It was concluded that the increase in the fuel's ash content results in a lower heat uptake from the furnace and the radiant SHs, an increase in particle impaction, and heat exchanger hot spot locations. The conversion-dependent models for the particle emissivity and scattering factors from the works of Lockwood et al. [26] and Yin et al. [27, 28] were utilised, as opposed to the constant values of 0.9 and 0.6, suggested by Ranade and Gupta [12]. Using the conversion-dependent models allows for accurate capturing of the particles' radiative behaviour which was illustrated in previous work conducted by the same authors [29], were the two approaches were compared. It was found that the conversion-dependent model corresponded better to experimental data and was able to predict the steam generation and exit steam temperatures better in relation to measured values. This is an important consideration for the current study, since the South African CFPP fleet uses coal with an ash content ranging from 21% to 40% by weight [30].

Recent CFD studies investigating the low-load operation of CFPP boilers have focused on the combustion stability, harmful emissions, and the gas flow-solid flow interactions [31]. Belosevic et al. [32] found that the low-load operation of boilers considerably affects the flow and temperature fields, the flame geometry, chemical reactions and concentrations of combustion products.

Hernik et al. [33] investigated the effects of using different mill system configurations at a minimum boiler load of 40%. The most favourable mill system configuration was selected based on the case that exhibited suitable combustion stability, defined for the study as the effective mixing of the fuel and oxidiser as well as maintaining sufficient temperature distributions. In addition, having a reduction in harmful emissions, such as CO and NO_x concentrations, was a beneficial attribute for the final mill configuration. Similarly, Chang et al. [34] investigated the various firing arrangements of a 630 $[MW_e]$ tangentially fired boiler. A downward burner angle of 15° was determined as the optimal arrangement resulting in the best compromise between combustion stability and lower emissions.

Another CFD approach that pre-dates the conventional EL is the Eulerian multi-fluid or multiphase modelling approach. The Eulerian-Eulerian (EE) modelling approach is not a new concept; before the increase in fast and efficient computing power, the EE model was utilised due to its economy. This approach models the gas and solid phase using an Eulerian reference frame. Researchers such as Knaus et al. [35] and Benim et al. [36] compared the EE and EL approaches for coal-fired utility boiler simulations. The predicted combustion products calculated using the two approaches showed only minor differences, with carbon monoxide being more accurately predicted when using the EL approach. The computational effort of the EE approach proved to be less so with faster convergence times being recorded. It should be stated that these studies were conducted using in-house CFD codes, which is difficult to apply by engineers and scientists outside the mentioned authors' respective research groups. Cai et al. [37] used a multi-fluid EE model, similar to the two-fluid approach of Zhou et al. [38], to resolve the particle size distributions and size-dependent heterogeneous reaction rates for a coal ignition flame. Using a new radiation formulation that can account for the non-gray gas-solid mixtures, it was found that radiation effects can lead to a 500 $[K]$ difference in the solid phases. This highlights the critical need to consider radiation to improve temperature and the CO_2 volume concentration predictions. However, using an in-house source code limits the application of the methodology for industrial applications. Also, tracking additional particle size bins increases the number of solved transport equations and the required computational resources.

Limitations of the published EE approaches is the assumption of mechanical and thermal equilibrium between the particle and gas-phases. The assumption of thermal non-equilibrium between the gas and particles has a pronounced effect on the estimation of the various combustion processes such as moisture evaporation, devolatilisation and char combustion, because these processes depend on the particle temperatures, as described in depth in the works of Sankar et al. [8]. Therefore, the convective and radiative heat transfer to and from the solid phase should be accounted for while explicitly accounting for the particulate matter thermal mass. Therefore, accurately capturing the particle temperatures becomes even more critical when studying high throughput fuel flow and combustion stability, as is the case in the present work where the goal is to analyse low-load operation of high-ash coals.

2.1.2 1-D process modelling of CFPPs

The use of 1-D process modelling techniques for capturing the steady-state and dynamic response of CFPPs has been highlighted in the work of Alobaid et al. [10]. There have been many developments of simulation codes over the past decades, with the advanced process simulation software (APROS) [39] being the most popular for CFPPs. Due to their efficient use of computational resources, process modelling techniques have been extensively used to investigate dynamic applications such as start-up procedures, flexible operation, and the oxy-fuel concept.

Starkloff et al. [40] provided a sufficiently accurate dynamic model of a large once-through boiler located in Germany. The proposed model was validated using operational data for a load change from 100% to 27.5% maximum continuous rating (MCR). Uncertainties proved to be a significant problem for the study, which included the exact coal composition used at the station and the slagging and fouling levels present in the furnace and downstream heat exchanger. Nonetheless, the results showed good agreement, and the validated model is to be used for further investigations for flexible operation. Similarly, a 500 $[MW_e]$ subcritical boiler model was developed by Oko and Wang [9] and was validated for 70%, 80%, 94,4% and 100% steady-state operating conditions. However this study fails to determine how well the model reacts to the transient conditions of the actual plant. Another study conducted by Kuronen et al. [41] on a 750 $[MW_e]$ plant presented accurate simulated results for an 87% to 100% load change of the plant. The results were validated for both steady and transient applications using the measured site data. Based on a lumped variable model, the boiler furnace flue gas side was modelled and empirically tuned. The focus of the study was to develop a model for testing and design purposes for flexible operation.

The furnaces of CFPP boilers are comprised of a multitude of complex and interacting phenomena, such as the combustion dynamics, the gas-solid interactions, fluid dynamics, and radiation heat transfer. As a result, the heat transfer in CFPP furnaces incorporate many non-uniformities, thus, making 1-D process models of furnaces unable to resolve the fire-side interactions with sufficient accuracy. This results in many researchers [9, 40, 41] using a lumped parameter analysis when dealing with the furnace section of a CFPP boiler, which is primarily based on the Gurvich/Blokh method [42]. However, process modelling can adequately resolve the water-side energy and momentum transport in a computationally inexpensive manner. Deng et al. [43] developed a process model of the start-up system of an existing 600 $[MW_e]$ supercritical once-through boiler. The model incorporated the two-phase homogeneous flow model to resolve the water/steam networks. The simulation software APROS was used to build the entire model, including the fire-side which assumed complete combustion with a stable flame. The model was able to provide sufficient resolution of the steam characteristics during start-up with a 2.29% relative error between the design and simulated steam exit temperatures and flow rate.

Researchers Hajebzadeh et al. [44] utilised a 1-D process modelling approach to investigate six different loads of a 320 [MW_e] tangentially fired boiler. The results were validated for both the flue gas and water/steam working fluids using measured plant data. The fire-side components were modelled using the Gurvich/Blokh method [42]. The developed models water/steam calculated values displayed absolute relative errors in the range of 0.1% to 7.3% between the measured data.

2.1.3 Co-simulation of CFPP heat transfer processes

The use of coupled simulations has proven to solve the deficiencies of a full 1-D process model by coupling the fire-side CFD results to a 1-D water-side process model. Many coupled simulations can be classified as fully separated models, as coined by Filimonov et al. [45], whereby the 2-D/3-D (CFD) and the network models are calculated separately, and the data obtained from one model would form the input parameters of the other. Laubscher and Rousseau [25] used the above-mentioned coupling approach to investigate the effects coal quality have on the heat transfer distribution to the furnace water walls and radiant superheaters. The results showed that it was possible to identify a range of effects that the various high-ash coals have on the furnace heat uptake, the steam generation rates and the superheater wall temperatures. ANSYS Fluent® and Flownex SE® were used in modelling the gas- and water-side components, respectively. Similarly, the same researchers used the coupled modelling approach in investigating the impact of using a variable particle emissivity and scattering efficiency on the evaporator and radiant superheater process conditions, including the furnace steam generation rate and final steam temperature [29]. The study highlighted the importance of incorporating the conversion-dependent particle emissivity and scattering models in investigating high-ash content coal combustion systems, which had a 0.7% error in predicting the furnace heat load and exit steam temperature, while the constant property models resulted in a 6.5% error.

Schuhbauer et al. [46] showcased the use of a co-simulation methodology for a 550 [MW_e] supercritical boiler. The paper aimed to provide detailed information on how to couple the fire and steam side using commercial software, specifically ANSYS Fluent® and APROS. The results show a good correlation to that of the design data with a maximum 6% deviation. However, the use of porous media for the superheater banks resulted in the lack of radiation participation in these areas. The use of uncharacteristic source terms was needed to correct this. Similarly, Park et al. [47] considered the effects of burner settings and coal blending compositions on boiler efficiency. An 800 [MW_e] tangentially fired boiler located in South Korea was the boiler of interest. The coupled models, consisting of ANSYS CFX® and the 1-D process modelling software PROATES, exchanged temperature and wall flux values of the furnace and heat exchangers for each calculation iteration. The model was validated against plant data and was in good agreement. Furthermore, plant engineers successfully used the model to optimise burner settings.

Yu et al. [48] used a coupled simulation methodology to estimate the superheater (SH) metal temperatures of a 660 [MW_e] tangentially-fired coal boiler. Using ANSYS Fluent® v14.5 and MATLAB, the study found that using a positive 20° for the separated over-fire air kept the surface temperatures below the allowable temperature of the heat exchanger material. Hovi et al. [49] demonstrated the transient simulation of a bubbling fluidised bed boiler furnace using a coupled approach. A fast load change was modelled with the process behaviour being analysed based on the control protocol. It was found that the coupled transient simulation was reasonably slow and best suited for the evaluation of significant changes in the control and process design.

The coupling of steady-state CFD and dynamic process models is a promising development in simulation techniques. However, the main limitation is the simulation time required for the CFD component. Replacing the traditional CFD model with a data-driven model of the furnace can lead to a promising integrated model that is both efficient and fast.

2.2 Application of machine learning in energy sciences

Machine learning techniques have found many uses in industry, covering many fields, such as neuroscience [50, 51], geology [52, 53], finance [54, 55] and agricultural applications [56, 57]. The application of machine learning techniques in the energy sciences have seen a recent surge. Kalogirou [58] highlighted the uses of machine learning in resolving the modelling and control of thermal energy systems for a broad range of applications. Muller and Keller [59] used an artificial neural network (ANN) to model the combustion process for waste incineration plants, with the aim being to reduce toxic emissions. The model effectively simulated various process parameters and used optimisation algorithms along with the reduced models to lower the plants emissions. Recently various authors have applied machine learning techniques to develop regression models of different energy system components with training data generated using real world processes. Fei et al. [60] used a fast set of reduced order models (ROMs), using the Kriging method, based on CFD data to investigate the retrofitting of a coal-fired power plant under oxy-fuel conditions. Using an integrated ROM and a whole plant process model, a range of air-coal ratios were investigated, with the model illustrating sufficiently accurate results. However, no operational uncertainty was incorporated into the input parameters to account for real-world operational effects such as plant disturbances and varying local atmospheric conditions.

Raidoo and Laubscher [61] compared both a deterministic and a probabilistic model to predict the backpressure of a utility-scale air-cooled condenser using a mixture density network (MDN) model and recurrent neural networks (RNNs). The probabilistic model was found to predict air-cooled condenser backpressure with a mean absolute accuracy of 82%. Another dynamic application saw Laubscher [62] use an RNN the predict the reheater metal temperatures 5 minutes into the future with sufficient accuracy. In the modelling of thermal power plants, feed-forward models offer a simple and robust approach. Liu et al. [63] demonstrated the efficiency in modelling the turbo-generator unit for a 1000 [MW_e] coal-fired boiler using an ANN compared to a linear model.

In the absence of sufficient measurable data, simulated datasets based on validated computational models can be used as an alternative source of data for training and testing of machine learning models. Haffejee and Laubscher [64] used simulation data from a 1-D process model to develop a condition monitoring platform capable of predicting backpressures for the dry cooling component of a thermal power plant using deep neural networks. Singh and Abbassi [65] incorporated the use of an ANN and CFD model to investigate the transient thermal modelling of an off-highway machinery cabin. The ANN training data was obtained from a 1-D process model for the refrigeration cycle. The methodology successfully integrated the ANN capabilities with a 3-D CFD simulation model, negating the need for a coupled simulation procedure. Similarly, Warey et al. [66] used CFD solution data, for a wide range of climatic conditions, to develop a machine learning model that can predict the thermal comfort of a vehicle cabin based on the equivalent temperature for each passenger and the volume-averaged cabin temperature. The developed model enabled predictions for a wide range of boundary conditions in real-time without the need for CFD simulations.

Predicting and recognising system/load uncertainties in conventional coal-fired power plants are paramount for the safe operation and maintenance of these plants [67]. The uncertainty associated with the operational parameters of a thermal power plant, such as fuel quality, combustion processes, and burner biasing, can significantly change the thermal-hydraulic response [68]. The design space load uncertainty of a combined cooling, heating and power system was investigated by Lu et al. [69]. Using a multi-objective optimisation model, factors such as pollutant emission, economy and system reliability were incorporated to improve the operational performance.

It is noted that CFD cannot meet the real-time requirement for online performance monitoring due to the complex solving mechanisms and time-consuming calculations. However, a feasible alternative is to generate training and testing datasets for ANN implementation. Furthermore, using CFD does not interfere with the regular operation of the plant, and it can capture the radiative and fluid flow characteristics with sufficient accuracy. In addition to this, a more comprehensive range of appropriate operating conditions can be simulated. Thus, data-driven machine learning models based on CFD simulation data combined with a 1-D thermofluid model can provide insights into flexible operation and off-design conditions of utility-scale boilers

Part I of II

Chapter 3

Numerical modelling theory

This chapter discusses the theory used in this study, emphasising the following:

- The governing equations for basic fluid flow, species transport, energy transport, momentum transport, and turbulence closure.
- Conventional particle transport modelling.
- Solid fuel combustion theory and modelling.
- Radiative heat transfer theory and modelling.
- The governing equations and solution strategy, specifically for 1-D boiler heat exchanger gas- and water-side modelling.

Figure 3.1 highlights the content that is discussed and indicates the research objective addressed in this chapter for the readers convenience.

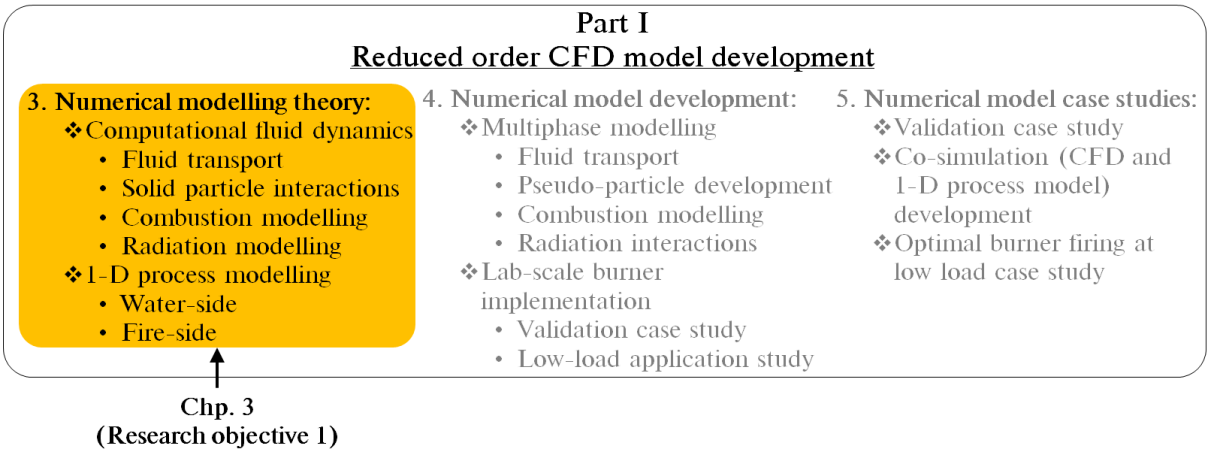

Figure 3.1: Content overview and research objective addressed in Chapter 3

The theory sets the foundation for subsequent discussions of the CFD modelling methodologies and co-simulation techniques utilised to develop a fast thermal non-equilibrium Eulerian-Eulerian model for surrogate model development, and the integration of the model into a full-scale system model. The specific model parameters will be discussed in the model development section of the current work.

3.1 Governing transport equations

3.1.1 Global continuity equation

The conservation of mass principle states that the net mass transfer to/from a control volume equals the net change in mass within the control volume over time. Thus, the differential continuity equation can be written as:

$$\frac{\partial \rho_g}{\partial t} + \frac{\partial}{\partial x}(\rho_g u_x) + \frac{\partial}{\partial y}(\rho_g u_y) + \frac{\partial}{\partial z}(\rho_g u_z) = S_{con} \tag{3.1}$$

where S_{con} $[kg/m^3 s]$ is the continuity source term which can account for mass additions stemming from combustion related processes (such as moisture evaporation and devolatilisation) or user-defined sources, and u_i $[m/s]$ is the velocity vector in Cartesian coordinates.

In reactive flows, the density of the gas mixture, ρ $[kg/m^3]$, depends on the mixture temperature, pressure, and species concentration [20]. The gas density is calculated from an equation of state, namely the ideal gas law, which is given as:

$$P = \frac{\rho_g R_u T_g}{\bar{M}} \tag{3.2}$$

where P $[Pa]$ is the absolute pressure, R_u $[J/kmolK]$ is the universal gas constant, T_g $[K]$ is the cell gas temperature, and $\bar{M}$ $[kg/kmol]$ is the mean molecular weight of the mixture calculated using the following expression

$$\bar{M} = \left(\sum_{k=1}^{N} \frac{Y_k}{M_k} \right)^{-1} \tag{3.3}$$

where Y_k $[kg/kg]$ is the mass fraction for species k and M_k is the molecular weight of species k.

For this work, the variation of the gas density due to pressure variations are negligible compared to the variation induced due to temperature changes, thus the pressure can be assumed constant in the state Equation (3.2). However, the flow being modelled is highly turbulent, and therefore the Reynolds/Favre averaged form of the Navier-Stokes (RANS) governing equations were used. The quasi steady-state form of Equation (3.1) is written as:

$$\frac{\partial}{\partial x_i}(\rho_g \bar{u}_i) = S_{con} \tag{3.4}$$

Subsequent formulations of the governing equations are written using the Reynolds averaged form, with the time-dependent term and overbar on the mean fluid variables (e.g. $\bar{u}_i$) are dropped for the sake of simplification.

3.1.2 Species transport

To correctly account for the transport of reactant and product species throughout the boiler gas domain the species transport approach was applied. The species transport conservation equation resolves all the species mass fraction distributions. The transport equation takes the following form for a species mass fraction Y_k:

$$\frac{\partial}{\partial x_i}(\rho_g u_j Y_k) = -\frac{\partial}{\partial x_j}(\vec{J_k}) + \dot{\omega}_k + S_k \qquad (3.5)$$
$$k = 1, 2, 3...N$$

where $\dot{\omega}_k$ $[kg/m^3 s]$ represents the net rate of production or destruction of species k due to chemical reactions, and S_k is the source term of species k due to mass transport between the gas and solid phases. The $\vec{J_k}$ term is the mass diffusion flux, and for turbulent flows, it can be written as:

$$\vec{J_k} = -\left(\rho_g \vec{D}_k\right)\frac{\partial Y_k}{\partial x_j} + \rho_g \overline{u_j' Y_k'} \qquad (3.6)$$

where $\vec{D}_k$ $[m^2/s]$ is the binary diffusion coefficient, which is assumed constant for all the species [20]. This is a reasonable assumption since the turbulent flux of the species, occurring due to turbulent fluctuations, dominates. The resolution of the species turbulent flux ($\rho_g \overline{u_j' Y_k'}$) is provided in Section 3.1.5.

The species properties, such as the specific heat at constant pressure, thermal conductivity, and viscosity, are calculated using polynomials extracted from the National Institute of Standards and Technology (NIST) database [70]. The full list of polynomials used in this study are provided in Appendix C. All the gas mixture properties are subsequently calculated using the mass-weighted mixture approach.

3.1.3 Energy equation

The conservation of energy principle, or the first law of thermodynamics, states that energy can neither be destroyed nor created during a process: it can only change form [1]. Energy entering/leaving a system comes in various forms, such as microscopic, kinetic, and gravitational energies. The steady-state energy equation is written as:

$$\frac{\partial}{\partial x_i}(u_i[\rho_g E + P]) = \frac{\partial}{\partial x_j}\left[\lambda_l \frac{\partial T_g}{\partial x_j} + \rho_g \overline{u_j' E'} + u_i \tau_{eff}\right] + S_h \qquad (3.7)$$

where E $[J/kg]$ is the total energy of the fluid, λ_l $[W/mK]$ is the laminar thermal conductivity, $\rho_g \overline{u_j' E'}$ is the turbulent energy flux, further defined in Section 3.1.5, τ_{eff} is the viscous dissipation term, and S_h is the energy source term used to account for radiation, chemical reactions, and user-defined energy sources/sinks [21].

The total energy term is a function of the internal and kinetic energy [1], which is given below for compressible flows as:

$$E = h - \frac{P}{\rho_g} + \frac{u^2}{2} \qquad (3.8)$$

The sensible enthalpy h $[J/kg]$ for an ideal gas mixture is defined below as:

$$h = \sum_{k=1}^{N} Y_k h_k \tag{3.9}$$

where the individual species enthalpies are calculated using the expression for specific heat at constant pressure, determined as:

$$\begin{aligned} c_{p_k} &= \left(\frac{\partial h_k}{\partial T}\right)_P \\ h_k &= \int_{T_{ref}}^{T} c_{p_k} dT \end{aligned} \tag{3.10}$$

The energy source term, S_h, of Equation (3.7) includes a chemical reaction component calculated as:

$$S_{h,reaction} = -\sum_{k=1}^{N} \frac{h_k^0}{M_k} \dot{\omega}_k \tag{3.11}$$

where h_k^0 $[J/kmolK]$ is the enthalpy of formation of species k, and $\dot{\omega}_k$ is the net volumetric generation term for species k.

3.1.4 Momentum equation

Newton's second law states that the rate of change of momentum of a fluid equals the net force acting on the fluid body [20]. Two types of forces acting on an arbitrary control volume can be distinguished: body forces (e.g. electromagnetic and gravitational) and surface forces (e.g. pressure and viscous). It is common practice to use the contributions due to surface forces as separate terms and to include the effects of body forces as source terms [20]. The RANS form of the momentum equation is given as:

$$\frac{\partial}{\partial x_i}(\rho_g u_i u_j) + \frac{\partial \bar{P}}{\partial x_j} = \frac{\partial}{\partial x_i}\left[\mu_l \left\{\frac{\partial u_j}{\partial x_i} + \frac{\partial u_i}{\partial x_j} - \frac{2}{3}\delta_{ij}\frac{\partial u_i}{\partial x_i}\right\}\right] + \frac{\partial}{\partial x_i}(-\rho_g \overline{u_i' u_j'}) + S_{mom} \tag{3.12}$$

where the Reynolds stress term $(-\rho\overline{u_i' u_j'})$, due to turbulence fluctuations, is related to the mean velocity gradient using the Boussinesq hypothesis, discussed in the subsequent section.

3.1.5 Turbulence closure

Turbulence can be described as the chaotic and random state of motion where the velocity and other flow properties change continuously with time [20]. There are three computational approaches that can be used to model turbulent flow regimes in combustion systems, namely the RANS approach, Large Eddy Simulation (LES) approach and Direct Numerical Simulation (DNS) approach [71]. However, the latter models are computationally expensive and are unsuitable for industrial applications and the current work. Thus, the present research employs the RANS method using the two-equation approaches to resolve the turbulence field. The $k-\varepsilon$ and the realizable $k-\varepsilon$ models are the most suitable approaches used in modelling reactive flows (refer to [13], [23] and [72]), where the kinetic energy and dissipation rate are solved in parallel with the conservation equations.

The standard $k-\varepsilon$ model performs well for confined boundary layer flows [20] but does not perform well for flows with high mean shear rates or large separation zones [73], which is the case for swirling jet flows. Thus, the realizable $k-\varepsilon$ model performs better when the flow has a strong streamline curvature, vortices, and jets [73], which are all present within a utility-scale pulverised fuel boiler. The inaccuracies of the standard $k-\varepsilon$ model are due to the poor prediction of the spreading rate for antisymmetric jets due to the dissipation rates model formulation.

The realizable $k-\varepsilon$ model, as developed by Shih et al. [73], makes use of a new formulation of the turbulent viscosity (μ_t). The formulation uses a variable C_μ and a new dissipation rate model based on the mean-square vorticity fluctuations. The resultant steady-state realizable $k-\varepsilon$ transport equations for the kinetic energy and dissipation rate are written as:

$$\frac{\partial}{\partial x_j}(\rho_g k u_j) = \frac{\partial}{\partial x_i}\left\{\left(\mu_l + \frac{\mu_t}{\sigma_k}\right)\frac{\partial k}{\partial x_j}\right\} + G_k G_b - \rho_g \varepsilon - Y_M \tag{3.13}$$

$$\begin{aligned}\frac{\partial}{\partial x_j}(\rho_g \varepsilon u_j) &= \frac{\partial}{\partial x_i}\left\{\left(\mu_l + \frac{\mu_t}{\sigma_\varepsilon}\right)\frac{\partial \varepsilon}{\partial x_j}\right\} + \rho_g S C_1 \varepsilon + \rho_g C_2 \frac{\varepsilon^2}{k+\sqrt{\vartheta\varepsilon}} - C_{1\varepsilon}\frac{\varepsilon}{k}C_{3\varepsilon}G_b \\ C_1 &= max\left(0.43, \frac{\eta}{\eta+5}\right),\ \eta = S\frac{k}{\varepsilon},\ S = \sqrt{2S_{ij}S_{ij}}\end{aligned} \tag{3.14}$$

where G_b, G_k and Y_M in Equations (3.13) and (3.14) are the turbulence production term due to buoyancy forces, the turbulence production term due to velocity gradients and the term that accounts for the fluctuating dilatation of compressible turbulent flows, respectively. At the same time, the model constants C_2, C_{1_ε}, σ_k, and σ_ε have set values of 1.9, 1.44, 1.0, and 1.2, respectively.

As with the standard $k-\varepsilon$ model, the realizable $k-\epsilon$ model makes use of a turbulent viscosity expressed as a function of k and ϵ, written as:

$$\mu_t = \rho_g C_\mu \frac{k^2}{\varepsilon} \tag{3.15}$$

where the difference lies in the non-constant formulation of the variable C_μ employed by the realizable $k-\varepsilon$ model. The variable C_μ is calculated as follows:

$$\begin{gathered} C_\mu = \frac{1}{A_0 + A_s \frac{kU^*}{\epsilon}} \\ A_0 = 4.04,\ A_s = \sqrt{6}cos\phi,\ \phi = \frac{1}{6}cos^{-1}\left(\sqrt{6}W\right), W = \frac{S_{ij}S_{jk}S_{ki}}{\tilde{S}^3},\ \tilde{S} = \sqrt{S_{ij}S_{ij}} \\ U^* = \sqrt{S_{ij}S_{ij} + \tilde{\Omega}_{ij}\tilde{\Omega}_{ij}},\ \tilde{\Omega}_{ij} = \Omega_{ij} - 2\epsilon_{ijk}\omega_K,\ \Omega_{ij} = \bar{\Omega}_{ij} - \epsilon_{ijk}\omega_K \end{gathered} \tag{3.16}$$

where $\tilde{\Omega}_{ij}$ is the mean rate of rotation tensor in a moving reference frame with an angular velocity ω_K $[rad/s]$. The Boussinesq hypothesis is typically employed along with a two-equation turbulence model, which relates the Reynolds stresses to mean velocity gradients and the kinetic/dissipation energy in the flow field [74] and is written as:

$$-\rho_g \overline{u_i' u_j'} = \mu_t \left(\frac{\partial u_i}{\partial x_j} + \frac{\partial u_j}{\partial x_i}\right) - \frac{2}{3}\delta_{ij}\left(\rho_g k + \mu_t \frac{\partial u_k}{\partial x_k}\right) \tag{3.17}$$

Using the turbulent dynamic viscosity, along with the realizable $k-\varepsilon$ model, the turbulent flux terms, as seen in the conservation Equations (3.5), (3.8) and (3.12), can be closed off. Furthermore, the Reynolds stress term of Equation (3.12) is closed by substituting in Equation (3.17), allowing for the turbulent velocity field to be resolved on the computational domain. The turbulent energy flux from Equation (3.7) can be modelled using the gradient assumption as shown by [71]:

$$\rho_g \overline{u_j' E'} = \frac{c_p \mu_t}{Pr_t} \frac{\partial T_g}{\partial x_j} \tag{3.18}$$

with the default turbulent Prandtl number Pr_t of 0.85 used by Fluent ® v19.5. From this, the turbulent thermal conductivity (as a function of the turbulent viscosity) can be defined as:

$$\lambda_t = \frac{c_p \mu_t}{Pr_t} \tag{3.19}$$

Utilising Equation (3.19) an effective thermal conductivity can be obtained for the energy conservation Equation (3.7) as:

$$\lambda_{eff} = \lambda_l + \lambda_t \tag{3.20}$$

Similarly, the turbulent species flux, found in Equation (3.6), can be equated to the gradient of the species mass fractions multiplied by a proportional value as a function of the turbulent viscosity, which is given as:

$$\rho_g \overline{u_j' Y_k'} = \frac{\mu_t}{Sc_t} \frac{\partial Y_k}{\partial x_j} \tag{3.21}$$

where Sc_t is the turbulent Schmidt number. Fluent® v19.5 uses a default Schmidt number of 0.7 [21]. Generally, in turbulent combustion, the turbulent diffusion overwhelms the laminar diffusion, and the effect of laminar diffusion is almost negligible.

3.2 Discrete phase modelling

The conventional procedure for modelling particle dispersion and solid phase combustion using CFD is via using the discrete phase modelling (DPM) approach. The approach tracks the individually dispersed solid fuel particles in a Lagrangian framework, with the continuous gas-phase being resolved in a Eulerian reference frame. ANSYS Fluent® does offer Eulerian multiphase approaches to model particle dispersion, called the mixture model and Eulerian model. However, these models are incompatible with non-premixed, partially premixed, and premixed combustion models [21]. This section discusses the DPM approach in relation to the governing equations of motion and the turbulence interactions that the solid particles would experience.

3.2.1 Equations of motion

A discrete phase particle trajectory is calculated by considering a force balance using Newton's second law. The force balance considers the particle inertial effects and the forces, such as drag and gravity, acting on the particle. Thus, the equation of motion for a dispersed particle is given in Equation (3.22) as:

$$m_p \frac{d\vec{u}_p}{dt} = F_D(\vec{u}_p - \vec{u}_g) + \frac{\vec{g}(\rho_p - \rho_g)}{\rho + g} + S_{PF} \tag{3.22}$$

where m_p, $\vec{u}_p$, $\vec{u}_g$, F_D, ρ_p and S_{PF} are the particle mass, particle velocity, gas/fluid phase velocity, drag force factor, particle density and additional forces acting on the particle, respectively. The drag force factor is defined using the particle relaxation time, from the works of Gosman and Ioannides [75], as:

$$F_D = \frac{3\mu}{\rho_p d_p^2} \frac{C_d Re_d}{4} \tag{3.23}$$

where d_p, C_d, and Re_d is the particle diameter, drag force coefficient and the relative Reynolds number based on the diameter of the particle. The relative Reynolds number is defined as follows:

$$Re_d = \frac{\rho d_p |\vec{u}_p - \vec{u}_g|}{\mu_{eff}} \tag{3.24}$$

The particles in pulverised fuel systems are typically modelled as smooth spherical particles. Thus, the drag force coefficient can be defined using the correlation of Morsi and Alexander [76] as:

$$C_D = a_1 + \frac{a_2}{Re_d} + \frac{a_3}{Re_d^2} \tag{3.25}$$

where constant a_1, a_2, and a_3 are varying constants applicable over several ranges of the relative Reynolds number.

3.3 Combustion modelling

There are fundamentally three criteria needed for a combustion process to commence namely a sufficiently high temperature (needed to activate chemical reactions), turbulence (adequate mixing of reactants and oxidiser), and residence time (to ensure complete combustion). A combustion process can usually be described as either being temperature limited, mixing limited, or product mixing limited.

The modelling of solid fuel combustion includes the modelling of both heterogeneous and gas-phase homogeneous reaction rates. Heterogeneous reactions form the basis of solid fuel processes and produce the oxidising reactants for the gas-phase homogeneous reactions to commence. The subsequent subsections discuss these methodologies.

3.3.1 Heterogeneous reactions

The solid fuel combustion process comprises four sequential steps: heating, evaporation/boiling, devolatilisation and char oxidation. The process is shown graphically in Figure 3.2 and includes the homogeneous gas reactions that occur in parallel depending on the availability of reactants and oxidiser.

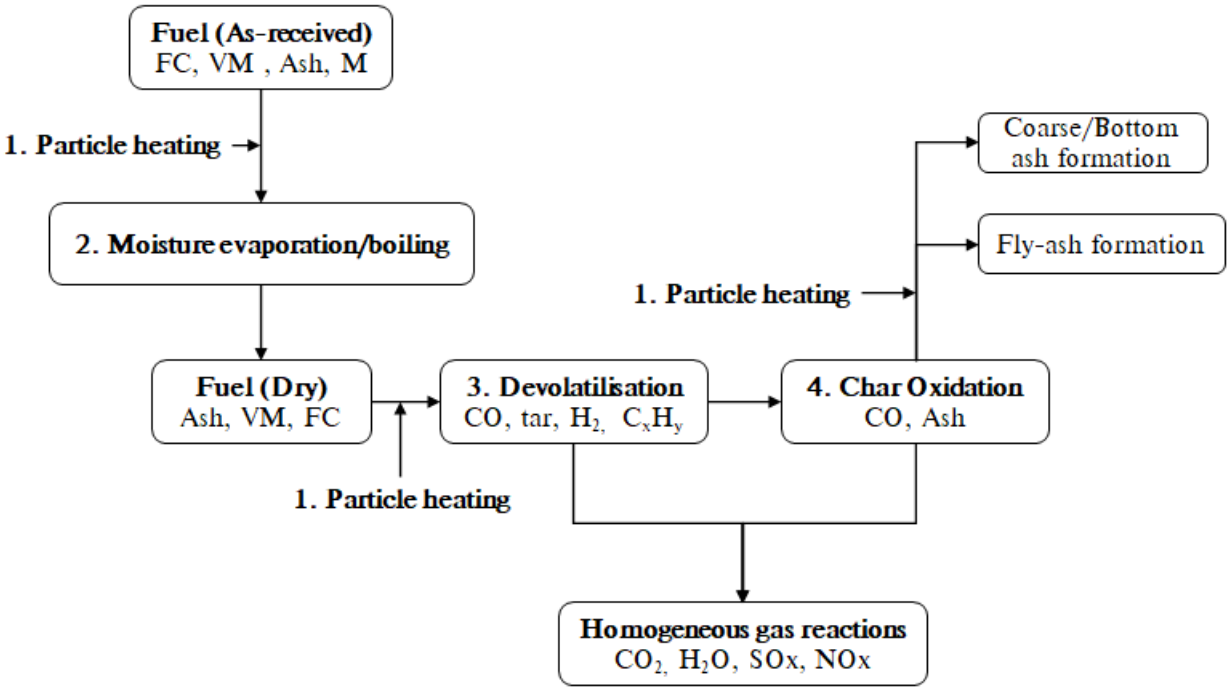

Figure 3.2: Total combustion process schematic

The solid fuel combustion steps are assumed to occur sequentially, meaning that for the devolatilisation step to occur, all the moisture must be driven out of the particle. The combustion process starts with the particles' initial heating, attributed to the phenomena of convection and radiation to/from the particle. Next, the particles are heated to a temperature of 373 $[K]$, at which point the moisture present in the particles begin to evaporate at constant temperature, adding mass to the surrounding gas-phase. The evaporation/boiling rate can be defined using a simple heat balance of the convective ($\dot{Q}_{conv}$) and radiative ($\dot{Q}_{rad}$) heat transfer to the particle, which is expressed in Equation (3.26) as:

$$\frac{dm_{evap}}{dt} = \frac{\dot{Q}_{conv} + \dot{Q}_{rad}}{h_{fg}} \tag{3.26}$$

where h_{fg} is the latent heat of vaporisation.

The devolatilisation process follows with the 'volatiles' present in the fuel being liberated. The initialisation temperature of the devolatilisation process was found to vary between $553-800$ $[K]$ for various coals by Ranade and Gupta [12]. Thus, particle heating needs to ensue after the moisture evaporation to bring the particles to the initialisation temperature.

The case studies of Sections 4.2 and 5.1 use devolatilisation temperatures of 773 $[K]$ and 553 $[K]$, respectively, since vastly different coals are combusted for each study. The works of Sankar et al. [8] discuss the two main types of devolatilisation models, namely Arrhenius and phenomenological type models. The phenomenological models exhibit the following advantages: predicting the tar and gas yields, nitrogen species yield and secondary pyrolysis reactions. However, the single-rate Arrhenius based models are generally easier to implement and computationally inexpensive, as shown by Farokhi and Birouk [77]. In the present work, the change in volatile mass of the fuel particles is calculated as follows using an Arrhenius type model:

$$\frac{dm_{vol}}{dt} = R_{vol}(m_{0,vol} - m_{vol}) \tag{3.27}$$

where R_{vol} $[1/s]$, $m_{0,vol}$ $[kg_{0,vol}]$ and m_{vol} $[kg_{vol}]$ are the Arrhenius rate, the initial volatile mass of the particle before combustion, and the mass of volatiles released from the particle during combustion, respectively. R_{vol}, is expressed in terms of the activation energy ($E_{a,vol}$ $[J/kmol]$) and pre-exponential factor (A_{vol} $[1/s]$) specific to every coal and is expressed as:

$$R_{vol} = A_{vol} exp\left(\frac{-E_{a,vol}}{R_u T_p}\right) \tag{3.28}$$

where T_p $[K]$ is the particle temperature.

A constant devolatilisation rate $R_{vol,cnst}$ $[1/s]$ can also be implemented when the coal kinetic parameters are unknown; thus, a constant rate can be employed with the change of volatile mass being formulated as [21]:

$$\frac{dm_{vol}}{dt} = R_{vol,cnst}(f_{0,vol}m_{0,vol}) \tag{3.29}$$

where $f_{0,vol}$ is the fraction of volatile matter initially present in the particle [21]. During the devolatilisation process the particles tend to undergo swelling, which is caused by the release of pressure due to the trapped volatile matter. To capture this phenomenon the relationship defined in the ANSYS Fluent ® v19.5 theory guide [21] was employed using a swelling coefficient of 1.4 for the case studies of Sections 4.2 and 5.1.

Char oxidation can commence following the complete release of volatiles from the solid phase to the gas-phase. The diffusion-kinetics limited model of Baum and Street [78] was used to model the surface combustion of the char. The model assumes that char oxidation is influenced by the diffusion and kinetic rate of the oxidation process. The rate of char oxidation rate can be expressed as follows:

$$\frac{dm_c}{dt} = -A_p \frac{R_c R_{diff}}{R_c + R_{diff}} \tilde{P}_{O_2} \tag{3.30}$$

where A_p $[m^2]$ and $\tilde{P}_{O_2}$ $[Pa]$ are the particle surface area and partial pressure of the oxygen surrounding the particle. The diffusion rate coefficient, R_{diff}, is calculated as:

$$R_{diff} = \frac{5 \times 10^{-12}}{\bar{d}_p} \left(\frac{T_p + T_g}{2} \right)^{0.75} \tag{3.31}$$

Furthermore, the chemical rate coefficient, R_c, is expressed in terms of an Arrhenius rate as:

$$R_c = A_c exp \left(\frac{-E_{a,c}}{R_u T_p} \right) \tag{3.32}$$

The char oxidation model can be configured to produce either species CO_2 or CO. Boyd et al. [79] show that for a product species of CO_2, the heat absorbed by the particle near the particle's surface, due to the oxidation of char to CO, comes to a value of 30%. On the other hand, using a product species of CO, the heat absorbed by the particle near the particle surface comes to a value of 100%. The oxidation reaction is thus written as:

$$C_{(s)} + 0.5O_{2(g)} \rightarrow CO_{(g)} \tag{3.33}$$

where the heat of reaction for the char burnout of Equation (3.33) is set to 1.01×10^7 J/kg [1]. The volatiles from the devolatilisation and the CO produced from the char oxidation reaction are released into the gaseous phase. Provided there is an oxidiser, a sufficiently high temperature, and adequate mixing; these species will react and release heat into the domain.

3.3.2 Homogeneous reactions

Homogeneous gas reactions account for most of the heat released into the domain for solid fuel combustion processes [8]. The gaseous species released from the heterogeneous reactions described previously are given in Equation (3.34).

$$\begin{aligned} &C_xH_yO_zN_mS_n + iO_2 \rightarrow xCO + \frac{y}{2}H_2O + nSO_2 + \frac{m}{2}N_2 \\ &i = \frac{x}{2} + \frac{y}{4} + n - z \\ &CO + 0.5O_2 \rightarrow CO_2 \end{aligned} \tag{3.34}$$

where $C_xH_yO_zN_mS_n$ is the pseudo volatile species released into the domain. The rate of gas-phase reactions is a function of the Arrhenius rates of the chemical reactions and the turbulent-chemistry interactions.

Two main approaches are used to model the gas-phase reactions in solid fuel systems [8]: fast reaction assumption models and the detailed chemical kinetic models. The Eddy-dissipation concept (EDC), as proposed by Magnussen [80], forms part of the detailed kinetic model and solves the chemical kinetic differential equations in the fine cell structure regions of each cell, making the EDC model very computationally expensive. The EDC model has been successfully used in predicting the pollutant emissions such as CO and NO_x for both biomass and CFPP boilers ([81],[82]).

According to Sankar et al. [8], the turbulent mixing time scales found in CFPP furnaces are typically much larger than the chemical kinetic time scales. In addition, the chemical gas-phase reactions occur at a rapid rate. Thus, the use of the EDC model was not utilised in modelling the homogeneous reactions. Furthermore, fast reaction models have been used successfully in modelling the gas-phase reactions found in boilers since the time scale of the chemical reactions are much smaller than the turbulent mixing time scales ([13],[83]). Thus, the chemical kinetic rates can be neglected, and the fast reaction chemistry can be assumed. The eddy dissipation model (EDM) proposed by Magnussen et al. [84] is based on the consideration of the reaction rate to be dependent on the mean species concentration instead of the species fluctuation as in the Eddy-break up (EBU) model of Spalding [85].

ANSYS Fluent ® v19.5 provides the finite rate/eddy dissipation model (FR/EDM), which is used in the current study. It calculates the turbulent chemical reaction rate in relation to the dissipation/mixing time scales of the products and reactants, which in turn is used to determine whether the combustion reaction is kinetically limited or mixing limited. The FR/EDM model can predict the distributions of the average temperature and major species reasonably well, which are necessary to adequately resolve the various heat transfer phenomena experienced in a utility-scale boilers heat exchanging surfaces. However, the predictions of pollutants such as CO and NO_x are deemed unacceptable, as indicated by Farokhi et al. [77].

The FR/EDM model calculates three rates, namely the chemical Arrhenius rate of the reaction (R_r), the rate of turbulent production eddies ($R_{k,r,P}$) and the rate due to the dissipation of reaction eddies ($R_{k,r,R}$). The smallest of the three is used as the net production of species into the domain. The finite rate model is crucial as it acts as a kinetic switch in combustion systems near fuel and oxidiser inlets [21]. However, in the absence of fuel-specific kinetic characteristics, the EDM model has exhibited adequate resolution of pulverised fuel combustion. The reaction rates are expressed below in Equations (3.35) through (3.37):

$$R_r = A_r exp\left(\frac{-E_{a,r}}{R_u T_g}\right)\left[\vartheta'_{k,r} - \vartheta_{k,r}\right]\prod_L [C_{l,r}]^{m,r} \tag{3.35}$$

$$R_{k,r,P} = \vartheta_{k,r} M_{w,k} AB\rho\frac{\varepsilon}{k} min\left(\frac{\sum_p Y_p}{\sum_j \vartheta_{j,r} M_{w,j}}\right) \tag{3.36}$$

$$R_{k,r,R} = \vartheta_{k,r} M_{w,k} A\rho\frac{\varepsilon}{k} min\left(\frac{Y_R}{\varepsilon_{R,r} M_{w,R}}\right) \tag{3.37}$$

In Equation (3.35), $\vartheta_{k,r}$ is the stoichiometric coefficient of reactant k in reaction r, $[C_{l,r}]^{m,r}$ is the molar concentration of species l in reaction r with a rate exponent of m. In Equations (3.36) and (3.37), Y_p is the mass fraction of any product species, Y_R is the mass fractions of any reactant species, A and B are model constants, while $M_{w,j}$ is the molecular weight of the j^{th} species. According to Sankar et al. [8], the failings of the fast chemistry assumption-based models is the drawback of only using a single or two-step chemical reaction mechanism, making the model unsuitable for multi-step reactions. In the present work, the focus is not on the formation of pollutants. Thus, the use of the FR/EDM model was deemed acceptable.

3.4 Radiative heat transfer modelling

Solid fuel combustion systems incorporate the three fundamental modes of heat transfer, namely, radiation, convection, and conduction, which can all occur simultaneously [86]. In solid fuel furnaces, radiation heat transfer accounts for a large portion of heat absorption by the combustion chamber walls [42]and thermal energy transport through the gas-particulate dispersion volume. Therefore, modelling the gaseous and particle heat transfer interactions due to radiation is an essential aspect of any solid fuel combustion process to accurately represent reality. The radiation transport between the gas, particles and heat exchanger surfaces is solved by applying the radiation transport equation (RTE), which is shown in Equation (3.38) for a gray-participating gas and particle medium [87].

$$\underbrace{\frac{dI(r,\omega)}{ds}}_{\text{Radiation intensity}} = \underbrace{\alpha_g I_b}_{\text{Gas emission}} + \underbrace{\alpha_p I_{b,p}}_{\text{Particle emission}} - \underbrace{(\alpha_g + \alpha_p + \sigma_p) I(r,\omega)}_{\text{Absorption and scattering losses}} + \underbrace{\frac{\sigma_p}{4\pi} \int_{4\pi} I(r,\omega)\Phi d\omega}_{\text{Internal scattering}} \tag{3.38}$$

where $dI(r,\omega)$ $[W/m^2 sr]$ is the radiation intensity at position r and in direction ω, I_b is the intensity of radiation emitted by a black body, α_g $[1/m]$ is the overall gas absorption coefficient, α_p $[1/m]$ is the particle absorption coefficient, and Φ is the phase function. Assuming isotropic scattering the phase function tends to zero.

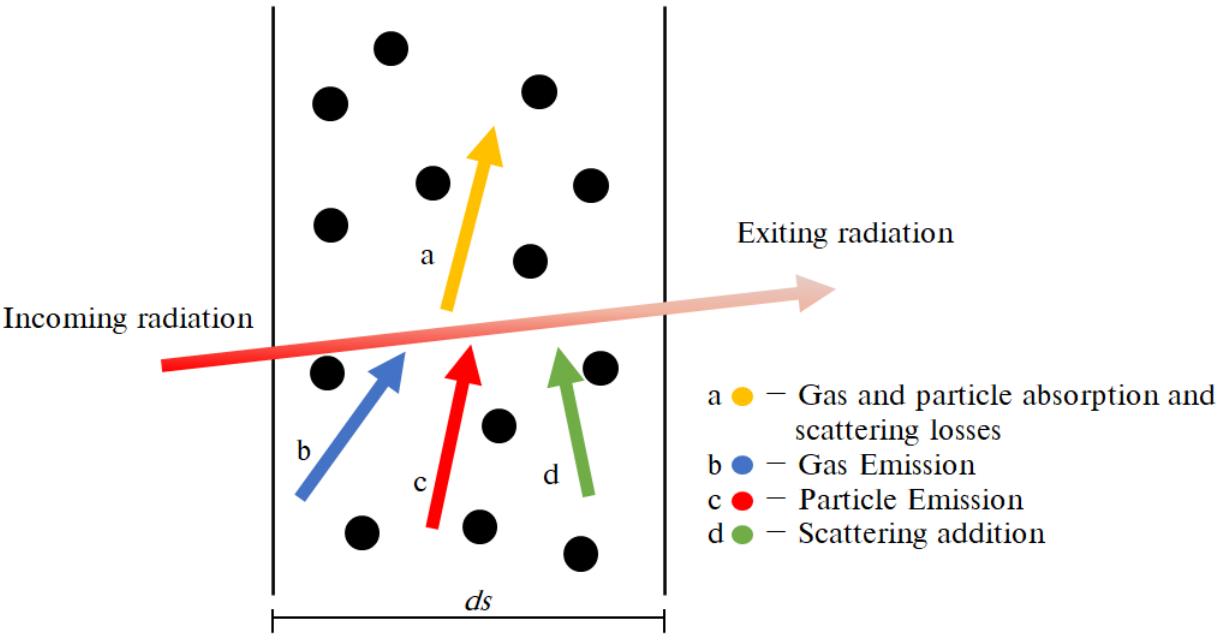

Figure 3.3: Radiative heat transfer attenuation contributions

Figure 3.3 graphically highlights the attenuation effects that the right-hand side terms of Equation (3.38) have on a radiative beam passing through a gas and particle-laden domain in the path length ds.

3.4.1 Radiation numerical models

The exact solution of the RTE for radiative heat transfer in solid fuel combustion systems is not available ([88] and [89]). The main approximate approaches include either a statistical, zonal, or flux method. Statistical methods offer the most accurate method for simulating radiation. However, it is computationally expensive compared to zonal and flux methods. The Hottel zone method [90] uses multiple zones in the computational domain with uniform temperature and radiation properties, with the radiation heat exchange being estimated based on direct exchange areas. Flux methods assume that the radiation intensity is uniform over discrete intervals of the solid angle. This assumption allows the transformation of the RTE (Equation (3.38)) from its integro-differential form to that of a differential form. This differential form can easily be resolved in a CFD framework making the flux methods the most popular approach when modelling solid fuel combustion systems [8].

Approximate methods, such as the P-1 harmonics series and Discrete Ordinates (DO) method (a flux model), have been widely used in modelling solid fuel combustion furnaces. The DO method solves the RTE for a finite number of discrete solid angles, each associated with a direction vector, and has been used by researchers to accurately resolve the radiative field in utility-scale boilers [27, 91]. However, the added transport equations increase the computational burden. The P-1 radiation model is the simplest approximation of the P-N model, which is based on expanding the local radiation intensity in terms of orthogonal series of spherical harmonics [87]. The P-1 model is considered suitable for systems with a large optical thickness and has been used successfully for modelling solid fuel systems, as in the works of Asotani et al. [92], Blackreedy et al. [93] and Sazhin et al. [94]. Both models are popular in pulverised fuel systems since the models can account for particulate effects and conform to control volume formulations [12].

The present study makes use of the P-1 radiation model due to its computational efficiency when compared to the DO method ([94] & [34]). Ranade and Gupta [12] illustrated minimal differences between the two radiation models (P-1 and DO) for the resultant wall heat transfer rate when modelling a 210 $[MW_e]$ CFPP boiler. The P-1 transport equation for modelling gray radiation along with the particulate effects is written as follows:

$$\begin{aligned} \frac{\partial}{\partial x_i}(\Gamma_p \frac{\partial}{\partial x_j} G) &= (\alpha_g + \alpha_p)G - 4\pi \left(\alpha_g \frac{\sigma_{SB} T_g^4}{\pi} + E_p \right) \\ \Gamma_p &= \frac{1}{3(\alpha_g + \alpha_p + \sigma_p)} \end{aligned} \tag{3.39}$$

where G $[W/m^2]$ is the incident radiation flux, σ_{SB} $[W/m^2K^4]$ is the Stefan-Boltzmann constant, and E_p $[W/m^3]$ is the equivalent emissive power of the particles. Scattering due to the gas-phase (σ_g) is assumed negligible compared to particle scattering effects [95].

3.4.2 Gas radiative effects

Using the gray gas assumption, the gaseous mixture absorption coefficient (α_g) is calculated using the domain-based weighted-sum-of-gray-gases-model (WSGGM). This model captures the radiative effects of the tri-atomic gas species CO_2, H_2O, and SO_2, produced from the homogeneous gas reactions. The WSGGM assumes that total emissivity can be evaluated as follows [88, 96]:

$$\epsilon_g = \sum_{i=0}^{I} a_{\epsilon,i}(T_g) \left[1 - exp(-\kappa_i \tilde{P}_m L_{mb})\right] \tag{3.40}$$

where $a_{\epsilon,i}$ denotes the emissivity weighting factors for the i-th gray gas, κ_i $1/mPa$ is the i-th gray gas absorption coefficient, $\tilde{P}_m$ is the partial pressure of the mixture, and L_{mb} $[m]$ is the mean beam length. The work of Smith et al. [96] is used to obtain the values for $a_{\epsilon,i}$ and κ_i. The values of the emissivity weighting factors depend on the gas temperature and can conveniently be written as a polynomial function of order $(J-1)$, which is shown in Equation (3.41).

$$a_{\epsilon,i} \approx \sum_{j=1}^{J} b_{\epsilon,i,j} T_g^{j-1} \tag{3.41}$$

where $b_{\epsilon,i,j}$ are the polynomial emissivity coefficients. By calculating the emissivity using Equation (3.40), the gaseous absorption coefficient can be estimated using the following correlation.

$$\alpha_g \approx \frac{ln(1-\epsilon_g)}{L_{mb}} \tag{3.42}$$

where $L_{mb}\,[m]$ is the mean beam length.

3.4.3 Particle radiative effects

The particle radiative effects are defined by the equivalent emission (E_p), absorption coefficient (α_p) and scattering coefficient (σ_p). These parameters, as described by Modest [88], are subsequently defined in Equations (3.43) through (3.45) as:

$$E_p = \lim_{V \to 0} \sum_{n=1}^{N} \frac{\epsilon_{p,n} A_{proj,n} \sigma_{SB} T_p^4}{\pi V} \tag{3.43}$$

$$\alpha_p = \lim_{V \to 0} \sum_{n=1}^{N} \frac{\epsilon_{p,n} A_{proj,n}}{V} \tag{3.44}$$

$$\sigma_p = \lim_{V \to 0} \sum_{n=1}^{N} (1-\epsilon_{p,n})(1-f_{p,n}) \frac{A_{proj,n}}{V} \tag{3.45}$$

where $\epsilon_{p,n}$, $A_{proj,n}$ $[m^2]$ and $f_{p,n}$ are the emissivity, projected area and scattering factor of a particle n.

The parameters $\epsilon_{p,n}$, $A_{proj,n}$ and $f_{p,n}$ are calculated using a Lagrangian approach, where the summation of particles (N) present in a volume is computed during particle tracking of the dispersed phase. However, this work uses a Eulerian approach to resolve particle dispersion and radiation transport. The necessary Eulerian transformations will be presented in the next chapter.

The particle emissivity and scattering factor values are typically set to constant values of 0.9 and 0.6, respectively, as seen in the works of Yang et al. [97] and Guo et al. [98]. However, conversion-dependent formulations, developed by Lockwood et al. [26] and Yin et al. [27], have been successfully implemented by researchers Laubscher and Rousseau [29]. Their findings highlighted the impact particle radiative properties have in resolving wall heat fluxes and radiation transfer, with the particle properties overwhelming gaseous radiation in pulverised fuel combustion systems. The formulations for both emissivity and the particle scattering factor are defined in Equations (3.46) and (3.47) as:

$$\epsilon_{p,n} = 0.4U_C + 0.6 \tag{3.46}$$

$$f_{p,n} = 0.9U_{VM,C} + 0.6(1 - U_{VM,C}) \tag{3.47}$$

where U_C $[kg_C/kg]$ and $U_{VM,C}$ $[kg_{VM,C}/kg]$ are the fraction of unburned carbon and the fraction of unburned combustibles (volatiles and carbon) present in the particle, respectively.

One of the products of solid fuel combustion is ash, which is the solid inert residue left over after the oxidation processes are completed. Ash is classified as either bottom or fly ash. Bottom ash is collected in the hopper of a furnace and is characterised as large and heavy particles, whereas fly ash are small particles carried along with the flue gas through the boiler gas path. Typically, bottom ash makes up 10% to 20% ([8]), with fly ash making up the difference. Fly ash plays an important role in radiation, for it contributes to the radiative emission and impedes the transport of radiation to the wall through scattering. Equations (3.46) and (3.47) aid in determining the radiative contributions of fly ash particles in solid fuel combustion systems, as the fly ash particles will contribute to the emission and scattering throughout the domain.

In addition, ash contributions can lead to slagging and fouling of heat exchanging components. Both phenomena are essentially the same, with slagging referring to the furnace section and fouling referring to the downstream heat exchanger components [42]. At a temperature above 1400-2000 $[K]$ [24], ash particles tend to melt/soften, which lowers the viscosity of the ash particles, which results in particles sticking to heat exchanger walls and solidifying. This phenomenon creates an ash layer, which impedes heat transfer to the working fluid. In addition, the ash layer also affects the surface emissivity, thereby further degrading the radiative heat transfer to the walls [99]. Figure 3.4 illustrates the heat transfer through an ash deposition layer found in most pulverised fuel furnaces and heat exchanging components.

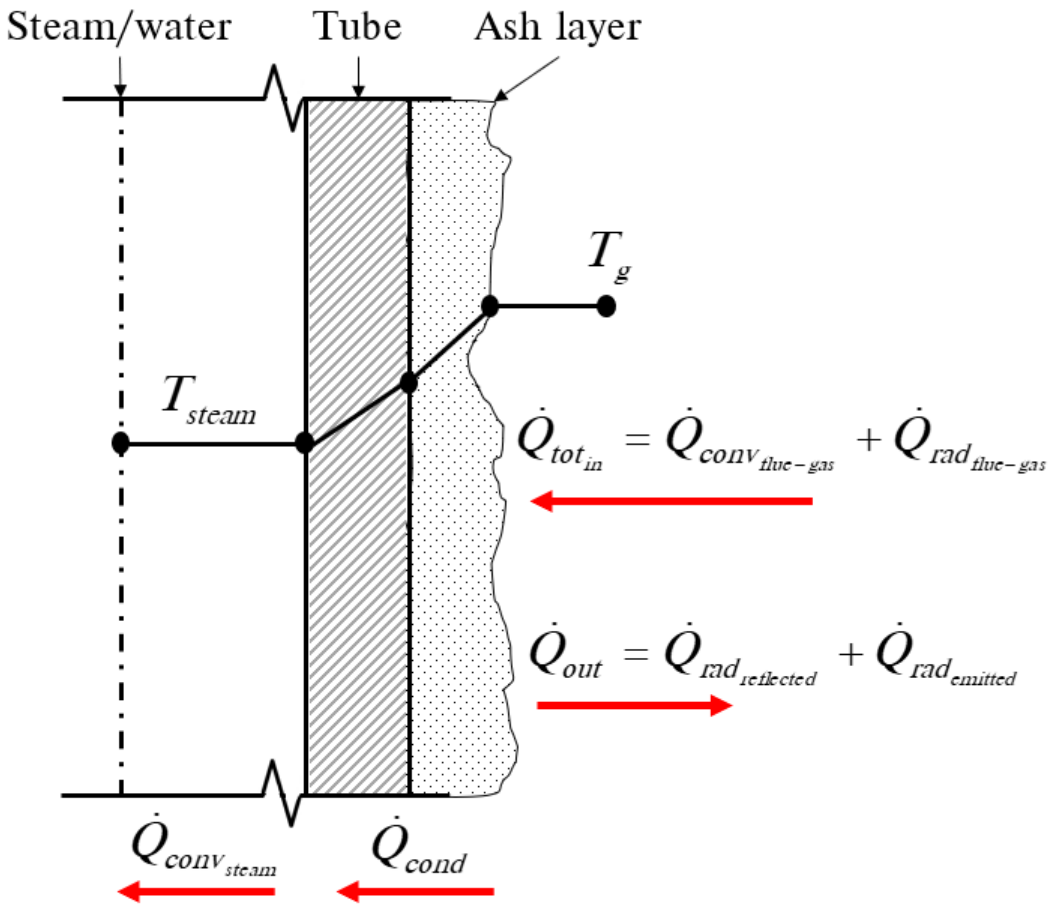

Figure 3.4: Heat transfer through an ash layer wall

The modelling of a fouling/slagging layer is important to adequately resolve the heat transferred to the walls of the heat exchanger components. Thermal resistance values in the range of $0.0047 - 0.015$ $[K/W]$ are typically used when the thickness of the ash layer is unknown [42]. Thus, the boundary conditions for a numerical study must include the effects of an ash layer to account for the expected reduction in heat transfer to the walls.

3.5 Process modelling governing equations

Discretised, 1-D process models can capture the thermofluid response of a CFPPs water/steam network consisting of multiple heat exchanger inner and outer fluid streams. The inner fluid stream can consist of a two-phase mixture made up of water and steam, whereas the outer fluid stream consists of a homogeneous mixture of combustion gases. Thus, the modelling of the water-side and fire-side streams requires different formulations of the governing equations, which are provided in the subsequent sections.

1-D process models are computationally inexpensive and efficient [10] due to the small number of solution variables and lower dimensional discretisation. Analysing these thermal-fluid networks requires the numerical solution of the fluid dynamic and heat transfer governing equations. The governing conservation equations are similar to those discussed in Section 3.1; however, turbulence modelling is neglected and is rather included by the use of turbulent friction factor correlations. Furthermore, a 1-D coordinate system is used.

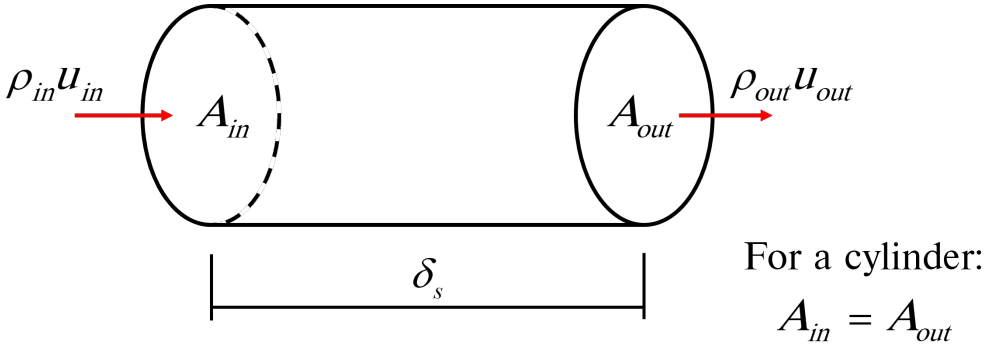

Figure 3.5: 1-D cylindrical control volume

Figure 3.5 illustrates a cylindrical 1-D control volume over distance δ_s, the 1-D assumption states that the variables will change only in the flow direction, with the value at any given point considered the average value across the cross-sectional area (A_{in}) of the control volume [100].

3.5.1 Water-side modelling

Modelling the water-side component of heat exchangers found in CFPPs requires the use of the homogeneous two-phase mixture approach, since water and steam can exist in parallel due to the phase change phenomenon. Heat exchangers that exhibit this phenomena are primarily the furnace evaporator walls and the downstream superheaters and reheaters. The modelling approach assumes that the liquid and gas-phases are distributed evenly over the cross-sectional area of the flow path and that the pressure, temperature, and velocity of the phases are equal [100]. The homogeneous two-phase mixture approach uses the mixture void fraction (ψ) and mixture density (ρ_M) which can be defined using the densities of the liquid (ρ_L) and gas (ρ_G) phases and the thermodynamic quality/gas mass fraction (x). The correlations are expressed in Equations (3.48) and (3.49).

$$\psi = \frac{\rho_L x}{\rho_L x + \rho_G(1-x)} \tag{3.48}$$

$$\rho_M = (1-\psi)\rho_L + \psi\rho_G \tag{3.49}$$

Applying the mixture density, the steady-state governing equations, written for a 1-D coordinate system, can be defined for mass, momentum and energy.

Mass conversation:

$$\frac{\partial}{\partial s}(\rho_M A u) = 0 \tag{3.50}$$

Momentum conservation:

$$\frac{1}{A}\frac{\partial}{\partial s}(\rho_M A u^2) = -\frac{\partial P}{\partial s} - \frac{\tau_W p}{A} - \rho_M g \frac{\partial z}{\partial s} \tag{3.51}$$

where τ_W $[N/m^2]$ is the shear stress accounting for frictional forces and p $[m]$ is the perimeter of the control parameter. Finally, the energy conservation equation is written as:

$$\frac{1}{A}\frac{\partial}{\partial s}(\rho_M A u h_M) + \frac{1}{2A}\frac{\partial}{\partial s}(\rho_M A u^3) = \frac{\dot{Q}_w}{V} - g\rho_M u \frac{\partial z}{\partial s} \tag{3.52}$$

where h_M and $\dot{Q}_w$ are the effective mixture enthalpy and control volume heat additions, respectively. The effective mixture enthalpy is defined using the thermodynamic quality and is shown in Equation (3.53).

$$h_M = h_L(1 - x) + x h_G \tag{3.53}$$

Heat additions to the control volume would be transferred either by conduction, convection, or radiation. The water-side network of an integrated/coupled model typically has a heat flux coming into the control volume, which incorporates the gas side convective and radiative effects. Thus, conduction through the tube walls and internal forced convection must be considered when the input fluxes are known. Components that require external convection and radiation heat transfer are further discussed in Chapter 4. Conduction is a mode of heat transfer where no bulk fluid motion is present and is commonly found in solid materials. The amount of heat conducted through a solid material of thickness dx and a surface area A_s, can be defined in differential form as follows:

$$\dot{Q}_{cond} = -\lambda A_s \frac{dT}{dx} \tag{3.54}$$

This formulation is known as Fourier's law of heat conduction [86]. Convection heat transfer, as with conduction, requires the presence of a material medium but differs in its requirement of fluid motion to be present. Convection can be described as either forced (external or internal) or natural, with the latter being neglected in this discussion. The rate of heat transfer due to convection can be written using Newton's law of cooling [86], expressed as:

$$\dot{Q}_{conv} = \tilde{h} A_s (T - T_\infty) \tag{3.55}$$

where $\tilde{h}$ $[W/m^2K]$ is the convective heat transfer coefficient. Convective heat transfer correlations are derived using empirical data and non-dimensional analysis of the heat transfer coefficient, with the Nusselt number being defined as:

$$Nu = \frac{\tilde{h}_{conv} L_c}{\lambda} \tag{3.56}$$

where L_c is the characteristic length. The Nusselt number represents the enhancement of heat transfer through a fluid layer as a result of convection relative to conduction across the same layer [86].

The internal forced convection coefficient for a cylinder can be expressed either using the popular Dittus-Boelter [101] equation or the more complex Gnielinski [102] equation. The expressions are given in Equations (3.57) and (3.58), respectively.

The Dittus-Boelter correlation is written as follows:

$$\tilde{h} = \frac{Nu_{DB}\lambda}{d_h} = \frac{\lambda}{d_h} 0.023 Re^{0.8} Pr^n \tag{3.57}$$

where for the heating of a fluid n=0.4 and cooling of a fluid n=0.3. The Gnielinski expression is written as follows:

$$\tilde{h} = \frac{Nu_G\lambda}{d_h} = \frac{\lambda}{d_h} \frac{0.125\tilde{f}(Re-1000)Pr}{1+12.7(0.125\tilde{f})^{0.5}(Pr^{0.666}-1)} \tag{3.58}$$

where d_h $[m]$ and $\tilde{f}$ are the hydraulic diameter and friction factor, respectively.

3.5.2 Fire-side modelling

The solution of the fire-side or flue gas path in a CFPP can be solved by means of the single phase governing equations for 1-D flow regimes. Thus, the steady-state governing equations are written for the mass, momentum, and energy, with flue gas modelled as an incompressible gas.

Mass conservation:

$$\frac{\partial \rho u}{\partial s} = 0. \tag{3.59}$$

Momentum conservation:

$$\frac{\partial P_o}{\partial s} = \frac{\partial P_{o,M}}{\partial s} - \frac{f\rho|u|u}{2d_h} \tag{3.60}$$

where P_o $[Pa]$ and $P_{o,M}$ $[Pa]$ are the stagnation pressure and the pressure loss due to machine work, respectively. Finally, the energy equation can be written as:

$$\frac{\partial \rho u h_o}{\partial s} + \rho g u \frac{\partial z}{\partial s} = \dot{Q} - \dot{W} \tag{3.61}$$

where h_o $[J/kg]$ is the stagnation enthalpy of the flue gas mixture.

In a CFPPs furnace, heat transfer to the waterwall is mainly comprised of radiation with only about 5% of the total energy being transferred via convection [42, 103]. However, heat exchangers downstream of the furnace experience an increase in the convective heat transfer the further away the heat exchanger is from the flame ball [104]. Convective heat transfer to the external tube surfaces can be described using Equation (3.55), with the heat transfer coefficient being defined for forced external flow. The downstream heat exchangers are typically made up of tube banks which can either conform to an in-line or staggered arrangement.

An in-line tube arrangement is usually preferred over a staggered tube arrangement for solid fuel systems to minimise fly ash particles from fouling and impacting the downstream heat exchangers [103]. The current work makes use of the Zukauskas [105] Nusselt number correlations for in-line tube arrangements. The correlations have the following form:

$$\tilde{h} = \frac{Nu_Z \lambda}{d_h} = \frac{\lambda}{d_h} C Re_D^m Pr^n (\frac{Pr}{Pr_s})^{0.25} \tag{3.62}$$

where C, m, n are constants dependent on the Reynolds number. Pr_s is Prandtl number evaluated at the surface temperature. The Reynolds number Re_D is based on the maximum velocity, which for an in-line arrangement is written as:

$$u_{max} = \frac{S_T}{S_T - d} u \tag{3.63}$$

where S_T $[m]$, d $[m]$ and u $[m/s]$ are the transverse pitch, the pipe diameter, and the approach velocity, respectively. The subsequent 1-D process components of the case studies, found in Chapters 5 and 9, used the correlations of Equations (3.58) and (3.62) for determining the internal and external convective heat transfer coefficients, respectively.

Chapter 4

Numerical model development

This section aims to describe in detail the developed numerical CFD model. The CFD model uses a Eulerian representation for both the gas and particulate phases. The discussion focuses on the key differences between the developed model in relation to conventional CFD modelling. The key differences that will be elaborated on are listed as follows:

- The pseudo-particulate (Eulerian solid phase) interactions with the fluid phase concerning momentum transport.
- The resolution of the pseudo-particle transport through the domain.
- Combustion of the solid phase and the subsequent fluid phase interactions.
- Radiation modelling that includes the pseudo-particulate interactions.

Subsequently, a validation case study of a 2.165 $[MW_{th}]$ pulverised fuel swirl burner utilising the developed CFD model is presented and discussed. This case study illustrates the developed models' performance in terms of the computational time, multiple load validations and accuracy of key parameters. Figure 4.1 highlights the content that is discussed and indicates the research objectives addressed in this chapter for the readers convenience.

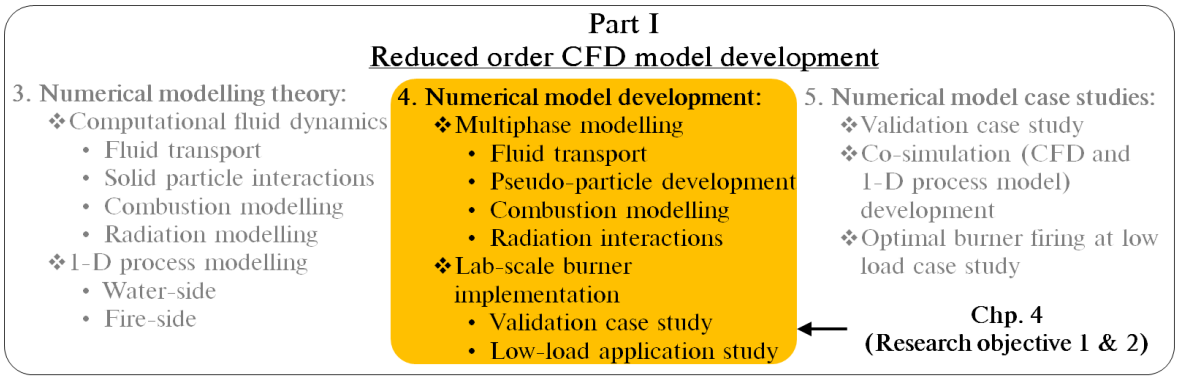

Figure 4.1: Content overview and research objectives addressed in Chapter 4

4.1 Multiphase modelling

The proposed EE model employs a reference frame whereby the gas and solid phases are assumed to be in an inter-penetrating continuum. The solid phase is best understood as a pseudo-particle component of the gas mixture modelled using scalar transport fields. Furthermore, the assumption of mechanical equilibrium is introduced, implying that the local mean velocities of the gas-phase and pseudo-particles are assumed to be the same (i.e. $\bar{u}_g \approx \bar{u}_p$), except for the calculation of convective heat transfer to or from the gas to the particulate phase. This will be elaborated on in Section 4.1.3. The simulation procedure is greatly simplified by introducing the assumption of mechanical equilibrium, with only a single set of momentum equations needing to be solved.

This assumption has been used by other researchers. Knaus et al. [35] and Schnell [106] employed an EE approach for full-scale boilers and pulverised fuel burners with adequate results being obtained. Benim et al. [36] further simplified the modelling approach by assuming thermal equilibrium with adequate results being obtained for the various test cases. Custom code needed to be developed to implement the above in ANSYS Fluent® v19.5 for the scalar transport, combustion reactions, mass transfer and heat transfer. The custom code interfaced with the commercial CFD solver through the Fluent® User-Defined Function (UDF) interface.

4.1.1 Governing equations

The gaseous mixture is modelled using the species transport approach, where a separate conservation equation is solved for each mixture component (i.e. H_2O, CO_2, O_2, SO_2 and CO). The governing equations are approximated using the steady-state Reynolds-averaged conservation equations for mass, species, energy, momentum and turbulence closure equations, discussed in Chapter 3. However, the energy and momentum equations have additional source terms that capture the pseudo particulate effects.

The fluid-solid mixture density is calculated using the ideal gas equation. However, the formulation of the momentum transport equation an effective density (ρ_{eff}) is used that incorporates the pseudo-particle mass effects. Thus, the momentum conservation equation solved for the gas-solid mixture is given in Equation (4.1).

$$\frac{\partial}{\partial x_i}(\rho_{eff} u_i u_j) + \frac{\partial \bar{P}}{\partial x_j} = \frac{\partial}{\partial x_i}\left[(\mu_l + \mu_t)\left\{\frac{\partial u_j}{\partial x_i} + \frac{\partial u_i}{\partial x_j} - \frac{2}{3}\delta_{ij}\frac{\partial u_i}{\partial x_i}\right\} - \frac{2}{3}\rho_g k \delta_{ij}\right] + S_{mom} \quad (4.1)$$

The effective density is used to capture the translational inertial effects that would arise due to the drag of the pseudo-particles on the fluid phase flow regime and is written as:

$$\rho_{eff} = \frac{\rho\rho_p(\phi_{mp} + 1)}{\rho\phi_{mp} + \rho_p} \quad (4.2)$$

where ρ_p and ϕ_{mp} are the particle density and mass fraction of particles in a cell, respectively.

To achieve the corrected momentum expression of Equation (4.1), linearised source terms of the form given in Equation (4.3), are implemented using user-defined sources for each coordinate direction.

$$
\begin{aligned}
&S_{mom_x} = (\rho_g - \rho_{eff})(A + Bu) \\
&A = 2u\frac{\partial u}{\partial x} + v\frac{\partial u}{\partial y} + u\frac{\partial v}{\partial y} + w\frac{\partial u}{\partial z} + u\frac{\partial w}{\partial z} \\
&B = \frac{\partial A}{\partial u} = 2\frac{\partial u}{\partial x} + \frac{\partial v}{\partial y} + \frac{\partial w}{\partial z}
\end{aligned}
\tag{4.3}
$$

Complete derivations of the effective density and the linearised source terms for all coordinate directions are provided in Appendix A.

4.1.2 Pseudo-particle transport

The pseudo-particles transported into the domain are modelled using a scalar field of necessary quantities and distributed over the computational domain. The pseudo-particle scalar fields define the fuel based on its proximate analysis composition. The proximate analysis provides an estimate of the fuel sample's moisture, volatile matter, fixed carbon and ash contents. The diffusion terms are neglected since the scalar variables involve very small Peclet numbers. In addition, the scalars can be seen as passive scalars since the inertial effects have been accounted for [107]. Table 4.1 lists the scalar fields used in the solution of the pseudo-particle phase along with the solved scalar transport equations.

Table 4.1: Pseudo-particle scalar fields per kilogram of the continuous phase

Scalar	**Description**	**Unit**	**Transport equation**
ϕ_{mp0}	Original/initial mass of particles	kg_{fuel}/kg	$\frac{\partial}{\partial x_i}(\rho_g u_i \phi_{mp0}) = 0$
ϕ_{H_2O}	Moisture present in particles	kg_{H_2O}/kg	$\frac{\partial}{\partial x_i}(\rho_g u_i \phi_{H_2O}) = \frac{1}{V}\frac{dm_{evap}}{dt}$
ϕ_{VM}	Volatile matter present in particles	kg_{VM}/kg	$\frac{\partial}{\partial x_i}(\rho_g u_i \phi_{VM}) = \frac{1}{V}\frac{dm_{vol}}{dt}$
ϕ_{FC}	Fixed carbon present in particles	kg_{FC}/kg	$\frac{\partial}{\partial x_i}(\rho_g u_i \phi_{FC}) = \frac{1}{V}\frac{dm_c}{dt}$
ϕ_{ASH}	Ash present in particles	kg_{ASH}/kg	$\frac{\partial}{\partial x_i}(\rho_g u_i \phi_{ASH}) = 0$
ϕ_{hp}	Enthalpy of particle	J/kg	Equation (4.4)

The particle concentration transport is captured via the scalar transport equations of Table 4.1, whereby the summation of the scalar variables, namely the moisture, volatile matter, fixed carbon and ash contents, allow for the resolution of the actual average mass/-particle concentration throughout the domain.

The particles' energy transport is accounted for with the scalar variable (ϕ_{hp}), representing the enthalpy of the particles. The transport of (ϕ_{hp}) provides a mechanism for resolving the particle temperature throughout the domain, allowing for the combustion processes and the particulates' radiative effects to be captured. The particulate phase energy balance is given in Equation (4.4).

$$\frac{\partial}{\partial x_i}(\rho u_i \phi_{hp}) = \left(f_{heat} \frac{dm_c}{dt} h_{rxn} + \dot{Q}_{rad} + \dot{Q}_{conv} - \frac{dm_{evap}}{dt} h_{fg} \right) \frac{1}{V} \tag{4.4}$$

where h_{rxn}, h_{fg}, $\dot{Q}_{rad}$ and $\dot{Q}_{conv}$ are the heat of reaction due to char oxidation, the latent heat of evaporation, and the radiative and convective heat transfer to the particulate matter, respectively. The fraction of heat absorbed by the particulate matter from the char oxidation process is represented by the variable f_{heat}, where the near-surface char oxidation product species is CO, $f_{heat} = 1$ [79].

The terms $\frac{dm_c}{dt}$ and $\frac{dm_{evap}}{dt}$ denote the rate of char oxidation mass loss and rate of moisture evaporation driven out of the particle. These terms are essential in resolving the combustion phenomena, subsequently discussed in Section 4.1.4. In addition, by tracking the enthalpy of the particles, the pseudo-particle's temperature can be resolved by using the expression for specific heat at constant pressure given in Equation (3.10). Thus, the pseudo-particle temperature can be defined as:

$$T_p = \frac{\phi_{hp}}{\phi_{mp} cp_p} + T_{ref} \tag{4.5}$$

where variables ϕ_{mp}, cp_p, and T_{ref} are the tracked particle mass in a cell, the particle specific heat, and the standard reference state temperature of 298.15 $[K]$. The importance of knowing the particle temperature becomes apparent in Section 4.1.4 when determining the combustion procedure and moves the model away from the thermal equilibrium assumption.

4.1.3 Turbulent dispersion of particles

The inclusion of particle dispersion due to local turbulence perturbations from the fluid phase increases the effects of convective heat transfer to and from the pseudo-particles. The local turbulent perturbations introduce a local slip factor between the gas and the pseudo-particle. With the assumption of mechanical equilibrium and turbulent flow, the turbulent dispersion of particles is either modelled as a stochastic or as a 'cloud' representation of a group of particles about a mean trajectory. The turbulent dispersion of the pseudo-particles is modelled using a stochastic modelling approach, namely the discrete random walk (DRW) model.

The DRW model includes the effect of turbulent velocity fluctuations using a Gaussian distributed random velocity fluctuation (u', v' and w'). These values obey a Gaussian probability distribution, such that the velocity fluctuation can be written as follows:

$$u' = \zeta \sqrt{\bar{u'^2}} \tag{4.6}$$

where ζ is a normally distributed random number, and the remainder of the right-hand side is the local RMS value of the velocity fluctuation [21]. With the turbulent kinetic energy, k, known at each point in the flow and assuming isotropy, the RMS fluctuating components can be written as:

$$\sqrt{\bar{u'^2}} = \sqrt{\bar{v'^2}} = \sqrt{\bar{w'^2}} = \sqrt{\frac{2k}{3}} \tag{4.7}$$

The use of Equations (4.6) and (4.7) results in a slight deviation from the mechanical equilibrium assumption, allowing the model to include the effects of velocity fluctuations on convective heat transfer to the pseudo-particle. External convection occurs between the particles and the continuous phase in solid fuel combustion systems. This convective heat transfer component contributes to the pseudo-particle's inert heating/cooling effects needed to initiate the combustion modelling sequence. A popular correlation for determining the external convection heat transfer coefficient to a sphere was proposed by Marshall and Ranz ([108],[109]) and is given in Equation (4.8) as:

$$Nu_{MR} = \frac{\tilde{h}_{MR}\bar{d}_p}{\lambda_g} = 2.0 + 0.6Re_d^{\frac{1}{2}}Pr^{\frac{1}{3}} \tag{4.8}$$

where $\tilde{h}_{MR}$ and Re_d is the external heat transfer coefficient, and the Reynolds number is based on the area-weighted average particle diameter ($\bar{d}_p$) and the mean velocity. The mean velocity ($\bar{u}$) is based on the dispersed turbulent velocity fluctuations (refer to Equations (4.6) and (4.7)) for a cell and is derived as:

$$\bar{u} = \sqrt{\frac{2k}{3}(\zeta_u^2 + \zeta_v^2 + \zeta_w^2)} \tag{4.9}$$

where $\bar{u}$ and the ζ_i values is the mean velocity and the normally distributed random values for each coordinate direction, respectively. Making use of Equations (4.8) and (4.9), the convective heat transfer source term from gas to particle and vice versa is written as:

$$\dot{Q}_{conv} = \tilde{h}_{MR}A_pN_p(T_p - T_g) \tag{4.10}$$

where A_p is the surface area of a spherical particle, and N_p is the number of pseudo-particles present in a cell, further discussed in Section 4.1.5. By considering the average convective heat transfer coefficient, particle thermal conductivity, and the average particle's characteristic length, the Biot number was calculated to be lower than the 0.1 threshold, making the proposed methodology suitable for lumped parameter analysis.

4.1.4 Combustion modelling

As discussed in Section 3.3.1, the modelling of solid fuel combustion, i.e. heterogeneous reactions, follows a sequential procedure. Figure 4.2 illustrates the general combustion process from inert heating/cooling of the particles, moisture evaporation, devolatilisation and char oxidation. The volatiles and carbon monoxide products from the devolatilisation and char oxidation processes would react in the gas-phase domain, as discussed in Section 3.3.2.

The description of the overall combustion process is implemented by using the pseudo-particle scalar fields of Section 4.1.2 and the pseudo-particle temperature. The effect of moisture vaporisation is ignored due to the rapid heating of the particles once the secondary air stream mixes with the fuel particles.

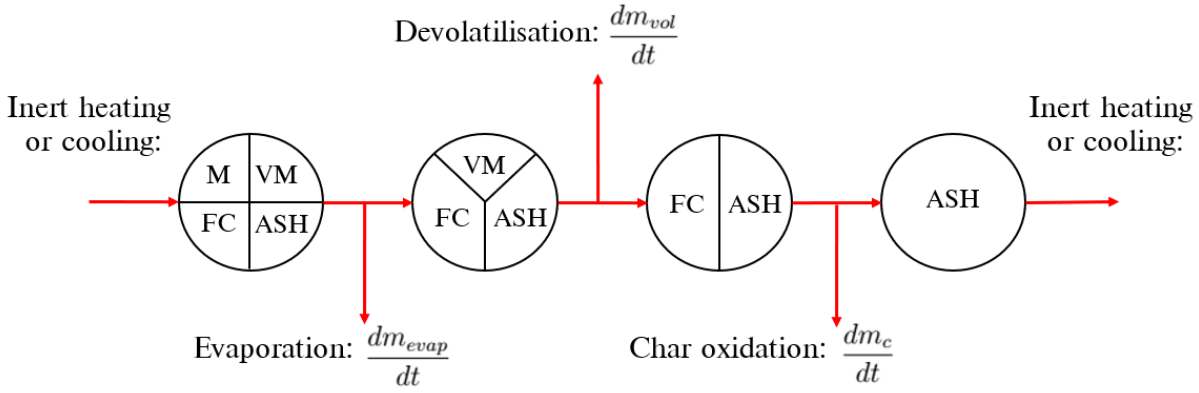

Figure 4.2: Combustion schematic

The realisation of the boiling temperature would initiate moisture release based on a boiling/evaporation rate, which can be derived from Equation (4.4) by assuming that the particle temperature remains constant once boiling has been initiated and until all the moisture is driven off, resulting in the formulation given in Equation (4.11).

$$\frac{dm_{evap}}{dt} h_{fg} = \dot{Q}_{rad} + \dot{Q}_{conv}. \tag{4.11}$$

Equation (4.11) shows that the boiling rate is determined by the radiation and convection heat transfer rates to the particle. The convective heat transfer ($\dot{Q}_{conv}$) to the particle matter present in a cell was given by Equation (4.10). The particle radiative heat transfer is calculated using the following formulation:

$$\dot{Q}_{rad} = \epsilon_p \sigma_{SB} A_p \left(\frac{G}{4\sigma_{SB}} - T_p^4 \right) \tag{4.12}$$

where ϵ_p and the term $\frac{G}{4\sigma_{SB}}$ are the particle emissivity and radiation temperature, respectively.

The subsequent devolatilisation and char oxidation processes are determined using Equations (3.27) and (3.30), respectively, provided the kinetic characteristics of the fuel are known. The numerical implementation required the extensive use of user-defined source terms and scalars to account for the energy, species, mass, and radiation interactions due to the solid fuel combustion phenomena.

4.1.5 Radiation modelling

Including the effects that the pseudo-particles have on the radiative field requires manipulating the P-1 radiation transport equation and homogenised formulations of the particles' radiative properties. Thus, the following section aims to derive the radiative source terms employed to incorporate the pseudo-particulate effects.

The energy conservation can be explicitly written to include the thermal radiation source term $-\frac{\partial q_r}{\partial x_i}$ as follows:

$$\frac{\partial}{\partial x_i}(u_i[\rho E + P]) = \frac{\partial}{\partial x_j}\left[\lambda_{eff}\frac{\partial T_g}{\partial x_j} + \rho\overline{u_j^{'}E^{'}} + u_i\tau_{eff}\right] - \frac{\partial q_r}{\partial x_i} + S_h \tag{4.13}$$

The transport equation for the incident radiation flux (G) in the default P-1 model utilised by ANSYS Fluent® v19.5 for the gaseous phase (excluding particles) is given by:

$$\begin{aligned}\frac{\partial}{\partial x_i}(\Gamma_g\frac{\partial}{\partial x_j}G) &= \alpha_g G - 4\alpha_g n^2\sigma_{SB}T_g^4 + S_{rad}\\ \Gamma_g &= \frac{1}{3(\alpha_g+\sigma_g)} \approx \frac{1}{3\alpha_g}\end{aligned} \tag{4.14}$$

where S_{rad} is the user-defined radiative source term, n is the refractive index of the medium, σ_g is the gas-phase scattering coefficient, and C is the linear anisotropic phase function coefficient. Assuming isotropic scattering (equally likely in all directions) the linear anisotropic phase function coefficient tends to a value of zero ($C \rightarrow 0$). The coupling between the P-1 radiation model (Equation (4.14)) and the Eulerian gaseous phase energy conservation equation (Equation (4.13)) (excluding particles) is given by:

$$-\frac{\partial q_r}{\partial x_i} = \alpha_g G - 4\alpha_g n^2\sigma_{SB}T_g^4 \tag{4.15}$$

When implementing the homogenised Eulerian solid-phase model, the application of these default models needs careful consideration. The effect of the particles on the incident radiation field must be accounted for without actually having a separate dispersed phase of particles present. When particles are present, ANSYS Fluent® v19.5 ignores scattering in the gas-phase (i.e. $\sigma_g \approx 0$) and solves the alternative transport equation for the incident radiation as given in Equation (3.39) of Section 3.4.1. For the readers' convenience, the equations are rewritten below as:

$$\begin{aligned}\frac{\partial}{\partial x_i}(\Gamma\frac{\partial}{\partial x_j}G) &= (\alpha_g+\alpha_p)G - 4\pi\left(\alpha_g\frac{\sigma_{SB}T_g^4}{\pi} + E_p\right)\\ \Gamma_p &= \frac{1}{3(\alpha_g+\alpha_p+\sigma_p)}\end{aligned} \tag{4.16}$$

The gaseous phase P-1 model (Equation (4.14)) can be manipulated using a user-defined radiative source term to include the particle effects. The radiative source term can be written as follows:

$$S_{rad} = \frac{\partial}{\partial x_i}\left(\frac{\alpha_p+\sigma_p}{3\alpha_g(\alpha_g+\alpha_p+\sigma_p)}\frac{\partial G}{\partial x_i}\right) + \alpha_p G - 4\pi E_p. \tag{4.17}$$

Although this manipulation is valid, it leads to a non-trivial source term formulation for the solution of the G field. Therefore, an alternative approach is followed in the present model that leads to a more convenient source term formulation. In the alternative approach, the value of α_g is expanded to include the particle absorption and scattering coefficients as follows:

$$\alpha_g = \alpha_g + \alpha_p + \sigma_p. \tag{4.18}$$

Γ_g is therefore effectively redefined for a homogenised gaseous and particle-laden medium (Γ_p) by the substitution of Equation (4.18)

$$\Gamma_p = \Gamma_g \approx \frac{1}{3\alpha_g} \approx \frac{1}{3(\alpha_g + \alpha_p + \sigma_p)}. \tag{4.19}$$

This manipulation adds additional unwanted terms to the RHS of Equation (4.14). To compensate for this the source term (S_{rad}) can now be defined as,

$$S_{rad} = 4(\alpha_g + \sigma_p)\sigma_{SB}T_g^4 - \sigma_p G - 4\pi E_p \tag{4.20}$$

This convenient formulation of S_{rad} implies that by solving the default P-1 incident radiation field model for the gaseous phase in ANSYS Fluent® v19.5 (Equation (4.14)), we are effectively solving the alternative transport equation (Equation (4.16)) that includes the effects of the particles.

However, this more convenient formulation of the source term formulation (Equation (4.20)) leads to a new issue related to the coupling between the P-1 model and the continuous phase energy equation. The expanded value of α_g in Equation (4.18) implies that the default coupling given by Equation (4.15) will now effectively lead to a radiation source term in the energy equation that contains unwanted terms, namely:

$$-\frac{\partial q_r}{\partial x_i} = (\alpha_g + \alpha_p + \sigma_p)G - 4(\alpha_g + \alpha_p + \sigma_p)n^2\sigma_{SB}T_g^4. \tag{4.21}$$

Furthermore, we want to provide for thermal non-equilibrium with different gas and particle temperatures. Therefore, the aim is to employ the continuous phase energy equation to solve the gas temperatures only and then solve an additional separate energy equation for the particle temperatures with the interaction between the two phases controlled via appropriate source terms. To cancel out the unwanted terms in Equation (4.21) and to explicitly account for the convection heat transfer, of Equation (4.10), the S_h source term of the energy equation shown in Equation (4.13) should be:

$$S_h = \left[4(\alpha_p + \sigma_p)n^2\sigma_{SB}T_g^4 - \sigma_p G\right] - \left[\frac{N_p}{V}\tilde{h}_{MR}A_p(T_g - T_p)\right]. \tag{4.22}$$

where N_p is defined as the number of pseudo-particles in a cell and A_p is the surface area of a particle.

Utilising the ϕ_{mp0} scalar field, as described in Table 4.1, N_p can be calculated based on the average volume-weighted diameter ($\bar{d}_{p_V}$) of the particles as follows:

$$N_p = \frac{6\rho_g\phi_{mp0}V}{\rho_p\pi\bar{d}_{p_V}^3}. \tag{4.23}$$

The gas density (ρ_g) and particle density (ρ_p) are needed for the closure of Equation (4.23). It is noted that the use of the average volume-weighted diameter will subsequently affect the calculation of the projected area of the pseudo-particles, which leads to an averaging effect of pseudo-particle radiative properties. An increase in the effective radiative heat transfer area is accounted for by considering the area-weighted average diameter of the Rosin-Rammler particle distribution when calculating the pseudo-particles' radiative properties, namely E_p, α_p and σ_p.

The equivalent Eulerian descriptions of the terms E_p, α_p and σ_p, as first seen in Equations (3.43)-(3.45) of Section 3.4.3, are given in Equations (4.24) through (4.26).

$$E_p = \lim_{V\to 0} \sum_{n=1}^{N} \frac{\epsilon_{p,n} A_{proj,n} \sigma_{SB} T_p^4}{\pi V} \approx \frac{\epsilon_p A_{proj} N_p \sigma_{SB} T_p^4}{\pi V}. \tag{4.24}$$

$$\alpha_p = \lim_{V\to 0} \sum_{n=1}^{N} \frac{\epsilon_{p,n} A_{proj,n}}{V} \approx \epsilon_p \frac{A_{proj} N_p}{V}. \tag{4.25}$$

$$\sigma_p = \lim_{V\to 0} \sum_{n=1}^{N} (1-\epsilon_{p,n})(1-f_{p,n}) \frac{A_{proj}}{V} \approx (1-\epsilon_p)(1-f_p) \frac{A_{proj} N_p}{V}. \tag{4.26}$$

where A_{proj} is the projected area of the pseudo-particles.

The Lagrangian configuration (the LHS of the $\approx$ sign in Equations (4.24)-(4.26)) is the summation of the particles in a cell volume, whilst the Eulerian description (RHS) makes use of the number of particles present in a cell, as discussed previously. By employing the Eulerian definitions of the particle radiation properties, it can be shown that the S_h source term can conveniently be written as:

$$S_h = S_{rad} - \frac{N_p}{V}(\dot{Q}_{rad} + \dot{Q}_{conv}). \tag{4.27}$$

4.1.6 Numerical implementation

ANSYS Fluent® v19.5 was the CFD software package used to implement the developed simulation model. The source terms and scalar fields previously defined in this chapter were implemented using user-defined functions (UDF) and user-defined scalars (UDS). A UDF is a *C* function that is dynamically loaded with the ANSYS Fluent solver to enhance the standard features [110]. Uses include adjusting computed values on a per-iteration basis, initialising a solution and customising the source terms for either the ANSYS Fluent transport equations or UDS transport equations. Figure 4.3 illustrates the general iteration flow diagram for the pressure-based coupled solver utilised for all CFD model simulations.

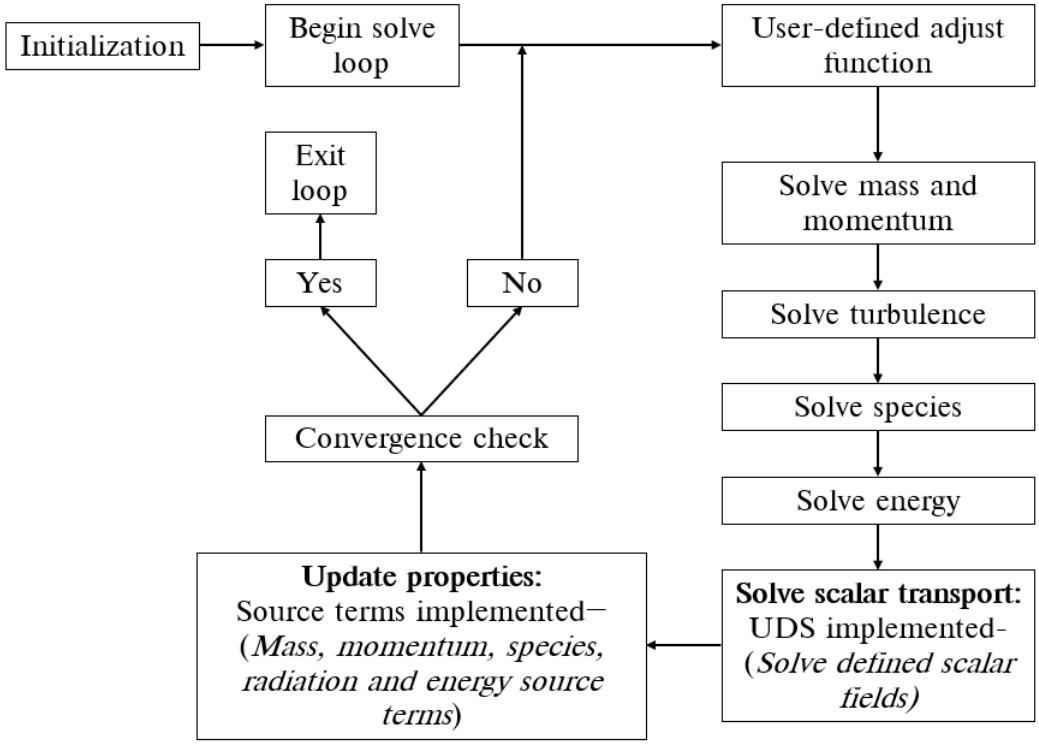

Figure 4.3: Pressure based coupled solver iteration flow diagram [110]

UDFs are defined using 'DEFINE' macros provided by ANSYS Fluent. They are coded using additional macros and functions and can access the ANSYS Fluent solver data and perform other tasks [110].

The following support macros are used in solving the developed CFD methodology, namely the 'DEFINE_INIT', 'DEFINE_ADJUST', and 'DEFINE_SOURCE'. These macros allow for the initialisation of any user-defined memory (UDM), variables and scalars, the adjustment/modification of variables, and to specify custom source terms, respectively. Note that the units of all source terms are of the form generation rate per unit volume. For example, a source term for the continuity equation would have units of $[kg/m^3]$ [110].

4.2 Model validation & application

The following section emanates from the work presented by Rawlins et al. [111]. The work presented the validation and application of the developed CFD methodology discussed in the previous sections, namely a fast thermal non-equilibrium Eulerian-Eulerian (EE) multiphase model for a pulverised fuel combustor.

The International Flame Research Foundation's (IFRF) 2.165 $[MW_{th}]$ lab-scale swirl burner, burning pulverised coal, was the primary validation case study for the proposed CFD modelling methodology. Detailed flame measurements were obtained from the works of Peters and Weber [112], whose main objective was the implementation of a mathematical model for pulverised coal combustion. The measurements extracted from the paper include the temperature, the chemical species concentrations, velocity measurements, the heat uptake of the furnace and cooling coils, and the coal burnout at several locations in the furnace.

The validation case study is for the lab-scale burner operating at 100% load. The CFD model results are validated against experimental and numerical data. Using the same modelling inputs, the numerical data results were also obtained from conventional Eulerian-Lagrangian (EL) based CFD computations.

The application case study considers the low-load operation at 60% and 40%, which are compared to EL simulation results illustrating the applicability of the model over various load ranges. The following subsections describe the computational domain, model inputs, the employed numerical strategy, and the results, both of the validation study and the application case study.

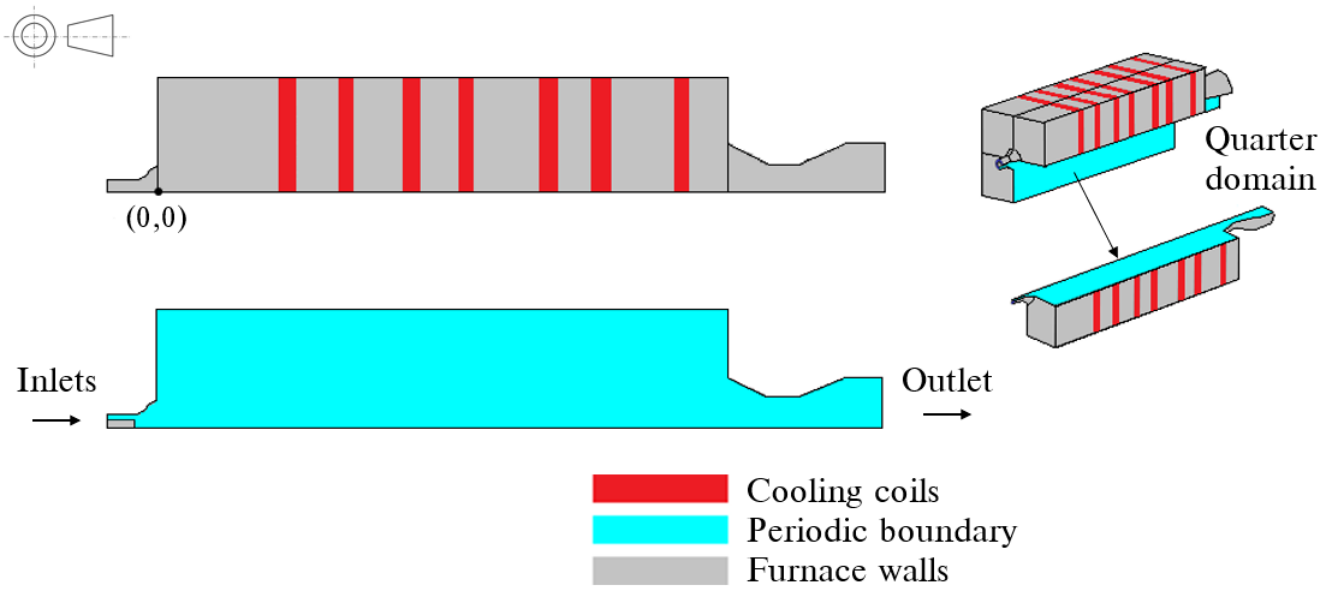

Figure 4.4: IFRF Furnace No. 1 computational domain

4.2.1 Computational domain

The geometric model is a quarter section representation of the IFRF burner and comprises periodic boundary conditions located on the centre planes. Figure 4.4 illustrates the 3-D IFRF computational domain, highlighting the inlets, outlet, walls, and periodic boundaries.

The final simulations were performed on a mesh consisting of 122,800 cells. To ensure mesh independence, simulations were also performed for meshes consisting of 84,300 and 280,000 cells. This was done for the developed CFD model and the EL modelling approach. The wall fluxes, velocity and combustion characteristics were compared for all three cases, and the 122,800-cell mesh was deemed acceptable for both modelling approaches. Finally, a different mesh size of 650,000 cells was run to demonstrate the developed CFD model speed-up capabilities compared to an EL modelling approach. To ensure numerical stability, the aspect ratio was kept below 15, and mesh orthogonality quality was kept above 0.15.

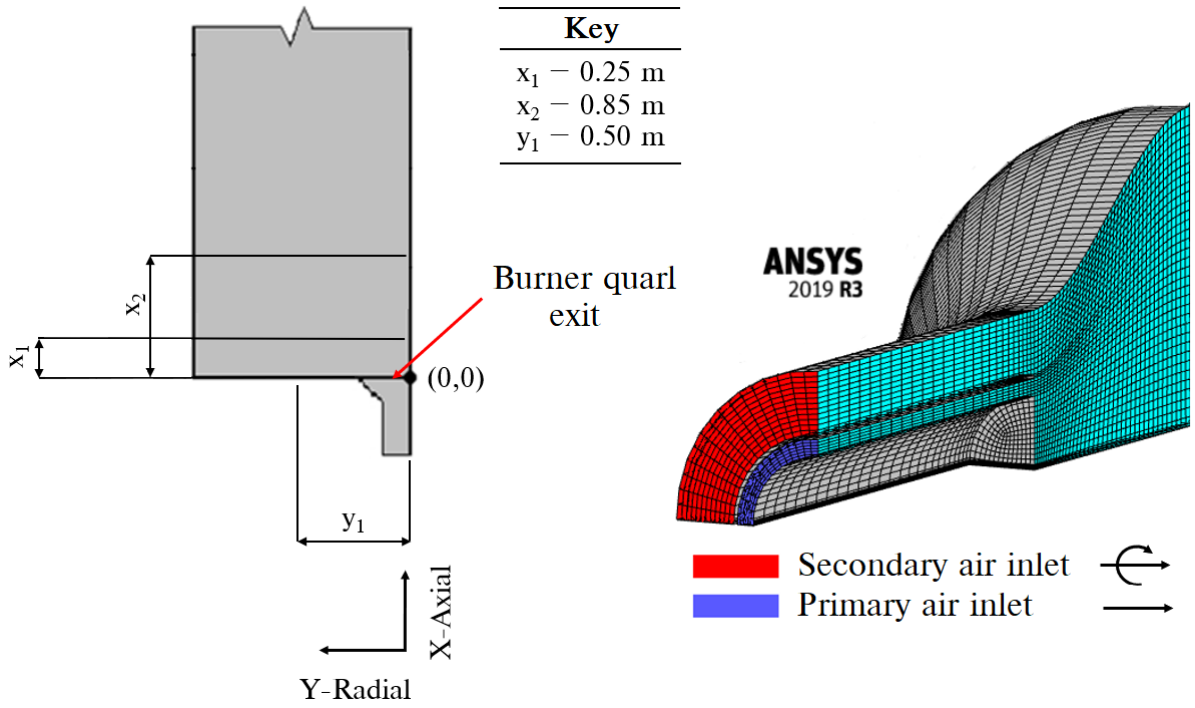

Figure 4.5: IFRF burner details alongside the axial and radial position schematic

Figure 4.5 shows the burner configuration and highlights the axial and radial probe locations. These locations are measured from the plane that runs through the point (0,0), known as the burner quarl exit plane.

4.2.1.1 Model inputs & boundary conditions

The coal combusted in the furnace is a Saar coal, namely Gröttelborn hvBp, and is fired with 22% excess air. The coal is injected into the primary air inlet of the burner, with the secondary air being fed through the outer annulus. Figure 4.5 highlights the secondary and primary air inlet annuli.

Table 4.2: Gröttelborn hvBp coal characteristics

Fuel constituent	**Fraction**	**Unit**
Ultimate analysis - (DAF)	-	-
Carbon	0.8036	kg/kg_{fuel}
Hydrogen	0.0508	kg/kg_{fuel}
Nitrogen	0.01445	kg/kg_{fuel}
Oxygen	0.1217	kg/kg_{fuel}
Sulphur	0.0094	kg/kg_{fuel}
Proximate analysis - (Dry)	-	-
FC	0.543	kg/kg_{fuel}
VM	0.374	kg/kg_{fuel}
Ash	0.083	kg/kg_{fuel}
Energy & coal kinetic characteristics	**Value**	
Net calorific value - (DAF)	32320	kJ/kg_{fuel}
Devolatisation		
Pre-exponential factor (A_{vol}) [36]	1.5×10^5	s^{-1}
Activation energy ($E_{a,vol}$) [36]	7.4×10^7	$J/kmol$
Char oxidation		
Pre-exponential factor (A_c) [112]	0.002	$kg/(m^2 sPa)$
Activation energy ($E_{a,c}$) [112]	7.9×10^7	$J/kmol$

The coal characteristics and the coal kinetic constants are shown in Table 4.2, with the ultimate analysis and the net calorific value being determined on a dry-ash-free (DAF) basis. The burner inlet boundary conditions for the 100%, 60% and 40% load cases are shown in Table 4.3. Included are the inputs for the pseudo-particle transport Eulerian-Eulerian models. An excess air value of 22% was used in the 100% case. Values of 32.5% and 37.75% were calculated for the 60% and 40% load cases.

The secondary air inlet only transports air into the combustion chamber; thus, the pseudo-particle scalar transport inputs (ϕ_{mp0}, ϕ_{H_2O}, ϕ_{VM}, ϕ_{FC}, ϕ_{ASH} and ϕ_{hp}) were all set to 0. The volume-weighted and area weighted diameters were calculated as 45.0×10^{-6} $[m]$ and 47.2×10^{-6} $[m]$, respectively. Other necessary boundary conditions, such as wall temperatures and emissivity values, are available in the work of Peters and Weber [112]. However, the wall boundary conditions are kept the same for the simulated lower loads.

Table 4.3: Burner inlet boundary conditions for simulated load cases

	Loads			
Primary air & fuel inlet	**100%**	**60%**	**40%**	**Unit**
Coal mass flow rate (Dry)	263	158	105	kg/hr
Temperature	343	343	343	K
Mean axial velocity	23.02	15.11	10.51	m/s
ϕ_{mp0}	0.631	0.577	0.555	kg_{mp0}/kg
ϕ_{H_2O}	6.31×10^{-5}	5.77×10^{-5}	5.54×10^{-5}	kg_M/kg
ϕ_{VM}	0.236	0.216	0.208	kg_{VM}/kg
ϕ_{FC}	0.343	0.314	0.302	kg_{FC}/kg
ϕ_{ASH}	0.052	0.047	0.045	kg_{ASH}/kg
ϕ_{hp}	31231	28581	27493	J/kg
Secondary air inlet				
Temperature	573	573	573	K
Mean axial velocity	43.83	28.75	19.93	m/s
Mean tangential velocity	49.42	32.41	22.56	m/s

4.2.1.2 Grid independence study

Three numerical grids of increasing size were generated for the IFRF quarter domain. This was done for both the EL and EE model to illustrate grid independence for both models. The mesh independence study focussed on operating the lab-scale burner at 100% MCR. A representative cell size , $x_{mesh}\,[m]$, for a 3-D domain was calculated using Equation (4.28) defined as [113, 114]:

$$x_{mesh} = \left(\frac{1}{N} \sum_{i=1}^{N} V_i \right)^{1/3} \tag{4.28}$$

where N is the number of cells in the domain and V_i is the cell volume of the i^{th} cell. Table 4.4 highlights the mesh refinement characteristics including the number of cells and the calculated representative cell size x for each grid refinement.

Table 4.4: Mesh refinement characteristics

Mesh	**Cell count (N)**	**Representative grid size ($\mathbf{x_{mesh}}$)**
Coarse - M1	52279	0.0374 $[m]$
Medium - M2	122797	0.0283 $[m]$
Fine - M3	282746	0.0213 $[m]$

The reported key parameters of the mesh study are the mass-weighted average exit temperature, total heat transfer rate to the furnace walls and the mass-weighted volume fractions of CO_2 and O_2 at the exit of the domain. Table 4.5 shows the percentage change of the key variables for each mesh refinement stage for both the EL and EE model.

Table 4.5: Mesh refinement error percentage data for key parameters

	EL model error %		**EE model error %**	
Key Variable	**M1 to M2**	**M2 to M3**	**M1 to M2**	**M2 to M3**
Exit temperature	1.21 %	1.05 %	0.43 %	0.34 %
Total wall heat load	4.52 %	1.81 %	2.32 %	1.21 %
X_{CO_2}	0.33 %	0.18 %	0.37 %	0.15 %
X_{O_2}	0.26 %	0.15 %	0.23 %	0.16%

The exit molar concentrations of X_{CO_2} and X_{O_2} , given in Table 4.5, show a comparable percentage change for both models highlighting a minimal change in the combustion characteristics for mesh refinement stages. A higher percentage change in the first refinement stage (M1 to M2) is reported for the EL model for the exit temperatures and total wall heat, while the EE model establishes a far lower percentage change for the same mesh refinement and key parameters. A further refinement from M2 to M3 highlights a significant reduction in the percentage error for the EL models' key parameters, especially when considering the total wall heat, indicating a finer mesh is needed to adequately resolve the furnace heat uptake.

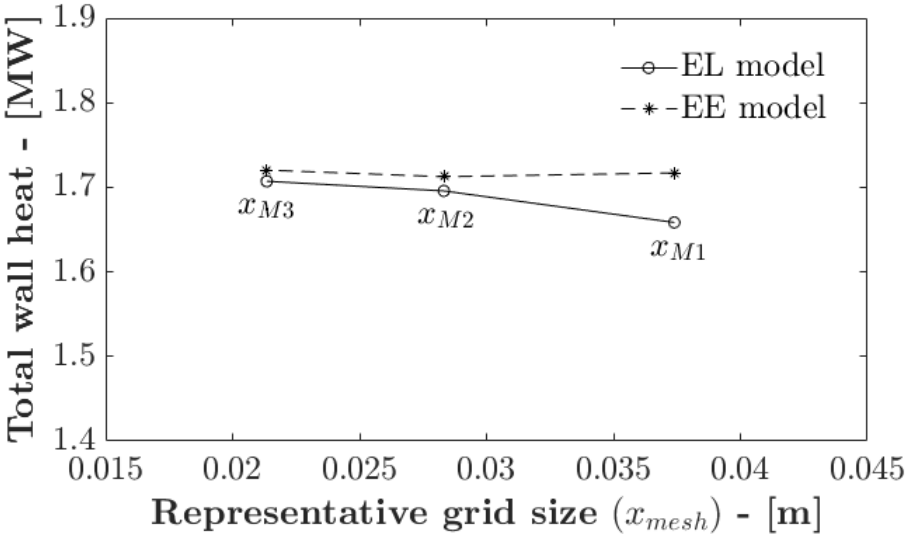

Figure 4.6: Absolute total wall heat for the representative grid size of the refined meshes M1 to M3

Figure 4.6 considers the total heat uptake against the representative grid size for meshes M1 to M3. By considering a linear relationship it can be shown that for an infinitesimally large mesh (M_∞ as $x_{mesh} \to 0$) the absolute values of total wall heat for the EL and EE model tend to values of 1.76 $[MW]$ and 1.75 $[MW]$, respectively. From the above analysis the medium mesh (M2) was used for both the EL and EE modelling methodology simulations.

4.2.1.3 Numerical solution strategy

The current simulations were performed using the ANSYS Fluent® v19.5 pressure-based solver. Pressure-momentum coupling was set to the SIMPLE technique, with momentum, energy and species equations discretised using the second-order upwind method. The pressure equation was discretised using PRESTO!. This setup holds for both the proposed EE and the detailed EL models. The difference arises between using scalar fields in the EE configuration and using the discrete phase modelling (DPM) approach in the EL setup. Scalar field equations were all solved using the first-order upwind method. The discrete phase equations were solved every 25 fluid phase iterations. The number of particles injected into the domain was set to 3800 particles. A validation run using 6000 particle injections was also run, with the results being sufficiently accurate when compared to the 3800 particle injections model. Therefore, 3800 particle injections were used for further EL simulations. To ensure a stable converged solution, the spatial discretisation for all fields was initially set to first-order upwind and solved for 500 iterations before the discretisation order was increased. Then, the solution was run for a further 30000 iterations. For all simulation cases, 72 Intel® Xeon® 2.6 GHz cores were made available by the Centre of High-Performance Computing in South Africa. For all cases, the maximum mass conservation imbalance was 0.0054 $[kg/s]$ for a total gas mass flow rate of 0.9264 $[kg/s]$ and a heat imbalance of 0.025 $[MW]$ for a total heat input of 2.165 $[MW]$. The remaining fields were all solved until convergence was reached.

4.2.2 Validation results

The results of the validation case are further discussed in terms of the following: momentum transport, temperature distributions, combustion characteristics (CO_2, O_2 and CO_{ppm}), wall heat flux distributions and radiative properties.

Table 4.6: Measured and numerical key parameter result comparison

Key parameters	**Measured**	**EL model**	**EE model**	**Unit**
Outlet temperature	1310	1338	1333	K
Outlet CO_{ppm}	30	28	25	$ppm,\ (dry)$
Outlet CO_2	15.6	15.47	15.43	$vol_{\%},\ (dry)$
Outlet O_2	3.0	3.14	3.15	$vol_{\%},\ (dry)$
Total wall radiative heat load	1280.0	1273.5	1289.3	kW
Heat input	2165.0	2206.1	2180.5	kW
Computational time	–	10176	4850	s

Table 4.6 highlights the key parameter comparison between the measured data, the EL model and the EE model. The outlet CO_{ppm} values highlight the highest absolute errors (approximately 12%) between the measured and numerical results. The EL is expected to perform better in predicting the CO_{ppm} due to its higher accuracy in tracking the particle evolution through the combustion stages. Overall, the EE and EL model results are within an approximate 7% absolute error between the measured values taken from the works of Peters and Weber [112], excluding the outlet CO_{ppm} concentrations.

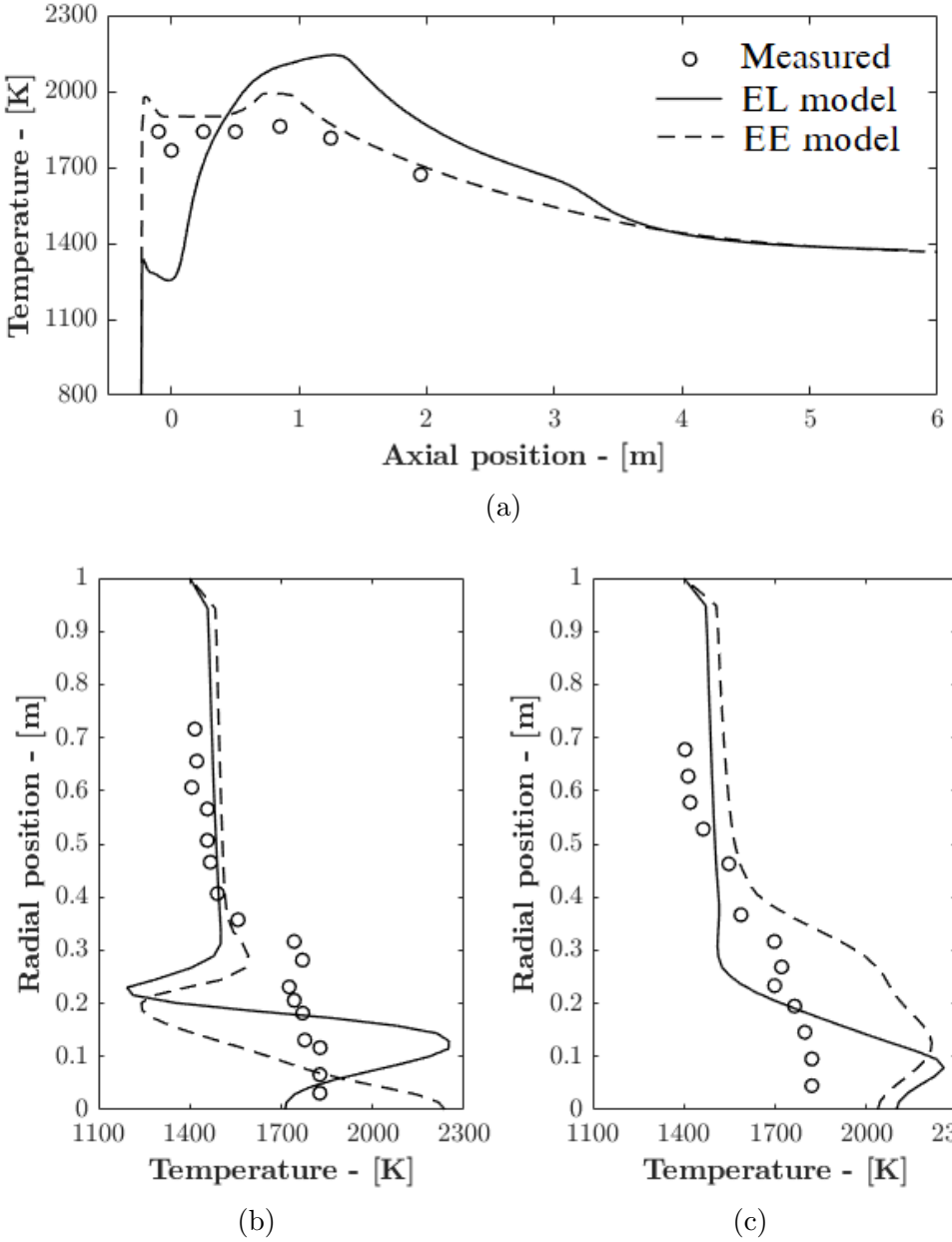

(a)

(b)

(c)

Figure 4.7: 100% load temperature plots. (a) Centreline axial plot, (b) radial plot at an axial location of 0.25 $[m]$ from point $(0, 0)$ (c) radial plot at an axial location of 0.85 $[m]$ from point $(0, 0)$

The axial and radial temperature distribution plots are provided in Figure 4.7 (a) to (c), which compares the measured data to the EL and EE model predictions. The centreline temperature plot of Figure 4.7 (a) shows that the EE model correlates well with the measurements, with the EL model underpredicting the temperature in the burner quarl zone (located left of point (0,0), refer to Figure 4.5). The EE models radial temperature plots of Figures 4.7 (b) and (c) show similar trends to the EL model. The agreement with the measured data is comparable in the upper radial sections of Figures 4.7 (b) and (c) when considering the EE and EL models.

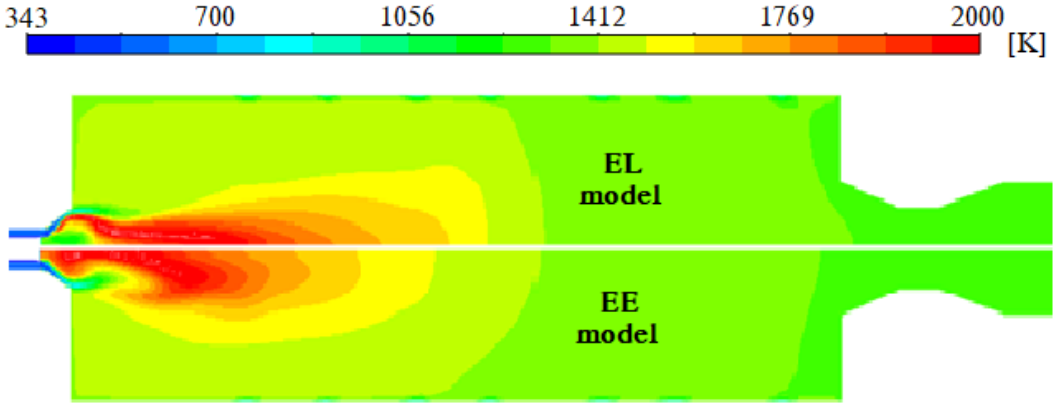

(a)

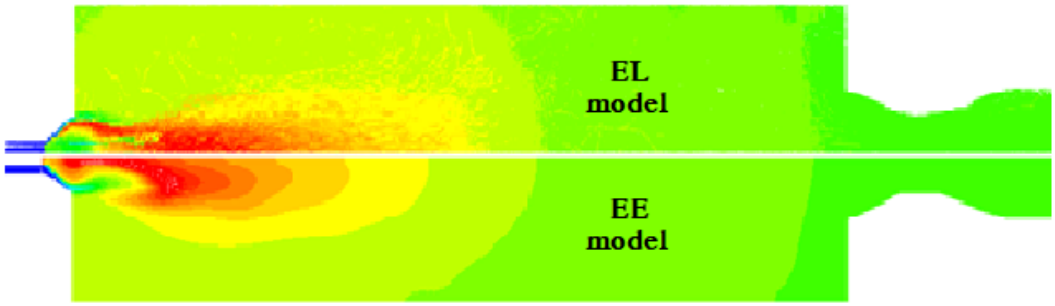

(b)

Figure 4.8: 100% load temperature contour plots. (a) Gas temperature and (b) particle temperature

The gas and particle temperature contour plots of Figures 4.8 (a) and (b) illustrate that the EE model can sufficiently resolve the trends compared to that of the EL model. However, the EE model predicts a higher temperature in the burner's quarl in comparison to the EL model. A noticeable difference between the EE and EL model results is seen in the area inside the burner quarl. This is primarily due to pseudo-particles of the EE model adhering to the streamlines of the flow field, whilst for the EL model, the heavier particles entering the quarl would break away from the streamlines due to their momentum, which is correctly accounted for by the Lagrangian formulation. The deeper penetration of the larger particles would lead to a higher CO_2 formation occurring further into the combustion chamber, as seen in Figures 4.9 (b) and (e). This highlights the near burner effects, observed by Knaus et al. [35], where larger particles were noted to break away from the no-slip (particle and fluid) condition and homogeneous mixture assumption. Considering that the furnace wall flux distributions are a key parameter of this study, the error was seen as acceptable.

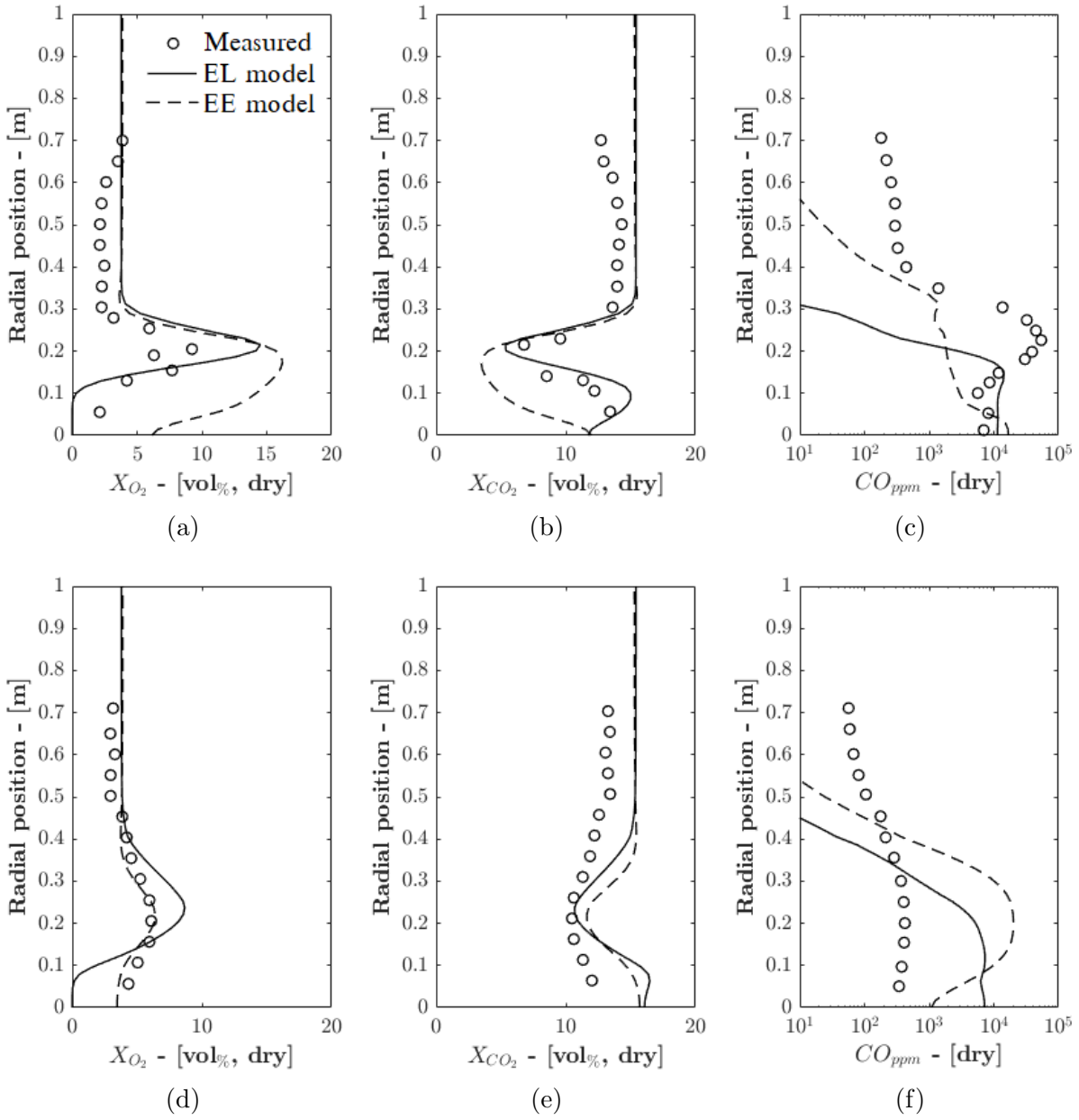

Figure 4.9: 100% load radial plots of combustion products, X_{O_2}, X_{CO_2} and CO_{ppm} at axial locations of 0.25 $[m]$ ((a)-(c)) and 0.85 $[m]$ ((d)-(f)) from point $(0, 0)$

The combustion and major species characteristics are discussed by considering the radial profiles of Figures 4.9 (a) to (f). Similar trends between the EE and EL models are observed. At a location of 0.25 [m] along the axial axis (Figure 4.9 (a) to (c)), the EE model tends to overpredict the O_2 and and underpredict the CO_2 molar concentrations closer to the furnaces' centreline. Similarly, at a location of 0.85 $[m]$ along the axial axis (Figure 4.9 (d) to (f)), the EE model provides similar trends to that of the state-of-the-art EL model, with comparable results to that of the experimental data.

The main discrepancies of both the EE and EL models are highlighted in the resolution of the CO_{ppm} concentrations in Figure 4.9 (c) and (f), both models tend to overpredict the CO_{ppm} concentrations further into the furnace (Figure 4.9 (f)). However, both can resolve the CO_{ppm} concentrations closer to the quarl exit with sufficient accuracy (Figure 4.9 (c)). Thus, the combustion modelling process and pseudo-particle tracking incorporated in the EE modelling methodology can be adequately resolved for the species formation and combustion characteristics in the domain.

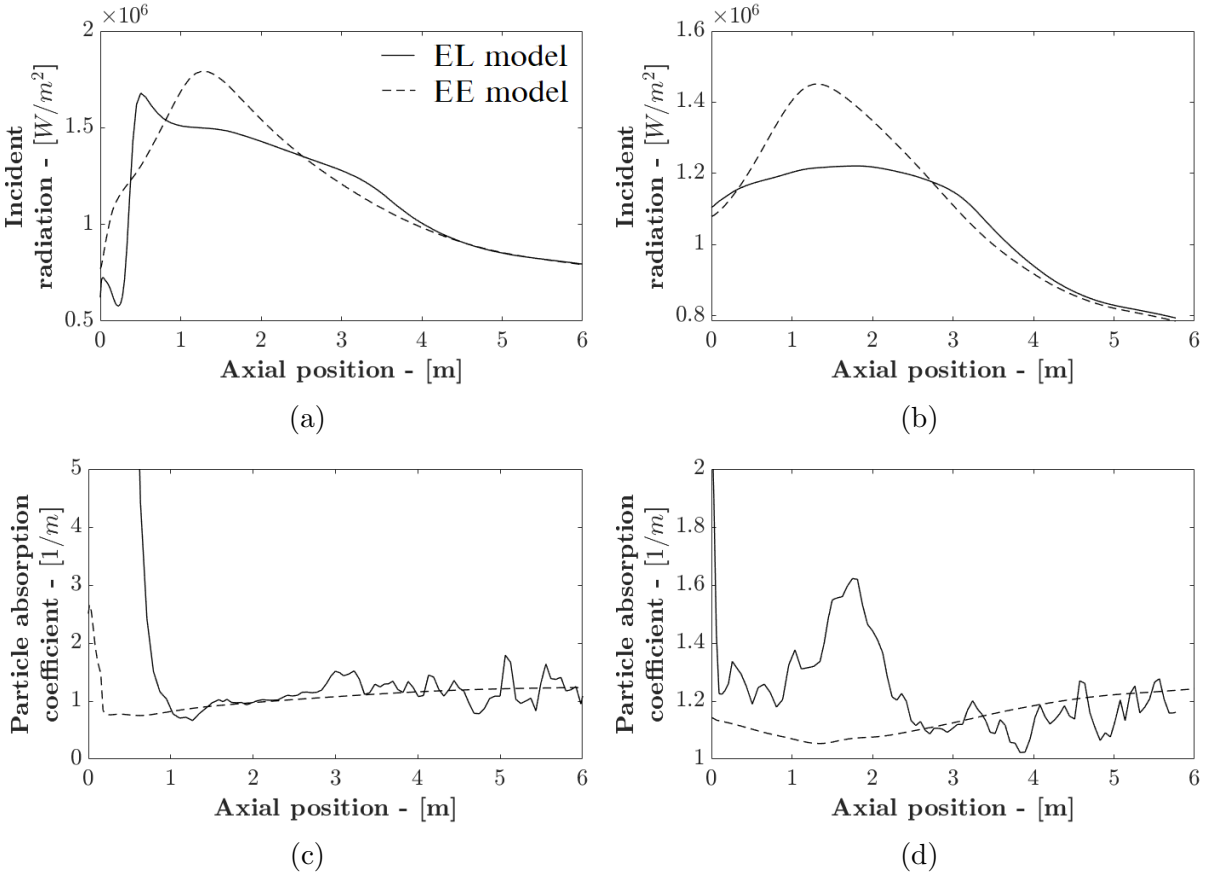

Figure 4.10: 100% load axial plots of radiative properties of the incident radiation and particle absorption coefficient at the centreline ((a) and (c)), and a radial position of 0.5 $[m]$ ((b) and (d))

The radiative heat transfer properties are highlighted in the axial profile plots of Figures 4.10 (a) to (d). By using the manipulation of the P-1 radiation equation to incorporate the pseudo-particle effects for the EE model, as discussed in Section 4.1.5, adequate resolution of the incident radiation field is highlighted in Figures 4.10 (a) and (b), with a slight over-prediction at 1.5 $[m]$ into the domain. The average particle diameter used to determine the particles' radiative properties resulted in a homogenising/smoothing effect of EE models absorption coefficient, highlighted in Figures 4.10 (c) and (d). The EL model displayed more jagged results, which arise from the discontinuities of the discrete phase particle concentrations.

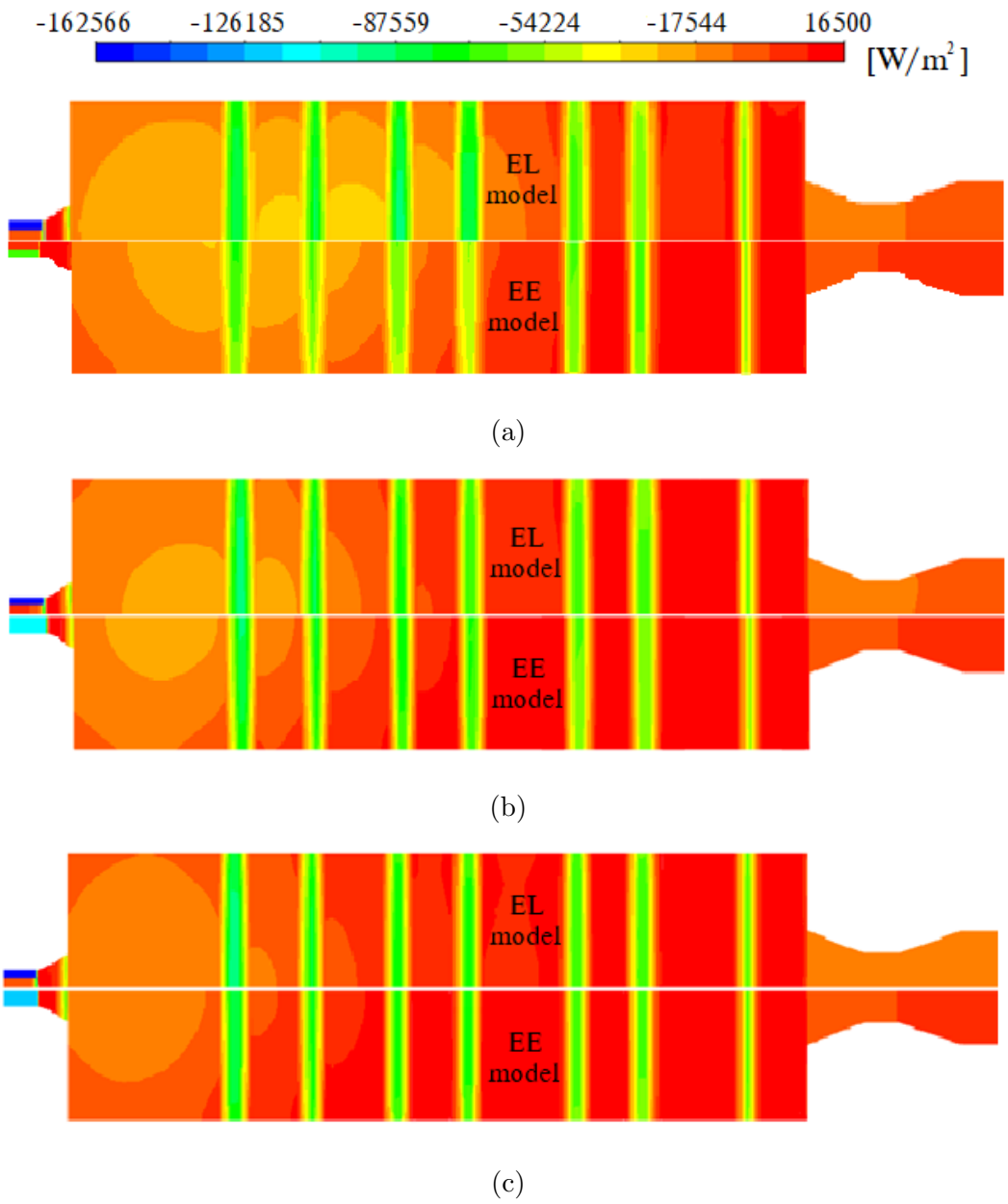

Figure 4.11: Wall heat flux profiles for the (a) 100%, (b) 60% and (c) 40% load cases

The heat fluxes to the walls for the various loads are illustrated using contour plots shown in Figures 4.11 (a) to (c). The EE model can adequately resolve the heat flux distribution compared to the EL model for the various load cases. The heat flux distributions correspond well to the axial temperature and incident radiation profiles of Figure 4.8 (a) and Figures 4.10 (a) and (b), respectively. The EE model shows a higher temperature flame closer to the burner outlet than the EL model's prediction, with a higher incident radiative flux.

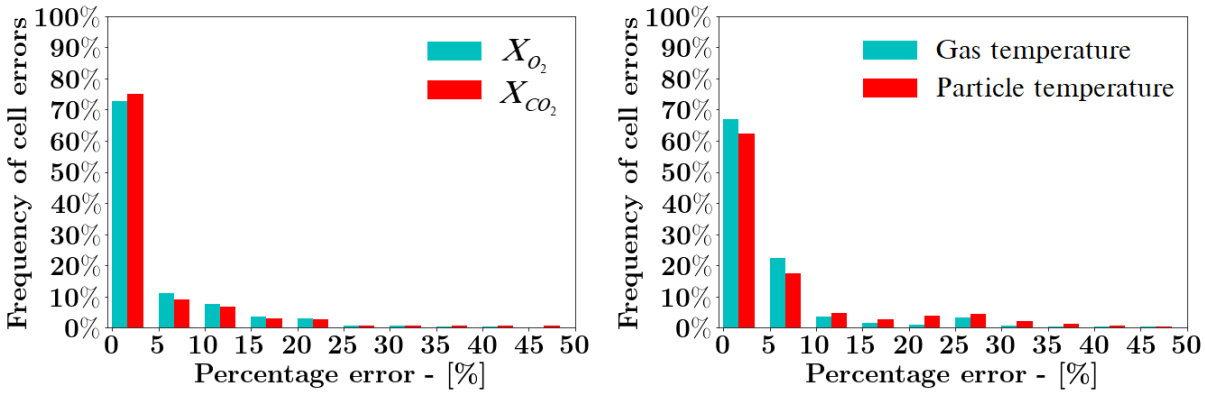

(a) (b)

Figure 4.12: Absolute error data between the EE and EL models solution data for key parameters, X_{O_2} and X_{CO_2} (a) and the gas and particle temperature (b)

The histogram plots of Figures 4.12 (a) and (b) show the key parameter absolute error between the EL and EE models, based on a per cell comparison. This highlights the EE model's sufficient resolution of the essential parameters compared to the EL model. For example, the combustion products of Figure 4.12 (a) show that approximately 80% of the EE solution data is below a 10% error band. Similarly, Figure 4.12 (b) illustrates that approximately 85% of the EE solution data is below a 10% error band for the gas temperature.

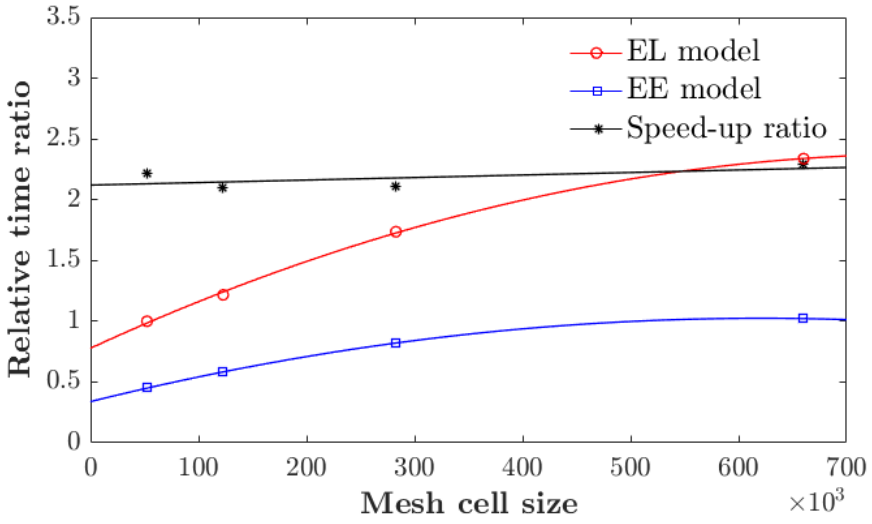

Figure 4.13: Relative time ratio versus mesh size increments for the EL and EE models

Figure 4.13 illustrates that the EE model has a substantial computational speed-up of approximately 50% whilst maintaining a sufficiently accurate resolution of the key parameters and heat flux profiles. The proposed modelling methodology speed-up is an essential feature regarding the application of the approach to generate a CFD database for surrogate modelling. The subsequent section highlights the developed CFD model's applicability at different loads.

4.2.3 Low-load case study results

The current work aims to build data-driven surrogate models capable of simulations at various loads. Therefore, the low-load cases investigated in this section are necessary to demonstrate the model's ability to resolve, with sufficient accuracy and in a computationally efficient manner, the overall flow, combustion, radiation, and temperature characteristics for a wide range of operational loads.

The results of the 60% and 40% load cases are given and discussed in the following section. Due to the lack of measured data at low-load operation, detailed EL simulation results are used to compare with the EE model results.

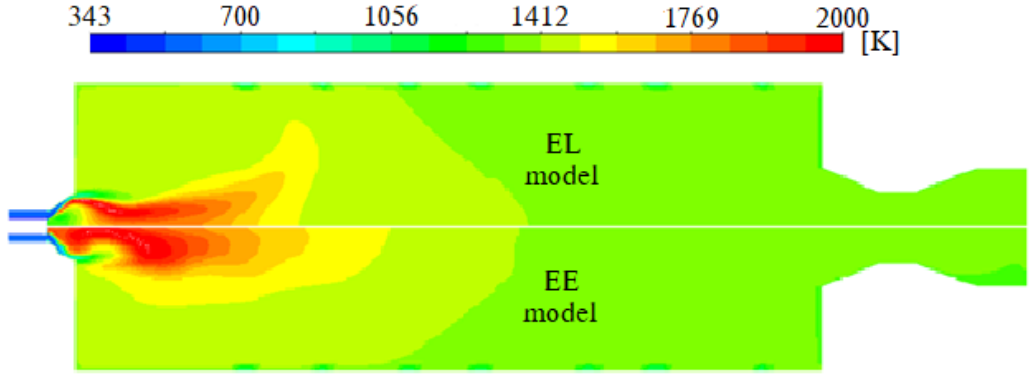

(a)

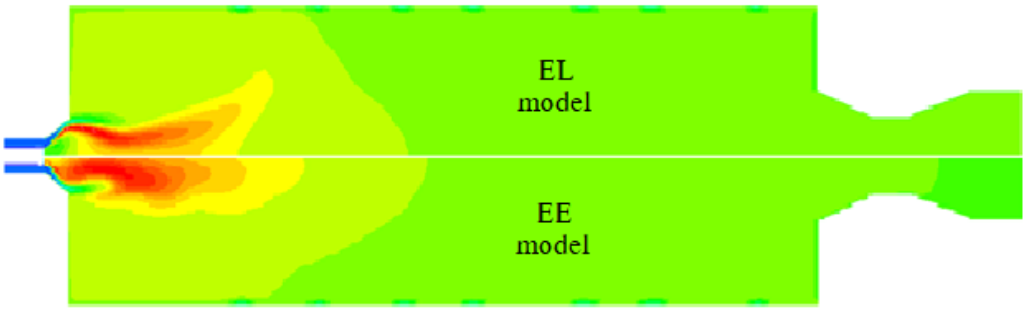

(b)

Figure 4.14: Low-load gas temperature contour plots. (a) 60% load and (b) 40% load

The gas temperature profiles of Figures 4.14 (a) and (b) demonstrate that adequate results are achieved via the EE model, with similar profiles being obtained than that of the numerical model. The total wall heat flux distributions are shown in Figures 4.11 (b) and (c) illustrate an acceptable resolution between the EE and the EL model. However, as discussed in Section 4.2.2, the EE model tends to overpredict the heat flux distribution near the burner inlet wall, confirmed in both the 60% and 40% cases.

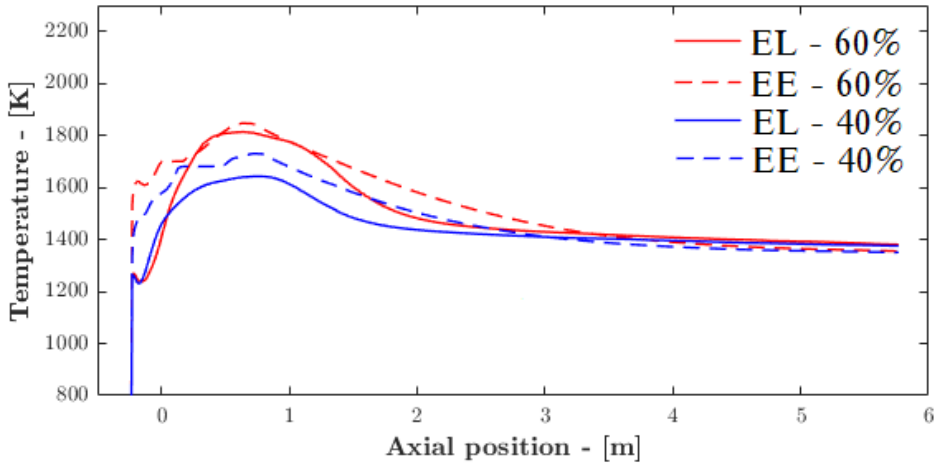

(a)

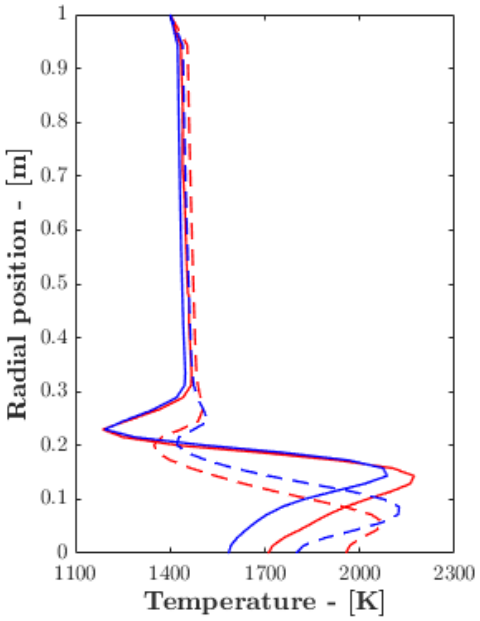

(b)

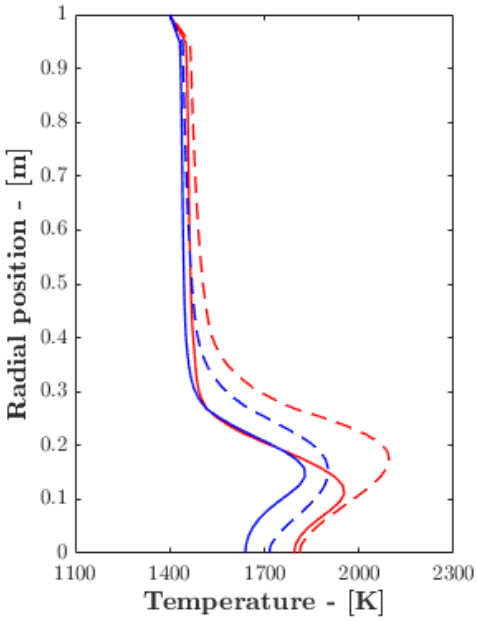

(c)

Figure 4.15: Low-load temperature plots. (a) Centreline axial plot, (b) radial plot at an axial location of 0.25 $[m]$ from point $(0, 0)$ (c) radial plot at an axial location of 0.85 $[m]$ from point $(0, 0)$

Figures 4.15 (a) to (c) illustrate the axial and radial temperature distribution plots. The EE model shows sufficient accuracy in resolving the temperature profiles for the various loads. The 100% validation case study showed that the EE model predicted a higher temperature in the burner quarl region, highlighted in the axial temperature distribution plot of Figure 4.7 (a). The radial plots of Figures 4.15 (b) and (c) illustrate the sufficient resolution of the EE models' predicted temperature profiles for low-loads compared to the detailed EL model.

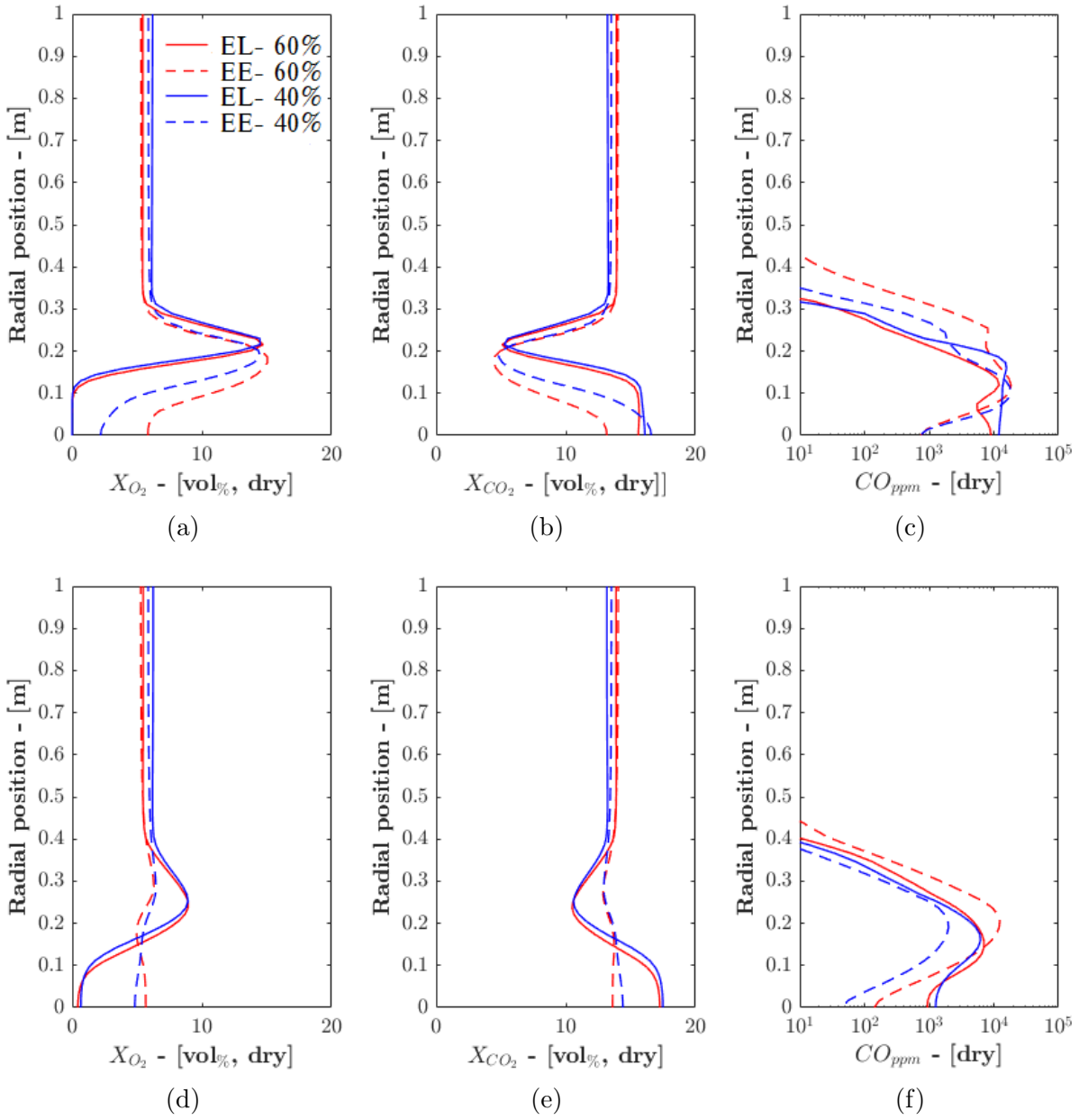

Figure 4.16: Low-load radial plots of combustion products, X_{O_2}, X_{CO_2} and CO_{ppm} at axial locations of 0.25 $[m]$ ((a)-(c)) and 0.85 $[m]$ ((d)-(f)) from point $(0, 0)$

Figures 4.16 (a) to (f) show the combustion characteristics and major species plots for the 60% and 40% EE models. The results show that the EE model can resolve the major species transport into the domain for the various loads when compared to the EL model.

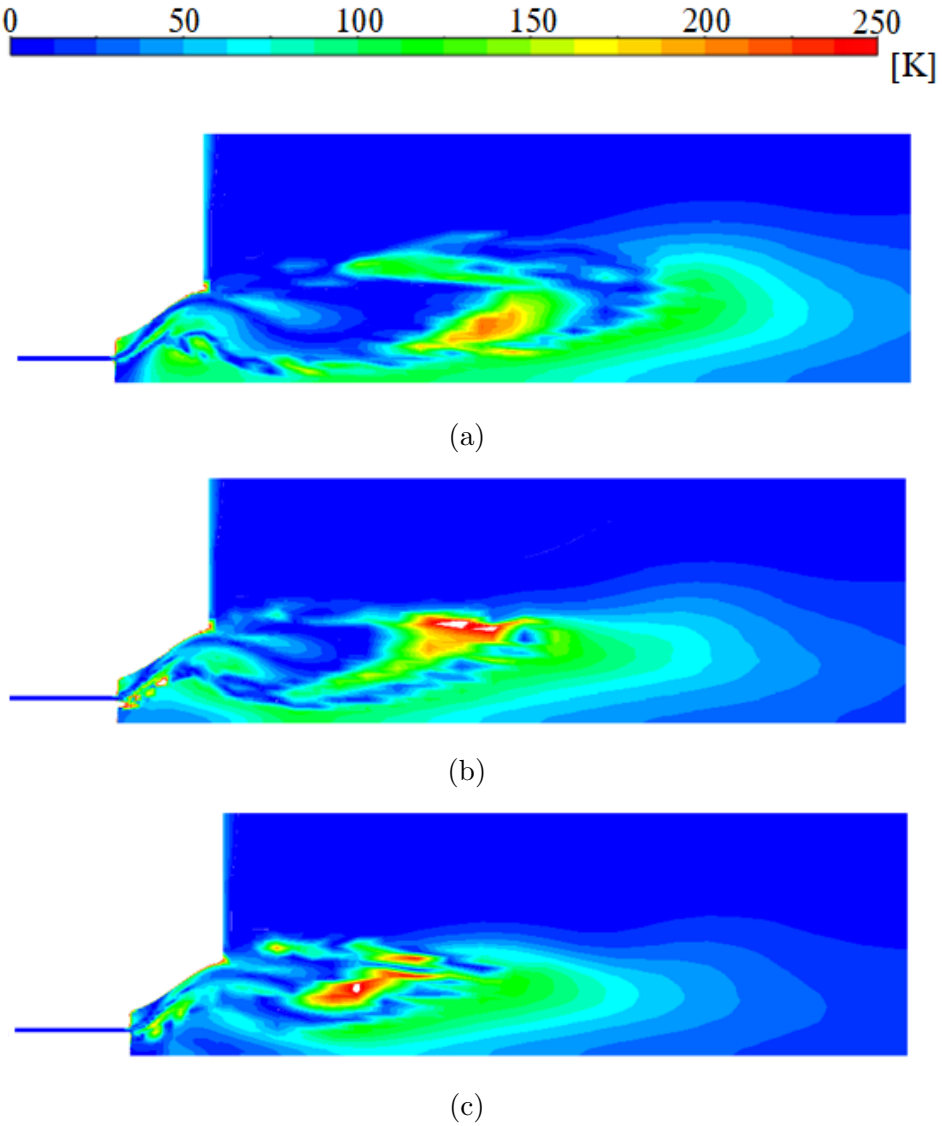

Figure 4.17: Absolute temperature difference $|T_p - T_g|$ for the EE model for (a) 100%, (b) 60% and (c) 40% load cases

Figure 4.17 shows the absolute temperature difference between the pseudo-particles and gas-phase, highlighting the importance of incorporating thermal non-equilibrium for lower loads. By assuming thermal non-equilibrium, the radiative particle emission effects can be adequately resolved. A thermal equilibrium solution would underpredict these particulate effects, leading to incorrect combustion activation in the domain.

The results provided in this section highlight the EE model's suitability for various load applications and the robustness of the incorporated combustion models. A speed-up of approximately 50% was observed, with an approximate 5% absolute error between important key parameters for the 60% and 40% load cases.

4.2.4 Summary of results

A thermal non-equilibrium Eulerian-Eulerian modelling methodology for CFD simulations of pulverised coal combustors was presented and applied. The model was validated against measured and numerical data for a 100% load case with relative errors ranging from 0.2% to 5% for the wall heat flux distribution. In addition, further low-load simulations were conducted, with validation data obtained from EL simulations.

The results show that the modelling methodology can resolve the combustor-level flow, species, temperature profiles, and wall flux distributions in the combustor with sufficient accuracy. Furthermore, the inclusion of particle effects in the radiation and energy transport proved to be beneficial in implementing the combustion laws, thereby illustrating the importance of the thermal non-equilibrium assumption. The computational speed enhancement between the traditional modelling methodology and the proposed model showed a 50% speed-up. It therefore fulfils the need for a fast yet sufficiently accurate three-dimensional CFD modelling methodology to generate databases of results for surrogate model development.

The methodology was developed and implemented in the ANSYS Fluent® v19.5 commercial software package, as opposed to an in-house academic or proprietary code, allowing it to be employed in industry to develop computationally inexpensive models for pulverised fuel systems.

Chapter 5

Numerical model case studies

Any numerical model used to represent real-world phenomena requires validation with a set of experimental results to ascertain the accuracy and reliability of the model. Chapter 4 discussed the foundation of the developed CFD modelling methodology and provided a validation case study for a 2.165 $[MW_{th}]$ lab-scale burner. In the current chapter, the numerical methodology was incorporated to simulate an actual 620 $[MW_e]$ utility boiler located in Southern Africa. The subsequent sections comprise of the following validation and application studies using the previously discussed CFD and process modelling methodologies, namely:

- A validation case study showcasing the implementation of the developed CFD model of a 620 $[MW_e]$ utility boiler for various operational loads using site data.
- Coupled simulation techniques, utilising CFD and 1-D process modelling to capture the steam-side performance of a utility-scale boiler.
- An application case study was conducted using the developed CFD modelling methodology in a co-simulation environment to investigate the optimal firing arrangement for low-load operation (approximately 30% MCR) of the 620 $[MW_e]$ utility-scale boiler.

Figure 5.1 highlights the content that is discussed and indicates the research objective addressed in this chapter for the readers convenience.

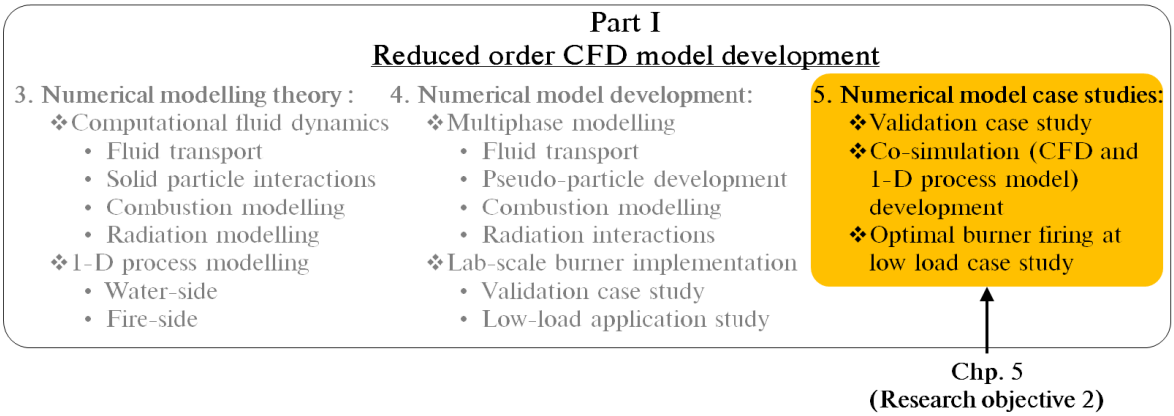

Figure 5.1: Content overview and research objective addressed in Chapter 5

5.1 Validation case study

The following section emanates from the work presented at the 12th South African Conference on Computational and Applied Mechanics (SACAM2020)[115]. The validation case study was conducted for 100%, 81%, and 60% maximum continuous rating (MCR) loads, with the results being compared to actual plant measurements and numerical results. As with Section 4.2, an Eulerian-Lagrangian (EL) based CFD computations provide the necessary numerical data for the validation study.

5.1.1 Computational domain

The case study boiler is a two-pass subcritical power boiler with a furnace depth of 13.77 $[m]$, a width of 14.01 $[m]$, and a height of 64 $[m]$. The CFD geometric model (Figure 5.2) uses a symmetry plane at half the width of the furnace; this was done to reduce the cell count of the numerical mesh. The platen (SH2) and final (SH3) superheaters are modelled as discrete solid wall panels with transverse pitches of 1.143 $[m]$ and 0.8 $[m]$, respectively. The boiler walls downstream from the superheaters are modelled as fully insulated. The reason for including SH3 in the downstream ducting was to ensure that no backflow profiles are created and the velocity profiles through the superheaters are representative of the actual boiler. There are three levels of burners located on both the front and rear walls at heights of 11.9 $[m]$, 19.3 $[m]$, and 26 $[m]$, respectively.

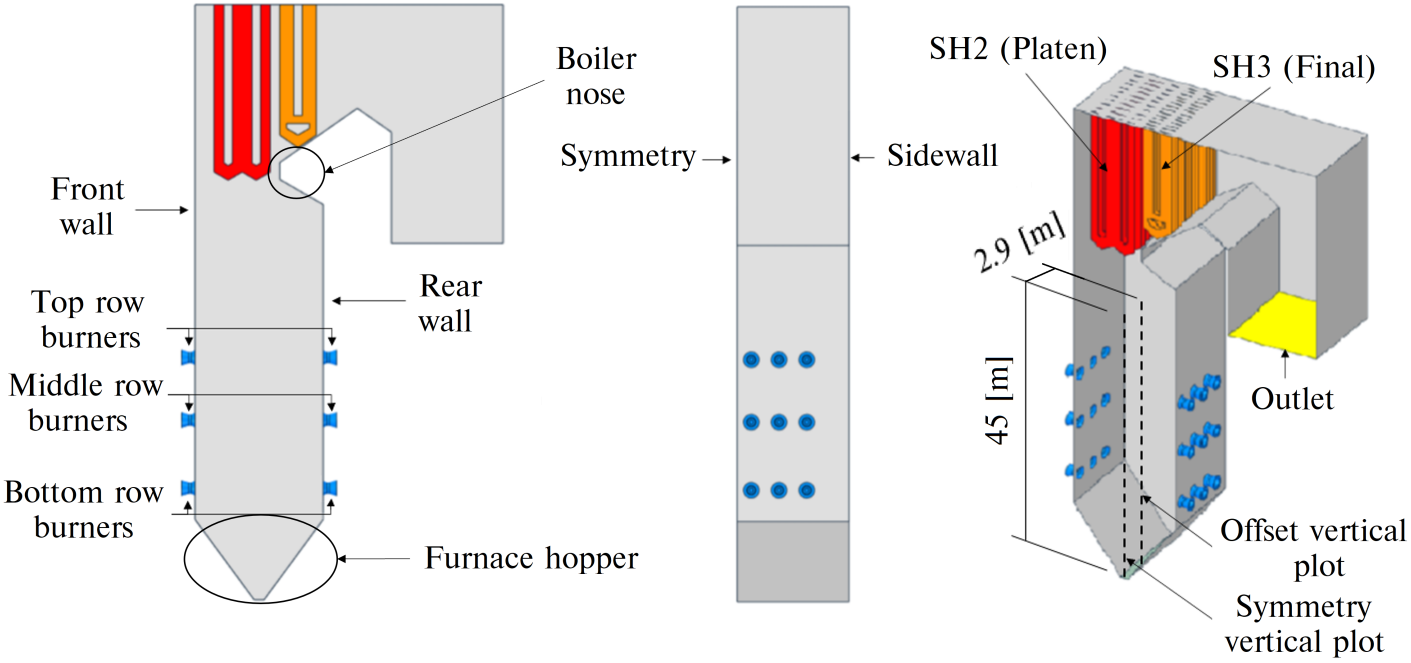

Figure 5.2: Computational domain and layout [104].

Figure 5.2 illustrates the computational domain and layout for the modelled half of the furnace, which includes the SH2, SH3, and the furnace boundary walls (front, rear, and side), as well as the domains outlet, symmetry and inlet (i.e. burners) planes.

The boiler furnace is fed by six mills, each supplying a pulverised fuel and primary air (PA) mixture to a burner row consisting of six opposing wall-mounted swirl burners. This study did not model the swirl vanes; instead, an axial and tangential velocity component was used for the secondary air (SA) inlets. These values were obtained from a detailed burner model supplied by the burner manufacturer, which included the vanes.

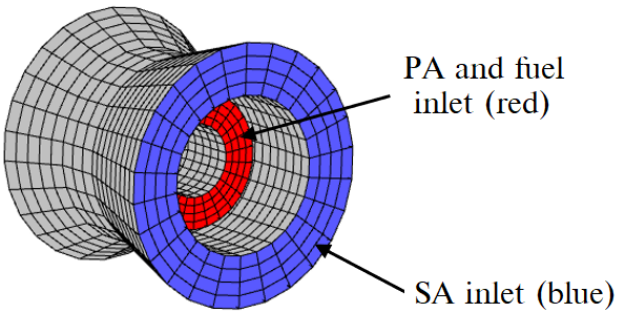

Figure 5.3: Burner layout and mesh details [104].

The fuel and PA mixture is injected through the inner annulus of the burner while the SA is fed through the outer annulus, as seen in Figure 5.3. At 100% maximum continuous rating (MCR), the PA annulus supplies the fuel and PA mixture at a temperature of 373 $[K]$, with the SA entering at a temperature of 577 $[K]$.

5.1.2 Model inputs & boundary conditions

The inlet mass flow rates and temperatures for MCR ratings of 100%, 81% and 60% are listed in Table 5.1.

Table 5.1: Validation case study input boundary conditions

Load cases	**100%**	**81%**	**60%**	**Unit**
Fuel mass flow rate (per burner)	3.15	2.52	1.67	kg/s
PA mass flow rate (per burner)	4.74	4.01	2.81	kg/s
SA mass flow rate (per burner)	14.31	12.04	8.43	kg/s
PA temperature	373	373	373	K
SA temperature	577	558	535	K
ϕ_{mp0}	0.657	0.628	0.594	kg_{mp0}/kg
ϕ_{H_2O}	0.036	0.035	0.032	kg_M/kg
ϕ_{VM}	0.129	0.123	0.116	kg_{VM}/kg
ϕ_{FC}	0.223	0.214	0.202	kg_{FC}/kg
ϕ_{ASH}	0.268	0.257	0.243	kg_{ASH}/kg
ϕ_{hp}	49657	47509	44929	J/kg

Appendix B provides sample calculations used to determine the fuel and air mass flow rates needed for the CFD simulations inlet boundary conditions. Furthermore, the specific heat, thermal conductivity, and viscosity, of the air and flue gas are resolved using temperature-based polynomials which are provided in Appendix C.

The plant is designed to operate at a 100% MCR with an excess air ratio of 15.5%. As the plant is turned down from 100% MCR, the excess air ratio increases to ensure sufficient air and fuel mixing. Based on the design schedule data, the excess ratios for MCR ratings of 81% and 60% were calculated as 20.9% and 26.3%, respectively. The fuel characteristics utilised in both the validation and low-load case studies of this chapter are provided in Table 5.2.

Table 5.2: Utility boiler fuel constituents

Fuel constituent	**Fraction**	**Unit**
Ultimate analysis - (DAF)	-	-
Carbon	0.7754	kg/kg_{fuel}
Hydrogen	0.041858	kg/kg_{fuel}
Nitrogen	0.0182	kg/kg_{fuel}
Oxygen	0.1474	kg/kg_{fuel}
Sulphur	0.0175	kg/kg_{fuel}
Proximate analysis	-	-
FC	0.340	kg/kg_{fuel}
VM	0.196	kg/kg_{fuel}
ASH	0.409	kg/kg_{fuel}
H_2O	0.055	kg/kg_{fuel}
Energy content - (As-received)	**Value**	
Higher heating value (HHV)	15070	kJ/kg_{fuel}
Devolatisation		
Pre-exponential factor (A_{vol})	2.0×10^5	s^{-1}
Activation energy ($E_{a,vol}$) [116]	6.7×10^7	$J/kmol$
Char oxidation		
Pre-exponential factor (A_c)	0.0053	$kg/(m^2 sPa)$
Activation energy ($E_{a,c}$) [116]	8.37×10^7	$J/kmol$

The CFD wall boundary conditions are modelled using ANSYS Fluent® v19.5's convection boundary condition, which requires the internal free stream temperature, the internal heat transfer coefficient, wall thickness, and material conductivities. Being a flux boundary condition, the wall heat flux ($\dot{q}_{wall}$) can be calculated using the following equation:

$$\dot{q}_{wall} = U_i(T_{wall,i} - T_{water}). \tag{5.1}$$

The overall heat transfer coefficient (U) is subsequently determined using the following expression:

$$U_i = \left(\frac{1}{\tilde{h}_{int}} + \frac{L_{wall}}{\lambda_{wall}} + \frac{L_{ash}}{\lambda_{ash}} \right)^{-1}. \tag{5.2}$$

In the present work, an effective thermal conductivity was derived to include the ash and wall conductivities. Thus, Equation (5.2) can be written using a single boundary thickness as:

$$U_i = \left(\frac{1}{\tilde{h}_{int}} + \frac{L_{wall}}{\lambda_{eff.wall}} \right)^{-1}. \tag{5.3}$$

The full derivation of the effective thermal conductivity ($\lambda_{eff.wall}$) is provided in Appendix A. A 1-D process model was used to estimate the furnace, platen, and final superheater internal heat transfer coefficients and internal temperatures for the low-load case. For the validation case study, the measured site data was used to estimate the mean water temperature in the heat exchangers, this value being close to the saturation temperature of the water at the steam drum pressure.

5.1.3 Grid independence study

A mesh independence study was conducted for mesh sizes consisting of 4.2, 8.2, 6.2 and 10.2 million cells respectively. To ensure an accurate numerical solution, the mesh aspect ratios were kept below 15 and the minimum orthogonal qualities were kept above 0.2. The utility-scale boiler was simulated for the 100% MCR load case utilising both the conventional EL and the developed EE modelling methodologies to illustrate grid independence of both models. Each simulation utilised the same numerical strategy as stipulated in the subsequent section and were solved to convergence.

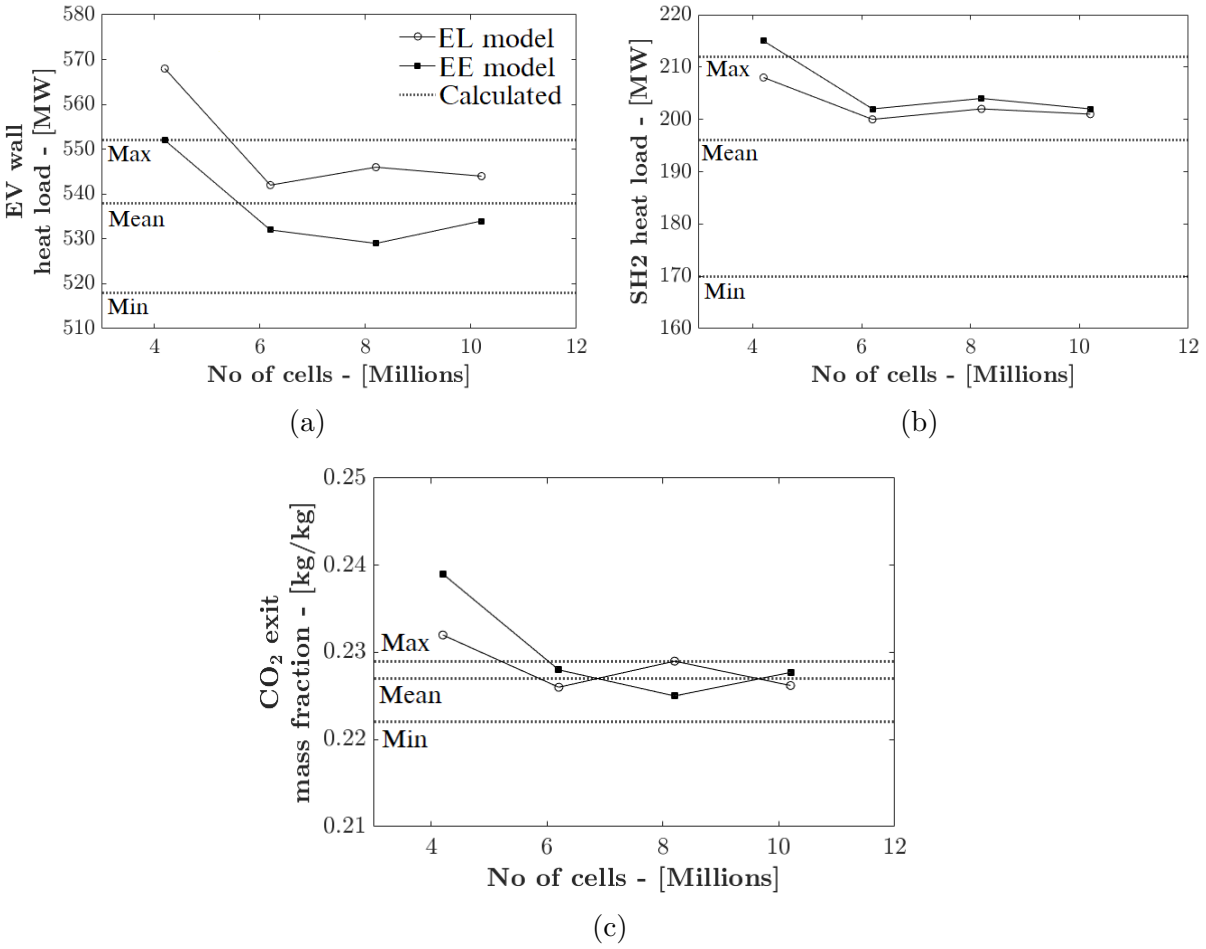

Figure 5.4: Mesh refinement study for key parameters (a) total heat load to the evaporator walls, (b) the total heat load to the SH2 walls and (c) the exit CO_2 mass fraction.

Figures 5.4 (a) to (c) illustrates the comparison between the calculated mean, minimum, and maximum values, and the simulation results of the mesh refinement study for the heat loads to the evaporator (EV) and SH2 walls, as well as the exit CO2 mass fractions. The calculated mean values were obtained from available measured data, except for the CO_2 mass fraction which was calculated using the assumptions of complete and infinitely fast combustion. Appendix A provides the methods and sample calculations employed to obtain the exit CO_2 mass fraction using the stated assumptions. The exit CO_2 and subsequent O_2 volume fractions are typically used as key indicators of near complete combustion for CFD simulations and were used as a further convergence criterion for the current CFD simulations.

A noticeable difference in the simulated results and the calculated mean value is shown in Figure 5.4 (b) for the heat load to the SH2 walls. Both numerical simulations tend to overpredict the heat loads, but are within the maximum limit of the calculated values. However, for meshes sizes greater than 6.2 million cells, the models predict values within 3% of the calculated mean value, which was deemed sufficiently accurate for the current work. Considering the key parameters utilised in Figure 5.4 (a) to (c), by increasing the mesh size above 6.2 million cells, the values of mesh sizes 8.2 and 10.2 million cells, are within a 1% range of the 6.2 million cell results. In addition, the simulated values are within a 5% range of the calculated mean values, which was deemed sufficiently accurate for the current work. This indicates that a solution value that is independent of the mesh size has been reached, and therefore the 6.2 million cell mesh was subsequently used for both the EL and EE simulation runs.

5.1.4 Numerical solution strategy

The validation simulations were performed using the ANSYS Fluent® v19.5 pressure-based solver. Pressure-momentum coupling was set to the SIMPLE technique, with momentum, energy and species equations being discretised using the second-order upwind method. The pressure equation was discretised using PRESTO!. The difference arises between using scalar fields in the EE configuration and using the discrete phase modelling approach in the EL setup. The under-relaxation strategy, for all the EE and EL simulations, utilised the same under-relaxation factors for the pressure, density, momentum, energy, turbulence, species, and P-1 source terms. However, the EL simulations required significant under-relaxation of the DPM sources to maintain stability of the coupled calculations between the discrete and continuous phase, to a value of 0.15. The discrete phase equations were solved once every 30 fluid phase iterations for the EL model. The number of particles injected per burner was set to about 7800, totalling 140,000 particles in the entire domain. The EE simulations achieved stable and computationally efficient runtimes when an under-relaxation factor of 0.5 was utilised for all the scalar transport variables. To ensure a stable converged solution, the spatial discretisation for all fields was set to first-order upwind (except pressure) and solved for 1500 iterations before increasing the discretisation order. The simulations were then run for a further 15,000 iterations for both the EE and EL simulations. The maximum mass imbalance was 0.046 $[kg/s]$ for a total gas flow rate of 376 $[kg/s]$ at 100% MCR conditions. The maximum heat imbalance for the full load case was 2.45 $[MW]$ for a total heat input of 855 $[MW]$.

5.1.5 Results & discussion

This section compares the results of the EL numerical model with the results of the developed EE modelling approach for the 100%, 81% and 60% MCR load cases. Overall, a 30% decrease in simulation time was observed across the simulated load cases. For all simulation cases, 192 Intel® Xeon® 2.6 GHz cores were made available using the Lengau® computing cluster provided by the Centre for High Performance Computing (CHPC), South Africa. The graphs shown in Figure 5.5 illustrate the measured values (calculated from measured plant data), EL and EE model results for the heat loads to the EV, platen (SH2) and final superheater (SH3) walls.

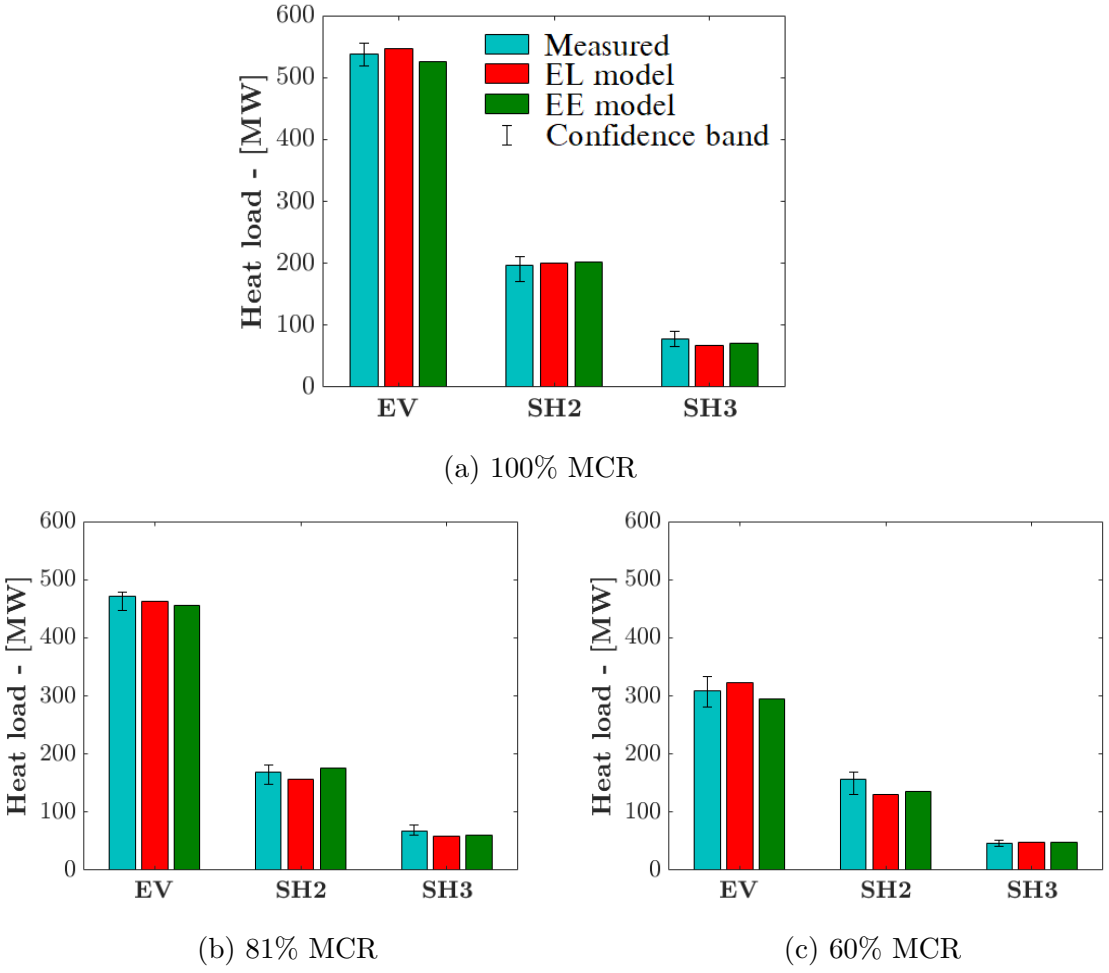

(a) 100% MCR

(b) 81% MCR

(c) 60% MCR

Figure 5.5: Overall heat load performance for (a) 100%, (b) 81% and (c) 60% MCR load cases

The EE model sufficiently captures the overall heat loads compared to the measured and EL model results. However, a notable difference is seen in the 60% load case of Figure 5.5 (c), where both the EL and EE numerical models underpredict the SH2 heat load. The EE model predicts a value of 136 $[MW]$, an approximate 13% deviation from the measured value, while the EL model predicted a value of 130 $[MW]$, an approximate 17% deviation from the measured value.

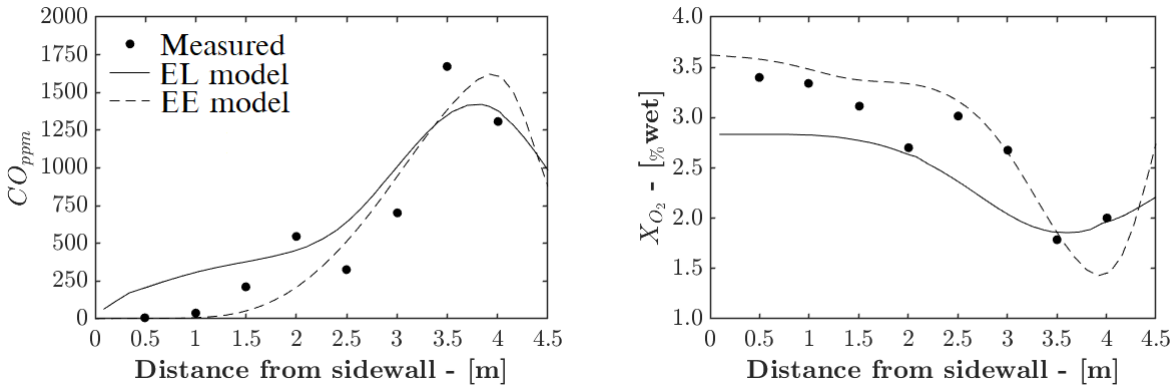

(a) (b)

Figure 5.6: Measured, EL predicted, and EE predicted CO_{ppm} (a) and X_{O_2} (b) concentrations

The EE CFD model was further validated by comparing the measured CO_{ppm} and X_{O_2} levels near the furnace outlet to the EL predictions, which are presented in Figure 5.6. The measurements were taken by experienced site personnel using a suction pyrometer. The probe measurements were taken at a furnace height of 37.5 $[m]$ near the centre of the boiler during full load (100% MCR) operating conditions. The probe was inserted from the side walls to a depth of 4.5 $[m]$, and measurements were taken every 0.5 $[m]$. The results show that the EE model can predict the CO_{ppm} and X_{O_2} concentrations at the given probe location with acceptable accuracy, compared to both the measured and the EL predictions.

Table 5.3: Relative percentage errors of key parameters between the EL and EE model

Load rating	**100%**	**81%**	**60%**
Furnace heat load	4.1%	8.2%	1.2%
Platen SH heat load	6.9%	7.4%	7.2%
Final SH heat load	2.8%	3.8%	4.2%
Furnace exit temperature	3.6%	4.8%	5.6%
Exit X_{CO_2} fraction	2.1%	1.6%	0.9%
Exit X_{O_2} fraction	1.9%	3.2%	2.8%

Table 5.3 highlights the relative errors obtained between the EL and EE numerical models. A maximum error of 8.2% occurs at the platen superheater for the 100% load case. The relative errors are deemed acceptable for the decrease in computational time provided by the EE model.

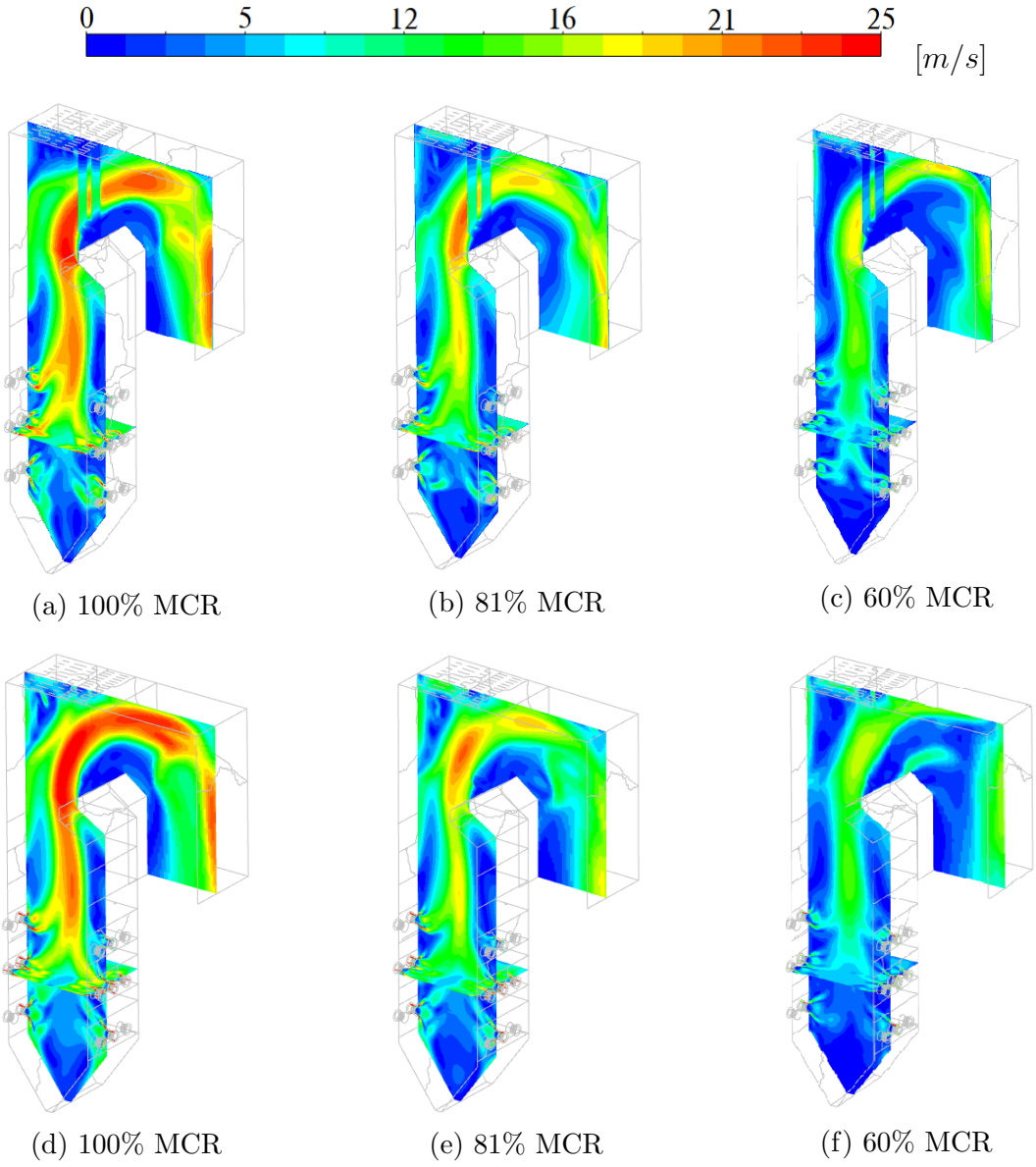

(a) 100% MCR (b) 81% MCR (c) 60% MCR

(d) 100% MCR (e) 81% MCR (f) 60% MCR

Figure 5.7: Gas velocity fields for the EL model ((a) to (c)) and the EE model ((d) to (f)), at 100%, 81% and 60% MCR loads

Figure 5.7 compares the gas velocity fields for the EL and EE model. The results are in good agreement. The EE model underpredicts the lower burner velocity transport resulting in combustion occurring closer to the burner quarl and the lower furnace walls. This effect is seen in the temperature contour plots of Figures 5.8 (d-f).

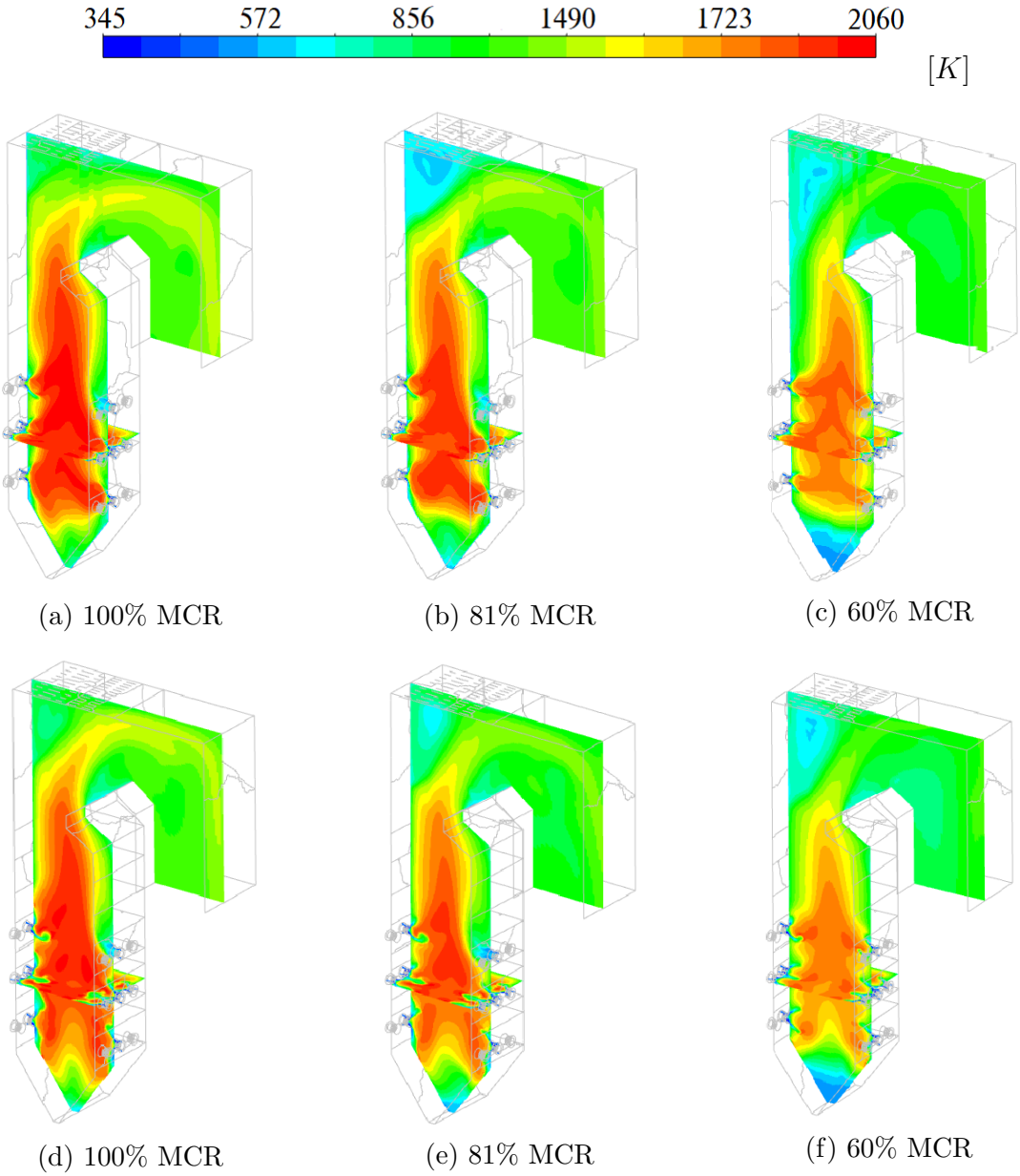

(a) 100% MCR (b) 81% MCR (c) 60% MCR

(d) 100% MCR (e) 81% MCR (f) 60% MCR

Figure 5.8: Temperature fields for the EL model ((a) to (c)) and the EE model ((d) to (f)), at 100%, 81% and 60% MCR loads

The temperature contour plots of Figures 5.8 (d) to (f) illustrate the EE model's ability to sufficiently resolve the temperature field compared to the EL model (Figures 5.8 (a) to (c)). The lower burners tend to initiate combustion closer to the burner leading to high temperatures due to the lack of velocity of the gas-phase in this area. In general, the temperature and velocity fields are deemed sufficiently accurate for surrogate model development since the parameter of interest is the resolution of the wall flux field.

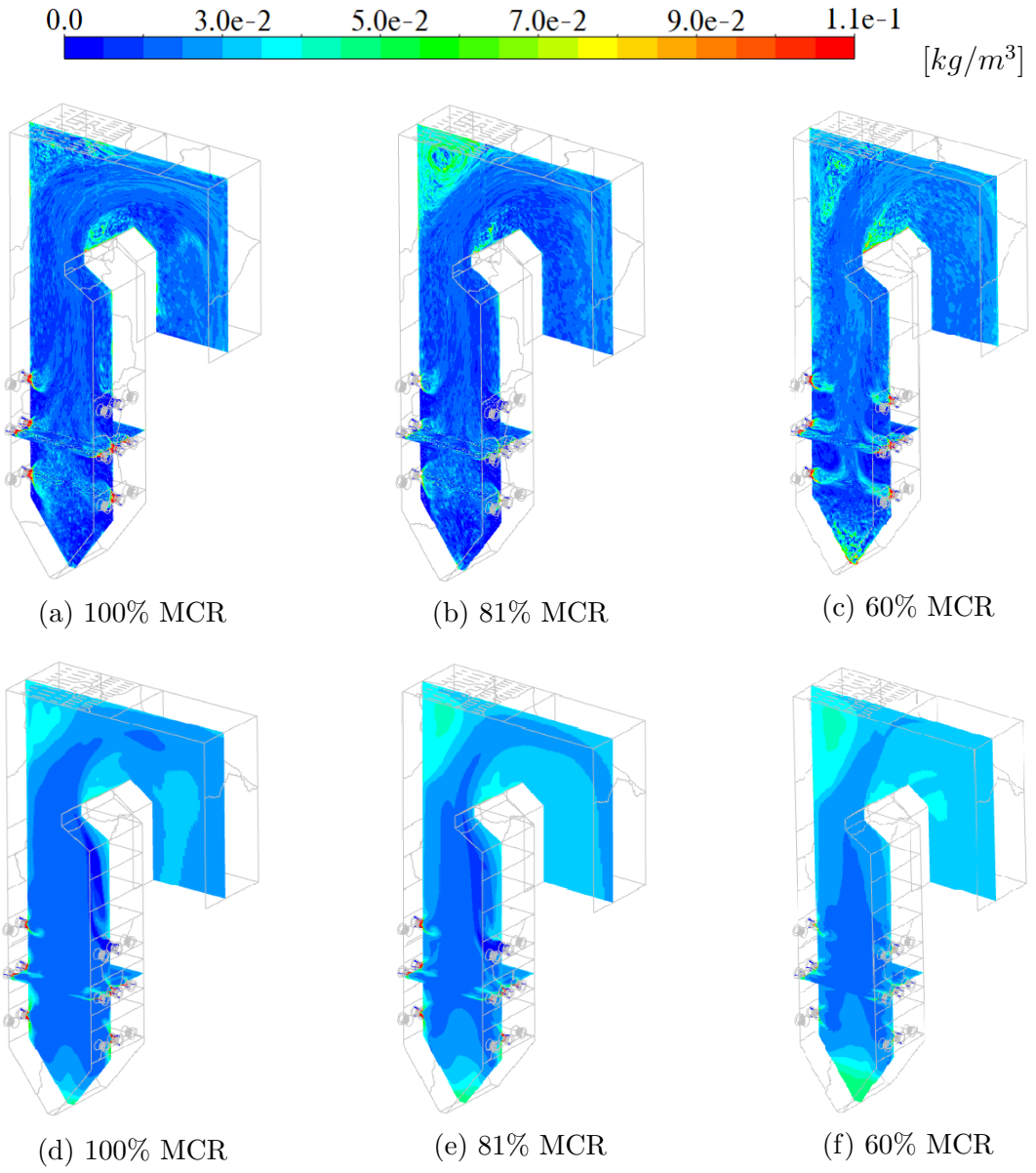

(a) 100% MCR (b) 81% MCR (c) 60% MCR

(d) 100% MCR (e) 81% MCR (f) 60% MCR

Figure 5.9: Particle distributions for the EL model ((a) to (c)) and the EE model ((d) to (f)), at 100%, 81% and 60% MCR loads

The spatial distribution of the particles (expressed in $[kg/m^3]$) shown in Figures 5.9 (a-f) highlights the EE model's ability to resolve the particle concentration throughout the domain for the various load cases. Notably, the EL model (Figures 5.9 (a) to (c)) predicts high particle concentrations located in areas such as in the top left corner of the furnace, above the boiler nose, and in the furnace hopper (refer to Figure 5.2). From Figures 5.9 (d) to (f) the EE model is able resolve these high concentration pockets of particles with sufficient resolution compared to the EL model, for a wide range of MCR loads. This enables the EE model to incorporate the pseudo-particulate radiative and fluid flow effects in these areas.

The validation of a full scale 620 $[MW_e]$ boiler was conducted using a thermal non-equilibrium Eulerian-Eulerian model for three load cases, namely a 100%, 81% and 60% steady-state loads. The validation cases included a comparison with results obtained by a numerical model using an EL approach and, where applicable measured site data. The developed EE model demonstrated adequate performance in predicting the flow field, wall heat fluxes and fluid property distributions. The relative accuracy of the EE model ranged from 2 to 8% for key parameters used in the study. The computational speed-up, of 30% is a beneficial attribute when considering the EE model's intended use in the development of a CFD data-driven surrogate model.

5.2 Coupled simulation methodology

The following section highlights the co-simulation techniques employed to account for the steam-side performance of a 620 $[MW_e]$ utility-scale boiler. The model is subsequently used in Section 5.3 to investigate the optimal firing arrangement for low-load operation. Figure 5.10 provides a labelled schematic of the process model and highlights the radiation and convective sections.

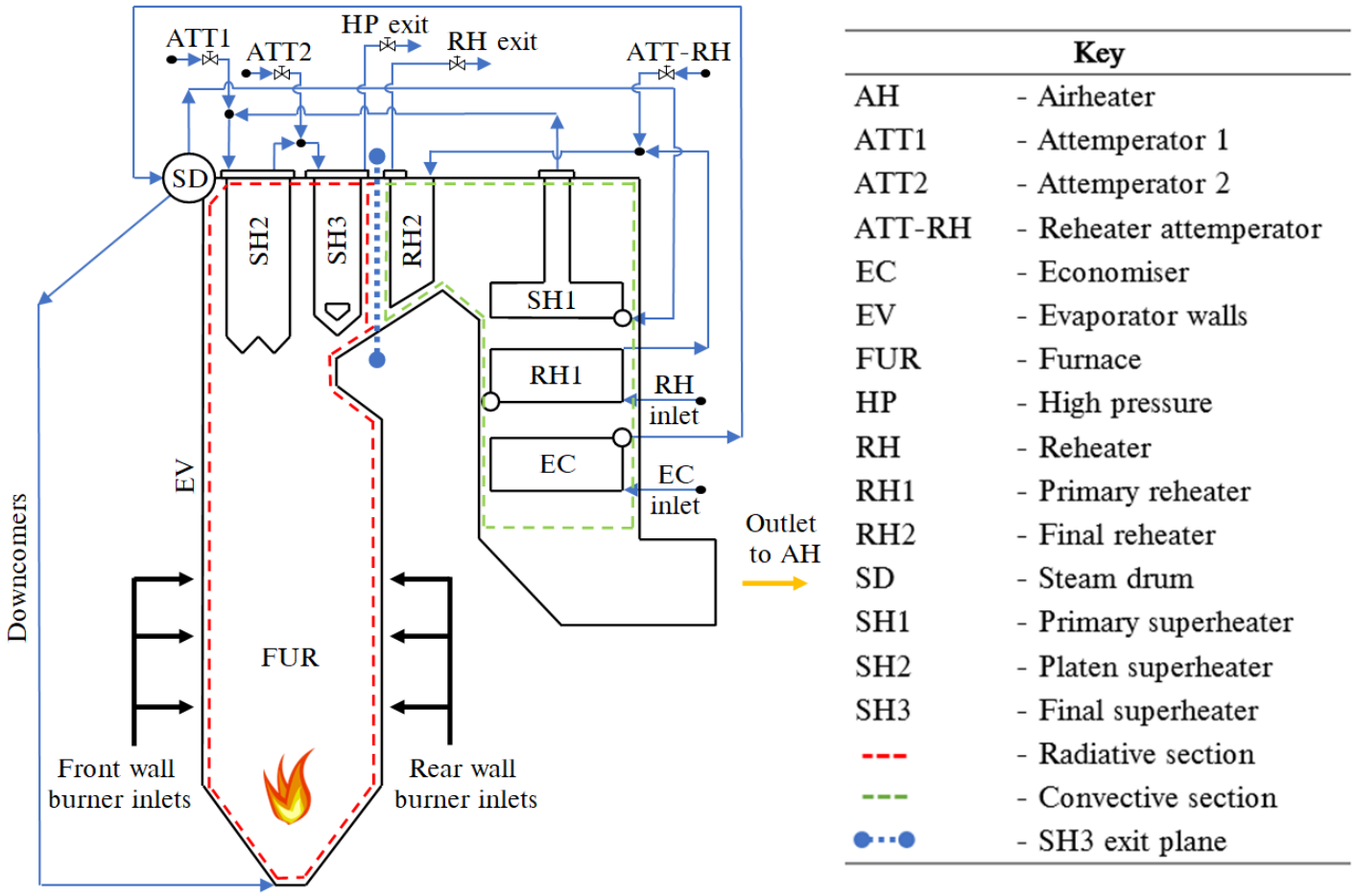

Figure 5.10: Labelled process model schematic for a 620 $[MW_e]$ utility-scale boiler

Coupled simulation approaches can be implemented in several ways; Filmonov [45] described the main implementations for simulating hydrodynamics and heat transfer in multi-scale models as either fully-separated, a hydro-dynamically unified or a hydro-dynamically disconnected model. The current work uses a fully-separated model, whereby the spatial (3-D CFD flue gas domain) and network components (1-D process model) are solved separately.

A 1-D discretised process model of the water/steam side piping network, which includes the furnace evaporator (EV) walls, platen superheater (SH2) walls, final superheater (SH3) walls, and the subsequent downstream heat exchangers of the convective section, was developed using Flownex® SE 2021. The convective section is comprised of the secondary reheater (RH2), primary superheater (SH1), primary reheater (RH1) and economiser (EC). In addition, the model includes all the relevant attemperators (ATT1, ATT2, and ATT-RH), inlets, and outlets. The process model is used to determine the required attemperation flow rates and water/steam side thermal response. The process model simulates the internal convection heat transfer inside the tubes and the conduction through the tube walls. In addition, the model can incorporate the attemperation flows and momentum transport through the steam/water circuit. The heat exchangers are modelled using a homogeneous two-phase mixture approach, which assumes that the fluid properties, phase velocities, and temperatures are uniform per cross-sectional area, as discussed in Chapter 3, Section 3.5. The EV water walls are represented by a single lumped pipe flow component that forms part of the natural circulation system which includes the downcomers and steam drum (SD). As with the EV walls, SH2 and SH3 are similarly represented by a single lumped parameter pipe flow component, interconnected with nodes that introduce the attemperation flows to the water/steam side.

The data transfer between the two models uses a one-way coupling approach, where the CFD simulation data is transferred to the FlownexSE® process model when convergence of each case is achieved. This coupling approach is valid since in the furnace and the radiant superheaters (SH2 and SH3) radiation heat transfer dominates, resulting in flue gas temperatures being much higher than the wall temperatures in these zones. Thus, a one-way coupling between the two models can be utilised since the wall temperatures are not that important in resolving the overall heat load to these components. Figure 5.11 shows the simplified flowchart for a fully connected coupled simulation.

The coupling interfaces between the simulation models are the selected heat-exchanger external heat transfer areas, namely, the EV, SH2, and SH3 walls. The CFD heat loads are used as energy sources for these components. The furnace heat load to the EV walls determines the steam generation rate through the evaporator. The SD separates the gas from the liquid. The liquid water is recirculated through the EV walls via the downcomers, and the saturated vapour (steam) is sent through the main steam line for superheating.

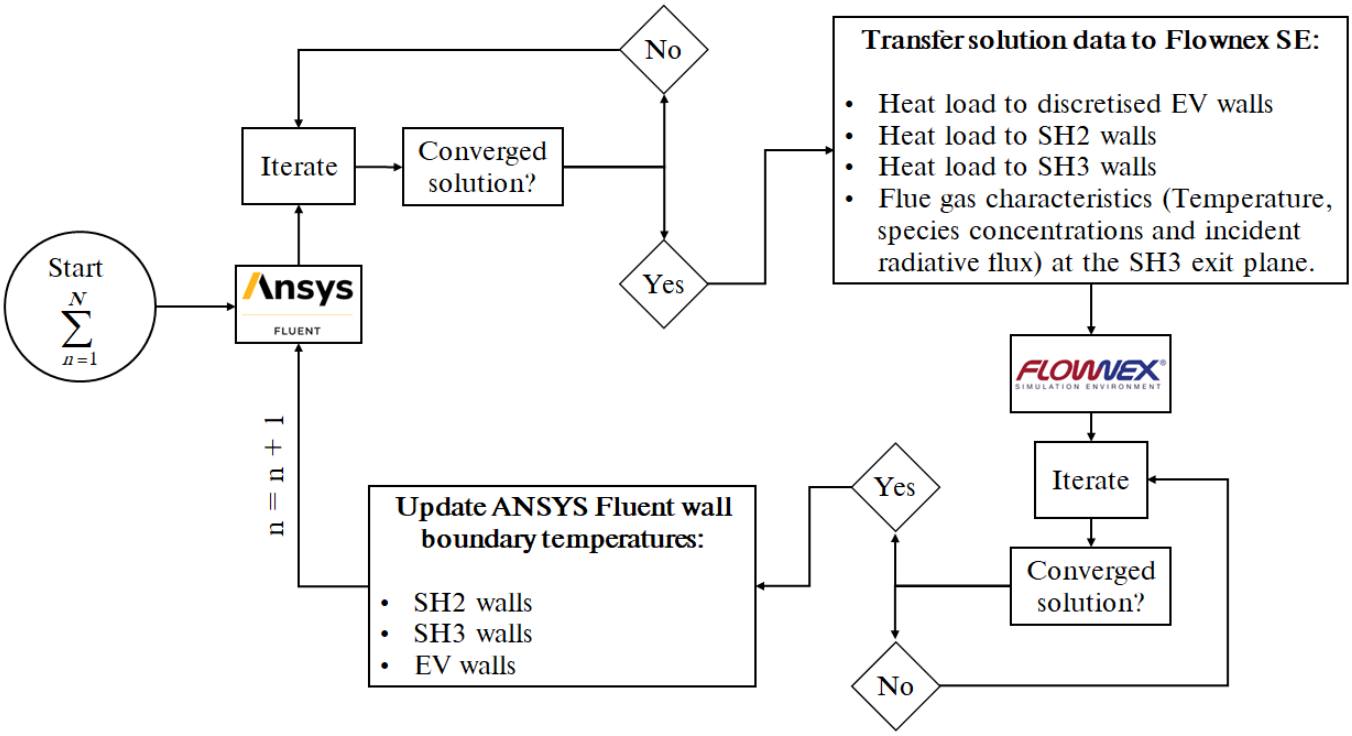

Figure 5.11: Coupled simulation flow chart

As mentioned, the heat transfer rates to the radiant superheaters (SH2 and SH3) calculated using the CFD model are also transferred to the process model as heat sources. Furthermore, the CFD flue gas results (i.e., composition, mass flow, and temperature) exiting SH3 are used as boundary value inputs to the SH3 exit plane, as shown in Figure 5.10. In addition to the flue gas values, the area weighted incident radiation (G_{CFD} $[W/m^2]$) at the convective plane is also used as a boundary value input. These inputs are used for the downstream components of the convective section of the boiler. The boundary values for the RH and EC inlets are fixed inlet mass flow rates and temperatures taken from site data, while the high pressure (HP) and RH exits are set to fixed pressure boundary values.

Figure 5.12 illustrates the heat-exchanger component process model. This component is used for the heat exchangers downstream of SH3 (Figure 5.10). The component accounts for the radiative (gas and direct), convective, and conduction heat transfer mechanisms to and from the flue gas-side and water-/ steam-side control volumes. The total heat transferred ($\dot{Q}_{steam}$) to the water-/ steam-side control volume can be written as the sum of the external heat transfer rates transmitted from the flue gas control volume, namely the absorbed direct radiation ($\dot{Q}_{abs}$) and a combined heat transfer rate ($\dot{Q}_{cr}$), which is shown in Equation (5.4).

$$\dot{Q}_{steam} = \dot{Q}_{cr} + \dot{Q}_{abs} \tag{5.4}$$

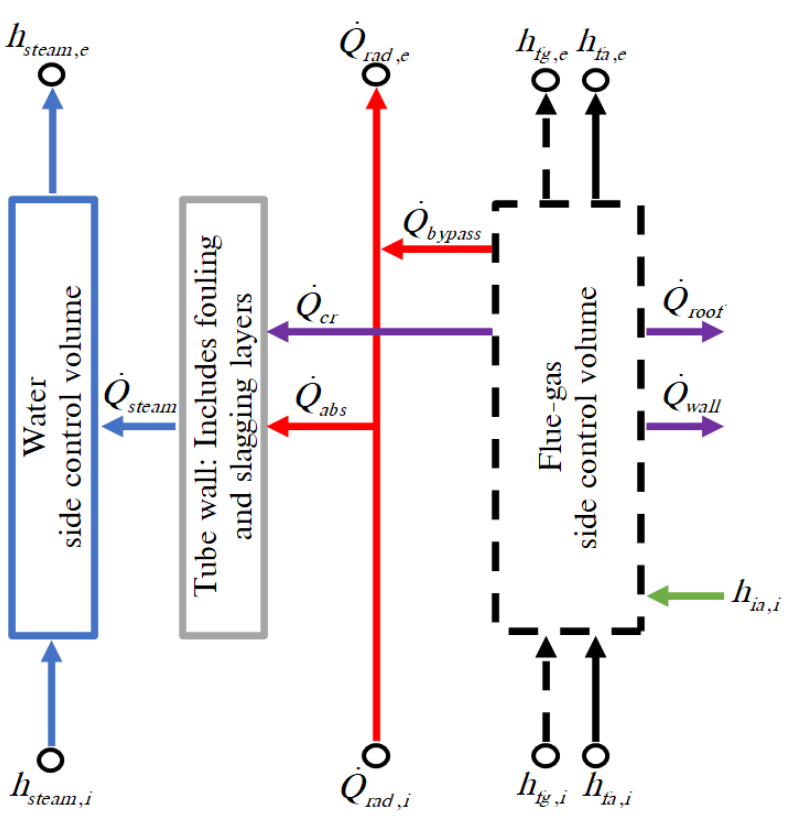

Key	
$h_{fa,i}$	- Enthalpy fly-ash in
$h_{fa,e}$	- Enthalpy fly-ash exit
$h_{fg,i}$	- Enthalpy flue gas in
$h_{fg,e}$	- Enthalpy flue gas exit
$h_{ia,i}$	- Enthalpy ingress air
$h_{steam,i}$	- Enthalpy steam in
$h_{steam,e}$	- Enthalpy steam exit
$\dot{Q}_{abs}$	- Absorbed direct radiation
$\dot{Q}_{bypass}$	- Bypass direct radiation
$\dot{Q}_{cr}$	- Heat due to convection and gas radiation
$\dot{Q}_{rad,i}$	- Direct radiation in
$\dot{Q}_{rad,e}$	- Direct radiation exit
$\dot{Q}_{roof}$	- Heat to roof
$\dot{Q}_{steam}$	- Heat to steam control volume
$\dot{Q}_{wall}$	- Heat to side walls

Figure 5.12: Heat exchanger component model used in modelling the convective section consisting of RH2, SH1, RH1 and the EC

In addition, the total heat transfer rate can also be written in terms of the internal components comprised of the water control volume, the tube wall layer, and the fouling layer as given in Equation (5.5).

$$\dot{Q}_{steam} = \Delta T_{int} \left(\frac{1}{\tilde{h}_{int} A_{int}} + \frac{ln(\frac{d_{out}}{d_{in}})}{2\pi L_{tube} \lambda_{tube}} + \frac{R_{ash}}{A_{ext}} \right)^{-1} \tag{5.5}$$

where ΔT_{int}, $\tilde{h}_{int}$, A_{int}, d_{out}, d_{in}, L_{tube}, λ_{tube}, and R_{ash} is the internal temperature difference between the fouling layer and the water control volume, the internal heat transfer coefficient (calculated using the internal Gnieslinki method [102, 117]), the internal tube surface area, the outer tube diameter, the inner tube diameter, the tube length, the tubes thermal conductivity and the fouling ash layers thermal resistance. The combined heat transfer rate is calculated using a combined external heat transfer coefficient, which accounts for the flue gas control volumes convective and radiative heat transfer and is expressed in Equation (5.6).

$$\dot{Q}_{cr} = (\tilde{h}_{conv,fg} + \tilde{h}_{rad,fg}) A_{ext} \Delta T_{ext} \tag{5.6}$$

where A_{ext} and ΔT_{ext} is the outer surface area and the temperature difference between the flue gas and the wall, respectively. The external convective heat transfer coefficient ($\tilde{h}_{conv,fg}$), from the flue gas to the heat-exchanger walls, the external Gnielinski correlation [102, 117] is utilised for in-line tube arrangements. The radiation heat transfer coefficient ($\tilde{h}_{rad,fg}$) is calculated using Equation (5.7).

$$\tilde{h}_{rad,fg} = \frac{\epsilon_{wall}}{\alpha_{fg} + \epsilon_{wall} - \alpha_{fg}\epsilon_{wall}} \sigma_{SB} \frac{\epsilon_{fg} T_{fg}^4 - \alpha_{fg} T_{wall}^4}{T_{fg} - T_{wall}} \tag{5.7}$$

where, T_{fg}, and T_{wall} is the average flue gas temperature and the average wall temperature, respectively. The external wall emissivity (ϵ_{wall}) is set to 0.8 [118], which is a value used for solid-fuel fired boilers. The gas-particle mixture emissivity (ϵ_{fg}) is calculated using the following correlations [95, 119].

$$\begin{aligned}
\epsilon_{fg} &= (1-\beta)\frac{1 - exp(-\Phi_{emi})}{1 + \beta exp(-\Phi_{emi}} \\
\beta &= \frac{\gamma - 1}{\gamma + 1} \\
\gamma &= (1 + \frac{2\bar{Q}_{bsc}}{\bar{Q}_{abs}})^{0.5} \\
\Phi_{emi} &= (\bar{Q}_{abs} A_{proj} L_p + K_{emi}) S_{mb} \gamma \\
K_{emi} &= \frac{-ln(1 - \epsilon_{g,fg})}{L_{mb}}
\end{aligned} \tag{5.8}$$

where Φ_{emi}, $\bar{Q}_{bsc}$, $\bar{Q}_{abs}$, A_{proj}, L_p, and $\epsilon_{g,fg}$ are the optical thickness, particulate backscattering [119], particulate absorption [119], projected area of the particles [m^2/kg], particulate loading [kg/m^3], and the gas emissivity. The gas emissivity uses a weighted sum of gray gas modelling approach which is evaluated at the average flue gas temperature. Similarly, the gas-particle absorption coefficient ($\alpha_{g,fg}$) is calculated using the correlations of Equation (5.8), however the wall temperature is utilised in resolving the gas absorption coefficient ($\alpha_{g,fg} \approx \epsilon_{g,fg}$).

Figure 5.12 also incorporates the direct radiative interactions in each heat exchanger [42]. The initial direct radiation component ($\dot{Q}_{rad,i}$) entering from the SH3 exit plane (shown in Figure 5.10) is calculated using the area weighted incident radiation from the CFD model (G_{CFD}) and the area (A_{CI} [m^2]) of the SH3 exit plane (i.e. $\dot{Q}_{rad,i} = G_{CFD} A_{CI}$). Figure 5.12 shows that the portion of direct radiation from the preceding heat exchanger that is not absorbed is joined by the bypass radiation ($\dot{Q}_{bypass}$) of the flue gas control volume, which together make up the direct radiation passed on to the downstream components [42].

5.3 Low-load case study

Since continuous low-load operation of utility-scale coal boilers are becoming an increasing imperative due to renewable energy penetration to the grid, the following study sets out to highlight the capability of the developed model to study these off-design conditions and how the model can be used to inform plant operators of system response. Specifically, the study is aimed at investigating the effect of burner firing configuration on the various process parameters, such as steam temperatures, spray water flow rates, and metal temperatures at low-loads. This was conducted using the developed CFD model on the gas side coupled with a comprehensive 1-D process model of the water/steam side. The case study simulates a boiler operation at 32% MCR for six different firing configurations. The best configuration is chosen based on flame stability, minimising the likelihood of high-temperature corrosion, and overall boiler performance. The work mainly stems from the recently published journal article in the ASME Journal of Thermal Sciences and Engineering Applications [104]. The same computational domain, as described in Figure 5.2, was utilised for the study while using the same fuel characteristics given in Table 5.2.

5.3.1 Model inputs

For a boiler load of 32% MCR, the existing plant operational protocol prescribes using the bottom front and rear burner rows to meet the low-load demand during start-up. For this study, six cases were simulated using different burner firing arrangements. Figure 5.13 illustrates the various firing arrangements of the active and non-firing burners.

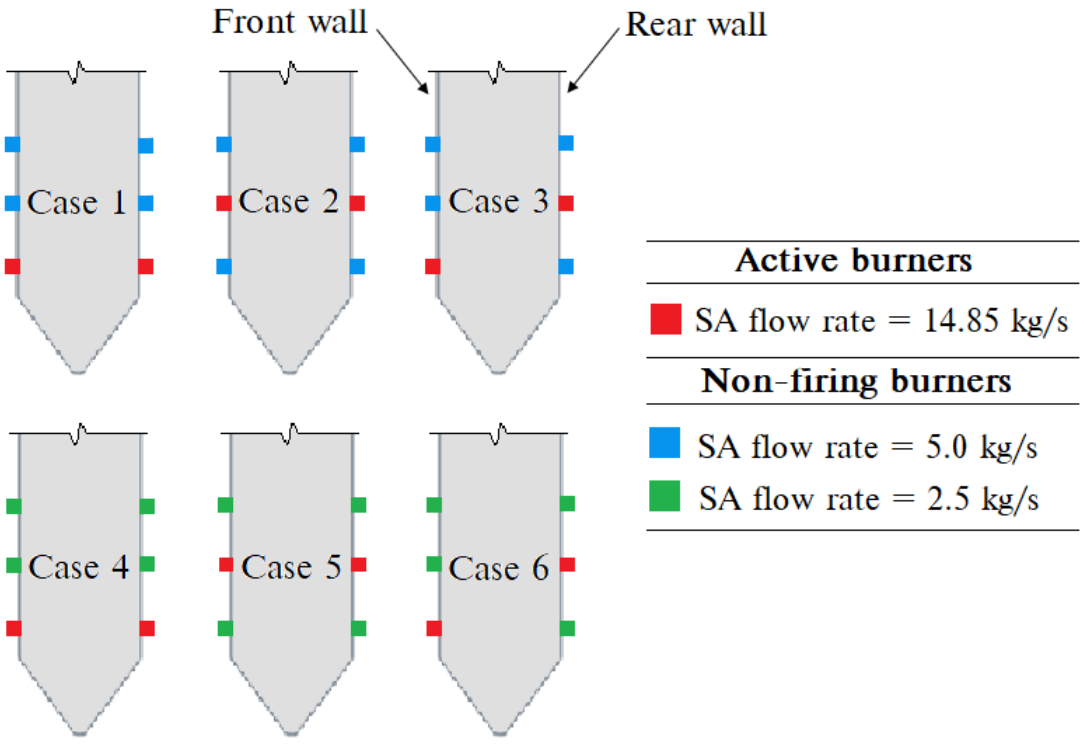

Figure 5.13: Active and non-firing burner arrangements for Cases 1 to 6

Cases 1 and 4 have the same active burner firing arrangement, that being the bottom front and rear wall mounted burners are active, but have a different non-firing secondary air requirement. Similarly, Cases 2 and 5 have the same active burner firing arrangements with different secondary air requirements. The same is observed for Cases 3 and 6 with the same active burner arrangements but different secondary air requirements. Typically, a secondary air (SA) flow rate of 5 $[kg/s]$ is fed through the non-firing burners to ensure sufficient cooling of the burner and mixing of fuel and air in the combustion chamber, this SA flow rate was utilised in Cases 1,2 and 3. The result is a high air-fuel ratio in the furnace, which leads to higher boiler dry gas loss. In an effort to lower this loss, this study investigated the effect of reducing the air-fuel ratio by lowering the non-firing burner SA flow rate from 5 to 2.5 $[kg/s]$, which was implemented for Case 4, 5, and 6.

Table 5.4: Cases 1-6 model inputs on a per burner basis

Input variable	**Case 1-3**	**Case 4-6**	**Units**
Active burners			
Fuel flow rate	3.14	3.14	kg/s
Primary air flow rate	4.95	4.95	kg/s
Secondary air flow rate	14.85	14.85	kg/s
ϕ_{mp0}	0.634	0.634	kg_{mp0}/kg
ϕ_{H_2O}	0.035	0.035	kg_M/kg
ϕ_{VM}	0.124	0.124	kg_{VM}/kg
ϕ_{FC}	0.215	0.215	kg_{FC}/kg
ϕ_{ASH}	0.259	0.259	kg_{ASH}/kg
ϕ_{hp}	47939	47939	J/kg
Non-firing burners			
Secondary air flow rate	5.00	2.50	kg/s
Inlet air temperatures			
Primary air	373	373	K
Secondary air	520	510	K
Excess air coefficients	1.37	1.32	-

Table 5.4 shows the input conditions for Cases 1 to 6, with the data being obtained via conventional boiler mass and energy balance calculations. A sample mass and energy calculation is provided in Appendix B.

5.3.2 Numerical solution strategy

The same numerical mesh utilised in the validation study consisting of approximately 6 million cells, was used for the CFD simulations of this case study. The CFD simulations were performed using ANSYS Fluent® v19.5 pressure-based solver. The pressure–momentum coupling utilised the SIMPLE method. Second-order upwind discretisation was used to discretise the momentum, energy, scalar field and species equations, whereas PRESTO! was used to discretise the pressure equation.

The spatial discretisation for all fields (except pressure) was set to first-order upwind for the first 1000 iterations to ensure a stable solution, after which the discretisation order was increased. For all cases, the maximum mass imbalance was 0.024 kg/s for a total gas flow rate of 190 $[kg/s]$ and a heat imbalance of 1.8 $[MW]$ for a total heat input of 283 $[MW]$. The remaining fields were solved until convergence.

5.3.3 Results & discussion

The results presented below were obtained using the coupled CFD and 1-D process model to study the effects of the burner configuration at a low boiler load of 32% MCR. The best configuration was selected based on the boiler efficiency, the safe operation of the heat exchanger components, and minimising the likelihood of high temperature corrosion developing during operation. Using the process model of Figure 5.10 and the results of the CFD simulations, the important process control parameters were determined.

Table 5.5: Process model control parameter results

	Cases						
Control parameter	**1**	**2**	**3**	**4**	**5**	**6**	**Units**
Main steam flow rate	175.8	172.9	180.5	180.2	179.1	184.1	kg/s
Main steam exit temp	535	535	535	535	535	535	$°C$
RH steam flow rate	158.2	155.6	162.5	162.2	161.2	165.6	kg/s
RH steam exit temp	524	527	531	512	510	520	$°C$
Boiler efficiency	85.3	84.1	88.9	87.2	85.9	89.1	%
ATT1	10.4	16.9	13.9	7.9	5.5	10.9	kg/s
ATT2	1.7	3.8	4.2	3.8	3.6	4.2	kg/s
ATT-RH	0.0	0.0	0.0	0.0	0.0	0.0	kg/s

Table 5.5 summarises the results with the highest boiler efficiencies observed for Cases 3 and 6. With a lower SA flow rate, Cases 4–6 exhibit a higher boiler efficiency due to the decrease in dry gas losses, when compared to the corresponding Cases 1–3. All cases exhibit adequate control of the main steam exit temperature by using ATT1 and ATT2. The exit temperature of the reheaters, for all cases, is determined to be within the 20 $[°C]$ tolerance for the intermediate turbine inlet conditions, as stipulated in the design C-schedules for the plant. However, a sudden decrease in steam generation can lead to RH overheating and possible RH failure due to the lack of ATT-RH control.

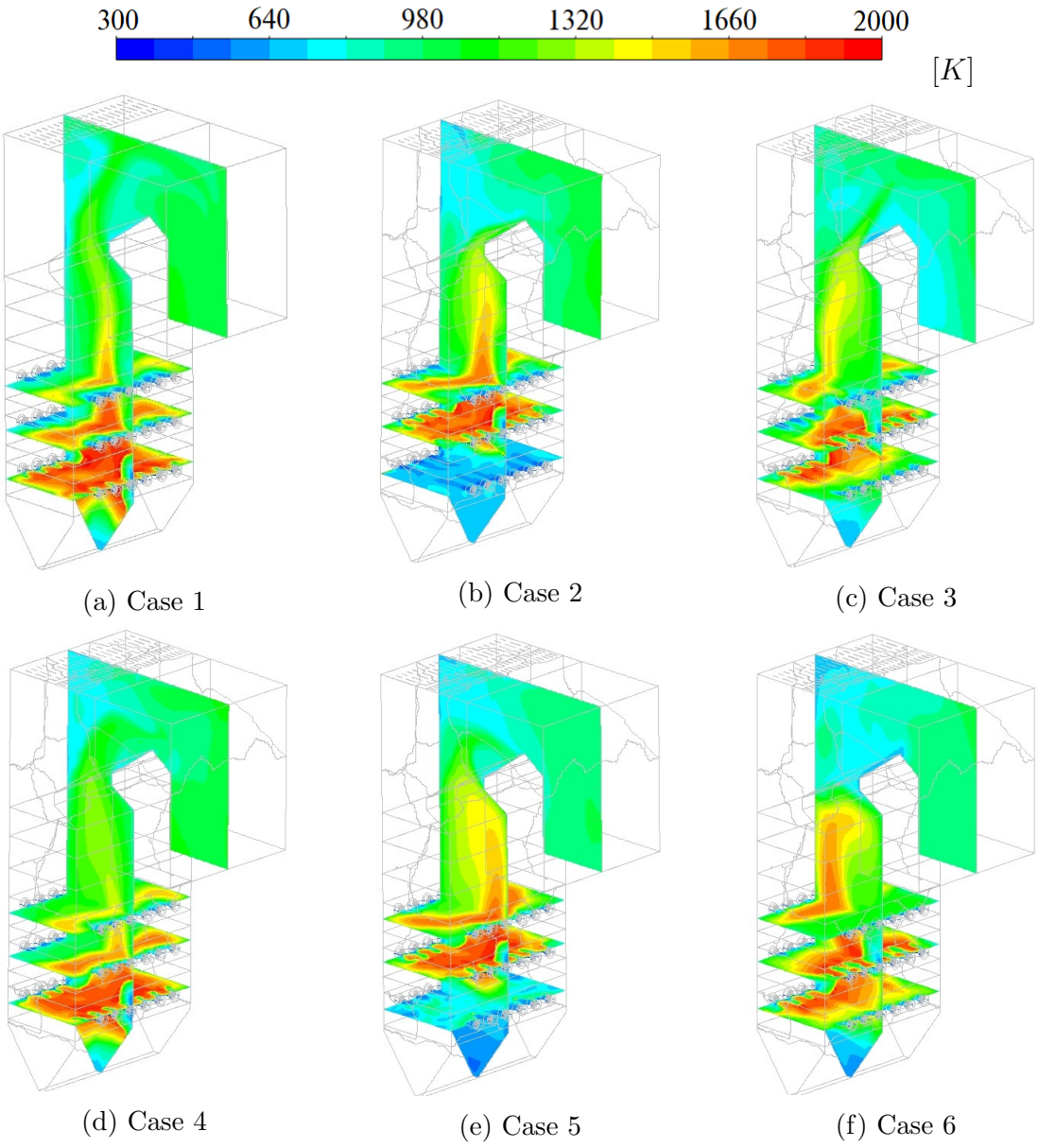

(a) Case 1 (b) Case 2 (c) Case 3

(d) Case 4 (e) Case 5 (f) Case 6

Figure 5.14: Temperature fields for Cases 1 through 6 (a)-(f)

Considering the temperature profiles of Figures 5.14 (a) to (f), the bottom-firing arrangements (Cases 1 and 4) results in a high-temperature zone located in the bottom half of the burner, while the mixed firing arrangement (Cases 3 and 6) results in an even distribution of high-temperature gases across the furnace domain. This leads to the highest steam generation rate in the furnace and associated high boiler efficiency, as shown in Table 5.5. However, considering the middle burner rows firing arrangements (Cases 2 and 5), a substantial cold region is formed in the lower half of the furnace, resulting in the lowest heat uptake. This is further exacerbated when considering Table 5.5, where it is illustrated that the mid-firing arrangements (Cases 2 and 5) produce the lowest steam flow rates resulting in the lowest boiler efficiencies.

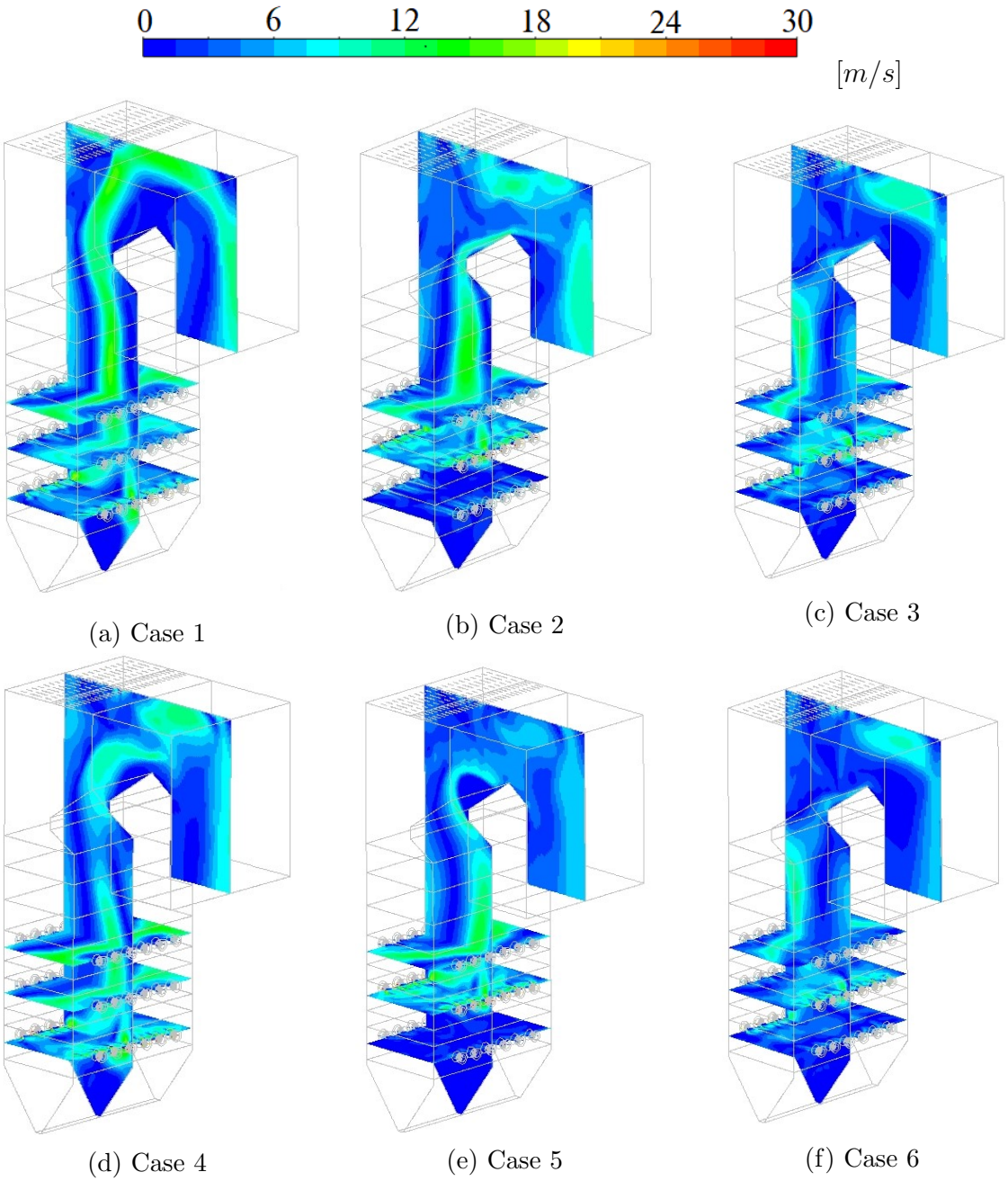

(a) Case 1 (b) Case 2 (c) Case 3

(d) Case 4 (e) Case 5 (f) Case 6

Figure 5.15: Velocity fields for Cases 1 through 6 (a)-(f)

Figure 5.15 presents the velocity fields for Cases 1 to 6. It shows that for a lower SA flow rate the general trend is that the hot gases and velocity profiles impinge on the furnace walls, which can be seen in Cases 4–6 of Figures 5.14 (d)-(f) and 5.15 (d)-(f), respectively.

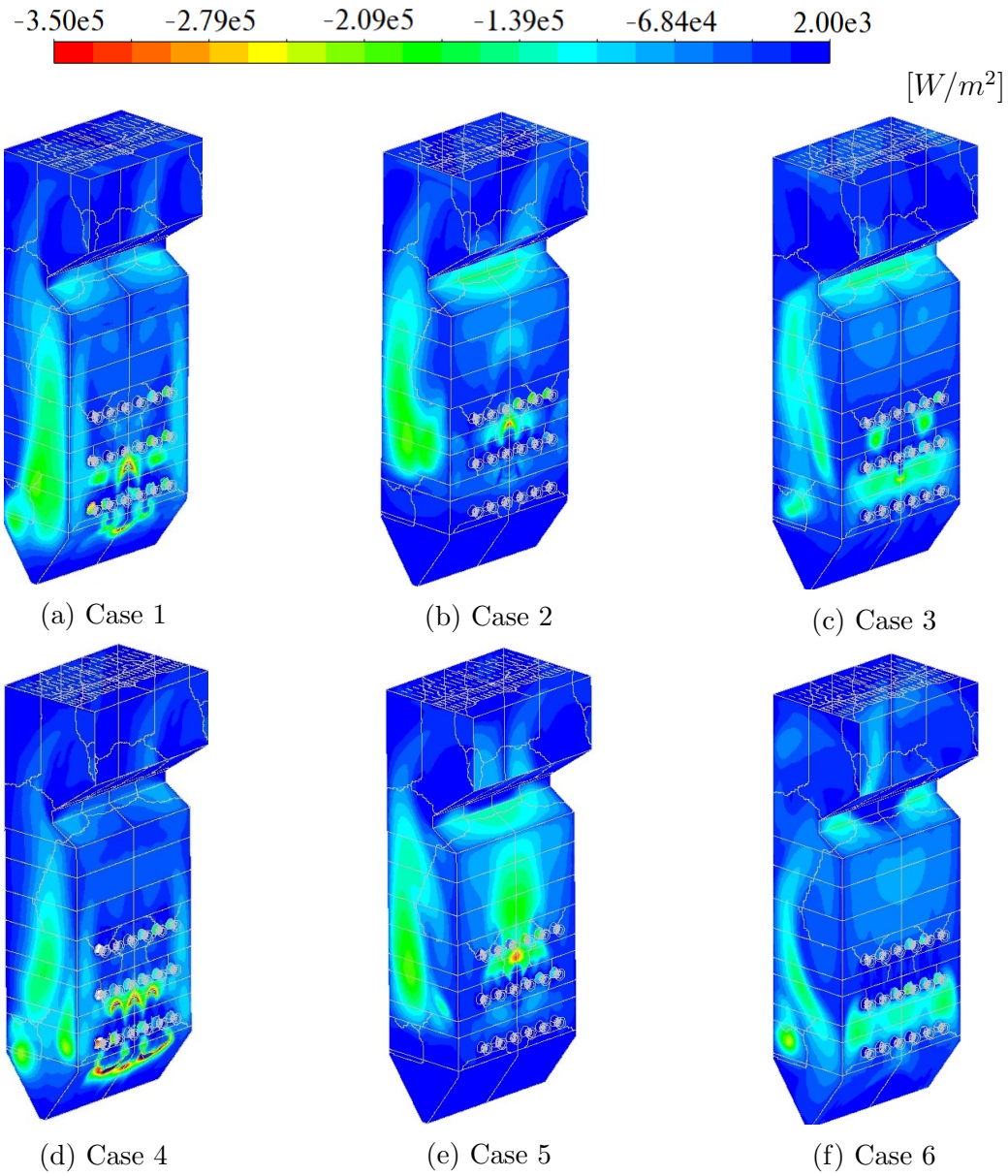

(a) Case 1 (b) Case 2 (c) Case 3

(d) Case 4 (e) Case 5 (f) Case 6

Figure 5.16: Heat fluxes profiles for Cases 1 through 6 (a)-(f)

Figure 5.16 illustrates the heat flux profiles for the simulated cases. Both Cases 1 and 4 highlight high heat flux zones near the burner inlets, which can lead to high-temperature corrosion in the presence of high temperatures and incomplete combustion near these regions [23]. An even distribution of heat fluxes is seen in Cases 3 and 6, with minimal localised heat flux concentrations being observed. Cases 2 and 5 show that most of the heat is absorbed in the upper half of the boiler, with Case 5 showing a higher heat flux on the rear wall. This could be due to a lower SA flow rate leading to higher velocity profiles developing closer to the rear wall, as seen in Figure 5.15. With high-gas temperatures and high-velocity impingement, Cases 4–6 (of Figure 5.16) experience concentrated heat fluxes around the burner inlets compared to the corresponding Cases 1–3.

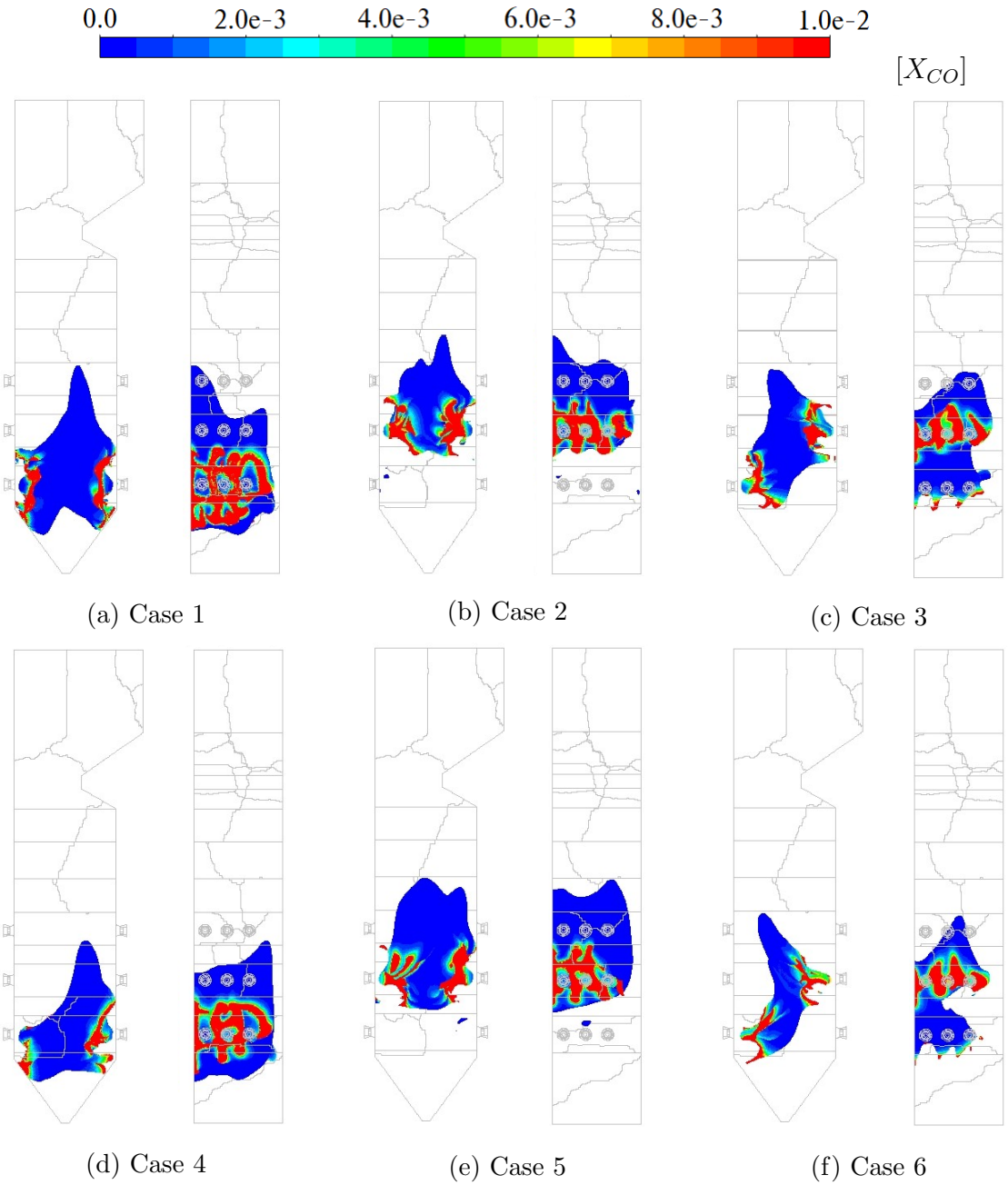

(a) Case 1 (b) Case 2 (c) Case 3

(d) Case 4 (e) Case 5 (f) Case 6

Figure 5.17: CO molar fraction (X_{CO}) concentrations for Cases 1 through 6 (a)-(f) on a temperature iso-surface of 1600 $[K]$

Dugum and Hanjali [23] highlighted the issue of high-temperature corrosion caused by significant levels of CO (X_{CO} 0.01–0.1) and no-free O_2 near regions of high wall temperatures. For a low-load operation, this phenomenon becomes important to avoid since combustion instability can lead to these non-ideal circumstances. Figure 5.17 shows the CO molar concentration in the domain on an iso-surface set at 1600 $[K]$. The figures generally highlight the location and distribution of the flame core for each case.

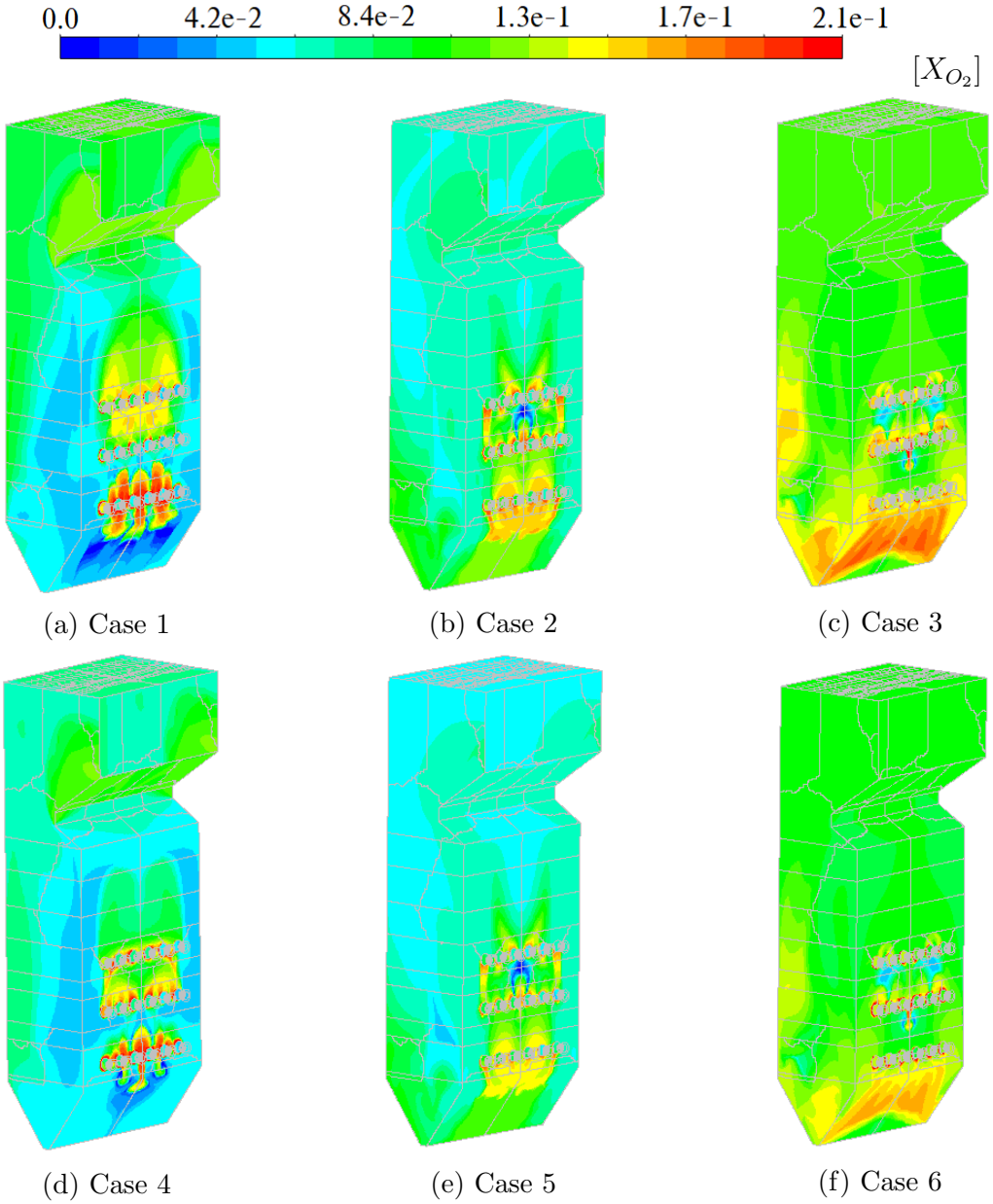

(a) Case 1 (b) Case 2 (c) Case 3

(d) Case 4 (e) Case 5 (f) Case 6

Figure 5.18: O_2 molar fraction (X_{O_2}) concentrations for Cases 1 through 6 (a)-(f) near the furnace wall surfaces

By considering Figure 5.17 and the oxygen molar concentrations (X_{O_2}) near the furnace wall surfaces shown in Figure 5.18 in conjunction, it can be concluded that Cases 1 and 4 illustrate the highest likelihood of high-temperature corrosion occurring near the furnace hopper due to the region's high X_{CO} concentration, low X_{O_2} concentrations near the furnace walls, and high gas temperatures.

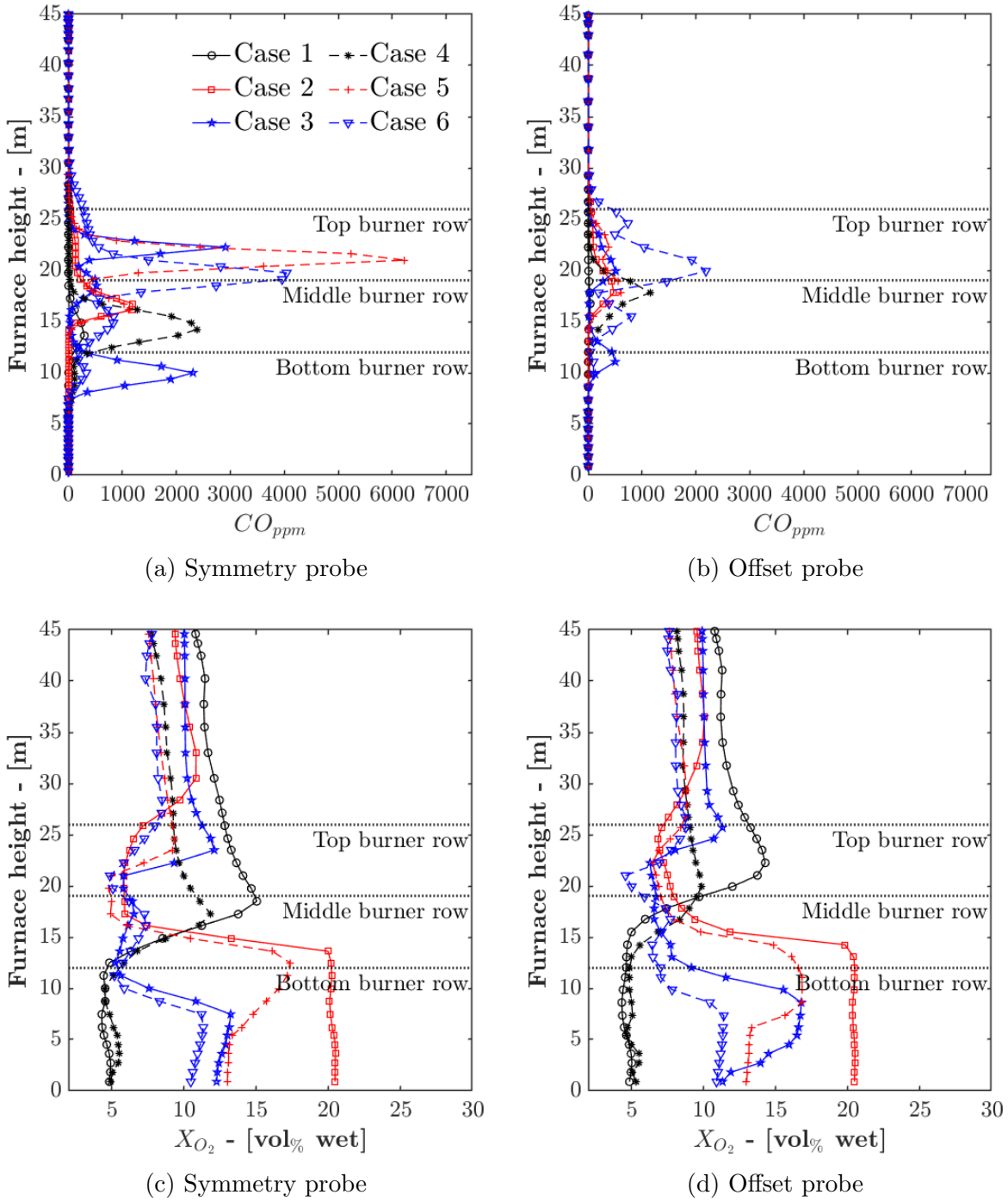

(a) Symmetry probe

(b) Offset probe

(c) Symmetry probe

(d) Offset probe

Figure 5.19: CO_{PPM} [(a) and (b)] and X_{O_2} [(c) and (d)] line plots on the symmetry and offset vertical probe lines (refer to Figure 5.2)

Investigating the combustion stability for all the cases, the symmetry and offset vertical probe plots (as highlighted in Figure 5.2) are given in Figure 5.19. Cases 2 and 5 illustrate the highest X_{O_2} concentration in the lower half of the burner since minimal combustion occurs.

The unburnt carbon content and exit flue gas temperatures for each case are reported in Table 5.6. Using the middle burners (Cases 2 and 5), the highest exit temperature and unburnt carbon content are observed since the flame core is located in the furnace's upper half, leading to the least possibility of complete combustion due to the shorter residence time. Cases 3 and 6 exhibit the best characteristics, with the least amount of observed unburnt carbon content. It is important to note the effects a lower SA mass flow rate has on the furnace exit conditions for non-firing burners, which generally lead to a hotter exit gas temperature, as seen in Cases 4–6.

Table 5.6: Furnace exit conditions and SH wall temperatures

	Cases						
Variable	**1**	**2**	**3**	**4**	**5**	**6**	**Units**
Furnace exit							
Exit temperature	1168	1230	1215	1208	1306	1298	K
Unburnt carbon	1.83	1.94	1.54	1.81	1.89	1.62	$(\times 10^{-3})\,\%$
Platen SH							
Max wall temperature	477	492	481	480	493	490	$^{\circ}C$
Mean wall temperature	439	453	446	454	442	451	$^{\circ}C$
Final SH							
Max wall temperature	602	624	608	595	626	612	$^{\circ}C$
Mean wall temperature	520	523	517	512	520	511	$^{\circ}C$

The external tube metal temperatures, shown in Table 5.6, were calculated using Equation (5.9), which considers the temperature drop due to the ash deposit present on SH2 and SH3 walls. Fouling thermal resistances of 0.0067 and 0.015 $[m^2K/W]$ were used for SH2 and SH3, respectively:

$$T_{metal} = T_{wall} - \left(\frac{\dot{q}_{SH} t_{ASH}}{\lambda_{ASH}} \right) \tag{5.9}$$

The maximum surface temperature for the superheaters SH2 and SH3 is observed for Cases 2 and 5. For comparison, at 100% MCR load, the maximum and mean temperatures reported for the superheaters SH2 and SH3 are 500 & 446 $[^{\circ}C]$ and 623 & 531 $[^{\circ}C]$, respectively, with the SH3 superheater operating in the materials creep range [7]. Thus, continued operation using the firing arrangement of Cases 2 and 5 could lead to SHs failure.

Table 5.7 shows the radiative heat percentage of the total heat input into each heat exchanger for Cases 3 and 6. It can be seen that heat transfer to the furnace and radiant SHs are dominated by radiation, with approximately 10% being transferred via convection at low-load. Considering the convective pass heat exchangers (RH2 through to the EC, Figure 5.10), the convective heat transfer becomes more apparent, as seen with the reduction in radiative heat transfer percentage. Case 6 involves less convective heat transfer due to the SA flow rate for non-firing burners. This will reduce the total amount of flue gas flowing through the boiler, thereby reducing the convective heat transfer.

Table 5.7: Radiative heat transfer percentage for Cases 3 and 6

Heat exchanger	**Case 3**	**Case 6**
Furnace	89.2%	88.9%
Platen SH (SH2)	92.5%	93.4%
Final SH (SH3)	93.5%	94.0%
RH2	47.6%	52.2%
SH1	37.2%	40.7%
RH1	18.7%	21.5%
EC	5.4%	6.5%

The mixed firing arrangements of Cases 3 and 6 exhibit the best boiler utilisation efficiencies. In addition, these Cases displayed the best X_{CO} molar concentration distributions with minimal X_{O_2} molar concentrations near the wall surfaces, highlighting the minimal likelihood of inducing fire-side corrosion in the furnace when utilising this firing configuration. A 4.8% decrease in unburnt carbon percentage is observed when using Case 3 compared to Case 6. The predicted reheater exit steam temperature of Case 3 is substantially closer to the desired temperature of 535 $[^{\circ}C]$, thus allowing for better control. Based on the analyses Case 3 was considered the best operational strategy at this low-load for the boiler under investigation. In addition, this section aids in showcasing the benefits of utilising coupled simulation techniques to resolve operational protocols for low-loads.

Part II of II

Chapter 6

Machine learning theory

Machine learning techniques have seen extensive use in various scientific fields [50–57], with their application extending to thermal energy systems [62, 63, 65, 66]. The use of machine learning techniques in this study forms part of the research objective to develop a data-driven surrogate model for investigating the heat transfer inside a utility-scale boiler furnace using high-level inputs. This chapter summarises the theory used in the development of a data-driven surrogate model using machine learning techniques. In the following chapters, multivariate linear regression, multilayer perceptron networks (MLP) and mixture density neural networks (MDN) will be applied to develop the required surrogate model. There are three broad categories used in defining data-driven learning methods: supervised, unsupervised, and reinforcement learning [120]. The category used in the present research is supervised learning. In supervised learning, the network is provided with training sets (inputs and outputs) of the desired network behaviour. All the models discussed herewith fundamentally provide a mapping of the inputs to output variables with varying degrees of accuracy depending on the non-linearities of the training data. Figure 6.1 highlights the content that is discussed and indicates the research objectives addressed in this chapter for the readers convenience.

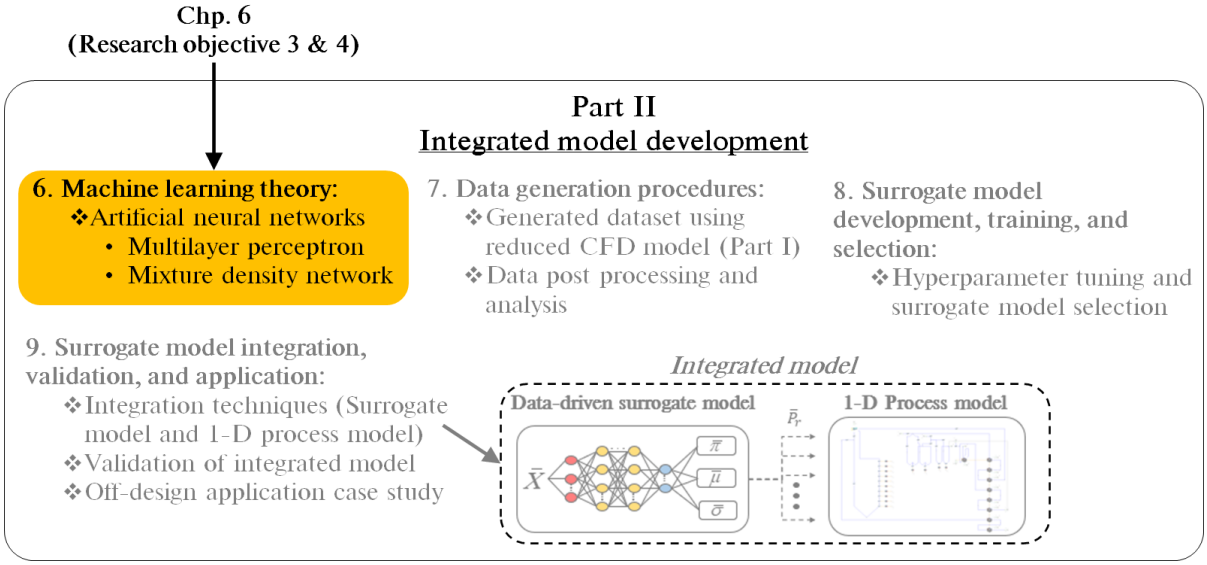

Figure 6.1: Content overview and research objectives addressed in Chapter 6

6.1 Multivariate linear regression

The primary assumption of a multivariate linear regression model is that the output/s can be calculated from a linear combination of the input variables. In other words, a linear regression model aims to determine the quantitative linear relationship between the dependent and independent variables [121]. The representation of the i-th dependent variable (y_i) can be written as follows for the m-number of independent variables (x_{mi});

$$\begin{aligned} &y_i = \beta_0 + \beta_1 x_{1i} + ... + \beta_m x_{mi} \\ &i = 1, 2, 3...n \end{aligned} \tag{6.1}$$

where β_0 is a constant term, β_m is the m-th coefficient, and n is the total number of observations.

The optimal solution can be estimated by minimising the cost function (J). A cost function calculates the difference between the estimated and the desired values and is reported as a single number. Multivariate linear regression problems typically utilise the mean square error (MSE) between the desired (y_i) and estimated ($\hat{y_i}$) values [122] to calculate the cost function, which is given in Equation (6.2).

$$J_{MSE} = \frac{1}{n} \sum_{i=1}^{n} (y_i - \hat{y_i})^2 \tag{6.2}$$

The gradient descent algorithm is an iterative procedure used to find the local minimum/maximum of a function, whereby the goal of the algorithm is to find model parameters that minimise the error of the model on the training dataset [123]. Three approaches can be used for configuring the gradient descent algorithm, namely batch, mini-batch and stochastic. Batch gradient descent takes into consideration the entire training dataset and performs model updates at the end of a training epoch. This approach typically results in slow training of large datasets, since the approach requires the entire dataset to be stored in memory. Stochastic gradient descent calculates the error and updates the model for each example in the training dataset, resulting in a computationally expensive approach with a higher variance of the gradient signal. The mini-batch approach splits the training dataset into smaller batches which are used to calculate the model error and update the model coefficients [124]. Doing this results in a computationally efficient process, since a reduction in memory requirements is achieved and the frequent model updates allows for a more robust convergence in comparison to the batch and stochastic approaches.

The present work utilised the gradient descent algorithm [121] to minimise the cost function of Equation (6.2). The gradient descent algorithm can be written as shown in Equation (6.3) by considering the cost function as a function of the weight.

$$\beta_m = \beta_m - \eta \frac{\partial}{\partial \beta_m} J_{MSE}(\beta_m) \tag{6.3}$$

where η is the pre-set learning rate.

In most cases, the relationship between the dependent and independent variables is not linear. Special non-linear basis models, such as polynomial, sinusoidal, and radial, can be used to optimise the training results [122]. For the current work, a multivariate linear regression model was developed to provide a benchmark against which the subsequent models of Sections 6.2 and 6.3 were tested. This was done to highlight the non-linear nature of the relevant datasets and to emphasise the need to use higher order machine learning techniques, which are discussed in the subsequent sections.

6.2 Multilayer perceptron networks

Artificial neural networks (ANN) are machine learning systems inspired by biological neural activity [124]. There are many classifications of ANNs, with multilayer perceptron networks (MLP) being the standard representation [125]. Typically, MLPs are adapted for supervised learning problems where the input variables are mapped to labelled output variables. The relationship between the input and output variables is learned by optimising the weights ($\bar{w}$) and biases ($\bar{b}$) to minimise a selected cost function, which in most cases is the MSE given in Equation (6.2). In MLP networks, neurons are interconnected through several layers, each comprised of multiple neurons. Figure 6.2, illustrates the standard topology of an MLP, consisting of the input, hidden and output layers.

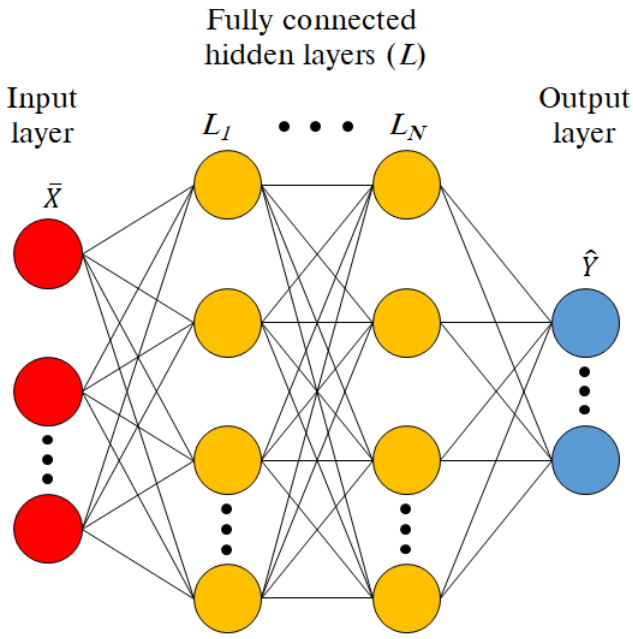

Figure 6.2: Traditional MLP schematic mapping the input $\bar{X}$ output and $\bar{Y}$ layers

To calculate the output values ($\hat{y}_i$) the forward propagation algorithm is utilised, which calculates the output for each layer and moves sequentially through the network until the output is determined. Each network layer output is calculated using two steps: the calculation of the summed signal ($\bar{z}_l$) and the use of an activation function to generate the output signal ($\bar{h}_l$). A schematic of a single neuron is given in Figure 6.3, highlighting the two-step process.

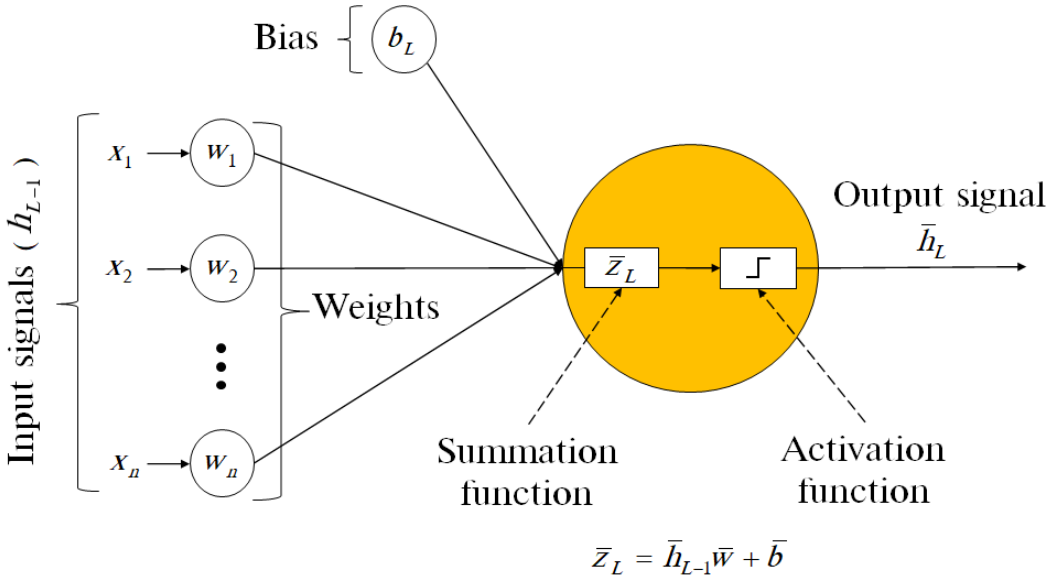

Figure 6.3: Schematic of a single neuron highlighting the two-step process

Equation (6.4) highlights the first step, where $\bar{h}_{l-1}$ is the output signal from the previous layer.

$$\bar{z}_l = \bar{h}_{l-1} \cdot \bar{w}_l + \bar{b}_l \tag{6.4}$$

The result of Equation (6.4) is subsequently passed to an activation function ($\bar{h}_l = \sigma_l(\bar{z}_l)$). Various activation functions can be utilised, such as linear, ReLu, Elu, and the hyperbolic tangent [125]. The final layer activation function is usually linear to enable the scaling of the output signal to numeric values larger than unity. Figure 6.4 provides a graphical representation of the hyperbolic tangent, linear and ReLu activation functions.

The current work uses ReLu activation functions for the hidden layers, since ReLu functions are simple to implement and fast to compute [122], and a linear activation function for the output layer/s. The hyperbolic tangent activation function is not utilised since, like the sigmoid function, it is susceptible to the vanishing gradients problem [125]. The ReLu and linear activation functions are shown in Equations (6.5) and (6.6).

$$\bar{h}_l = \sigma_{ReLu}(\bar{z}_l) = \begin{cases} \bar{h}_{l-1} \cdot \bar{w}_l + \bar{b}_l & if \quad \bar{z}_l > 0 \\ 0 & if \quad \bar{z}_l < 0 \end{cases} \tag{6.5}$$

$$\bar{h}_l = \sigma_{linear}(\bar{z}_l) = \bar{h}_{l-1} \cdot \bar{w}_l + \bar{b}_l \tag{6.6}$$

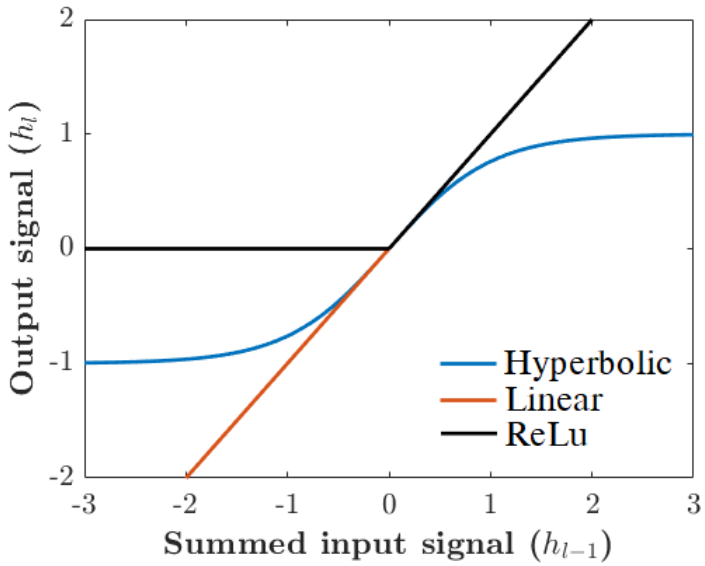

Figure 6.4: Graphical interpretation of various activation functions

When the forward propagation step is complete, the network weights and biases can be updated to minimise the cost function (refer to Equation (6.2)). This step uses the backward propagation method [125, 126] which applies forward- or reverse-mode automatic differentiation to calculate the parameter gradients [122]. The methodology calculates the gradient of the cost function with respect to the weights and biases for each layer. The backward propagation is given in Equation (6.7).

Algorithm 1 (Backward propagation)

Compute the gradient of the output layer with respect to the target variable:
$\bar{g} \leftarrow \nabla_{\hat{y}} J_{MSE}$
Calculate the pre-activated gradient of the output layer L:
$\bar{g} \leftarrow \nabla_{\bar{z}_L} J_{MSE} = \bar{g} \odot f'(\bar{z}_L)$
Compute the gradients for the weights and biases in the output layer L
$\nabla_{\bar{w}_L} J_{MSE} = \bar{g} \cdot \bar{h}_{L-1}^T$
$\nabla_{\bar{b}_L} J_{MSE} = \bar{g}$
Loop through hidden layers and compute the gradients for
the weights and biases:
$\bar{g} \leftarrow \nabla_{\bar{h}_l} J_{MSE} = \bar{w}_l^T \cdot \bar{g}$
$\bar{g} \leftarrow \nabla_{\bar{z}_l} J_{MSE} = \bar{g} \odot f'(\bar{z}_l)$
$\nabla_{\bar{w}_l} J_{MSE} = \bar{g} \cdot \bar{h}_{l-1}^T$
$\nabla_{\bar{b}_l} J_{MSE} = \bar{g}$
Repeat till the input layer is reached. (6.7)

Once the gradients have been calculated, the weights and biases are updated using the gradient descent algorithm. Following the gradient calculation steps forward- and backward-propagation algorithms are applied iteratively until the cost function is reduced to below the desired threshold.

The current work uses the adaptive moment estimation or Adam [127] alternative to the gradient descent algorithm. The Adam optimiser is a momentum-based method that computes adaptive learning rates for each parameter, which is achieved from the estimates of the first and second moments of the gradient [127]. Being a momentum-based method allows the algorithm to accelerate gradient descent in the relevant direction and dampen oscillations [128]. This is done via adding a fraction (β_1) of the update vector of the previous step to the current update vector.

The Adam optimiser has the advantage of having a faster computational time while requiring fewer parameters for tuning compared to other optimisation algorithms [129–131]. The Adam algorithm is illustrated in Equation (6.8).

Algorithm 2 (Adam)

$$
\begin{aligned}
&\bar{m}_t \leftarrow \beta_1 \bar{m}_{t-1} + (1-\beta_1)\nabla_\theta J_{MSE}(\bar{\theta}_t) \\
&\bar{s}_t \leftarrow \beta_1 \bar{s}_{t-1} + (1-\beta_2)\nabla_\theta J_{MSE}(\bar{\theta}_t) \otimes \quad \nabla_\theta J_{MSE}(\bar{\theta}_t) \\
&\hat{\bar{m}}_t \leftarrow \frac{\bar{m}_t}{1-\beta_1^t} \\
&\hat{\bar{s}}_t \leftarrow \frac{\bar{s}_t}{1-\beta_2^t} \\
&\bar{\theta}_t \leftarrow \bar{\theta}_{t-1} - \eta\, \hat{\bar{m}}_t \otimes (\sqrt{\hat{\bar{s}}_t} + \epsilon)^{-1}
\end{aligned}
\tag{6.8}
$$

The variable $\bar{\theta}_t$ in Equation (6.8) represents the model weights and biases of each layer. The scaling ($\bar{s}_t$) and the momentum ($\bar{m}_t$) matrices are initialised to zero ate the start of the training phase. The variable t is the iteration counter, while β_1 and β_2 are the momentum and scaling decay hyperparameters set to 0.9 and 0.999, respectively. Lastly, ϵ is a smoothing term set to 10^{-8}. In the present work, various learning rates (η) were investigated during the hyperparameter search for the MLP and MDN neural architectures. A hyperparameter is a parameter used to control the training process in machine learning applications. Commonly used hyperparameters include the training to test data split, the number of hidden layers, the number of neurons per layer and the mini-batch size.

6.3 Mixture density networks

Many practical applications that require machine learning techniques typically incorporate datasets that are comprised of non-Gaussian or multi-modal distributions [123]. Being able to estimate the confidence level, or uncertainty, of a prediction aids in formulating a decision management tool for real world applications. Mixture density models (MDN) are typically developed to achieve this. MDNs use the assumption that any general distribution can be broken down into a mixture of normal distributions

Fundamentally, MDNs are built from two components, a neural network, and a mixture model. The neural network can be comprised of any valid architecture which takes an input ($\bar{X}$) and converts it to a set of learned features. Examples of neural networks include a standard feed forward MLP or a recurrent neural network (RNN), with RNNs being used in transient applications with at least one feedback loop [132]. Figure 6.5 illustrates the architecture of an MDN, highlighting the parameters of a Gaussian distribution that the neural network would predict, allowing for multi-modal predictions and the modelling of generic distribution functions [133].

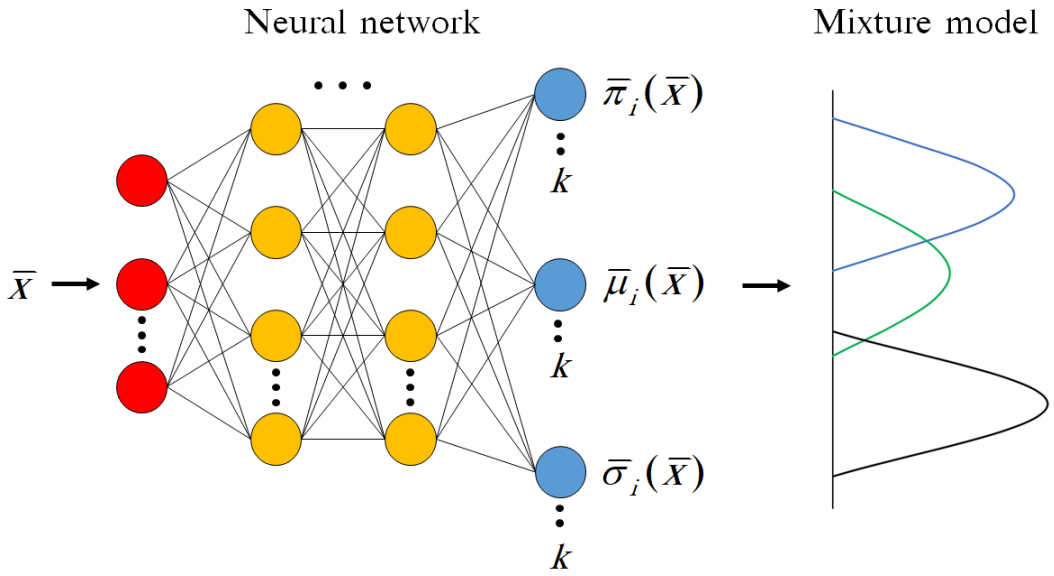

Figure 6.5: The output of a neural network parameterises a Gaussian mixture model for k number of distributions [133]

MDNs are used to predict the parameters of a probability distribution ($P(\bar{X} \mid \bar{Y})$), allowing non-Gaussian distributions to be modelled, thus making MDNs a probabilistic machine learning framework. MDNs estimate the conditional probability distribution as a mixture of Gaussian distributions where the mixing coefficients ($\bar{\pi}_k$) and component densities are flexible functions of the input data ($\bar{X}$). Equation (6.9) illustrates the conditional probability function, where it is assumed that the component densities can be described by a mixture of normal distributions $\mathbb{N}$.

$$P(\bar{X} \mid \bar{Y}) = \sum_{k=1}^{K} \bar{\pi}_k(\bar{X}) \cdot \mathbb{N}(\bar{Y} \mid \bar{\mu}_k(\bar{X}), \bar{\sigma}_k^2(\bar{X})) \tag{6.9}$$

where K represents the number of selected normal distributions,$\mathbb{N}$ is the normal distribution symbol with $\bar{\mu}_k$ and $\bar{\sigma}_k$ being the predicted means and variances for each distribution k given the input data $\bar{X}$, respectively.

A schematic of a simple MDN network is given in Figure 6.6. In addition, the activation functions of the various parameters are given. It is shown that modifications are made to the output layer by splitting the network output into three parts to calculate the $\bar{\pi}_k$, $\bar{\mu}_k$ and $\bar{\sigma}_k$ for each k distribution. This enables the MDN network to learn the conditional probability $P(\bar{X} \mid \bar{Y})$.

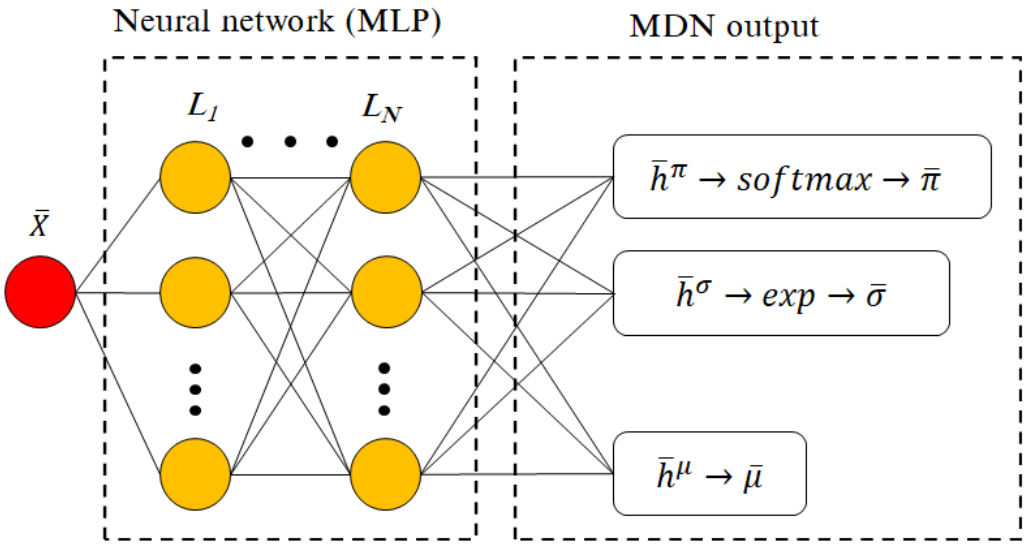

Figure 6.6: Simplified MDN network with the corresponding output layers

Bishop [133] proposed restrictions for the mixing coefficients and variance components of the MDN outputs. Since the mixing coefficients contain the discrete probabilities of an output belonging to each K normal distribution for all observations, the mixing coefficients must satisfy the constraints listed in Equation (6.10).

$$\begin{aligned} &\sum_{k=1}^{K} \bar{\pi}_k^n = 1 \\ &0 \leq \bar{\pi}_k^n \leq 1 \end{aligned} \tag{6.10}$$

These constraints are met by sending the output signal of the hidden layer ($\bar{h}^{\pi}$) through a *softmax* function. The calculation of the mixing coefficient entry for the k_{th} distribution and $n-th$ input observation ($\bar{x}^n$) is given in Equation (6.11).

$$\bar{\pi}_k^n(\bar{x}^n) = \frac{exp(\bar{h}_k^{\pi,n})}{\sum_{k=1}^{K} exp(\bar{h}_k^{\pi,n})} \tag{6.11}$$

Similarly, a constraint is applied to the standard deviation values ensuring a positive value, which is achieved using an exponential function applied to the standard deviation leg of the MDN output layer, namely $\bar{h}^{\sigma,n}$. Equations (6.12) shows the imposed constraint and exponential function used on the standard deviation leg.

$$\begin{aligned}&(\bar{\sigma}_k^n(\bar{x}^n))^2 \geq 0\\&\sigma_k^n(\bar{x}^n) = exp(\bar{h}_k^{\sigma,n})\end{aligned} \tag{6.12}$$

Finally, the mean values consist of real values, composed of all the output/target features per observation and k distribution. Thus, they can be taken as the network output layer ($\bar{h}^{\mu,n}$) for the nth observation, which is represented in Equation (6.13).

$$\bar{\mu}_k^n(\bar{x}^n) = \bar{h}_k^n \tag{6.13}$$

The MDN weights and biases, represented by $\bar{\theta}$, are optimised by minimising the error function defined by the negative log-likelihood for all observations (N). This is shown in Equation (6.14).

$$J_{NLL}(\bar{Y}, \bar{\pi}, \bar{\sigma}, \bar{\mu}) = -\sum_{n=1}^{N} ln \left\{ \sum_{k=1}^{K} \bar{\pi}_k(\bar{X}^n, \bar{\theta}) \cdot \mathbb{N}(\bar{Y}^n \mid \bar{\mu}_k(\bar{X}^n, \bar{\theta}), \bar{\sigma}_k^2(\bar{X}^n, \bar{\theta})) \right\} \tag{6.14}$$

If the MDN predicts an output $\bar{Y}$ having C features, and the mixture model consists of M components, the total number of network outputs ($\bar{Y}_{total}$) is given by $(C+2)M$. This is compared to the outputs of a standard MLP network, which consist of C outputs, which are simply the conditional means of the target variables [123]. However, mathematically the MDN layer with C standard deviations ($\bar{\sigma}$) produces uniform variance around each value of C for a given distribution M, which can be confining in the model training and development. For the current work, a unique $\bar{\sigma}$ is learned for each value of C, resulting in the $\bar{\sigma}$ MDN layer consisting of $M \times C$ components. The $\bar{\pi}$ and $\bar{\mu}$ MDN layers would remain with output sizes of M and $M \times C$, respectively. Thus, the total number of network outputs would be $(2C + 1)M$.

Chapter 7

Data generation procedures

The underlying objective of many machine learning algorithms is to estimate the unknown mapping function of output variables ($\bar{Y}$) for a given set off input variables ($\bar{X}$) [124]. The use of supervised learning techniques requires datasets of the input and output variables to be established in order for learning algorithms to be implemented, as discussed in Chapter 6.

In this chapter, the reduced order CFD simulation methodology described in Chapter 4 is used to generate the simulated output datasets given a user specified set of inputs needed for surrogate model development. The generation of the simulated dataset is required for the hyperparameter search, training and testing of the data-driven surrogate model, which will be further dissected in Chapter 8. The proposed surrogate model will effectively simulate and predict the required parameters associated with the flue gas side of the furnace, SH2 and SH3 combined.

Figure 7.1 highlights the content that is discussed and indicates the research objective addressed in this chapter for the readers convenience.

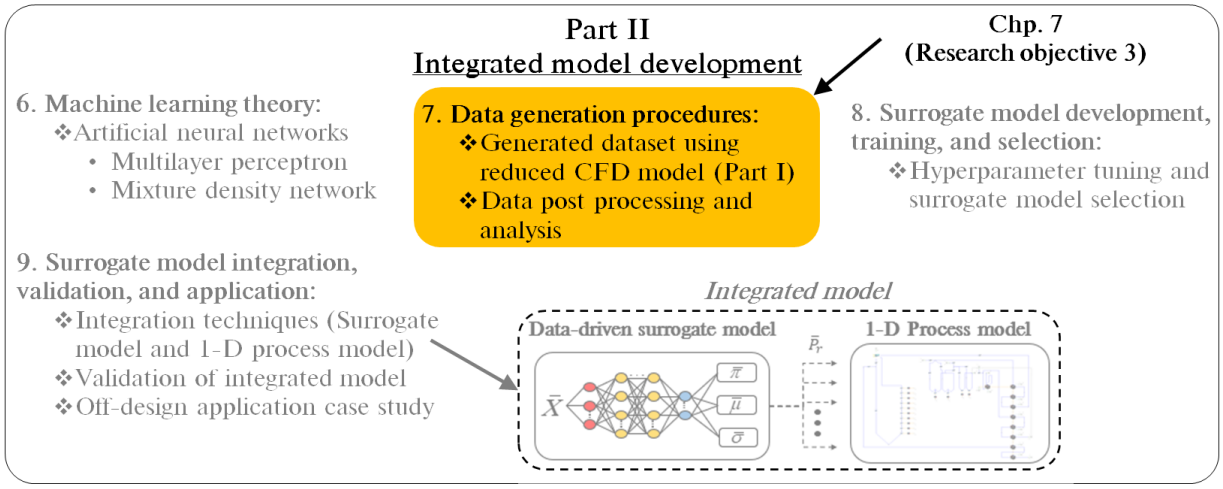

Figure 7.1: Content overview and research objective addressed in Chapter 7

7.1 Boiler model layout

The overall boiler layout is shown schematically in Figure 7.2. The boiler forms part of a 620 $[MW_e]$ power plant, which is the same boiler used in the validation and application case studies discussed in Chapter 5. It consists of the furnace section encompassing the combustion chamber with a water wall evaporator (EV), a radiative pass comprising of a platen superheater (SH2), final superheater (SH3), and a secondary reheater (RH2), as well as a convective pass incorporating the primary superheater (SH1), the primary reheater (RH1), and the economiser (EC).

In addition, it is shown that mills 1 to 3 provide the primary air and fuel mixture for the front wall mounted burners in the bottom, middle and top rows, respectively. Similarly, mills 4 to 6, provide the primary air and fuel mixture for the rear wall mounted burners in the bottom, middle and top rows, respectively. Chapter 5, Section 5.1, provides the numerical strategy and overall dimensions of the computational domain utilised for all the subsequent numerical simulations discussed in this chapter.

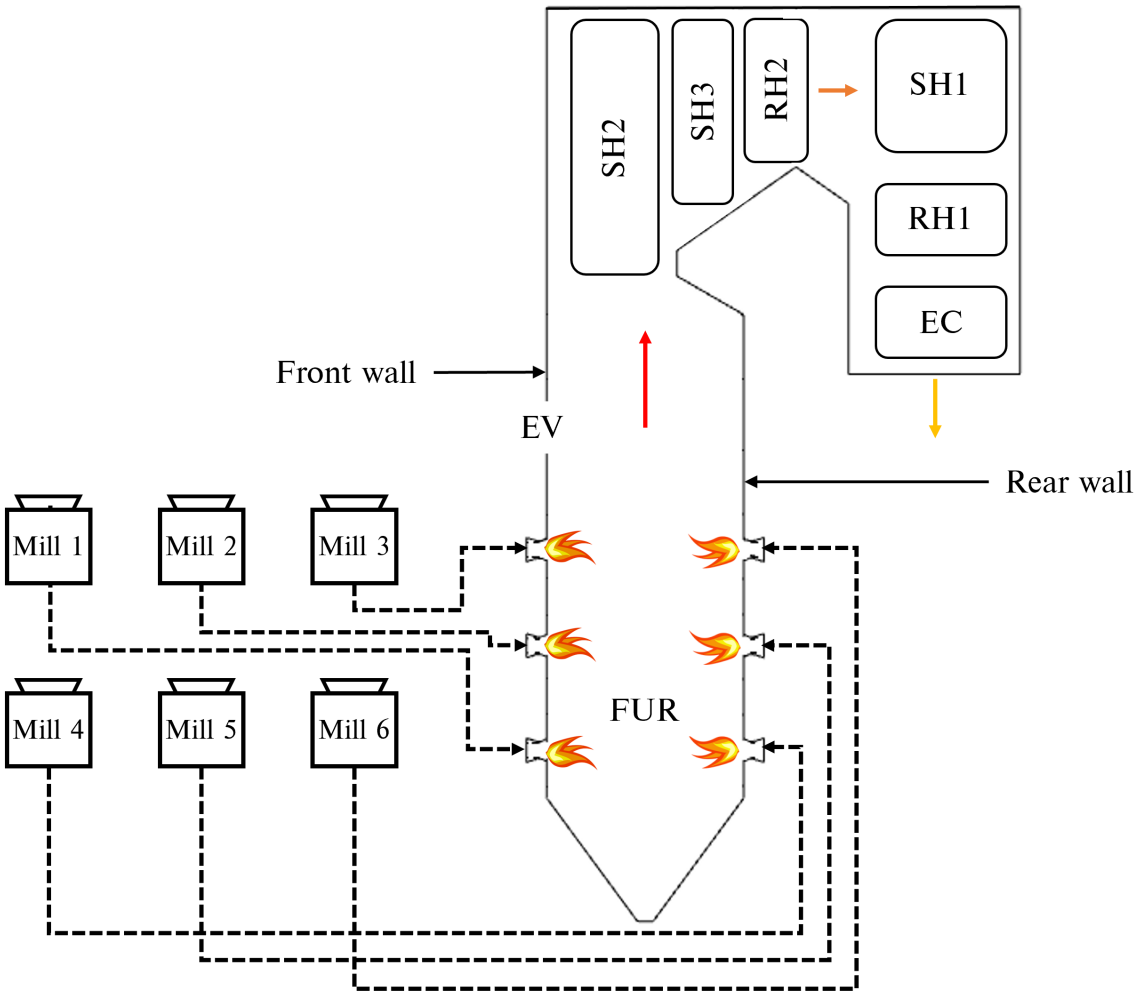

Figure 7.2: Overall boiler layout

7.2 Simulated data generation

The inputs to the surrogate model include the following: the combustin excess air ratio, the mill flow rate for each of the six mills in operation, the average steam-side temperatures of superheaters SH2 and SH3 respectively, the fouling resistance of superheaters SH2 and SH3 respectively, the mass fraction of ash and moisture in the fuel and the higher heating value of the fuel (which is a function of the fuel composition). Thus, the input field has a dimensionality of $d_{inputs} = 14$.

A total of 24 output target values ($d_{targets} = 24$) were extracted from the results for each CFD simulation case. The output simulation data includes: the heat loads to the EV walls, the roof, SH2 and SH3, as well as the flue gas composition (consisting of the CO_2, H_2O, O_2, SO_2, CO and unburnt carbon (UC) composition), the flue gas mass flow rate, the flue gas temperature, and the incident radiation flux at the SH3 exit plane. The EV walls were discretised into to ten wall sections to capture the non-uniformity of the heat flux distributions commonly found in industrial furnaces [103]. In addition, the heat loads to the SH2 and SH3 tube banks were each split into two legs consisting of five and seven tube sheets, respectively.

To obtain a representative set of results for training the surrogate model, a design of experiments (DOE) was conducted to generate the input data set of 180 simulation cases. The various model input ranges used in the DOE are provided in Table 7.1. The ranges were selected to cover a wide range of operational loads with the plant maximum continuous ratings (MCR) between 100% and 30%. The DOE matrix was populated using the Latin Hypercube Sampling (LHS) method provided in the Python *pyDOE* library version 0.3.8.

Table 7.1: Design of experiments input variable ranges and means

Input variables	**Mean**	**Min**	**Max**	**Units**
Total fuel flow rate, ($\sum_{i=1}^{6} \dot{m}_{fuel,i}$)	68.9	39.5	120.2	kg/s
Fuel moisture content, (Y_{H_2O})	0.056	0.025	0.085	kg/kg
Fuel ash content, (Y_{ash})	0.418	0.259	0.559	kg/kg
SH2 fouling resistance, (R_{SH2})	0.006	0.004	0.007	m^2K/W
SH3 fouling resistance, (R_{SH3})	0.014	0.008	0.017	m^2K/W
Higher heating value, (HHV)	14.987	12.535	19.105	MJ/kg
Excess air, (γ_{air})	1.145	1.101	1.272	%
SH2 steam temperature, ($\bar{T}_{SH2}$)	701	686	717	K
SH3 steam temperature, ($\bar{T}_{SH3}$)	781	768	796	K

The total fuel flow rate input range, given in Table 7.1, was obtained from the design and operational data of the plant. This was done to ensure that the mills and burners were modelled realistically. The values for the moisture and ash content were sampled using a normal distribution centred around the mean values with the standard deviations being set to 10% of the mean values. In a similar manner, the fouling resistances of superheaters SH2 and SH3 were generated. The HHV values were determined using the Dulong correlation for estimating the higher heating value of solid fuels [134]. The expression is given in Equation (7.1).

$$HHV = (33.8Y_{C,ar} + 144.3(Y_{H,ar} - \frac{Y_{O,ar}}{8}) + 9.4Y_{S,ar})\ MJ/kg \tag{7.1}$$

where $Y_{C,ar}$, $Y_{H,ar}$, $Y_{O,ar}$, and $Y_{S,ar}$ are the carbon, hydrogen, oxygen, and sulphur constituents of the solid fuel defined on an as-received basis, respectively.

The as-received basis is used to define a hydrocarbon fuel based on its five main elemental constituents, typically carbon, hydrogen, oxygen, nitrogen, and sulphur, along with the ash and moisture content [135]. For the current work, the dry-ash-free (DAF) fuel constituents, as given in Chapter 5, Table 5.2, where kept constant for all the simulation cases. However as shown in Table 7.1, the ash and moisture contents will vary between cases, thus the as-received contents will vary, which in turn affects the calculation of the HHV values. The as-received constituents can be calculated using the following relationship between the DAF and as-received bases.

$$Y_{i,DAF} = \frac{Y_{i,ar}}{1 - Y_{H_2O} - Y_{ash}} \tag{7.2}$$

where $Y_{i,DAF}$ is the mass fraction of the i^{th} constituent based on a DAF basis, and $Y_{i,ar}$ is the i^{th} constituent based on an as-received basis.

The excess air (γ_{air}) ratios were estimated by considering the air-to-fuel from operational and design data using the theoretical/stoichiometric air required for each case. Appendix B provides a sample calculation of determining the stoichiometric amount of air required using the same fuel as given in Chapter 5. The SH2 and SH3 internal steam temperatures were determined using a 1-D process model of the entire boiler, which calculated the heat transfer in the furnace and the estimated the furnace exit gas temperature using the Gurvich approach [103].

Figure 7.3 graphically illustrates the effects of the ash and moisture content on the higher heating value of the fuel. It can be seen that a high-ash content negatively effects the energy content of the fuel with lower HHV values being estimated.

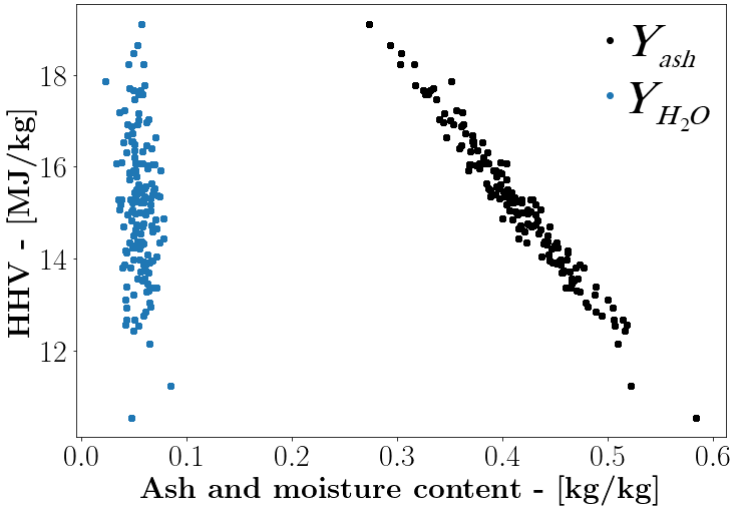

Figure 7.3: The effects the ash and moisture content have on the estimated HHV value

During the post-processing of the total fuel flow rates for mills 1 to 6 and the excess air percentage, a normally distributed noise component (ξ) was introduced to provide realistic operational inputs where slight variations from the design values are expected. Equation (7.3) illustrates the addition of a noise component for an input variable Z_i.

$$\begin{aligned} Z_i &= Z_i + f(\xi, \mu, \sigma^2) \\ f(\xi, \mu, \sigma^2) &= \frac{1}{\sqrt{2\pi\sigma^2}} e^{\frac{-(\xi-\mu)^2}{2\sigma^2}} \end{aligned} \tag{7.3}$$

The process of generating the data is described in the flowchart given in Figure 7.4. The primary step is an initial transformation of the DOE inputs to the applicable CFD input boundary conditions (e.g. mass flow rate to velocity values). Following this requires the loading/updating of the boundary/input conditions to ANSYS Fluent® for case n. Subsequently, using the pressure-based solver (Chapter 4, Section 4.1.6) and the Eulerian multiphase modelling methodology (Chapter 4, Section 4.1), each simulation case n is solved to convergence.

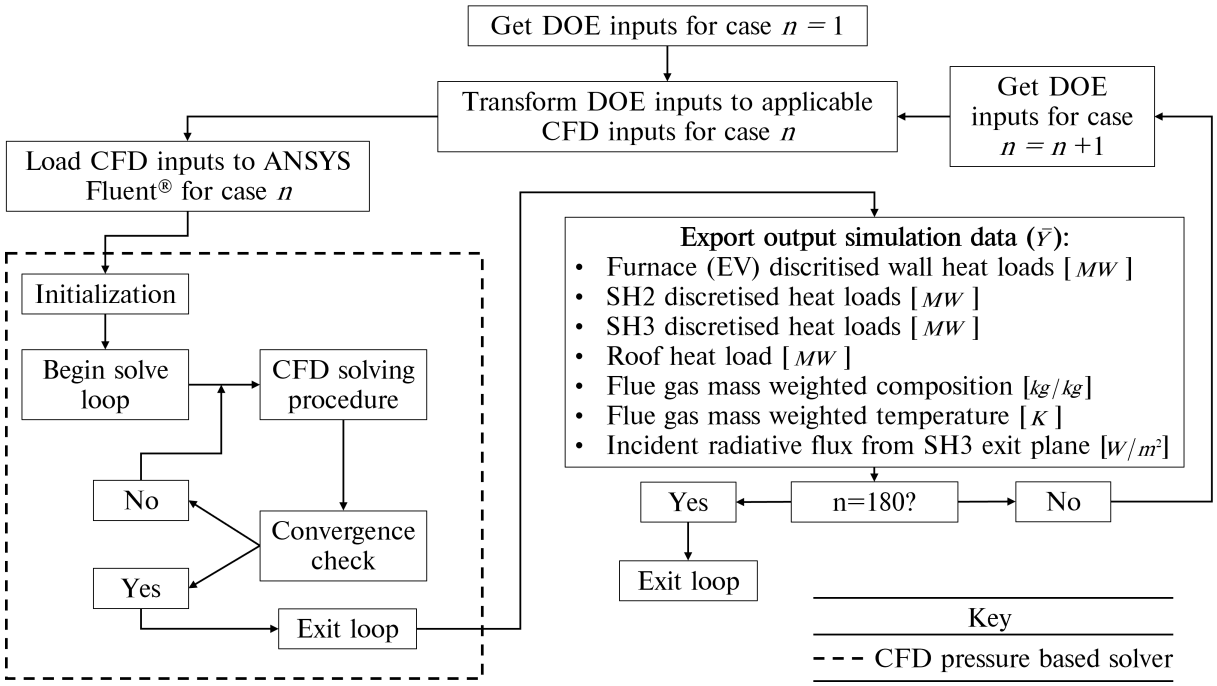

Figure 7.4: Data generation flowchart

Once the CFD simulations have achieved convergence, each simulation case's target data ($\bar{Y}$) is recorded. Figure 7.5 illustrates the output data reporting surfaces which includes the ten discretised EV wall sections, the SH2 and SH3 tube bank split, the roof section above SH2 and SH3 and the SH3 exit plane.

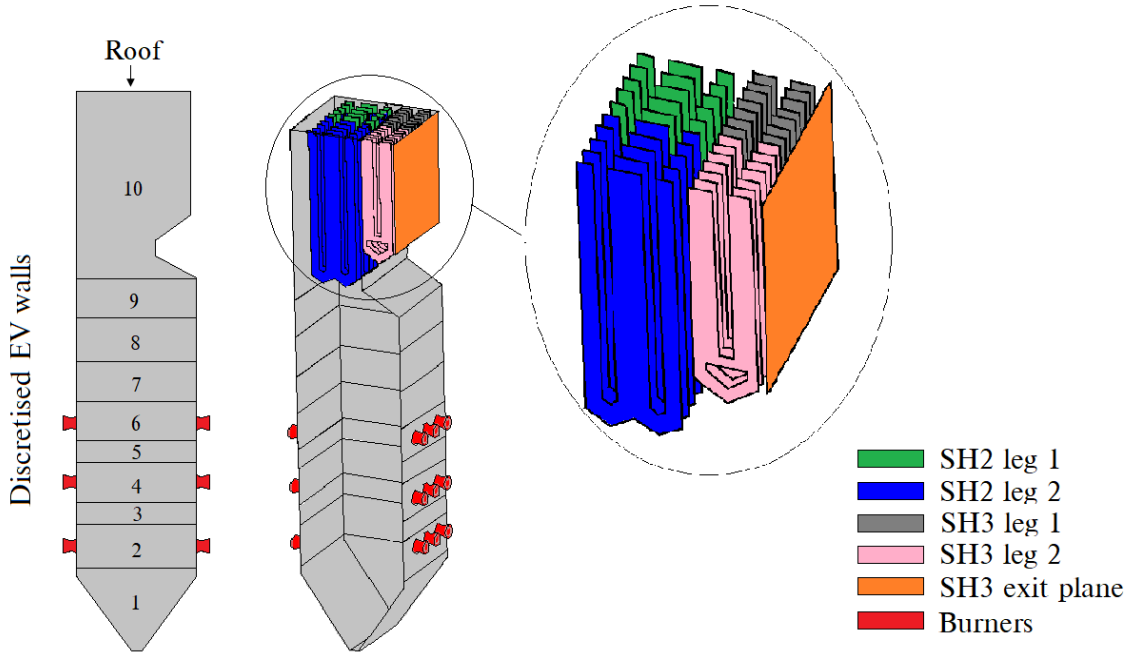

Figure 7.5: Output data reporting surfaces, including the ten discretised EV wall sections, the SH2 and SH3 tube bank split and the SH3 exit plane.

Due to the inherently unsteady nature of the CFD simulations, even when convergence has been achieved, the output target values were constructed with the values extracted after every 50 iterations for an additional 2500 iterations after convergence was achieved. This results in each CFD simulation case having a solution data matrix size of ($\bar{Y} \in \mathbb{R}(50 \times 24)$).

7.3 Exploratory data analysis of the generated output dataset

Exploratory data analysis (EDA) is a data analytical process used to analyse and interpret datasets with the help of data visualisation methods [136]. The purpose of the EDA is to summarise and identify common trends found in the CFD generated simulation dataset, which was generated using the inputs discussed in the previous section. The first step of the EDA investigation was to clean the dataset by removing unwanted values (e.g. *NaN*) and data irregularities, which prepares the dataset for analysis. The Python library *pandas* version 1.2.4 was used in identifying and removing unwanted values and irregularities, such as any out of range outputs suggesting unrealistic operations of the boiler (e.g. a substantial exit gas temperature in excess of 2300 [K], critical level heat loads to the SH2 and SH3 that can cause failure).

The current work made use of the Python library, *seaborn* version 0.11.2, to create univariate visuals of the output variables. Included in the visuals are histogram plots superimposed with a kernel density estimation (KDE) plot. The KDE is a method for estimating the probability density function of a variable [137]. This combination allows for a visual inspection of the estimated probability distribution and range of the output data.

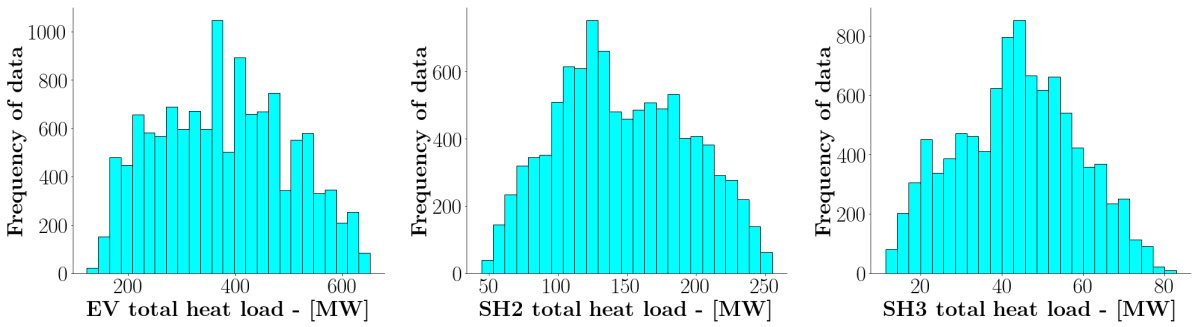

Figure 7.6: Total heat loads to the (a) EV walls, (b) SH2 walls and (c) SH3 walls

Figure 7.6 presents histogram plots illustrating the total heat loads to the EV, SH2 and SH3 walls. It can be seen that a wide range of total heat loads are captured. Considering the results of Chapter 5, Sections 5.1 and 5.3, the heat loads to the EV walls are within the expected 32% to 100% MCR load range (approximately 200 to 580 [MW]). Similarly, the heat loads to SH2 and SH3 are also within the expected MCR load range.

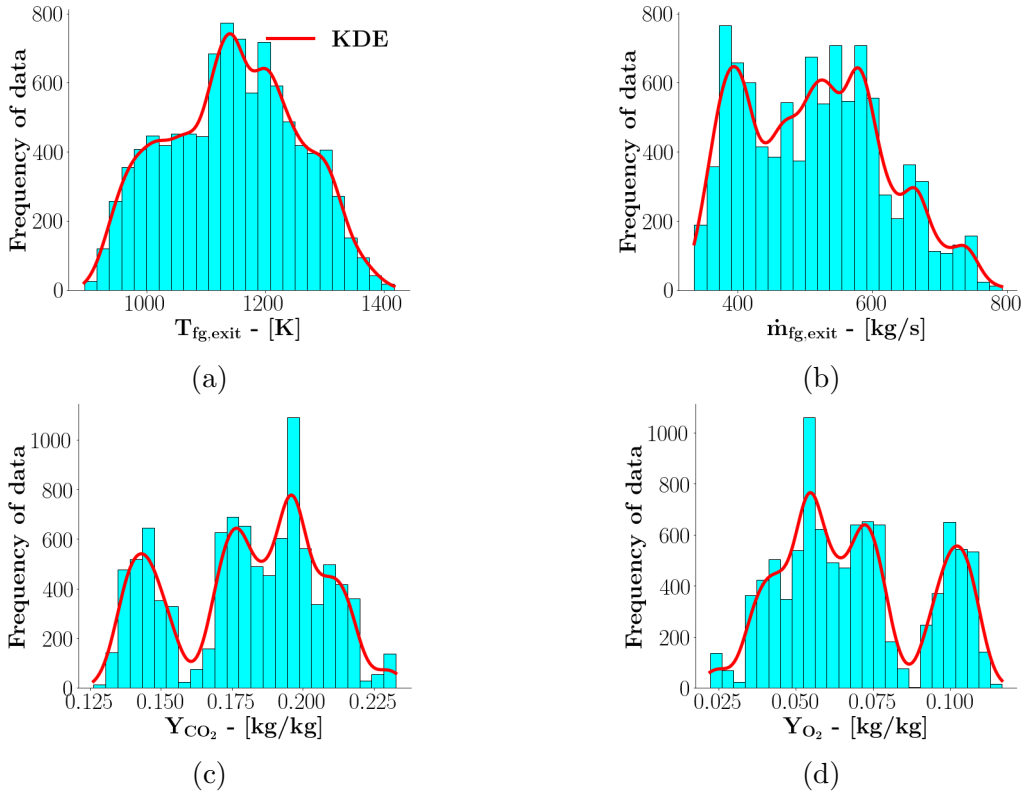

Figure 7.7: Superimposed histogram and KDE plots for output variables (a) $T_{fg,exit}$, (b) $\dot{m}_{fg,exit}$, (c) Y_{CO_2}, and (d) Y_{O_2} at the SH3 exit plane

Figures 7.7 (a) to (d) highlight distributions of the flue gas temperature, mass flow rate, CO_2 content, and O_2 content at the SH3 exit plane. The temperature of the flue gas has an approximately normal distribution with a mean in the range of 1100 to 1200 $[K]$, showing that for a wide range of loads the exit temperature at the SH3 exit plane is fairly stable. Considering the flue gas mass flow rate of Figure 7.7 (b), an approximate left skewed distribution can be seen with less information density available in the ranges of 450 to 500 $[kg/s]$ and higher load flow rates of 700 to 800 $[kg/s]$. Similarly, the Y_{CO_2} and Y_{O_2} mass fractions of Figures 7.7 (c) and (d) highlight a lack of information density in the ranges of 0.155 to 0.16 $[kg/kg]$ and 0.085 to 0.09 $[kg/kg]$, respectively.

Furthermore, the distribution shapes are very similar in comparison, showing that an underlying relationship exists between the oxygen and carbon dioxide content at SH3 exit plane. This is further explored using a bivariate plot of the Y_{CO_2} and Y_{O_2} mass fractions, given in Figure 7.8, which illustrates that an approximate linear relationship exists between the two mass fractions. In addition, the largest lack of information density is encircled which correlates to the ranges mentioned previously.

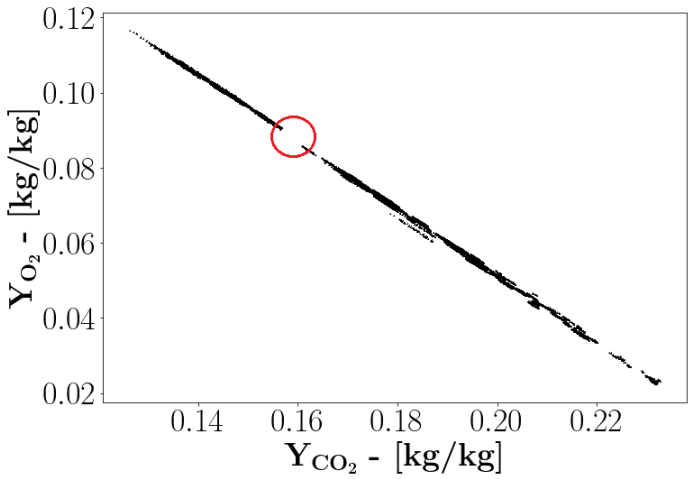

Figure 7.8: Bivariate plot of Y_{CO_2} and Y_{O_2} including an encircled region correlating to the largest information density gap

A summary of the generated CFD dataset is provided in Table 7.2, where the mean, standard deviation, minimum and maximum values for all 24 output variables are given. From Table 7.2, the carbon monoxide mass fraction (Y_{CO}) values are several orders of magnitude smaller than the rest of the flue gas composition at the SH3 exit plane. This is an indicator of complete combustion in the furnace. However, these small values can lead to substantial numerical errors when applied in a machine learning algorithm. Thus, for the training and selection of the most suitable machine learning algorithm discussed in the subsequent chapter, the Y_{CO} mass fraction was omitted from the output dataset, making $d_{targets} = 23$.

Considering the distributions of the heat fluxes to the EV wall sections of Figures 7.9 (a) to (j), a wide range of heat fluxes are reported across the wall height. The heat fluxes are below the design limit of 580 $[kW/m^2]$ [103], which is implemented to avoid excessive heat absorption by any part of the boiler heating surface. Wall sections 1, 2, 3, 4, and 7 have areas encircled highlighting the ranges where there is a lack of information density. Having a lack of information density in the dataset can lead to trained algorithms making unreliable predictions in the ranges where the information density is low. However, the MDN model discussed in Chapter 6 has the ability to also learn the uncertainty, which comes from using a probabilistic model in the modelling approach and takes into account the effect of information density in the training data.

The subsequent chapter uses the generated DOE high-level inputs and the CFD simulated outputs to train and test a suitable machine learning algorithm.

Table 7.2: Summary of the CFD generated output data

Output variables	**Mean**	**Standard deviation**	**Min**	**Max**	**Units**
		Heat loads			
Wall - 1	30.76	25.85	1.01	98.12	MW
Wall - 2	21.56	7.68	0.84	43.24	MW
Wall - 3	20.85	8.03	1.17	38.37	MW
Wall - 4	29.17	8.82	5.20	46.99	MW
Wall - 5	22.77	8.61	4.70	43.24	MW
Wall - 6	30.97	10.19	4.95	52.99	MW
Wall - 7	39.92	14.26	10.98	84.82	MW
Wall - 8	38.70	11.06	13.66	67.89	MW
Wall - 9	30.62	8.22	11.78	52.06	MW
Wall - 10	78.06	20.70	30.04	148.02	MW
SH2 leg - 1	65.96	25.47	13.70	124.01	MW
SH2 leg - 2	78.98	26.13	15.56	132.30	MW
SH3 leg - 1	23.65	7.97	2.63	45.12	MW
SH3 leg - 2	24.46	7.58	3.80	43.75	MW
Roof	12.14	3.34	3.15	22.81	MW
		Flue gas composition at the SH3 exit plane			
Y_{CO_2}	0.188	0.025	0.126	0.235	kg/kg
Y_{H_2O}	0.041	0.005	0.031	0.051	kg/kg
Y_{O_2}	0.062	0.020	0.023	0.117	kg/kg
Y_{SO_2}	2.47×10^{-3}	3.2×10^{-3}	1.73×10^{-3}	3.02×10^{-3}	kg/kg
Y_{CO}	8.65×10^{-12}	2.62×10^{-11}	3.76×10^{-17}	3.54×10^{-10}	kg/kg
Y_{UC}	1.87×10^{-4}	3.17×10^{-5}	9.17×10^{-5}	2.96×10^{-4}	kg/kg
		Flue gas conditions and the incident radiative flux at the SH3 exit plane			
Temperature, ($T_{fg,exit}$)	1143	109	894	1417	K
Mass flow rate, ($\dot{m}_{fg,exit}$)	514.6	102.9	298.3	791.8	kg/s
Incident radiation, (G_{exit})	399.0	126.5	126.7	750.8	kW/m^2

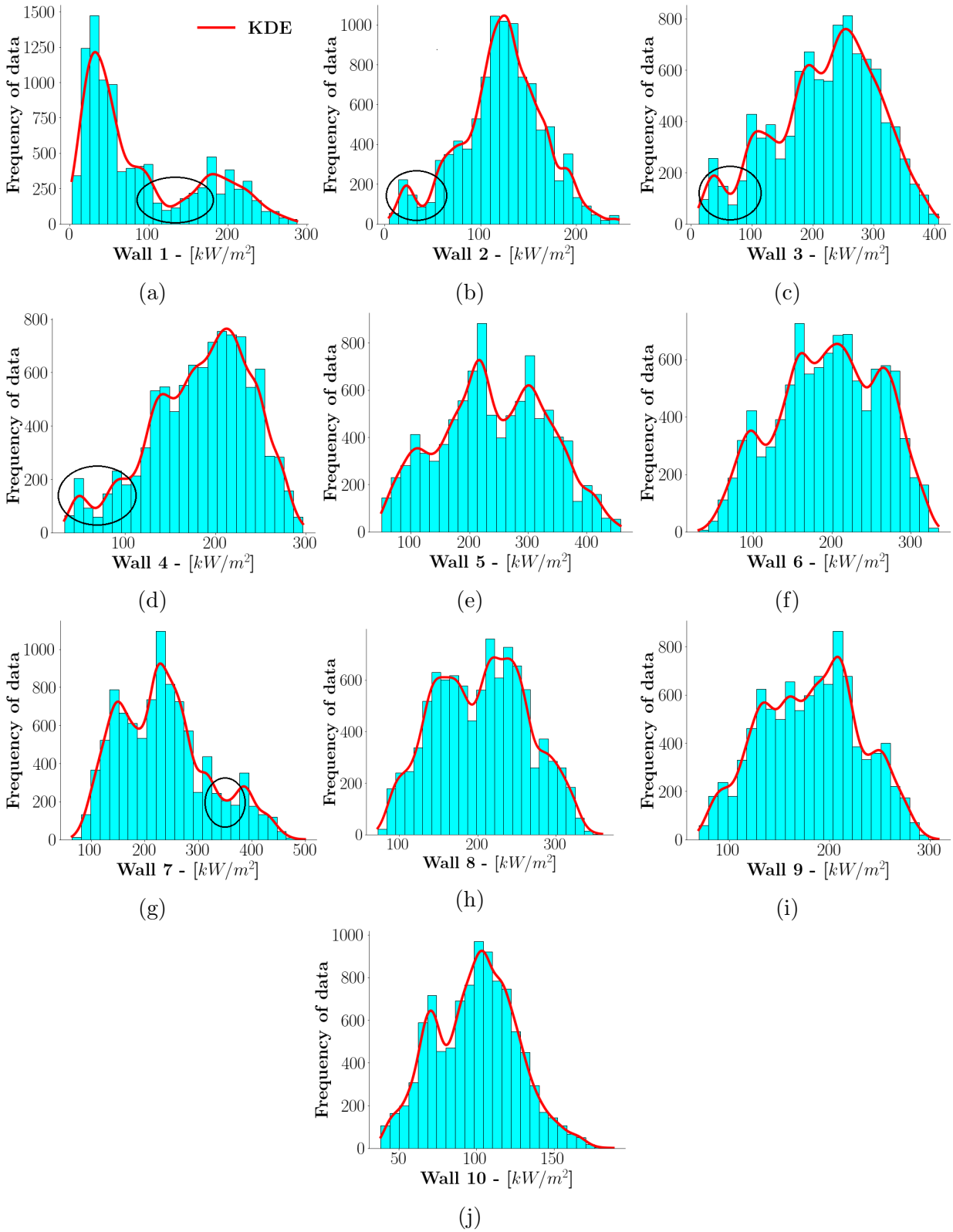

Figure 7.9: Heat loads to the EV wall sections for walls 1 to 10

Chapter 8

Surrogate model development, training, and selection

Selecting the best machine learning model requires hyperparameter tuning, whereby different combinations are tested to evaluate the best-performing model settings, resulting in the lowest training and testing errors. Examples of hyperparameters are the optimisation learning rate, number of fitting coefficients (model parameters) and mini-batch sizes.

In this chapter the database generated using the reduced order CFD model is used to train the surrogate model of the radiant heat exchanger section of a 620 $[MW_e]$ utility-scale boiler. Both an MLP and an MDN were considered in the hyperparameter tuning process, with the best model being selected based on the minimisation of the MAEs and root mean square error (RMSE) values.

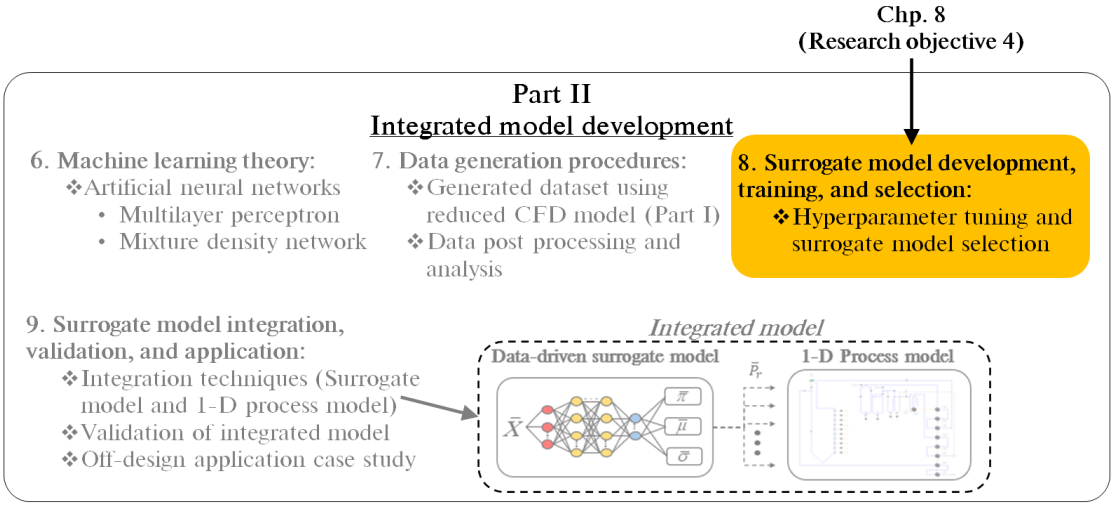

Figure 8.1: Content overview and research objective addressed in Chapter 8

Figure 8.1 highlights the content that is discussed and indicates the research objective addressed in this chapter for the readers convenience.

8.1 Surrogate model configuration

The surrogate model aims to predict the heat load distributions to the EV walls, the SH2 tubes, the SH3 tubes, as well as the flue gas composition and temperatures at the exit of the radiative section (which is at the exit of SH3), using the 14 high-level inputs ($d_{inputs} = 14$) as given in Table 7.1. Recall that for each CFD simulation, the output matrix size comes to ($\bar{Y} \in \mathbb{R}(50 \times d_{targets})$), with $d_{targets} = 23$, where the targets are the predicted output variables mentioned previously.

The total CFD solution data matrix size ($\bar{Y}_{tot}$) will consist of 180 different simulations, each with its own set of output data ($\bar{Y}$); thus, $\bar{Y}_{tot} \in \mathbb{R}(180 \times \bar{Y})$ results, to provide a total of 207,000 data points. During the training and testing phase of the various machine learning models, a combination of forward propagation, cost function calculation, back propagation and parameter optimisation is used to train/test the network parameters to minimise the loss calculated from the cost function, as described in Chapter 6. Using the total solution data matrix for training and testing would typically result in a high memory consumption for very large datasets [125].

To negate the high memory consumption, mini-batches can be used to pass training/testing samples through the machine learning model network. Mini-batches train significantly longer compared to full-batch training but requires less GPU memory. Additionally, mini-batch models have better generalisation because of the sequential feeding of the data. The mini-batch size is a term used in machine learning that specifies the number of training/testing examples utilised in one iteration [122]. Thus, for a data mini-batch size, m_b, the output tensor for the developed MLP model will be $\hat{Y} \in \mathbb{R}(m_b \times d_{targets})$. However, the output data for the developed MDN model will consist of three parts, namely; the mixing coefficients tensor of shape $\bar{\pi} \in \mathbb{R}(m_b \times K)$, the output standard deviation tensor of shape $\bar{\sigma} \in \mathbb{R}(K \times m_b \times d_{targets})$, and the predicted means of tensor shape $\bar{\mu} \in \mathbb{R}(K \times m_b \times d_{targets})$, where K is the number of distributions. The input data fed into both the MLP and MDN will have shape $\bar{X} \in \mathbb{R}(m_b \times d_{inputs})$.

8.2 Hyperparameter tuning & model selection

For the current study the following hyperparameter search spaces were considered for the hyperparameter tuning process: the number of layers, the number of neurons per layer, various learning rates, various mini-batch sizes, and where the MDN is concerned, the number of distributions.

The training to testing split is an important pre-processing technique used to evaluate the performance of a machine learning algorithm [138]. The procedure involves splitting the dataset into two subsets, namely a training data subset utilised to fit the machine learning model and a testing data subset utilised to evaluate the fitted machined learning model. The testing data subset is not used to train the model, instead the input element of the dataset is fed to the trained model and the predictions are compared to the expected output values of the testing data subset [138]. The current work employed an 80% to 20% split of the training and testing data [11, 64].

In addition, min-max scaling of the input and output parameters was done to ensure that they were scaled between 0 and 1 [138]. The use of min-max scaling safeguards against exploding or vanishing error gradients during back propagation when utilising ReLu activation functions, which the current work employs in the hidden layer of both the MLP and MDN neural network architectures. Min-max scaling for an input parameter can be defined as follows [138]:

$$\bar{X}_{std,i} = \frac{\bar{X}_i - X_{min}}{X_{max,i} - X_{min,i}} \tag{8.1}$$

In Equation (8.1), $\bar{X}_i$ is a vector of input samples for one input parameter, $X_{min,i/max,i}$ is the minimum and maximum of the input sample and $\bar{X}_{std,i}$ the scaled vector of input samples for one input parameter. Similarly, the labelled output samples ($\bar{Y}$) are also scaled using a min-max scaler.

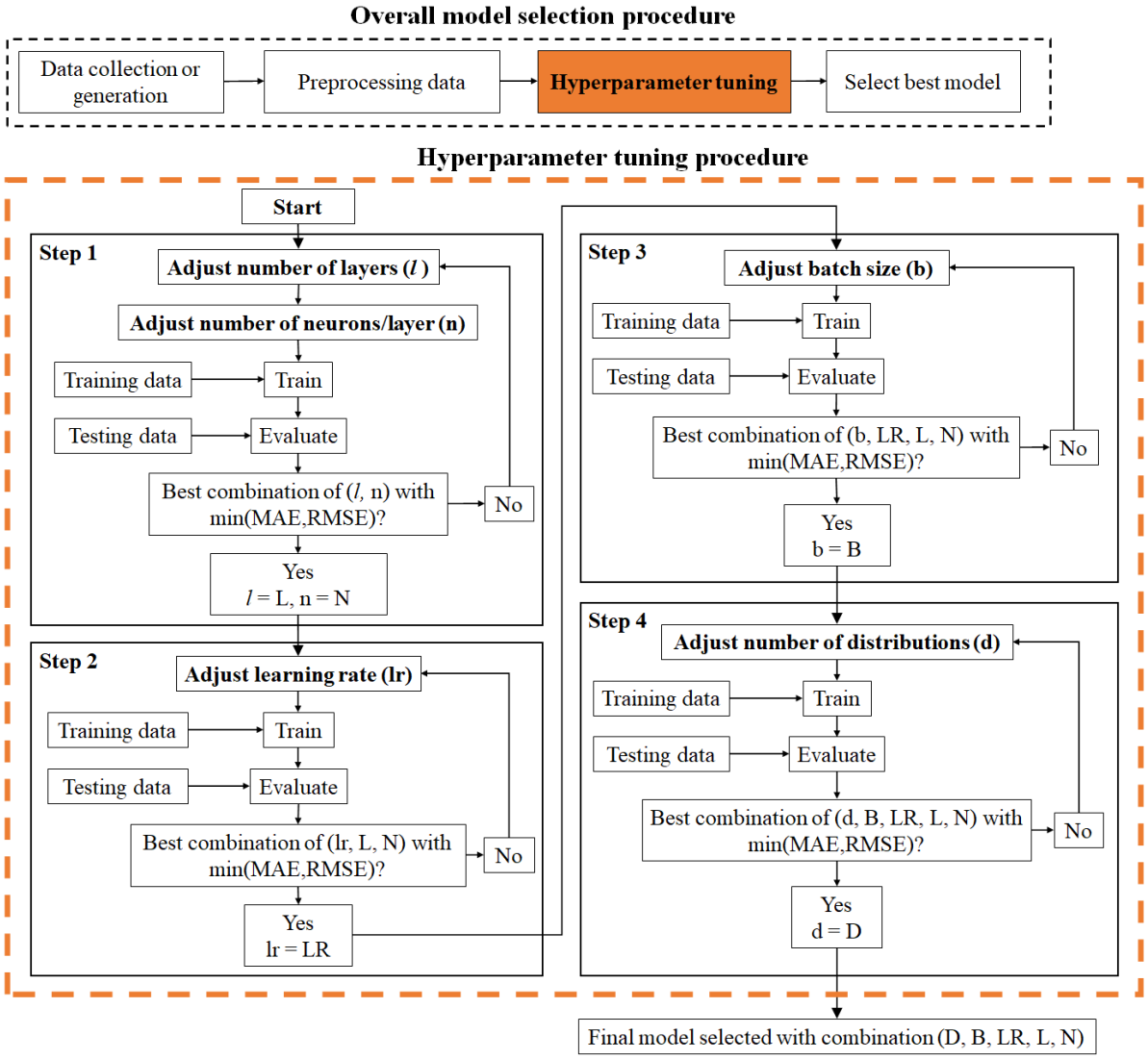

Figure 8.2: Overall model and hyperparameter tuning steps for the MDN model

Figure 8.2 highlights the process of hyperparameter tuning in the overall model selection procedure. In the present work, it was decided to perform a sequential hyperparameter tuning process where parameters are tuned to their best-performing values sequentially before the next parameter is tuned. A more appropriate process would be to use a formal optimiser to find the best-combination of hyperparameters. That being said, the sequential process develops a better intuition of the effects of the various hyperparameters on the developed model accuracy. Each sequential process in the process considers a single/pair of hyperparameter/s and finds the best combination that minimises the MAE and RMSE values. Then, with the best combination, the subsequent hyperparameter can be set and varied until the best combination is found. The MLP model would follow a similar process; however, only steps 1 to 3 must be considered.

Table 8.1: Hyperparameter search space for the MLP and MDN models

Parameter	**MLP search space**	**MDN search space**
Number of distributions	-	1,2,3,4
Number of layers	2,3,4	3,4,5
Number of neurons per layer	10, 40, 80, 100	40, 80, 100, 120
Learning rates	1e-3, 1e-4, 1e-5, 1e-6	1e-4, 1e-5, 1e-6
Mini-batch sizes	32, 64, 128, 256	32, 64, 128

The hyperparameter search spaces for both the MLP and MDN models are illustrated in Table 8.1. In addition, the MDN has an added parameter, namely the number of additional distributions that the MDN would need to fit the output data. The hyperparameter tuning of the MLP and MDN models used 1000 epochs; this was deemed adequate to train and test the models for the various hyperparameter search spaces. The hyperparameter search was conducted sequentially, with the MAEs and RMSE being taken as important performance indicators for each trained and validated case (as indicated in Figure 8.2).

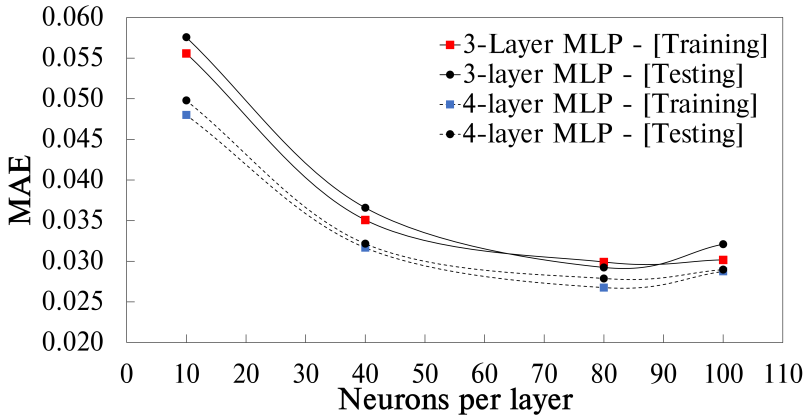

Figure 8.3: MLP hyperparameter tuning of the hidden layer architecture

Firstly, the hidden layer architecture of both models (MLP & MDN) was varied by considering the number of hidden layers and neurons per layer. Figure 8.3 illustrates the MLP model performance for the various hidden layer architectures.

The neuron capacity reaches a minimum MAE at 80 neurons per layer for a four-layer architecture. Further increasing the neuron capacity increases the MAE, possibly overfitting the data.

Secondly, the learning rates were varied for the best-performing architecture of the first hyperparameter tuning step, which was an MLP consisting of four hidden layers with 80 neurons per layer. The learning rate hyperparameter generally controls the rate or speed at which the model learns. Generally, a large learning rate allows the model to learn faster, at the cost of arriving at a sub-optimal final set of weights. Conversely, a smaller learning rate may allow the model to learn a more optimal or globally optimal set of weights but may take significantly longer to train [138].

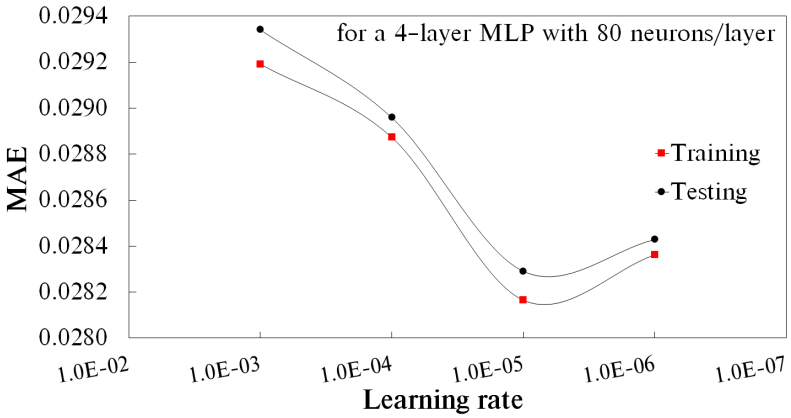

Figure 8.4: MLP hyperparameter tuning of the learning rate

Considering Figure 8.4, a decrease in the learning rate shows an improvement in the MAE, with a learning rate of 1×10^{-5} being the best for the current epoch size. The final step of the MLP hyperparameter tuning process required the mini-batch sizes to be varied using an MLP with four hidden layers having 80 neurons per layer and a learning rate of 1×10^{-5}. For comparative purposes, learning rates of 1×10^{-5} and 1×10^{-6} were used. Figure 8.5 highlights the comparison for a fixed epoch, with a mini-batch size of 32 and a corresponding learning rate of 1×10^{-5} showing the best MAE improvement.

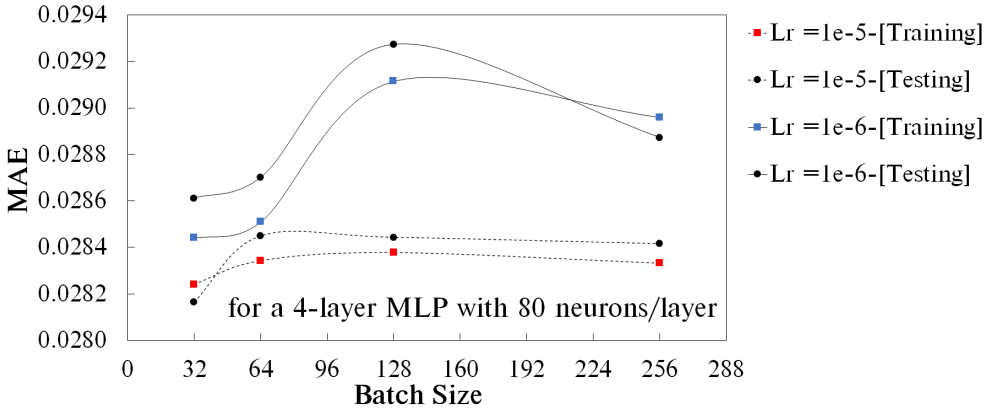

Figure 8.5: MLP hyperparameter tuning of the mini-batch size

The MDN hyperparameter tuning was conducted in a similar sequential manner as demonstrated with the MLP model of Figures 8.3 to 8.5. Thus, the results of steps 1-3 of Figure 8.2 are presented for the MDN model in Figures 8.6 (a) to (c).

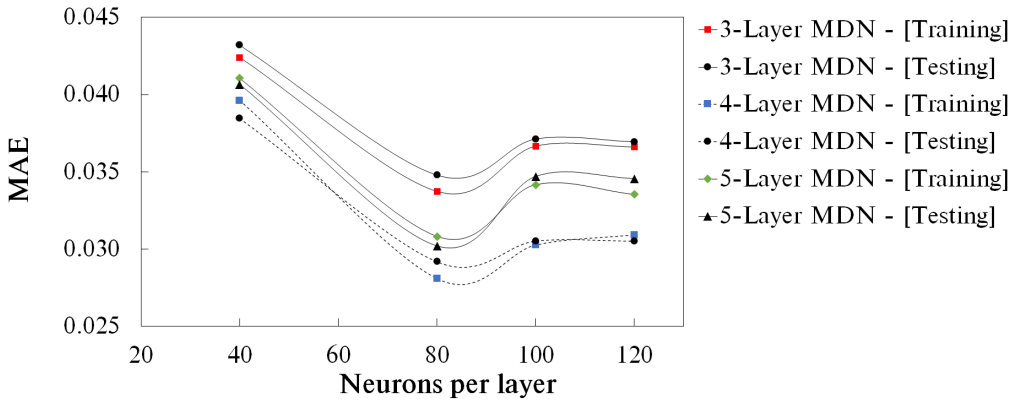

(a)

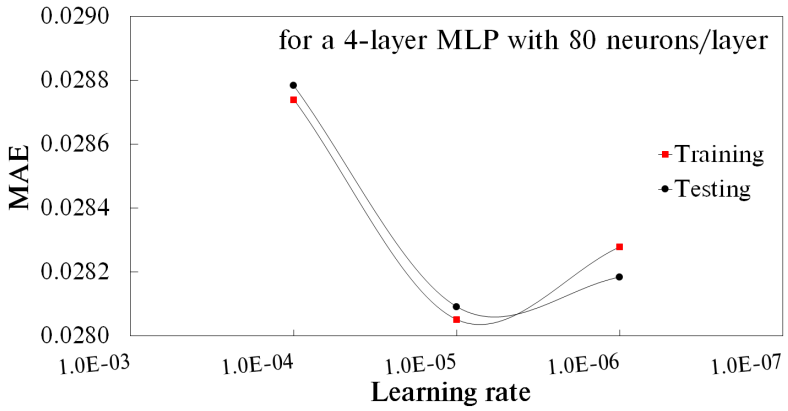

(b)

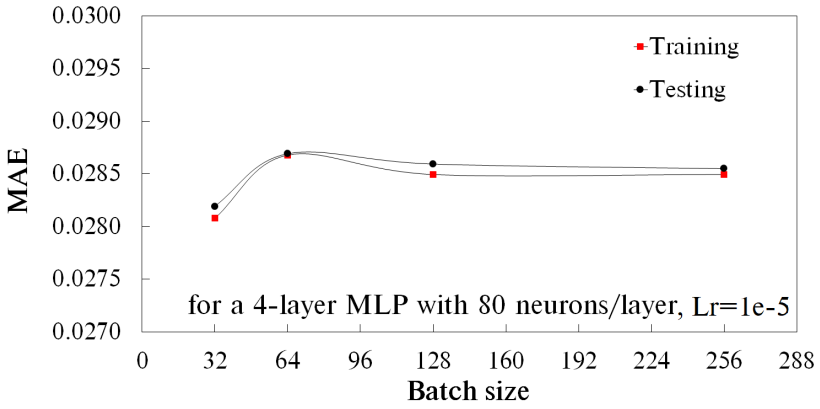

(c)

Figure 8.6: MDN hyperparameter tuning of the (a) hidden layer architecture, (b) learning rate and (c) mini-batch size

An additional step was required for the MDN hyperparameter optimisation process: to consider the number of distributions the MDN would use to capture the probabilistic characteristics.

Figure 8.7 shows the MAE for the various distributions, with a distribution of one representing the best MLP model. An increase in the number of distributions tends to improve the MAE; however, it is evident that a threshold of three distributions results in the best improvement.

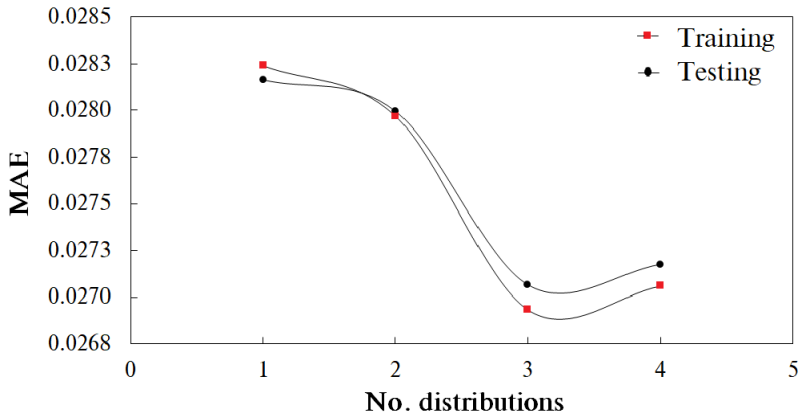

Figure 8.7: MDN hyperparameter tuning of the number of distributions

The results of the hyperparameter search are given in Table 8.2. It is shown that both the MLP and MDN produce the best results using a four-layered architecture having 80 neurons per layer, with the learning rate and mini-batch sizes set to 1×10^{-5} and 32, respectively. In addition, the MDN requires three distributions.

Table 8.2: Hyperparameter search results for the MLP and MDN models

Parameter	**MLP**	**MDN**
Number of distributions	-	3
Number of layers	4	4
Number of neurons per layer	80	80
Learning rate	1e-5	1e-5
Mini-batch size	32	32
Errors		
RMSE	0.0213	0.0211
MAE	0.0282	0.0263

Unlike the MLP, which can only produce a single set of predictions for an input, the MDN can produce a distribution of predictions based on the most probable mixing coefficient. This highlights one of the main advantages of using the MDN model, which is its ability to learn the uncertainty that comes from using a probabilistic model that enables the modelling approach to take into account the effect of information density in the training/testing data [123].

A sample of the error distributions of the flue gas composition and the heat load distributions to the EV walls is provided in Figures 8.8 (a)-(d). In addition to an MLP and MDN model a multivariate linear regression model was also established to serve as a base model to demonstrate the effectiveness of using higher order machine learning models. It can be seen that the error distributions of the flue gas composition (Figures 8.8 (a) and (b)) show that approximately 96% of the data is within a 10% error band for all the models (i.e. linear, MLP and MDN). Furthermore, the heat load error distributions of Figures 8.8 (c) and (d) showcase that approximately 83% of the testing and training data is within a 10% error band for both the MLP and MDN models, both outperforming the linear regression model results.

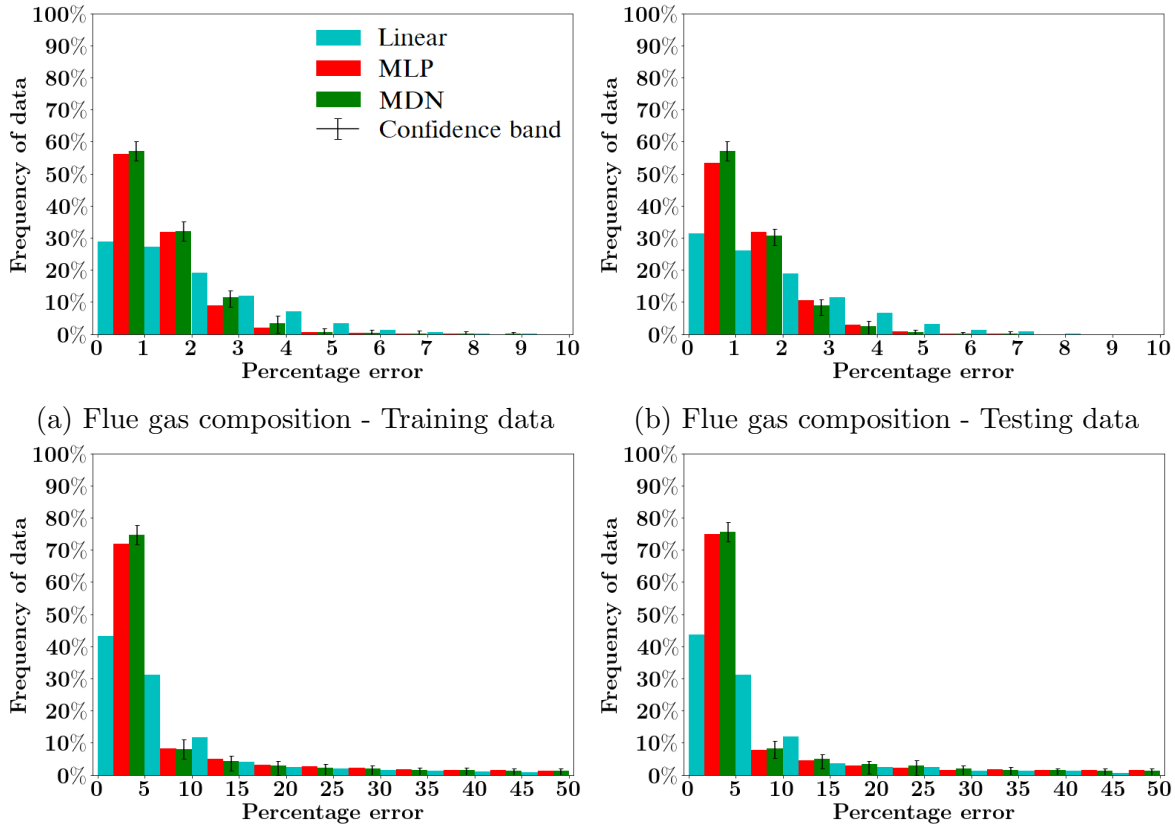

(a) Flue gas composition - Training data

(b) Flue gas composition - Testing data

(c) Heat loads to EV walls - Training data

(d) Heat load to EV walls - Testing data

Figure 8.8: Key parameter error distributions for the selected MLP and MDN models, (a)-(b) Flue gas composition training and testing results, (c)-(d) Heat load distributions to the EV walls training and testing results

As indicated previously, the MDN model is able to learn the uncertainty, which is illustrated by the confidence bands of Figures 8.8 and 8.9. Figures 8.9 (a) and (b) showcase the overall error distribution of the models key parameters. For the MDN model, it is seen that approximately 80-90% of the training data has mean absolute percentage errors (MAPEs) below 10%, with the MLP model showing a similar trend. Both models show considerable improvement in comparison to the linear regression model.

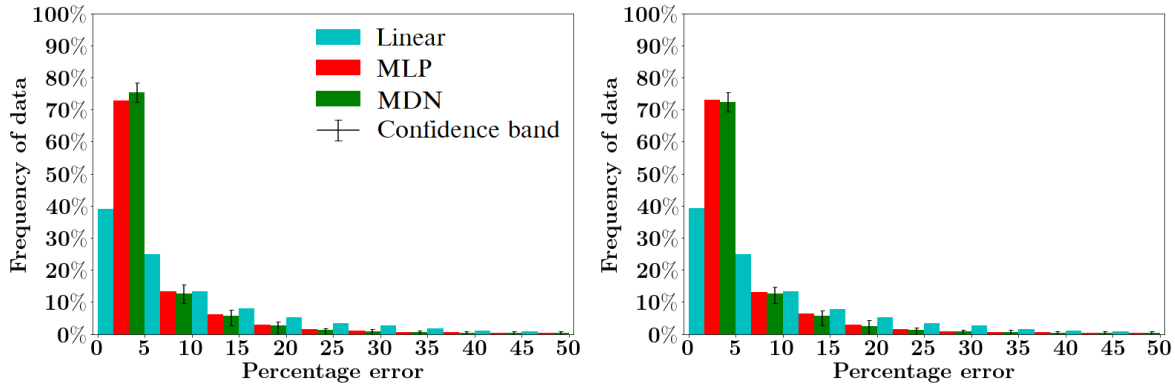

(a) Overall error - Training data (b) Overall error - Testing data

Figure 8.9: Overall error distributions for the selected MLP and MDN model; (a) training data and (b) testing data.

Based on the above analysis, the MDN model was selected as the best model to be used for the surrogate model implementation. The benefit of using the MDN surrogate model is the ability to provide the expected mean (most probable) value of each output parameter and the associated standard deviation. Having the mean value of each of the furnace and heat exchanger heat loads together with its uncertainty in the form of a standard deviation allows the uncertainty to be propagated through the entire integrated model. It is, therefore, possible to obtain the resultant mean values of the overall plant performance parameters together with their uncertainties emanating from the surrogate model prediction.

Chapter 9

Surrogate model integration, validation, and application

This chapter presents the validation and application case studies of the integrated surrogate and network-based 1-D process model of a 620 $[MW_e]$ utility-scale boiler. A summary of the chapter sections is listed below:

- The integration strategy of a data-driven surrogate model and a 1-D process model is presented, demonstrating the data transfer coupling and the modelling procedures.
- Validation case studies are presented using the integrated surrogate and 1-D process model, for MCR loads of 100%, 81% and 60%. The results are compared and validated against measured site data.
- Application case studies are presented showing the effects that the fuel composition has on the thermodynamic response for the utility-scale boiler operating at 100% MCR. The results are compared to the validated 100% MCR load case of the validation case study.

Figure 9.1 highlights the content that is discussed and indicates the research objective addressed in this chapter for the readers convenience.

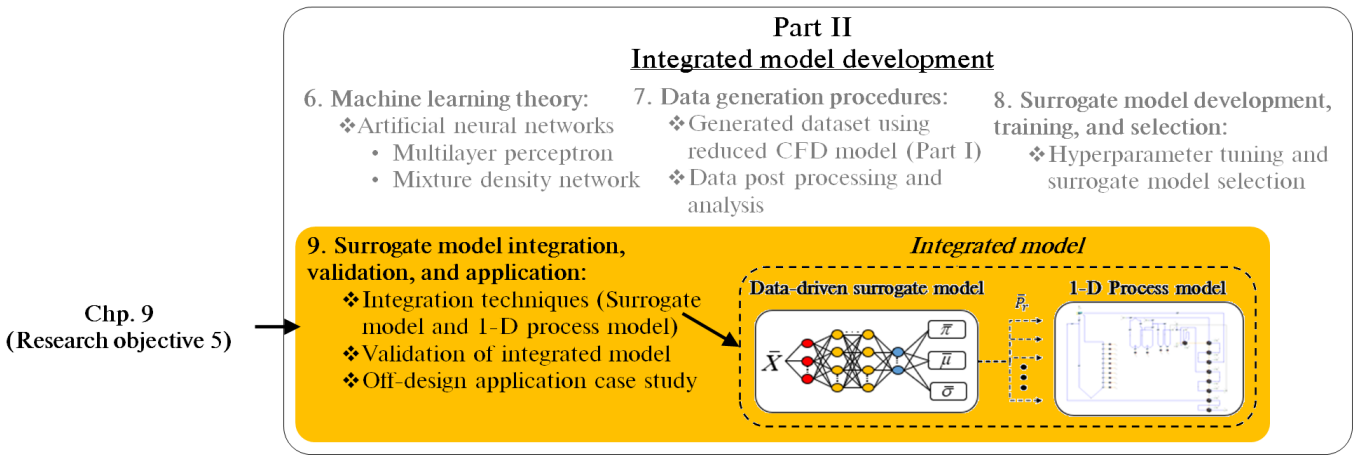

Figure 9.1: Content overview and research objective addressed in Chapter 9

9.1 Surrogate and 1-D process model integration

The results of Chapters 7 and 8 have led to the development of a data-driven surrogate model that can capture the fire-side response of the radiative section in a 620 $[MW_e]$ utility-scale boiler. The integrated model is obtained by integrating the surrogate model and a 1-D process model that includes both the flue gas flow elements and the water/steam side flow network. The integration follows a similar methodology as discussed in Section 5.2 of Chapter 5. The 1-D process model is used to capture the thermodynamic response of the flue gas side and the water/steam side of the boiler under investigation, with the data-driven surrogate model providing predictions of the flue gas-side thermal characteristics (i.e., combustion product species, temperature, and incident radiation fluxes) and the heat-exchanger heat loads to the EV, SH2 and SH3 walls. Figure 9.1 provides a schematic of the boiler layout, highlighting the radiative and convective sections, the water/steam network layout and the SH3 exit plane. Figure 9.2 provides a schematic of the boiler layout, highlighting the radiative and convective sections, the water/steam network layout and the SH3 exit plane.

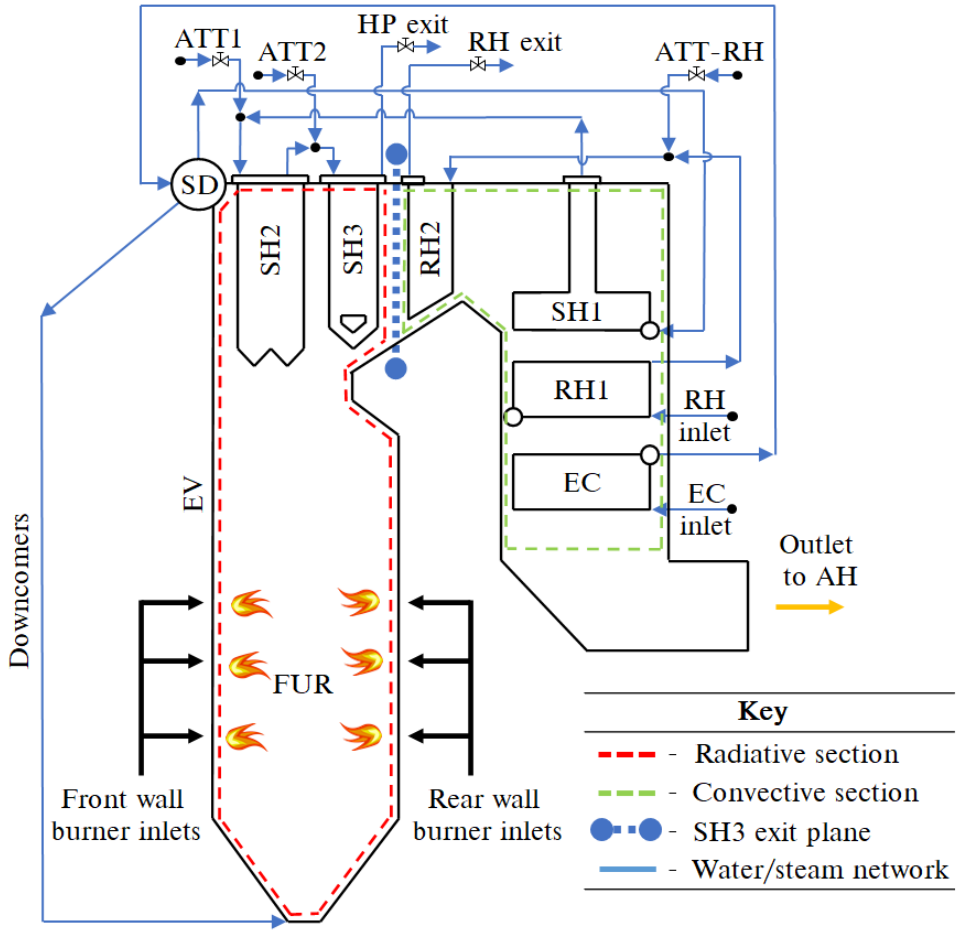

Figure 9.2: Schematic of the 1-D process models water/steam network highlighting the radiative and convective sections and the SH3 exit plane

The 1-D process model was developed using the process modelling software Flownex SE® 2021 [100]. The software makes it possible to add control elements to obtain a complete integrated dynamic system simulation model of a plant, sub-system, or component [139]. The 1-D process model employed a control strategy emulating the real operating protocols which utilises the ATT1, ATT2 and ATT-RH attemperators to provide cooling spray water to regulate the RH and HP exit temperatures during a simulation. In addition, the feed water entering via the EC inlet was controlled to maintain the water level in the steam drum. This was done to ensure a zero energy source in the steam drum node. To capture the thermal response of heat exchangers RH2, SH1, RH1 and EC in the convective section, the 1-D heat exchanger process model, as discussed in Section 5.2 of Chapter 5, was utilised, which resolves both the water/steam and flue gas control volume heat transfer and flow interactions.

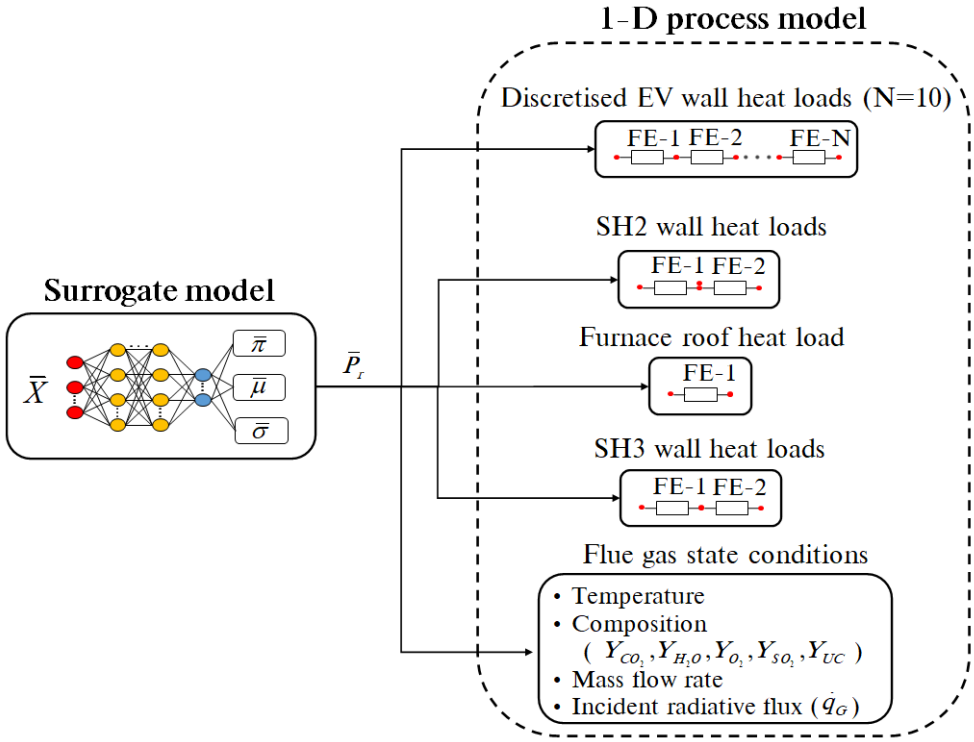

Figure 9.3: Schematic of the data transfer of the surrogate model predictions ($\bar{P}_r$) to the 1-D process model components

A schematic of the data transfer between the surrogate and 1-D process model is provided in Figure 9.3. The data-driven surrogate model accepts the high-level inputs ($\bar{X}$) for a MCR load case and generates a prediction dataset ($\bar{P}_r$). This dataset is compromised of the 23 output parameters (i.e. $d_{targets}$) discussed in Section 7.3 of Chapter 7. Included in the prediction dataset, are the heat load predictions to the EV, SH2, and SH3 walls as well as the heat load to the roof section directly above SH2 and SH3. These heat loads are applied to the corresponding 1-D process model components as inputs. In addition, the flue gas temperature, composition, and the radiative incident flux form part of the surrogate model prediction dataset and are transferred to the corresponding process model boundary node.

The water-/steam side flow and heat load interactions of the integrated model is as follows: the evaporation rate in the waterwalls is driven by the heat loads applied to the EV walls, the water/steam mixture that is generated flows to the steam drum component where the steam is separated and sent to SH1, while the water (liquid fraction) flows from the steam drum through the downcomers to be fed through the EV walls again (refer to Figure 9.2). Heat is transferred from the flue gas to the steam-side of SH1. The steam exiting SH1 is attemperated via ATT1, cooling the steam to a predefined control SH2 exit temperature. Further heat is added to the steam through the heat loads applied to the SH2 walls. Secondary attemperation is applied via ATT2 before the steam enters SH3, where the heat loads to SH3 are applied. The high pressure (HP) steam outlet flow rate is calculated as the sum of the attemperation flow rates (ATT1 and ATT2) and the evaporation flow rate. ATT1 and ATT2 are used to control the steam temperature at the HP outlet, while ATT-RH is applied in a similar manner to control the RH outlet steam temperature. The attemperators of a utility-scale boiler are an integral part of the control systems put in place to ensure safe operating conditions and to minimise water droplet formulation in the turbines [42]. The desired exit steam temperatures for both the HP and RH is a temperature of 808 $[K]$ for all MCR loads.

The wall sections of the EV, SH2, SH3 and roof are comprised of Flownex SE® flow elements which incorporate pipe components interconnected with nodes. Nodes represent the connection points between elements and can also be a physical reservoir or tank.

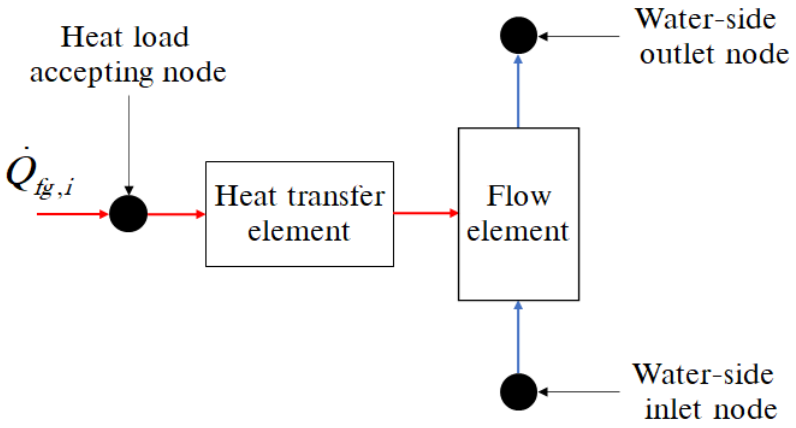

Figure 9.4: Schematic of a simple network highlighting the inlet and outlet nodes, a heat transfer element, and a flow element

Figure 9.4 illustrates a schematic of a flow element where an external heat load is applied to the heat accepting node of the heat transfer element which in turn transfers the applied heat load to the flow element. The heat transfer element can incorporate multiple layers by specifying each layer's material properties (such as the thermal capacitance and conductivity) and the thickness. This allows the 1-D model to capture the thermal inertia associated with the fouling and the heat exchanger tube thicknesses. In the case of the modelled SH2 and SH3 walls, two layers were needed, namely the fouling and tube wall layers.

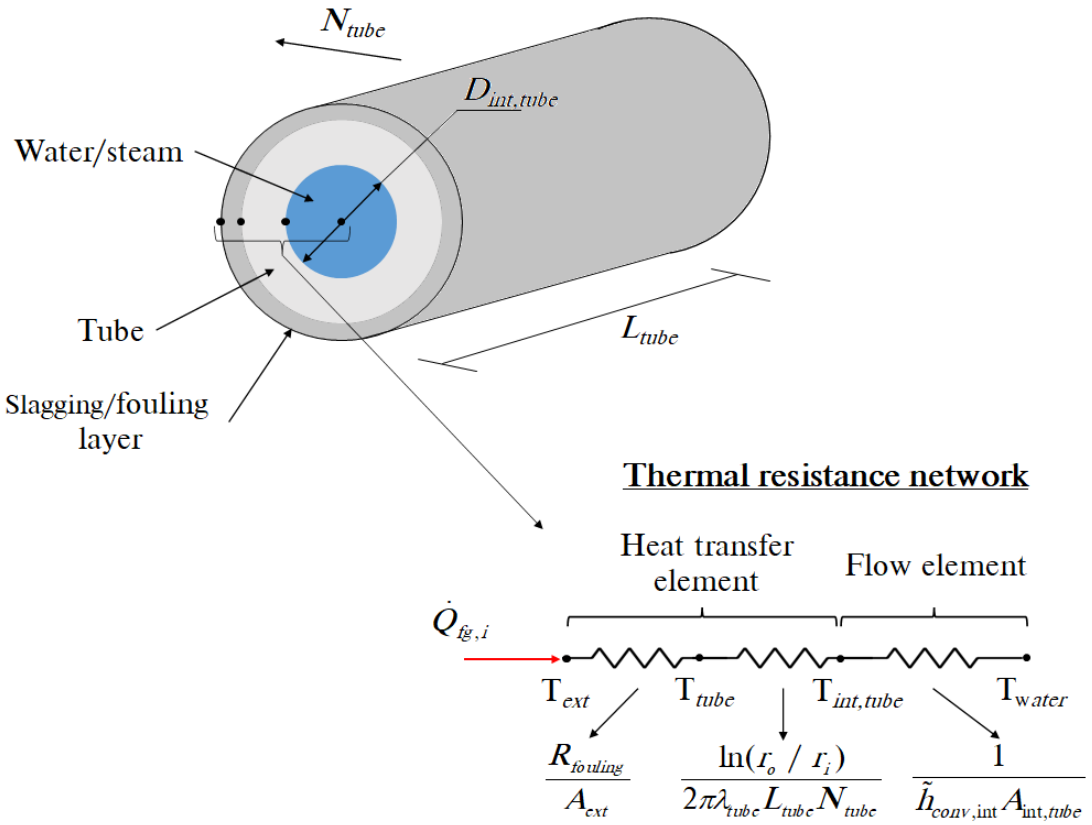

Figure 9.5: Thermal resistance network incorporating the use of a heat transfer element and a flow element for a simple pipe

A schematic of the thermal resistance network is provided in Figure 9.5. It is shown that the heat transfer element represents the flow of heat from the external fouling surface temperature (T_{ext}), exposed to the heat load, to the inner tube surface temperature ($T_{int,tube}$), while the flow element represent the flow of heat to the water/steam. It was assumed that the EV walls operate with negligible slagging, thus the effect of slagging was neglected when modelling the EV walls.

In addition to capturing the various layers using the heat transfer element, the characteristic dimensions are captured using the flow element. The dimensions include the inner tube diameter ($D_{int,tube}$), the effective total length of a single pipe (L_{tube}), and the amount of tubes that are in parallel (N_{tube}). Furthermore, losses resulting from the tubes surface roughness and the piping layout (e.g. inlets, bends and outlet) are captured to determine the pressure drop over a flow element. Thus, in the current work a single flow element was used to represent each discretised EV wall section and each tube bank leg section of SH2 and SH3 (refer to Figure 7.5).

The flue gas exit state predictions are transferred to a boundary node in the 1-D process model of the flue gas flow elements, which defines the boundary conditions for the fire-side interactions of the convective section. Included is the flue gas mass flow rate, the temperature, and the composition. The incident radiation flux is used to calculate the direct radiation entering RH2, by making use of the SH3 exit plane area ($A_{SH3,plane}$). The direct radiation entering is coupled directly to the fire-side stream of the heat exchanger process model for RH2. Figure 9.6 illustrates a schematic of the flue gas state predictions ($\bar{P}_{r,fg}$) accepted by the boundary condition node and the general setup of the heat exchanger process model used in the convective section.

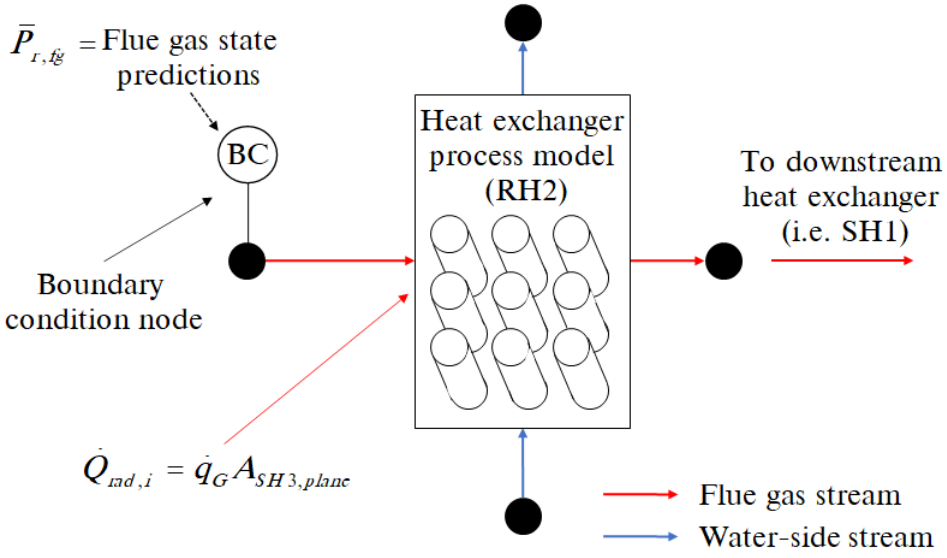

Figure 9.6: Schematic of the RH2 heat exchanger process model illustrating the flue gas and water-side flow streams, and the input flue gas state predictions ($\bar{P}_{r,fg}$) to the boundary node

To transfer the surrogate model predictions to the various process modelling components, a *C#* script was developed. The *C#* script was developed to utilise the Python application programming interface (API) of Flownex SE® 2021, since the surrogate model was primarily developed using Python code. The script is primarily utilised to send the high-level inputs to the surrogate model and retrieve the predictions thereof.

9.2 Integrated model validation using experimental data

The results of the integrated model were validated using available measured data for the 100%, 80% and 60% MCR load cases. From the measured data, the mean and standard deviations for the following operational parameters could be determined: the total heat loads to heat exchangers (EV through to the EC), the steam generation rates for the HP exit, the RH exit, and the EV walls (evaporation rate), as well as the attemperator flow rates for ATT1, ATT2 and ATT-RH (refer to Figure 9.2). Table 9.1 provides a summary of the operational parameters for the various load cases.

Table 9.1: Measured operational parameters summary statistics

Operational parameter	**Loads** 100%	81%	60%	**Units**
*Heat loads (**mean**, standard deviation)*				
EV	(**538.5**, 8.171)	(**471.3**, 5.332)	(**308.8**, 13.6)	MW
SH2	(**196.4**, 8.676)	(**168.7**, 5.381)	(**154.7**, 3.471)	MW
SH3	(**78.5**, 5.940)	(**68.1**, 4.027)	(**47.0**, 1.672)	MW
RH2	(**140.8**, 5.497)	(**79.3**, 0.821)	(**85.7**, 13.009)	MW
SH1	(**175.4**, 3.484)	(**124.1**, 3.445)	(**101.6**, 2.353)	MW
RH1	(**107.7**, 1.852)	(**112.5**, 6.175)	(**56.7**, 1.703)	MW
EC	(**91.8**, 4.837)	(**97.8**, 4.352)	(**61.9**, 3.547)	MW
*Steam generation rates (**mean**, standard deviation)*				
HP exit	(**472.1**, 1.483)	(**386.5**, 1.483)	(**305.9**, 2.020)	kg/s
RH exit	(**457.9**, 1.438)	(**374.9**, 1.601)	(**296.7**, 1.960)	kg/s
EV	(**430.1**, 4.815)	(**354.6**, 4.815)	(**228.9**, 6.455)	kg/s
*Attemperator flow rates (**mean**, standard deviation)*				
ATT1	(**38.9**, 3.398)	(**29.5**, 1.339)	(**38.9**, 3.398)	kg/s
ATT2	(**3.1**, 1.17)	(**2.3**, 0.744)	(**3.1**, 1.17)	kg/s
ATT-RH	(**13.5**, 0.536)	(**13.5**, 0.556)	(**13.5**, 0.536)	kg/s

The predictions of the surrogate model (refer to Figure 9.3) can only be used to estimate the mean and standard deviation values for the EV, SH2 and SH3 wall heat loads. However, the Monte Carlo method was utilised to propagate the uncertainty of the predictions and ascertain the summary statistics for the convective section heat exchangers (RH2, SH1, RH1 and EC), the steam generation rates and the attemperator flow rates, the Monte Carlo method was utilised. The Monte Carlo method is a mathematical technique used to estimate the outcome of a given stochastic process [140]. Using a probability distribution for any variable that has inherent uncertainty, such as the predictions from the surrogate model, the Monte Carlo method builds a set of possible results by recalculating the results for a set number of iterations. Each iteration utilises a different set of variables generated using random selections from a prescribed range and distribution. Thus, the core concept behind the Monte Carlo method is the random sampling from a given set of probability distributions. The current work made use of normal distributions defined by the mean ($\bar{\mu}$) and standard deviation ($\bar{\sigma}$) values that are predicted from the surrogate model.

The Monte Carlo method can be divided into three basic steps: Firstly, to set up the predictive model and identify both the dependent variables to be predicted and the corresponding input variables. Secondly, to specify the distributions of the input variables. Finally, running multiple simulations using randomly sampled values of the input variables [140].

Flownex SE® 2021 provides a sensitivity analysis tool that utilises a built-in Monte Carlo capability. It requires the mean and standard deviations to determine the range (minimum and maximum) for each input variable [100]. Figure 9.7 provides a flow chart of the Monte Carlo algorithm utilised in Flownex SE®.

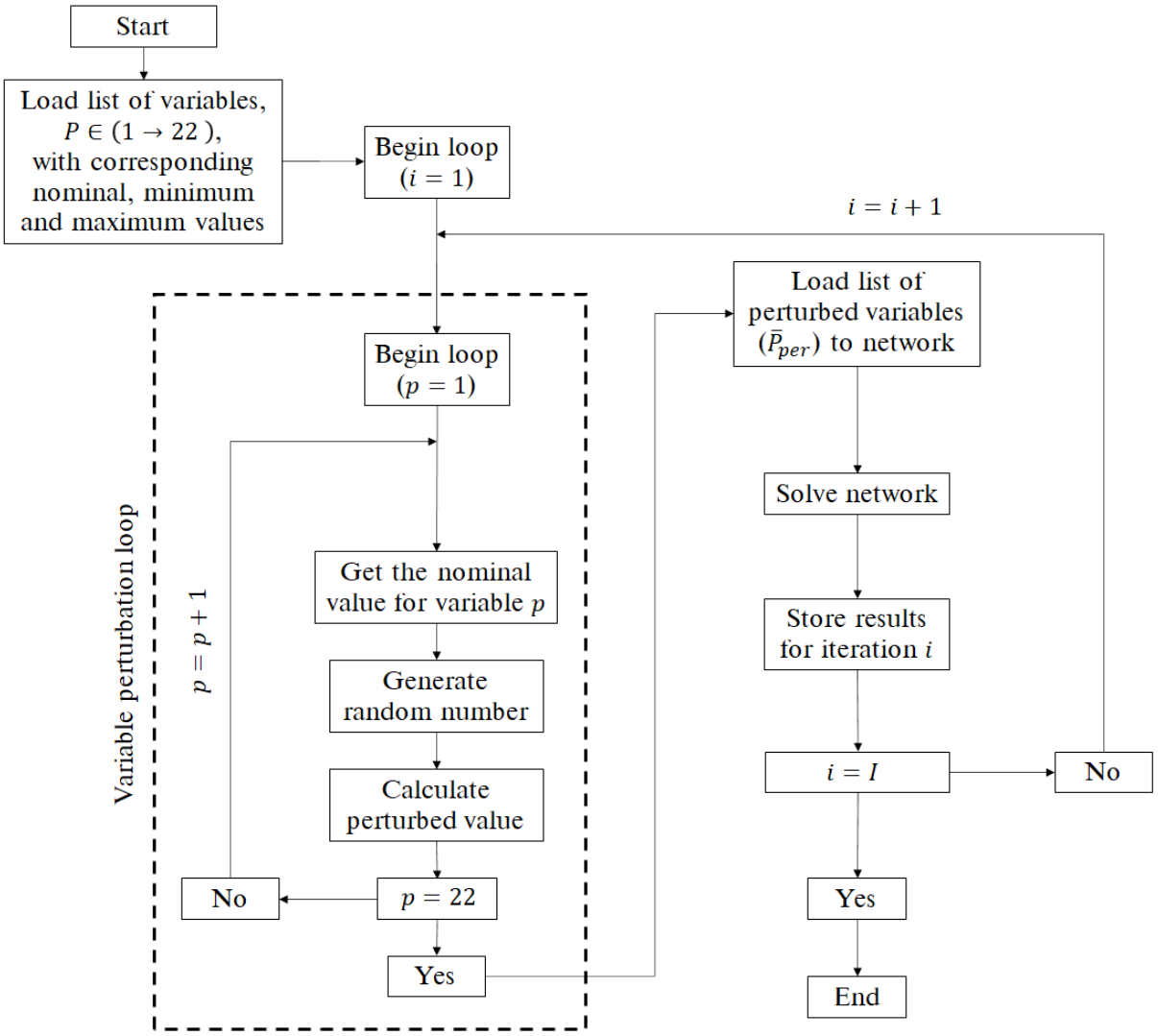

Figure 9.7: Flowchart of the Monte Carlo algorithm utilised in FlownexSE®

The analysis begins with the independent variables being compiled with their corresponding nominal/mean, minimum and maximum values. For the current work, the 23 outputs of the surrogate model are selected as the independent variables with the dependent variables being the operational parameters listed in the Table 9.1, excluding the heat loads to the EV, SH2 and SH3 walls. Following this, each independent variable undergoes a randomly calculated perturbation that complies with the selected probability distribution. A list of perturbated inputs would then be loaded to the Flownex SE® 1-D network and solved. With a converged solution the results are stored for each Monte Carlo iteration until the iteration limit is met. For this study, $I = 1000$ simulations were performed for each MCR load.

The perturbation values ($\bar{P}_{per}$) are determined using the Box-Muller transformation [141]. The Box-Muller transformed random numbers are calculated as follows:

$$BM = \sqrt{-2ln\zeta_1}cos(2\pi\zeta_2) \tag{9.1}$$

where ζ_1 and ζ_2 are random numbers between 0 and 1. Thus, the perturbated values of the independent variables are calculated as follows:

$$\bar{P}_{per} = \bar{\mu} + R_{min-max}(\frac{BM}{4}) \tag{9.2}$$

where $\bar{\mu}$ is the specified nominal/mean value, and $R_{max-min}$ is the range of the independent variable, defined as the difference between the maximum and minimum limits of the simulation variable.

Table 9.2 provides the input vectors ($\bar{X}$) to the surrogate model for both the validation and application case studies discussed in this chapter. The input vectors are utilised by the surrogate model to produce the output set of 23 independent variables. Utilising the predicted mean, and standard deviations to define the independent variables normal distributions, the Monte Carlo method was run to produce a set of results that incorporates the inherent uncertainty of the surrogate model predictions.

Table 9.2: MDN input vectors ($\bar{X}$) for the validation and varied fuel case studies

		Validation load cases			**Varied fuel load cases**	
Input variables		**100%**	**81%**	**60%**	**High-ash**	**High-moisture**
Excess air content		1.155	1.209	1.263	1.155	1.155
Y_{ASH} - $[kg/kg]$		0.409	0.409	0.409	0.501	0.409
Y_{H_2O} - $[kg/kg]$		0.055	0.055	0.055	0.055	0.151
HHV - $[MJ/kg]$		15.07	15.07	15.07	13.21	13.21
R_{SH2} - $[K/W]$		0.012	0.012	0.012	0.012	0.012
R_{SH3} - $[K/W]$		0.0067	0.0067	0.0067	0.0067	0.0067
SH2 steam temperature - $[K]$		698	697	781	698	698
SH3 steam temperature - $[K]$		787	793	781	787	787
Mill flow rates - $[kg/s]$						
MCR load	**Mill 1**	**Mill 2**	**Mill 3**	**Mill 4**	**Mill 5**	**Mill 6**
100%	19.14	20.22	19.92	19.98	19.41	0.00
81%	18.23	19.72	19.02	17.82	18.02	0.00
60%	15.46	16.13	0.00	15.11	15.32	0.00

Comparative results of the measured data and the integrated model responses for the three validation load cases are provided in the form of bar plots. Included on all the plots are confidence bands that represent the range/spread of data for each variable. The measured data's confidence bands were determined using Table 9.1, while the confidence bands of the model results were resolved utilising the Monte Carlo method.

Figures 9.8 (a) to (c) show the integrated model's response for the total heat loads to the various heat exchangers for the 100%, 81% and 60% MCR loads.

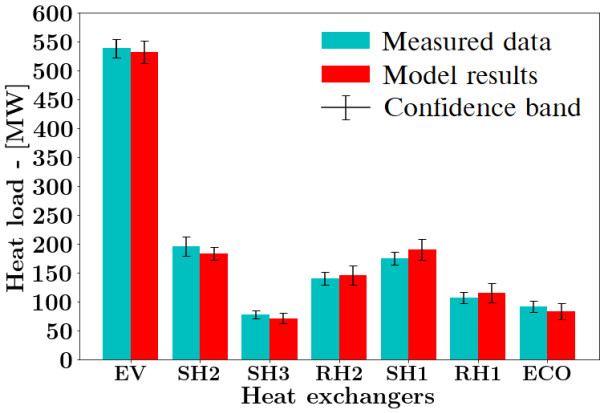

(a) 100% MCR

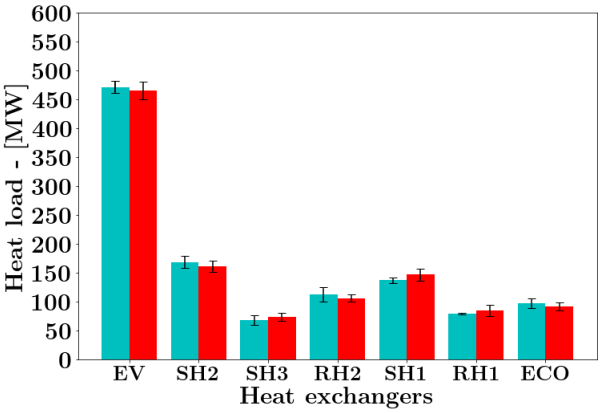

(b) 81% MCR

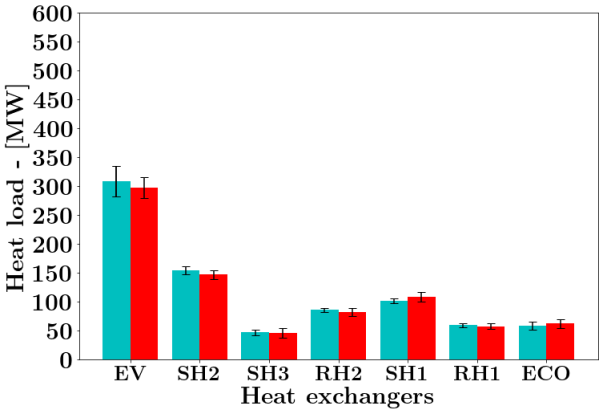

(c) 60% MCR

Figure 9.8: Load validation result comparison of the measured data and the integrated model results for the various heat exchangers

For the 100% MCR load, the integrated model under predicts the mean results of the heat loads in the radiative section (EV, SH2 and SH3) by a maximum of 4% (approximately 8 $[MW]$ for a mean SH2 heat load of 196 $[MW]$). Furthermore, the model over predicts the mean heat loads to the convective section (RH2 through EC) with a maximum deviation of 7% (approximately 10 $[MW]$ for a mean SH1 heat load of 175 $[MW]$). A similar trend is realised for 81% and 60% MCR loads, with the former showing an over prediction of 4% for the mean heat load to SH3. However, the associated uncertainty of the integrated model overlaps with the measured data uncertainty with minimal outliers. This implies that the model predictions are sufficiently accurate.

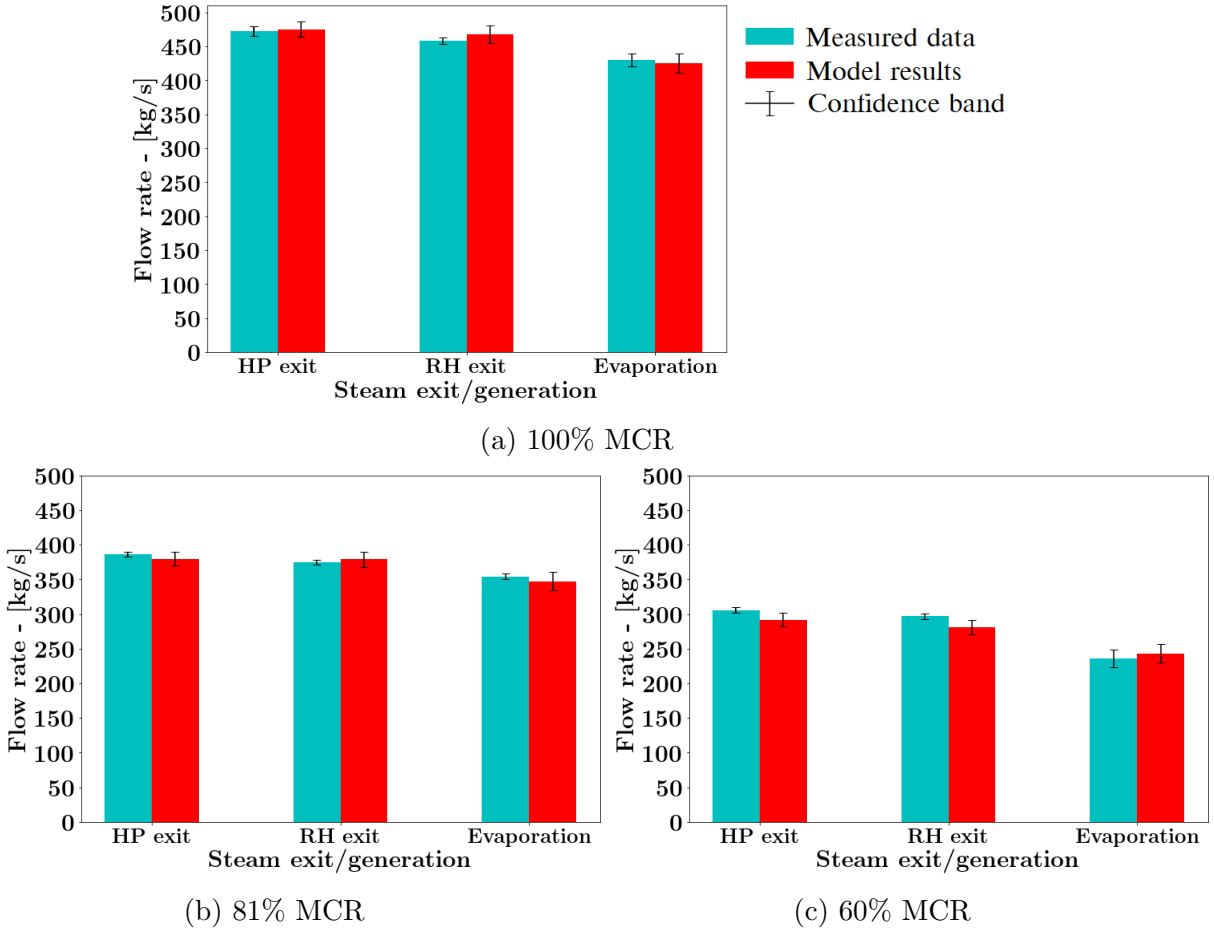

(a) 100% MCR

(b) 81% MCR

(c) 60% MCR

Figure 9.9: Load validation result comparison of the measured data and the integrated model results for the steam exit and steam generation flow rates

Figures 9.9 (a) to (c) highlight the steam exit flow rates at the HP and RH exits and the evaporation rate of steam in the EV walls. The integrated model is shown to sufficiently capture the hydraulic response of the case study boiler for a wide range of loads. The RH exit steam rates demonstrate the largest prediction errors for all three cases. The 60% MCR load under predicts the mean RH exit steam flow rate by a maximum error of 8% (approximately 28 $[kg/s]$ for a mean measured RH exit rate of 299 $[kg/s]$). In addition, the 100% MCR load over predicts the mean RH exit steam flow rate by a maximum error of 4% (approximately 22 $[kg/s]$ for a mean measured RH exit rate of 469$[kg/s]$). More uncertainty is associated with the integrated model, but this is deemed acceptable since the response overlaps with the measured data in all but one case, namely the 60% MCR cases HP and RH exit flow rates. The author believes this uncertainty can further be minimised by increasing the simulation data runs used to train the surrogate model.

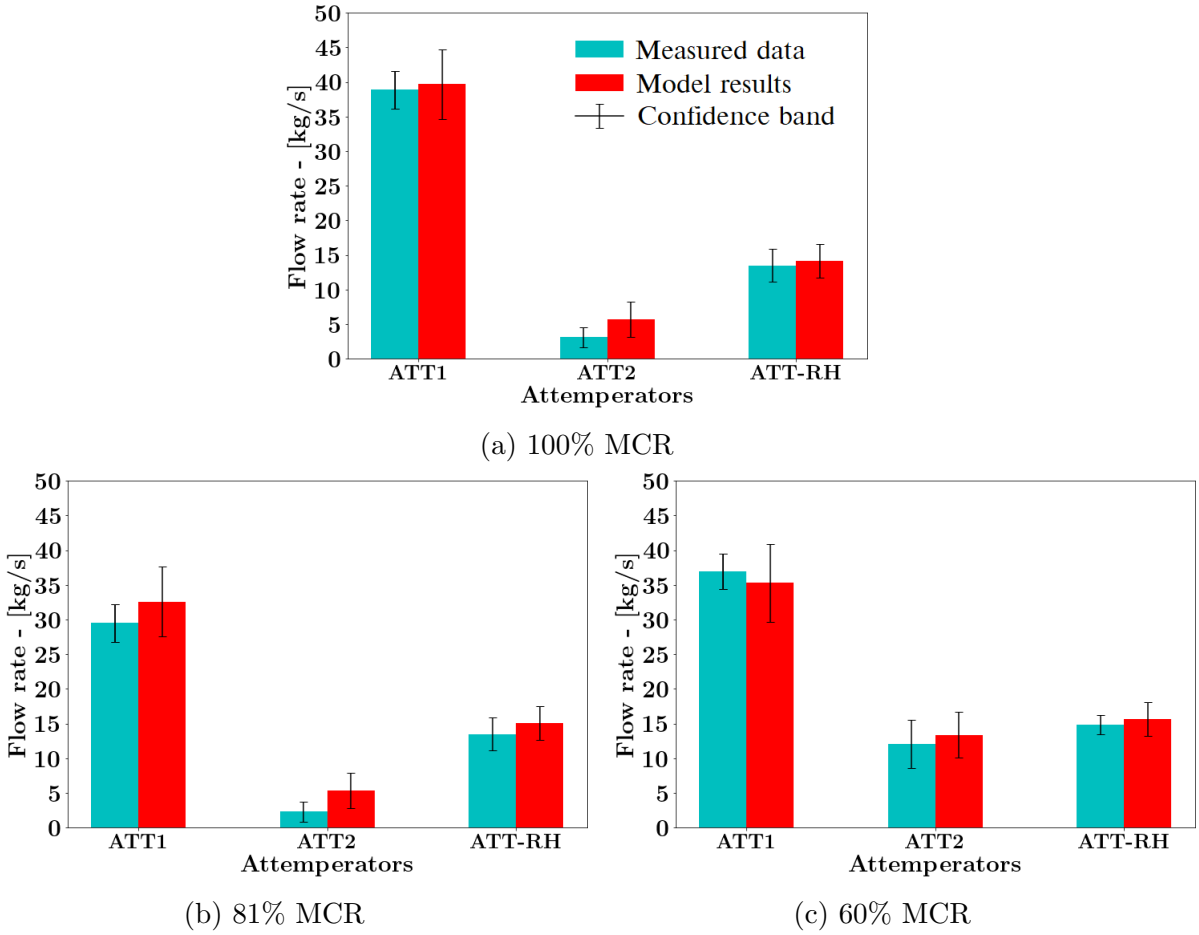

(a) 100% MCR

(b) 81% MCR

(c) 60% MCR

Figure 9.10: Load validation result comparison of the measured data and the integrated model results for the required attemperator flow rates to maintain operational integrity

Figure 9.10 (a-c) highlights the attemperator flow rates of ATT1, ATT2 and ATT-RH, which are injected into the steam lines as illustrated in Figure 9.2. The results of ATT1 show that the integrated model can capture the attemperator flow rate entering between SH1 and SH2 with adequate accuracy. However, the 81% MCR load tends to overpredict the mean ATT1 flow rate by 8%. Furthermore, the ATT1 flow rates demonstrate the largest uncertainty of the integrated model results, which all overlap with the measured data confidence bands. The attemperator ATT-RH, demonstrates sufficiently accurate results across all validation MCR loads.

Considering the results of ATT2, it is seen that for higher MCR loads (100% and 81%) the integrated model predicts a larger mean flow rate value, meaning the model tends to use more spray water to control the HP exit steam temperature. This anomaly is thought to arise from the thermal inertia of the SH3 pipe network due to the concentrated heat load additions of the integrated model, resulting in a higher average HP exit steam temperature. This anomaly was corrected by splitting ATT2 to feed spray water to feed each SH3 tube bank leg, as utilised in the utility boiler. This modelling improvement was incorporated for the entirety of the integrated model's high pressure attemperator system (SH1 through SH3, incorporating ATT1 and ATT2) of the 1-D process model. Figure 9.11 highlights the improved integrated model results for the 100% and 80% MCR loads.

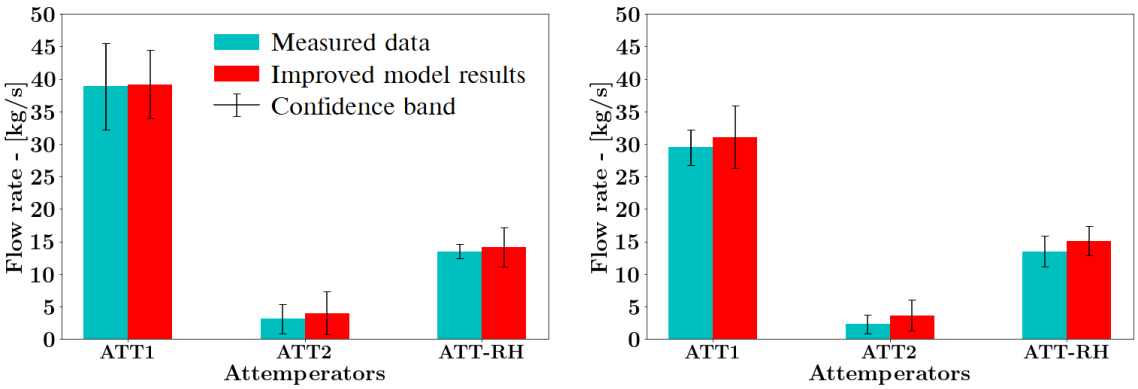

(a) 100% MCR (b) 81% MCR

Figure 9.11: Improved integrated modelling procedure attemperator results for (a) 100% and (b) 81% MCR loads

Using the improved integrated model, a reduction of the predicted mean values was achieved, namely a maximum over prediction of 150% was reduced to an over prediction of 10% as seen when comparing Figures 9.10 (b) and 9.11 (b). However, similar confidence bands were reported when using the improved integrated model for all MCR loads, highlighting the inherent uncertainty of the control systems utilising the attemperators. It has been shown that the integrated model can resolve the thermal response based on the predictions of the surrogate model for a wide range of loads with sufficient accuracy. The heat loads are within a 5% tolerance of the measured mean values, while the steam generation rates exhibit a maximum difference of 7%, which is seen in the 60% MCR load case (refer to Figure 9.9 (c)). The attemperator flow rate results show the most prominent uncertainty/confidence band of all the results (Figure 9.11). However, these overlap with the measured values in all but one case.

9.3 Off-design analysis using the integrated model

The following section demonstrates the application of the validated integrated model by investigating the impact of fuel quality on the overall plant performance. The fuel quality parameters that are varied are the ash (Y_{ASH}) and moisture (Y_{H_2O}) contents. As shown in Chapter 7, the energy content of the fuel (HHV) is a function of these fuel constituents, thus will be altered depending on the concentrations. Two case studies are considered to determine the impact that the varied fuel input parameters have on the boiler efficiency, heat pick-up and thermal response. The input vectors for the two fuel cases are provided in Table 9.2. All the inputs are the same as those of the 100% MCR load case except the ash, moisture, and HHV values for the respective fuels. Furthermore, the same mill biasing and fuel flow rate of the 100% MCR load were employed for the two off-design cases, which requires the maximum number of mills to be in service. Therefore, the 100% MCR reference case is used to show the effects that prolonged changes in the fuel quality will have on the boiler performance during operation.

As with the validation case studies of Section 9.2, the Monte Carlo method was employed to ascertain the mean and standard deviation (prediction uncertainty) values predicted via the integrated model. The integrated model predictions for the 100% case (refer to Figures 9.8 through 9.11 (a)) were used as the reference case for comparative purposes. Figure 9.12 (a) highlights the effects of poor-quality fuel on the heat load to the various heat exchangers, with a 20% drop observed on average, which can be expected since the energy content of the fuel is lower than that of the base case.

To maintain 100% load capabilities using poor quality fuel would require an increase in the fuel flow rate, which would provide more available energy content. For the high-ash case, an approximate increase of 42% of the mass flow rate of fuel is required to meet the steam generation energy needs. Similarly, the high-moisture case requires an approximate increase of 43% of the fuel mass flow rate. However, operational capacities of the mills are limited. Since operational protocol for the 100% load case uses five mills operating 30 of the 36 burners at full capacity, a standby mill and burner arrangement are placed in reserve to help mitigate operational risks, such as maintenance schedules and load changes. Using the standby mill would increase the fuel flow rate by a maximum of 17%. However, this would decrease the operational integrity and increase the associated risks. This situation would therefore imply an unwanted load loss.

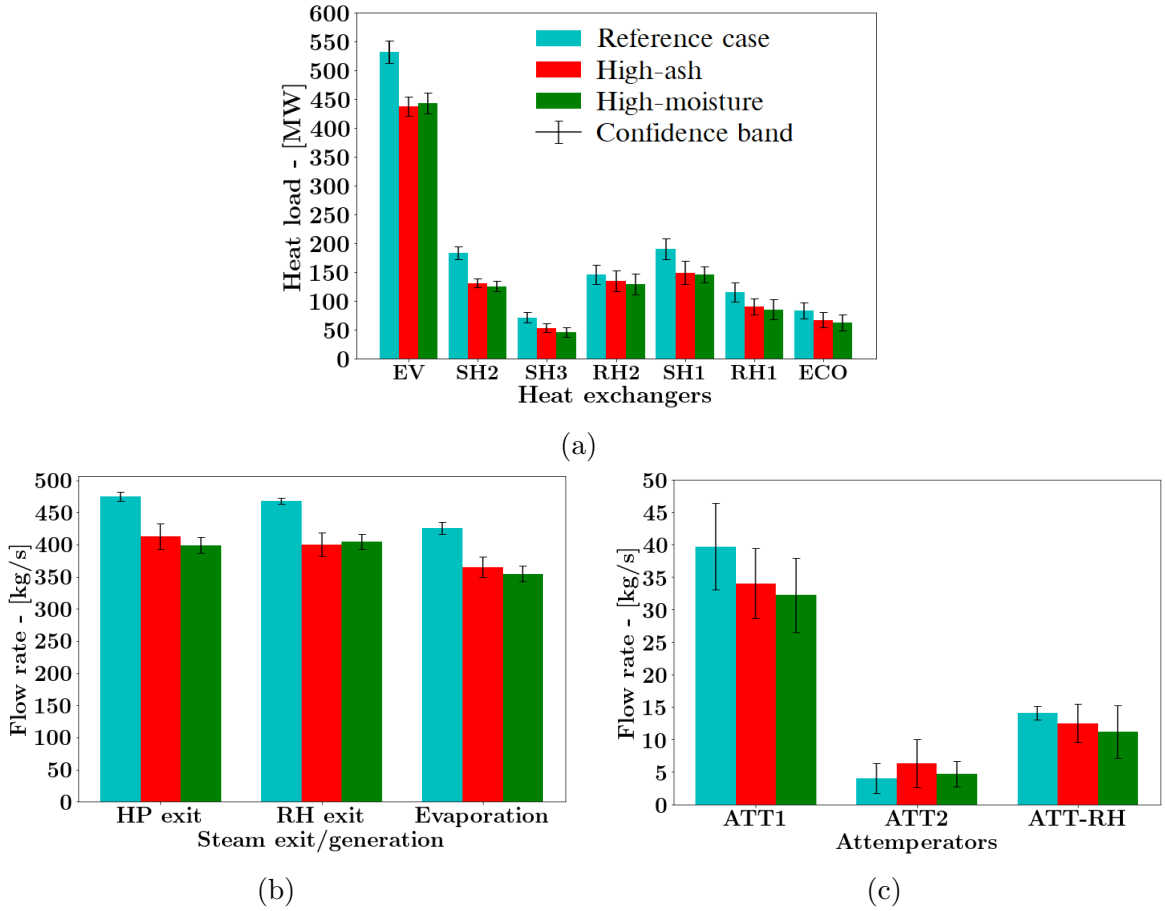

Figure 9.12: Integrated base model, high-ash, and high-moisture case study comparison for; (a) the various heat exchangers, (b) the steam exit and generation flow rates, and (c) the required attemperator flow rates to maintain operational integrity at 100% MCR

Figure 9.12 (b-c) similarly illustrates a decrease in the water/steam flow rates for the steam exit and attemperator conditions. The generation rates exhibit similar characteristics to the 80% load case of Figure 9.9 (b), illustrating a significant decrease in the operational capabilities when using a poor-quality fuel. The predicted flue gas temperatures entering the convective pass are shown in Table 9.3. It is shown that for an increase in the ash content of the fuel, the flue gas inlet temperature increases due to radiation attenuation, which results in a higher radiative heat transfer percentage for the convective pass components. This would lead to a higher attemperator flow rate as seen in Figure 9.12 (c). It is also interesting to note that a higher ash content results in the largest uncertainties in predicting the HP and RH exit steam and steam generation flow rates. The presence of more moisture in the fuel results in a lower inlet temperature, primarily since the extra moisture requires a higher rate of evaporation, leading to lower radiative heat transfer percentages.

Table 9.3: Model results for poor quality fuel characteristics

Variable - mean (*min*,*max*)	**Reference case**	**High-ash**	**High-moisture**
Boiler efficiency [%]	**88.2** (*75.6*, *91.2*)	**77.6** (*73.4*, *80.9*)	**75.9** (*69.8*, *78.3*)
SH3 exit plane flue gas temperature [K]	**1352** (*1339*, *1332*)	**1368** (*1354*, *1378*)	**1311** (*1295*, *1327*)
Radiative heat transfer percentage (Convective pass)			
RH2	**52.3** (*50.1*, *54.0*)	**56.2** (*52.9*, *58.5*)	**50.3** (*47.8*, *53.9*)
SH1	**46.3** (*43.0*, *49.2*)	**49.8** (*44.8*, *52.3*)	**47.2** (*43.2*, *50.8*)
RH1	**21.3** (*16.1*, *24.6*)	**26.7** (*20.6*, *30.1*)	**18.2** (*13.7*, *23.5*)
ECO	**6.7** (*5.1*, *9.8*)	**8.3** (*6.3*, *12.6*)	**5.4** (*2.8*, *9.7*)

The boiler efficiency is the measure used to convey how well the combustion heat is transferred to the working fluid and is defined as the ratio of the total amount of heat absorbed by the heat exchangers (i.e. sum of the furnace, radiative and convective pass heat loads) and the combustion energy released ($m_{fuel} \times HHV$). A significant decrease in the boiler efficiency is highlighted in Table 9.3 for both fuel cases, with the high-ash fuel showing a slightly better result. The drastic drop in boiler efficiency is primarily due to the drop in the HHV values used in the off-design fuel cases. The higher efficiency of the high-ash fuel is attributed to the heat loads of various heat exchangers being higher than that of the high-moisture fuel, which can be seen in Figure 9.12 (a).

9.4 Result summary for the validation and application case studies

The present work establishes the basis for utilising an integrated data-driven surrogate and 1-D process model to investigate the overall operational response for a 620 [MW_e] utility-scale boiler. The data-driven surrogate modelling approach using CFD simulations can predict the parameters needed to capture the combustion and heat transfer characteristics. These include the heat loads to the furnace evaporator walls (EV) and radiative superheaters (SH2 and SH3), as well as the flue gas characteristics entering the convective pass (i.e., SH3 exit plane), which include the temperatures, species mass fractions and radiation intensity flux.

A validation case study was performed using the integrated model for various operational loads. The model results were compared to the measured thermal response for all load cases. The resolution of the heat loads, steam flow rates and attemperator flow rates resulted in a maximum difference of 8%. In addition, the uncertainties predicted by the surrogate model were propagated through the integrated model using the Monte Carlo method, adding valuable insight into the operational limits of the power plant and the uncertainties associated with it. In addition, improvements to the 1-D process model of the integrated model were incorporated to accurately model the utility boilers attemperator control system.

The application case studies considered the impact of poor-quality fuels at 100% MCR operation. The results highlight the drop in performance due to the fuel quality resulting in a decrease of the boiler efficiency and the decrease in potential generation capability. Using a high-ash fuel can result in higher exit flue gas temperatures, resulting in a marginal increase in the performance of the convective pass heat exchangers compared to the high-moisture fuel. Although these trends are well-known and do not provide new insights into boiler performance in general, it demonstrates the ability of the proposed methodology to provide practical results. In addition, it shows that there is in greater uncertainty in the predicted steam exit and generation flow rates and increases the likelihood of ash deposition due to the increased ash loading.

The current work has shown that it is possible to adequately resolve the thermofluid response of a utility-scale boiler using a data-driven surrogate model trained on CFD simulation results. Integrating the surrogate and 1-D process models is paramount in modelling the thermal response and provides valuable operational insight for various load cases, including the uncertainty in the predicted results. Furthermore, engineers and other researchers can apply the methodology used in the present work to investigate various effects on the whole boiler operation. In addition, the developed methodology laid out in this thesis is not limited to subcritical boiler applications and can be used to model supercritical and ultra-supercritical boilers, provided the CFD modelling is adapted for supercritical applications. Since, the 1-D process modelling approach can handle a shift of the steam properties to the supercritical region using the implemented two-phase mixture approach.

Concluding remarks

Chapter 10

Summary, conclusions, and recommendations

The chapter presents a summary of the research as well as the conclusions and recommendations for future work.

10.1 Summary and conclusions

The primary aim of the research project was the development of a co-simulation methodology that combines the use of a data-driven surrogate model and a 1-D process model to investigate the flexible and low-load operating conditions of a subcritical CFPP boiler. The data-driven surrogate model was developed using machine learning techniques which required the development of a reduced order CFD approach to establish a CFD solution database. This database was subsequently used to train and test the data-driven surrogate model.

The reduced order CFD modelling methodology was initially validated using a 2.165 $[MW_{th}]$ lab-scale swirl burner. Following this, was the validation and application of the reduced order CFD model on a 620 $[MW_e]$ utility-scale boiler, which was used as the primary boiler for further application when utilising the integrated model. The reduced order CFD approach could adequately capture the 3-D spatial effects of combustion, fluid flow and heat transfer in a computationally efficient manner when compared to conventional CFD approaches. Part of the motivation behind the research was to address the long simulation times and the computational burden associated with the use of CFD in conventional coupled simulation approaches. The integration of the surrogate model and a 1-D process model demonstrated and resulted in significantly faster simulation times with a reduced computational burden when compared to conventional co-simulation modelling approaches. The integrated model development and application illustrated that an efficient and fast co-simulation modelling methodology can be developed to investigate the thermofluid performance of a CFPP at low-load and off-design conditions.

The subsequent sections provide detailed summaries and findings pertaining to the development of the reduced order CFD model, as well as the development of the integrated model.

Part I - Reduced order CFD model development

Part 1 of the thesis focussed on establishing the reduced order CFD modelling methodology. A complete theoretical background was provided in Chapter 3, covering the 3-D CFD conservation equations, conventional particle transport modelling, an overview of combustion modelling including both heterogeneous and homogeneous reactions, the relevant radiative heat transfer approaches, and the fundamentals of the 1-D process modelling techniques.

In Chapter 4, the numerical modelling techniques, assumptions, and the validation of the approach were presented. The multiphase modelling technique required a novel approach to establish a non-thermal equilibrium Eulerian-Eulerian modelling methodology. The developed methodology was able to adequately resolve the following phenomena: the momentum interactions between the continuous and particulate phases, the transport of particulate phase through the domain, the sequential particulate combustion processes, and the resolution of the radiative transport in the computational domain. User-defined functions were developed and linked into ANSYS Fluent® v19.5 to implement the multiphase approach in the CFD solver. Validation was conducted using a well-documented 2.165 $[MW_{th}]$ lab-scale swirl burner. Detailed measurement data and conventional Eulerian-Lagrangian CFD model results were used to showcase the accuracy and computational efficiency of the developed CFD model. The geometry and flow simulation setup were discussed, and the results were presented. The results of the validation case study showed relative errors in the range of 0.2% to 5% for the key parameters identified in the study. Key parameters included the heat load distributions to the furnace wall, the temperature fields, the radiative intensity distributions, and the flue gas composition used to demonstrate the combustion modelling effectiveness.

In addition, low-load simulations were conducted, with validation data obtained from Eulerian-Lagrangian simulations. The results showed that the modelling methodology could resolve the burner-level flow, species, temperature profiles, and wall flux distributions in the burner domain with sufficient accuracy. Furthermore, including particle effects in the radiation and energy transport proved beneficial in implementing the combustion laws, thereby illustrating the importance of the thermal non-equilibrium assumption. The computational speed enhancement between the traditional modelling methodology and the developed reduced order CFD model showed a 50% speed-up.

The reduced order CFD model was further utilised in modelling the primary boiler under investigation, namely a subcritical 620 $[MW_e]$ two-pass utility-scale power boiler which was presented in Chapter 5. Validation of the developed CFD model included a comparison of results obtained via a numerical model using the conventional Eulerian-Lagrangian approach and, where applicable, measured site data. The relative errors of the key parameters ranged from 2 to 8%, with a computational speed-up of 30%.

Furthermore, a coupled CFD to 1-D process model, which utilised the reduced order CFD model, was developed to investigate the burner firing arrangements of the 620 $[MW_e]$ boiler operating at a load of 32% MCR load. Six cases were considered, with the best arrangement resulting in the optimal flame ball position, the maximum boiler utilisation efficiency, and a minimised carbon monoxide concentration distribution throughout the domain, negating the risk of fire-side corrosion occurring at continuous low-load operation.

The findings of Part 1 aided in meeting the research objectives one and two discussed in Chapter 1. Namely, to investigate the complexity reduction that can be achieved via using a pseudo Lagrangian model (i.e. multiphase model) of the fuel particles and, secondly, to validate the developed model against experimental and measured data in the form of case studies. Furthermore, the developed model showed a significant computational speed-up of the CFD simulation time with a reduction in the computational burden while maintaining sufficient accuracy of the key parameters. Finally, the methodology was developed and implemented using the ANSYS Fluent® v19.5 commercial software package, as opposed to an in-house academic or proprietary code, allowing it to be employed in industry to develop similar computationally inexpensive models for pulverised fuel systems.

Part II - Integrated model development

Using the validated reduced order CFD modelling methodology discussed in Chapters 4 and 5, the development of the surrogate model could commence. The surrogate model was developed to adequately capture the heat loads to the furnace evaporator walls, the radiative superheater walls, and the thermodynamic state of the flue gas entering the convective section.

The relevant theory pertaining to machine learning techniques used in the development of the data-driven surrogate model was discussed in Chapter 6, which covered the use of MLP and MDN machine learning approaches. Chapter 7 highlighted the generation of CFD solution data using random samples of the high-level inputs. In total, 14 high-level operational inputs were identified that can capture a wide range of operating conditions. The random samples were used to create 180 unique CFD simulation cases, which were solved to convergence. For each CFD simulation, 23 output parameters were stored. Furthermore, an exploratory data analysis was conducted on the output data to identify any data irregularities and investigate underlying data trends between the output parameters. The generated high-level and output datasets were subsequently used to train and test the various machine learning techniques.

In Chapter 8, the optimal neural network architecture of the surrogate model was selected by conducting a hyperparameter search. For this, multiple MLP and MDN machine learning models were created using a hyperparameter search space that considered the following: the number of hidden layers, the number of neurons per layer, the learning rate, the batch size, and specifically for the MDN model the number of distributions. Increasing the number of hidden layers and neurons per layer improved the flexibility of the model allowing for a better fit of the training and testing data. A threshold of four hidden layers with 80 neurons per layer provided the optimal data fitting with minimal MAE and RMSE values.

Investigating the other hyperparameters resulted in a learning rate of 1×10^{-5}, and a batch size of 32 was selected, which aided in lowering the training and testing data generalisation error and improving stability. In addition, to capture the probabilistic characteristics of the MDN model a set of three distributions was selected. The MDN produced the best performing machine learning model when compared to a MLP network of a similar architecture. Furthermore, the MDN has the added benefit of producing the mean and associated standard deviation values for the output parameters, allowing for the uncertainty of the predictions to be propagated through the entire integrated model.

Utilising the knowledge gained in creating a coupled CFD to 1-D process model proved invaluable when integrating the surrogate model with a 1-D process model. Open-source software, namely Python, was used to integrate the surrogate and 1-D process model using an application programming interface, which was readily available in the 1-D process modelling software Flownex SE®. In Chapter 9, the integrated model was used to capture and investigate the thermofluid performance of the utility-scale boiler.

A validation case study was conducted for MCR loads of 100%, 81% and 60%. The integrated model predicted heat loads within 5% of the measured mean values, and resolved the thermofluid performance based on the predictions of the MDN surrogate model with sufficient accuracy. The steam generation rates exhibited a maximum error of 7%, while the attemperator flow rate results showed the most prominent uncertainty. However, these overlapped with the measured values in all but one case. Furthermore, the uncertainties predicted by the surrogate model were propagated through the integrated model using the Monte Carlo technique, adding valuable insight into the operational limits of the power plant and the uncertainties associated with it.

An application study was then conducted using the integrated model. It investigated the effects of fuel quality on the boiler performance at 100% MCR load. The results highlighted a significant drop in performance due to the fuel quality, leading to a decrease in the operational boiler efficiency. To increase the operational performance would require an increase in the fuel flow rate, which would provide more available energy content. However, the operational capacities of the mills are limited, which limits the ability of the boiler to meet the 100% MCR load. This would therefore result in a load loss with the boiler operating at a lower MCR load. Although the application case study did not provide new insights into boiler performance in general, it demonstrated the ability of the proposed methodology to provide practical results.

The outcome of Part 2 assisted with meeting the final three research objectives highlighted in Chapter 1. Firstly, utilising the reduced order CFD model of Part 1 to generate a CFD simulated database. Secondly, developing an optimal data-driven surrogate model employing the CFD simulated database, that can report the necessary heat loads, temperature profiles and the thermodynamic state of the flue gas for the primary utility-scale boiler. Finally, an integrated model incorporating the data-driven surrogate model and a 1-D process model of the water/steam network was validated and utilised to investigate the effects of fuel quality on the thermofluid performance of the boiler. Comparing the computational benefits of using the integrated surrogate model to the coupled modelling approach illustrated in Chapter 5, it was found that the integrated model significantly reduced the computational time required.

10.2 Recommendations for future work

The modelling methodology developed in this study further adds to the research focused on studying the flexibility of large, pulverised fuel power plants. The following research could be further investigated:

- Utilising the final integrated model to develop a plant operator training tool. Such a tool would be valuable for current plant operators to investigate, in a computationally efficient manner, the flexible operational limits, operational safety, and the operating behaviour during malfunctions of the boiler.
- The final integrated model was validated for multiple steady-state MCR load cases. The subsequent step is to incorporate the final integrated model in the application to investigate transient events, such as start-up and shut-down procedures. The integrated model would be suitable for these applications due to the fast simulation times and the minimal operational inputs required to resolve the furnaces fire-side interactions. The data-driven surrogate model would be used in a quasi steady state manner while the 1-D process model can be fully transient. Having the ability to investigate the boiler performance during start-up and shut-down procedures would allow plant operators to put in place operational protocols that can ensure safe operation.
- Further addition of components, such as the steam turbines and feedwater heaters to the 1-D process model would prove beneficial in creating a complete power plant model. This would enable the investigation of the effects load changes and malfunctions have on other critical power plant components.

References

[1] Y.A. Cengel and M.A. Boles. *Thermodynamics: An Engineering Approach.* 8th ed. McGraw-Hill, 2015.

[2] B. Matek and K. Gawell. "The benefits of baseload renewables: A misunderstood energy technology". In: *Electricity Journal* 28.2 (2015), pp. 101–112.

[3] K. Ratshomo and R. Nembahe. *The South African Energy Sector Report 2019.* Tech. rep. Pretoria, 2019, pp. 8–10.

[4] A. Rubino, A. Sapio, and M. La Scala, eds. *Handbook of Eenergy Economics and Policy, Fundamentals and Applications for Engineers and Energy Planners.* Vol. 1. London: Academic Press, 2021.

[5] M.A. Gonzalez-Salazar, T. Kirsten, and L. Prchlik. "Review of the operational flexibility and emissions of gas- and coal-fired power plants in a future with growing renewables". In: *Renewable and Sustainable Energy Reviews* 82.July 2017 (2018), pp. 1497–1513.

[6] N. Modliński, K. Szczepanek, D. Nabagło, P. Madejski, and Z. Modliński. "Mathematical procedure for predicting tube metal temperature in the second stage reheater of the operating flexibly steam boiler". In: *Applied Thermal Engineering* 146.October 2018 (2019), pp. 854–865.

[7] R. Laubscher and P.G. Rousseau. "CFD study of pulverized coal-fired boiler evaporator and radiant superheaters at varying loads". In: *Applied Thermal Engineering* 160 (2019).

[8] G. Sankar, D. Santhosh Kumar, and K.R. Balasubramanian. "Computational modeling of pulverized coal fired boilers – A review on the current position". In: *Fuel* 236.April 2018 (2019), pp. 643–665.

[9] E. Oko and M. Wang. "Dynamic modelling, validation and analysis of coal-fired subcritical power plant". In: *Fuel* 135 (2014), pp. 292–300.

[10] F. Alobaid, N. Mertens, R. Starkloff, T. Lanz, C. Heinze, and B. Epple. "Progress in dynamic simulation of thermal power plants". In: *Progress in Energy and Combustion Science* 59 (2017), pp. 79–162.

[11] R. Laubscher and P.G. Rousseau. "An integrated approach to predict scalar fields of a simulated turbulent jet diffusion flame using multiple fully connected variational autoencoders and MLP networks". In: *Applied Soft Computing* 101 (2021), p. 107074.

[12] V.V. Ranade and D.F. Gupta. *Computational Modeling of Pulverized Coal Fired Boilers.* CRC Press, Taylor & Francis Group, 2015.

[13] R. Laubscher and P.G. Rousseau. "Numerical investigation into the effect of burner swirl direction on furnace and superheater heat absorption for a 620 MWe opposing wall-fired pulverized coal boiler". In: *International Journal of Heat and Mass Transfer* 137 (2019), pp. 506–522.

[14] J. Gu, Q. Liu, W. Zhong, and A. Yu. "Study on scale-up characteristics of oxy-fuel combustion in circulating fluidized bed boiler by 3D CFD simulation". In: *Advanced Powder Technology* 31.5 (2020), pp. 2136–2151.

[15] Y. Du, C. Wang, Q. Lv, D. Li, H. Liu, and D. Che. "CFD investigation on combustion and NOx emission characteristics in a 600 MW wall-fired boiler under high temperature and strong reducing atmosphere". In: *Applied Thermal Engineering* 126.x (2017), pp. 407–418.

[16] J. Fan, L. Qian, Y. Ma, P. Sun, and K. Cen. "Computational modeling of pulverized coal combustion processes in tangentially fired furnaces". In: *Chemical Engineering Journal* 81.1-3 (2001), pp. 261–269.

[17] X. Liu, J. Zhang, H. Tan, Q. Mo, X. Wang, and Y. Wang. "Numerical and experimental study on co-firing of low volatile coal in a 330 MW tangentially fired boiler". In: *Journal of the Energy Institute* 96.x (2021), pp. 242–250.

[18] S. Chen, B. He, D. He, Y. Cao, G. Ding, X. Liu, Z. Duan, X. Zhang, J. Song, and X. Li. "Numerical investigations on different tangential arrangements of burners for a 600 MW utility boiler". In: *Energy* 122.x (2017), pp. 287–300.

[19] B. He, L. Zhu, J. Wang, S. Liu, B. Liu, Y. Cui, L. Wang, and G. Wei. "Computational fluid dynamics based retrofits to reheater panel overheating of No. 3 boiler of Dagang Power Plant". In: *Computers and Fluids* 36.2 (2007), pp. 435–444.

[20] H.K. Versteeg and W. Malalasekera. *Introduction to Computational Fluid Dynamics, The finite volume method*. Second. Pearson Prentice Hall, 2007.

[21] *ANSYS Fluent Theory Guide*. 20th ed. Ansys Inc., 2021.

[22] H. Wang, C. Zhang, and X. Liu. "Heat transfer calculation methods in three-dimensional CFD model for pulverized coal-fired boilers". In: *Applied Thermal Engineering* 166.135 (2020), p. 114633.

[23] A. Dugum and K. Hanjalić. "Numerical simulation of coal-air mixture flow in a real double-swirl burner and implications on combustion anomalies in a utility boiler". In: *Energy* 170 (2019), pp. 942–953.

[24] S.C Stultz J.B.Kitto, ed. *Steam its generation and use*. 41st ed. Barberton, Ohio, USA, 2005.

[25] P.G. Rousseau and R. Laubscher. "Analysis of the impact of coal quality on the heat transfer distribution in a high-ash pulverized coal boiler using co-simulation". In: *Energy* 198 (2020), p. 117343.

[26] F.C. Lockwood, S.M.A. Rizvi, and N.G. Shah. "Comparative predictive experience of coal firing". In: *Proceedings of the Institution of Mechanical Engineers* 200 (1986), pp. 79–87.

[27] C. Yin. "On gas and particle radiation in pulverized fuel combustion furnaces". In: *Applied Energy* 157 (2015), pp. 554–561.

[28] C. Yin and J. Yan. "Oxy-fuel combustion of pulverized fuels : Combustion fundamentals and modeling". In: *Applied Energy* 162 (2016), pp. 742–762.

[29] R. Laubscher and P.G. Rousseau. "Numerical investigation on the impact of variable particle radiation properties on the heat transfer in high ash pulverized coal boiler through co-simulation". In: *Energy* 195 (2020), p. 117006.

[30] R. Jeffrey, R. Falcon, and A. Kinghorn. "The benefits and challenges associated with coal in South Africa". In: *Cornerstone* 2.3 (2014), pp. 66–70.

[31] Y. Jiang, B. Lee, D. Oh, and C. Jeon. "Optimization of operating conditions to achieve combustion stability and reduce NOx emission at half-load for a 550-MW tangentially fired pulverized coal boiler". In: *Fuel* 306.February (2021), p. 121727.

[32] S. Belošević, I. Tomanović, N. Crnomarković, and A. Milićević. "Full-scale CFD investigation of gas-particle flow, interactions and combustion in tangentially fired pulverized coal furnace". In: *Energy* 179 (2019).

[33] B. Hernik and W. Zabłocki. "Numerical research of combustion with a minimum boiler load". In: *Archives of Thermodynamics* 41.4 (2020), pp. 93–114.

[34] J. Chang, X. Wang, Z. Zhou, H. Chen, and Y. Niu. "CFD modeling of hydrodynamics, combustion and NOx emission in a tangentially fired pulverized-coal boiler at low load operating conditions". In: *Advanced Powder Technology* 32.2 (2021), pp. 290–303.

[35] H. Knaus, U. Schnell, and R.G.H. Klaus. "On the modelling of coal combustion in a 550MWe coal fired utility boiler". In: *Progress in Computational Fluid Dynamics* 1 (2001), pp. 194–207.

[36] A.C. Benim, B. Epple, and B. Krohmer. "Modelling of pulverised coal combustion by a Eulerian-Eulerian two-phase flow formulation". In: *Progress in Computational Fluid Dynamics* 5.6 (2005), pp. 345–361.

[37] J. Cai, M. Handa, and M.F. Modest. "Eulerian-Eulerian multi-fluid methods for pulverized coal flames with nongray radiation". In: *Combustion and Flame* 162.4 (2015), pp. 1550–1565.

[38] L.X. Zhou, Y.C. Guo, and W.Y. Lin. "Two-fluid models for simulating reacting gas-particle flows, coal combustion and NOX formation". In: *Combustion science and technology* 150.1 (2000), pp. 161–180.

[39] *Advanced Process Simulation Software - APROS*.

[40] R. Starkloff, F. Alobaid, K. Karner, B. Epple, M. Schmitz, and F. Boehm. "Development and validation of a dynamic simulation model for a large coal-fired power plant". In: *Applied Thermal Engineering* 91 (2015), pp. 496–506.

[41] J. Kuronen, M. Hotti, and S. Tuuri. "Modelling and Dynamic Simulation of Cyclically Operated Pulverized Coal-Fired Power Plant". In: *Proceedings of The 9th EUROSIM Congress on Modelling and Simulation, EUROSIM 2016, The 57th SIMS Conference on Simulation and Modelling SIMS 2016* 142 (2018), pp. 122–128.

[42] S. Kakac. *Boilers, Evaporators, and Condensers*. Wiley Interscience, 1991.

[43] K. Deng, C. Yang, H. Chen, N. Zhou, and S. Huang. "Start-Up and dynamic processes simulation of supercritical once-through boiler". In: *Applied Thermal Engineering* (2017).

[44] H. Hajebzadeh, A.N.M. Ansari, and S. Niazi. "Mathematical modeling and validation of a 320 MW tangentially fired boiler: A case study". In: *Applied Thermal Engineering* 146.September 2018 (2019), pp. 232–242.

[45] S.A. Filimonov, E.I. Mikhienkova, A.A. Dekterev, and D.V. Boykov. "Hybrid methods for simulating hydrodynamics and heat transfer in multiscale (1D-3D) models". In: *Journal of Physics: Conference Series* 899.5 (2017).

[46] C. Schuhbauer, M. Angerer, H. Spliethoff, F. Kluger, and H. Tschaffon. "Coupled simulation of a tangentially hard coal fired 700°C boiler". In: *Fuel* 122.January (2014), pp. 149–163.

[47] H.Y. Park, M. Faulkner, M.D. Turrell, P.J. Stopford, and D.S. Kang. "Coupled fluid dynamics and whole plant simulation of coal combustion in a tangentially-fired boiler". In: *Fuel* 89.8 (2010), pp. 2001–2010.

[48] C. Yu, W. Xiong, H. Ma, J. Zhou, F. Si, X. Jiang, and X. Fang. "Numerical investigation of combustion optimization in a tangential firing boiler considering steam tube overheating". In: *Applied Thermal Engineering* 154.2 (2019), pp. 87–101.

[49] V. Hovi, M. Huttunen, I. Karppinen, T. Pättikangas, H. Niemistö, L. Karvonen, Si. Kallio, S. Tuuri, and V. Ylä-Outinen. "Integrated transient simulation of a BFB boiler with CFD models for the BFB furnace and dynamic system models for the steam cycle and boiler operation". In: *Energy Procedia* 120 (2017), pp. 508–515.

[50] J.I. Glaser, A.S. Benjamin, R. Farhoodi, and K.P. Kording. "The roles of supervised machine learning in systems neuroscience". In: *Progress in Neurobiology* 175.February (2019), pp. 126–137.

[51] I. Bilgen, G. Guvercin, and I. Rekik. "Machine learning methods for brain network classification: Application to autism diagnosis using cortical morphological networks". In: *Journal of Neuroscience Methods* 343.May (2020), p. 108799.

[52] D.J. Lary, A.H. Alavi, A.H. Gandomi, and A.L. Walker. "Machine learning in geosciences and remote sensing". In: *Geoscience Frontiers* 7.1 (2016), pp. 3–10.

[53] A.J.C. Witsil and J.B. Johnson. "Volcano video data characterized and classified using computer vision and machine learning algorithms". In: *Geoscience Frontiers* 11.5 (2020), pp. 1789–1803.

[54] L. Gan, H. Wang, and Z. Yang. "Machine learning solutions to challenges in finance: An application to the pricing of financial products". In: *Technological Forecasting and Social Change* 153.January (2020), p. 119928.

[55] M.R. Kumar, V. Deeban Chakravarthy, T.N. Ranganatham, and K. Ramana. "Personal finance transaction index scoring using machine learning model". In: *Materials Today: Proceedings* xxxx (2021).

[56] D. Ireri, E. Belal, C. Okinda, N. Makange, and C. Ji. "A computer vision system for defect discrimination and grading in tomatoes using machine learning and image processing". In: *Artificial Intelligence in Agriculture* 2 (2019), pp. 28–37.

[57] A. Rohani, M. Taki, and G. Bahrami. "Application of artificial intelligence for separation of live and dead rainbow trout fish eggs". In: *Artificial Intelligence in Agriculture* 1 (2019), pp. 27–34.

[58] S.A. Kalogirou. "Applications of artificial neural-networks for energy systems". In: *Applied Energy* 67.1-2 (2000), pp. 17–35.

[59] B. Muller and H. Keller. "Neural networks for combustion process modelling." In: *Proceedings of the International Conference on Engineering Applications of Neural Networks (EANN'96)*. London, 1996, pp. 87–90.

[60] Y. Fei, S. Black, J. Szuhánszki, L. Ma, D.B. Ingham, P.J. Stanger, and M. Pourkashanian. "Evaluation of the potential of retrofitting a coal power plant to oxy-firing using CFD and process co-simulation". In: *Fuel Processing Technology* 131 (2015), pp. 45–58.

[61] R. Raidoo and R. Laubscher. "Data-driven forecasting with model uncertainty of utility-scale air-cooled condenser performance using ensemble encoder-decoder mixture-density recurrent neural networks". In: *Energy* 238 (2022), p. 122030.

[62] R. Laubscher. "Time-series forecasting of coal-fired power plant reheater metal temperatures using encoder-decoder recurrent neural networks". In: *Energy* 189 (2019), p. 116187.

[63] X.J. Liu, X.B. Kong, G.L. Hou, and J.H. Wang. "Modeling of a 1000 MW power plant ultra super-critical boiler system using fuzzy-neural network methods". In: *Energy Conversion and Management* 65 (2013), pp. 518–527.

[64] R.A. Haffejee and R. Laubscher. "Application of machine learning to develop a real-time air-cooled condenser monitoring platform using thermofluid simulation data". In: *Energy and AI* 3 (2021), p. 100048.

[65] S. Singh and H. Abbassi. "1D/3D transient HVAC thermal modeling of an off-highway machinery cabin using CFD-ANN hybrid method". In: *Applied Thermal Engineering* 135.January (2018), pp. 406–417.

[66] A. Warey, S. Kaushik, B. Khalighi, M. Cruse, and G. Venkatesan. "Data-driven prediction of vehicle cabin thermal comfort: using machine learning and high-fidelity simulation results". In: *International Journal of Heat and Mass Transfer* 148 (2020), p. 119083.

[67] P. Madejski. "Numerical study of a large-scale pulverized coal-fired boiler operation using CFD modeling based on the probability density function method". In: *Applied Thermal Engineering* 145.July (2018), pp. 352–363.

[68] D.K. Sarkar. *THERMAL POWER PLANT Design and Operation*. Amsterdam: Elsevier Inc., 2015.

[69] C. Lu, J. Wang, and R. Yan. "Multi-objective optimization of combined cooling, heating and power system considering the collaboration of thermal energy storage with load uncertainties". In: *Journal of Energy Storage* 40.May (2021), p. 102819.

[70] P.J. Linstrom and W.G. Mallard, eds. *NIST Chemistry WebBook, NIST Standard Reference Database Number 69*. Gaithersburg MD.

[71] T. Poinsot and D. Veynante. *Theoretical and Numerical Combustion*. Second. Edwards, 2005.

[72] S. Echi, A. Bouabidi, Z. Driss, and M.S. Abid. "CFD simulation and optimization of industrial boiler". In: *Energy* 169 (2019), pp. 105–114.

[73] T.H. Shih, W.W. Liou, A. Shabbir, Z. Wang, and J. Zhu. "A new k-epsilon eddy viscosity model for high reynolds number turbulent flows". In: *Computers and fluids* 24.3 (1995).

[74] J.O. Hinze. *Turbulence*. 2nd. McGraw-Hill, 1975.

[75] A.D. Gosman and E. Ioannides. "Aspects of Computer Simulation of Liquid-Fuelled Combustors." In: *AIAA Paper* 7.6 (1981), pp. 482–490.

[76] S.A. Morsi and A.J. Alexander. "An investigation of particle trajectories in two-phase flow systems". In: *Journal of Fluid Mechanics* 55.2 (1972), pp. 193–208.

[77] M. Farokhi and M. Birouk. "Application of Eddy Dissipation Concept for Modeling Biomass Combustion, Part 1: Assessment of the Model Coefficients". In: *Energy and Fuels* 30.12 (2016), pp. 10789–10799.

[78] M.M. Baum and P.J. Street. "Predicting the Combustion Behaviour of Coal Particles Predicting the Combustion Behaviour of Coal Particles". In: *Combustion Science and Technology* 3 (1971), pp. 231–243.

[79] R.K. Boyd and J.H. Kent. "Three dimensional furnace computer modelling". In: *Twenty-first Symposium (International) on Combustion/The Combustion Institute* 21.1 (1986), pp. 265–274.

[80] B.F. Magnussen. "On the structure of turbulence and a generalized eddy dissipation concept for chemical reactions in trubulent fow." In: *AIAA Aerospace Science Meeting* 19 (1981).

[81] J.M. Heikkinen, B.C.H. Venneker, G. di Nola, W. de Jong, and H. Spliethoff. "CFD simulation and experimental validation of co-combustion of chicken litter and MBM with pulverized coal in a flow reactor". In: *Fuel Processing Technology* 89.9 (2008).

[82] M. Rehm, P. Seifert, and B. Meyer. "Theoretical and numerical investigation on the EDC-model for turbulence-chemistry interaction at gasification conditions". In: *Computers and Chemical Engineering* 33.2 (2009), pp. 402–407.

[83] M. von Bohnstein, M. Richter, P. Graeser, M. Schiemann, J. Ströhle, and B. Epple. "3D CFD simulation of a 250 MWel oxy-fuel boiler with evaluation of heat radiation calculation". In: *Renewable and Sustainable Energy Reviews* 137.December 2019 (2021).

[84] B.F. Magnussen and B.H. Hjertager. "On mathematical modeling of turbulent combustion with special emphasis on soot formation and combustion". In: *16th Symposium (International) on Combustion, Combustion Institute* (1976).

[85] D.B. Spalding. "Mixing and Chemical Reaction in Steady Confined Turbulent Flames". In: *Symposium (International) on Combustion* 13.1 (1970).

[86] Y.A. Cengel and A.J. Ghajar. *Heat and Mass Transfer, Fundamentals & Applications*. 5th. New York: McGraw-Hill Education, 2015.

[87] M.F. Modest. *Radiative Heat Transfer*. Third. Kidlington, Oxford, U.K.: Academic Press, 2013.

[88] M.F. Modest. *Radiative Heat Transfer*. Second. Burlington, MA, USA: Academic Press, 2003.

[89] R. Siegel and J.R. Howell. *Thermal Radiation Heat Transfer*. New Yory: Taylor & Francis, 2002.

[90] H.C. Hottel and A.F. Sarofim. *Radiative Transfer*. New York: McGraw Hill, 1967.

[91] H. Wang, C. Zhang, and X. Liu. "Heat transfer calculation methods in three-dimensional CFD model for pulverized coal-fired boilers". In: *Applied Thermal Engineering* 166.135 (2020), p. 114633.

[92] T. Asotani, T. Yamashita, H. Tominaga, Y. Uesugi, Y. Itaya, and S. Mori. "Prediction of ignition behavior in a tangentially fired pulverized coal boiler using CFD". In: *Fuel* 87.4-5 (2008), pp. 482–490.

[93] R.I. Blackreedy, J.M. Jones, L. Ma, M. Pourkashanian, A. Williams, A. Arenillas, B. Arias, J.J. Pis, and F. Rubiera. "Modeling pulverized coal combustion using a detailed coal combustion model". In: *Combustion science and Technolodgy* 178 (2006), pp. 763–787.

[94] S.S. Sazhin, E.M. Sazhina, O. Faltsi-Saravelou, and P. Wild. "The p-1 model for thermal radiation transfer: Advantages and limitations". In: *Fuel* 75.3 (1996), pp. 289–294.

[95] Hans-Gerd Brummel. "Thermal radiation of gas-solids-dispersions". In: *VDI Heat Atlas*. Ed. by Verein Deutscher Ingenieure and VDI-Gesellschaft Verfahrenstechnik und Chemieingenieurwesen. 2nd ed. 2016, pp. 989–998.

[96] T. Smith, Z. Shen, and J. Friedman. "Evaluation of Coefficients for the Weighted Sum of Gray Gases Model". In: *Journal of Heat transfer* 104 (1982), pp. 602–608.

[97] X. Yang, A. Clements, J. Szuhánszki, X. Huang, O. Farias Moguel, J. Li, J. Gibbins, Z. Liu, C. Zheng, D. Ingham, L. Ma, B. Nimmo, and M. Pourkashanian. "Prediction of the radiative heat transfer in small and large scale oxy-coal furnaces". In: *Applied Energy* 211.November 2017 (2018), pp. 523–537.

[98] J. Guo, Z. Liu, X. Huang, T. Zhang, W. Luo, F. Hu, P. Li, and C. Zheng. "Experimental and numerical investigations on oxy-coal combustion in a 35 MW large pilot boiler". In: *Fuel* 187 (2017), pp. 315–327.

[99] A. Ots. "Thermophysical Properties of Ash Deposit on Boiler Heat Exchanger Surfaces". In: *International Conference on Heat Exchanger Fouling and Cleaning* 2011 (2011), pp. 150–155.

[100] MTech. *Flownex Theory Guide*. MTech inc., 2021.

[101] F.W. Dittus and L.M.K. Boelter. *Heat transfer in automobile radiators of the tubular type*. English. Berkeley, Calif. SE: University of California Press, 1930.

[102] V. Gnielinski. "New equations for heat and mass transfer in turbulent pipe and channel flow". In: *International Chemical Engineering* 16 (1976), pp. 359–368.

[103] P. Basu, C. Kefa, and L. Jestin. *Boilers and Burners: Design and Theory*. New York: Springer, 2012.

[104] B.T. Rawlins, R. Laubscher, and P.G. Rousseau. "Application of Computational Fluid Dynamics and Process Modeling to Investigate Low-Load Operation of a Subcritical Utility-Scale Boiler". In: *ASME Journal of Thermal Science and Engineering Applications* 14.10 (2022), pp. 1–13.

[105] A. Žukauskas. *Heat Transfer from Tubes in Crossflow*. Vol. 8. Advances in Heat Transfer Volume 8. Orlando : Academic Press, 1972.

[106] U. Schnell. "Numerical modelling of solid fuel combustion processes using advanced CFD-based simulation tools". In: *Progress in Computational Fluid Dynamics* 1.4 (2001), pp. 208–218.

[107] V.E. Küng, F. Osmanlic, M. Markl, and C. Körner. "Comparison of passive scalar transport models coupled with the Lattice Boltzmann method". In: *Computers and Mathematics with Applications* 79.1 (2020), pp. 55–65.

[108] W.E. Ranz and W.R. Marshall. "Evaporation from Drops, Part I". In: *Chemical Engineering Progress* 3.48 (1952), pp. 141–146.

[109] W.E. Ranz and W.R. Marshall. "Evaporation from Drops, Part II". In: *Chemical Engineering Progress* 48.4 (1952), pp. 173–180.

[110] Ansys Inc. *Ansys Fluent Customization Manual*. January. 2022.

[111] B.T. Rawlins, R. Laubscher, and P.G. Rousseau. "A fast thermal non-equilibrium Eulerian-Eulerian numerical simulation methodology of a pulverized fuel combustor". In: *Proceedings of the 13th European Conference on Industrial Furnaces and Boilers*. Ed. by Viktor Scherer, Neil Fricker, and Albino Reis. 19-22 April 2022.

[112] A.F. Peters and R. Weber. "Mathematical modeling of a 2.4 MW swirling pulverized coal flame". In: *Combustion Science and Technology* 122.1-6 (1997), pp. 131–182.

[113] P.J. Roache. "Perspective: A method for uniform reporting of grid refinement studies". In: *Journal of Fluids Engineering, Transactions of the ASME* 116.3 (1994), pp. 405–413.

[114] I.B. Celik, U. Ghia, P.J. Roache, C.J. Freitas, H. Coleman, and P.E. Raad. "Procedure for estimation and reporting of uncertainty due to discretization in CFD applications". In: *Journal of Fluids Engineering, Transactions of the ASME* 130.7 (2008), pp. 0780011–0780014.

[115] B.T. Rawlins, R. Laubscher, and P.G. Rousseau. "Validation of a thermal non-equilibrium Eulerian-Eulerian multiphase model of a 620 MWe pulverized fuel power boiler". In: *12th South African Conference on Computational and Applied Mechanics (SACAM2020)*. Ed. by S Skatulla. Cape Town: MATEC Web of Conferences, 2021.

[116] C. Sheng, B. Moghtaderi, R. Gupta, and T.F. Wall. "A computational fluid dynamics based study of the combustion characteristics of coal blends in pulverised coal-fired furnace". In: *Fuel* 83.11-12 (2004), pp. 1543–1552.

[117] V. Gnielinski. “Heat transfer in cross-flow around single rows of tubes and through tube bundles”. In: *VDI Heat Atlas*. Berlin: Springer-Verlag, 2016, pp. 756–760.

[118] Y Zhang, Q Li, and Z Zhou. *Theory and Calculation of Heat Transfer in Furnaces*. 1st ed. London: Elsevier Ltd, 2016, p. 355.

[119] Hans-Gerd Brummel and D Vortmeyer. *Thermal radiation of gas-solid dispersions at higher particle loadings*. Ed. by In: Ingenieure VD and und Chemieingenieurwesen V-GV. Second. VDI heat atlas, 2016, pp. 989–98.

[120] M.T. Hagan, H.B. Demuth, M.H. Beale, and O. De Jesus. *Neural Networks Design*. 2nd ed. Hagan and Demuth, 1996, pp. 1–1012.

[121] D. Wen, Y. Pan, X. Chen, M. Aziz, Q. Zhou, and N. Li. “Analysis and prediction of thermal stress distribution on the membrane wall in the arch-fired boiler based on machine learning technology”. In: *Thermal Science and Engineering Progress* 28 (2022), p. 101137.

[122] M.J. Kochenderfer and T.A. Wheeler. *Algorithms for optimization*. 1st ed. Cambridge, Massachusetts: The MIT Press, 2019.

[123] CM Bishop. *Pattern Recognition and Machine Learning*. Ed. by M. Jordan, J. Kleinberg, and B. Scholkopf. Springer, 2006.

[124] C.E. Rasmussen and C.K.I. Williams. *Gaussian Processes for Machine Learning*. 1st ed. Cambridge, Massachusetts: The MIT Press, 2006.

[125] I. Goodfellow, Y. Bengio, and A. Courville. *Deep Learning*. First edit. Chennai: MIT Press, 2017.

[126] D.E. Rumelhart, G.E. Hinton, and R.J. Williams. “Learning representations by back-propagating errors”. In: *Nature* 323.6088 (1986), pp. 533–536.

[127] D. Kingma and J. Ba. “Adam: A Method for Stochastic Optimization”. In: *International Conference on Learning Representations* (Dec. 2015).

[128] Ning Qian. “On the momentum term in gradient descent learning algorithms”. In: *Neural Networks* 12.1 (1999), pp. 145–151.

[129] S. De, A. Mukherjee, and E. Ullah. “Convergence guarantees for RMSProp and ADAM in non-convex optimization and an empirical comparison to Nesterov acceleration”. In: (2018).

[130] A. Mustapha, L. Mohamed, and K. Ali. “Comparative study of optimization techniques in deep learning: Application in the ophthalmology field”. In: *Journal of Physics: Conference Series* 1743.1 (2021).

[131] Sebastian Ruder. “An overview of gradient descent optimization algorithms *”. In: ().

[132] E. Oko, M. Wang, and J. Zhang. “Neural network approach for predicting drum pressure and level in coal-fired subcritical power plant”. In: *Fuel* 151 (2015), pp. 139–145.

[133] C.M. Bishop. *Mixture Density Networks*. Tech. rep. Aston University, 1994.

[134] V. Ganapathy. *Industrial Boilers and Heat Recovery Steam Generators - Design, Applications, and Calculations*. New York: Marcel Dekker, Inc, 2003.

[135] R. Laubscher and P.G. Rousseau. *Power Plant Boilers Thermofluid Processes and Controls - MEC4117Z Course*. Rev A. Cape Town: University of Cape Town, 2021.

[136] S. Morgenthaler. "Exploratory data analysis". In: 1 (2009), pp. 33–44.

[137] L. Wasserman. *All of Nonparametric Statistics*. Ed. by George Casella, Stephen Fienberg, and Ingram Olkin. New York: Springer, 2006.

[138] A. Géron. *Hands-on Machine Learning whith Scikit-Learing, Keras and Tensorfow*. 2nd ed. O'Reilly Media, Inc, 2019, p. 510.

[139] P. G. Rousseau, C. G. Du Toit, J. S. Jun, and J. M. Noh. "Code-to-code comparison for analysing the steady-state heat transfer and natural circulation in an air-cooled RCCS using GAMMA+ and Flownex". In: *Nuclear Engineering and Design* 291 (2015), pp. 71–89.

[140] D. Chen and J.D. Chen, eds. *Monte-Carlo Simulation-Based Statistical Modeling*. Singapore: Springer, 2017.

[141] G.E.P. Box and M.E. Muller. "An Inverse Method for The Generation of Random Normal Deviates on Large-Scale Computers". In: *The Annals of Mathematical Statistics* 29.2 (1958), pp. 610–611.

[142] ASME. "PTC-4 Fired Steam Generators - Performance Test Codes." In: New York, NY: The American Society of Mechanical Engineers, 2008.

Appendices

Appendix A

Derivations

Derivations of the following variables will be discussed, namely, the effective density (ρ_{eff}) (Equation (4.2)), the linearisation of the momentum sources (Equation (4.3)), and the effective thermal conductivity of the superheater walls (Equation (5.3)).

A.1 Effective density derivation

The effective density of a mixture, including solid and gas-phases, can be derived by considering the volume and mass of a mixture. Assuming ideal gas relations, the density of the gas-phase can be written as;

$$\rho_g = \frac{P_g}{RT_g} \quad where \quad R = \frac{R_u}{\bar{M}} \tag{A.1}$$

The volume of a mixture (V_m) can be defined in this case as;

$$\begin{aligned} V_m &= V_p + V_g \\ &= \frac{m_p}{\rho_p} + \frac{m_g R T_g}{P_g} \end{aligned} \tag{A.2}$$

where V_p, V_p, and m_p are the particle or solid-phase volume, the gas volume and particle mass present in a control volume. The mass of the particle in a control volume can be expressed using the particle phase mass fraction (ϕ_{mp}), which indicates the amount of particle/solid phase present in the gas-phase and has units of $[kg_p/kg_g]$, where kg_p is the mass solid phase in a control volume and kg_g is the mass of gas present in a control volume. Thus, Equation (A.3) can be simplified as follows:

$$\begin{aligned} V_m &= \frac{\phi_{mp}\rho_g V_g}{\rho_p} + \frac{\rho_g V_g R T_g}{P_g} \\ &= \rho_g V_g (\frac{\phi_{mp}}{\rho_p} + \frac{RT_g}{P_g}) \end{aligned} \tag{A.3}$$

The mass of the mixture (m_m) can subsequently be defined as:

$$\begin{aligned} m_m &= m_p + m_g \\ &= \phi_{mp}\rho_g V_g + \rho_g V_g \\ &= \rho_g V_g(\phi_{mp} + 1) \end{aligned} \tag{A.4}$$

Using the definition of density, the effective density can be written using Equations (A.3) and (A.4) as,

$$\begin{aligned} \rho_{eff} &= \frac{m_m}{V_m} \\ &= \frac{\rho_g V_g(\phi_{mp} + 1)}{\rho_g V_g(\frac{\phi_{mp}}{\rho_p} + \frac{RT_g}{P_g})} \\ &= \frac{\rho_g \rho_p(\phi_{mp} + 1)}{(\phi_{mp}\rho_g + \rho_p)} \end{aligned} \tag{A.5}$$

A.2 Momentum sources derivation

The following derivation aids in determining the linearised momentum source terms to include the translational inertia effects due to the presence of the pseudo-particles. Typically, linearised sources terms (S^*) are written in the following form:

$$S^* = S + \frac{\partial S}{\partial \phi}\phi \tag{A.6}$$

where S, $\frac{dS}{d\phi}\phi$ and ϕ is the explicit part of the source term, the implicit part of the source term and the dependent variable, respectively [21]. For momentum sources, the independent variable is primarily the velocity component. For the x, y and z coordinate directions, the dependent variables are u, v, and w. The derivation is composed of two parts, namely derivations of the explicit and implicit forms of the source term. To transform Equation (3.12) to Equation (4.1), the general form of the source term (S_m) for the x-direction is given as follows:

$$S_{mom_x} = \frac{\partial}{\partial x_i}(\rho_g u_i u_j) - \frac{\partial}{\partial x_i}(\rho_{eff} u_i u_j) \tag{A.7}$$

Assuming the incompressible ideal gas formulation, the source term can be written as:

$$S_{mom_x} = (\rho_g - \rho_{eff})(\frac{\partial_i}{\partial x}(u_i u_j)) \tag{A.8}$$

Expanding the $(\frac{\partial}{\partial x_i}(u_i u_j))$ term, the following is derived:

$$\begin{aligned} \frac{\partial}{\partial x_i}(u_i u_j) &= (\frac{\partial}{\partial x}\hat{i} + \frac{\partial}{\partial y}\hat{j} + \frac{\partial}{\partial z}\hat{k}) \cdot (uu\hat{i} + vu\hat{j} + wu\hat{k}) \\ &= \frac{\partial}{\partial x}uu + \frac{\partial}{\partial y}vu + \frac{\partial}{\partial z}wu \\ &= 2u\frac{\partial u}{\partial x} + v\frac{\partial u}{\partial y} + u\frac{\partial v}{\partial y} + w\frac{\partial u}{\partial z} + u\frac{\partial w}{\partial z} \end{aligned} \tag{A.9}$$

Thus, the x-direction explicit source term can be written as follows:

$$S_{mom_x} = (\rho_g - \rho_{eff})(2u\frac{\partial u}{\partial x} + v\frac{\partial u}{\partial y} + u\frac{\partial v}{\partial y} + w\frac{\partial u}{\partial z} + u\frac{\partial w}{\partial z}) \tag{A.10}$$

Similarly, the explicit source term components for the y and z coordinates are written as follows:

$$\begin{aligned} S_{mom_y} &= (\rho_g - \rho_{eff})(u\frac{\partial v}{\partial x} + v\frac{\partial u}{\partial x} + 2v\frac{\partial v}{\partial y} + w\frac{\partial v}{\partial z} + v\frac{\partial w}{\partial z}) \\ S_{mom_z} &= (\rho_g - \rho_{eff})(u\frac{\partial w}{\partial x} + w\frac{\partial u}{\partial x} + v\frac{\partial w}{\partial y} + w\frac{\partial v}{\partial y} + 2w\frac{\partial w}{\partial z}) \end{aligned} \tag{A.11}$$

The implicit component of the linearised source term requires the derivative of the explicit component with respect to the dependent variable. Equation (A.12) illustrates the process of determining the derivative for the x coordinate direction.

$$\begin{aligned} \frac{\partial S_{mom_x}}{\partial u} &= (\rho_g - \rho_{eff})(2u\frac{\partial u}{\partial x} + v\frac{\partial u}{\partial y} + u\frac{\partial v}{\partial y} + w\frac{\partial u}{\partial z} + u\frac{\partial w}{\partial z})\frac{\partial}{\partial u} \\ &= (\rho_g - \rho_{eff})(2\frac{\partial u}{\partial x} + 2u\cdot 0 + 0\cdot\frac{\partial u}{\partial y} + v\cdot 0 + \frac{\partial v}{\partial y} + u\cdot 0 + 0\cdot\frac{\partial u}{\partial z} + w\cdot 0 + \frac{\partial w}{\partial z} + u\cdot 0) \\ &= (\rho_g - \rho_{eff})(2\frac{\partial u}{\partial x} + \frac{\partial v}{\partial y} + \frac{\partial w}{\partial z}) \end{aligned} \tag{A.12}$$

Similarly, the y and z coordinates implicit components are written as follows:

$$\begin{aligned} \frac{\partial S_{mom_y}}{\partial u} &= (\rho_g - \rho_{eff})(\frac{\partial u}{\partial x} + 2\frac{\partial v}{\partial y} + \frac{\partial w}{\partial z}) \\ \frac{\partial S_{mom_z}}{\partial u} &= (\rho_g - \rho_{eff})(\frac{\partial u}{\partial x} + \frac{\partial v}{\partial y} + 2\frac{\partial w}{\partial z}) \end{aligned} \tag{A.13}$$

Thus, the linearised source terms for all the coordinate directions are written using Equation (A.7) as follows:

$$\begin{aligned} S^*_{mom_x} &= (\rho_g - \rho_{eff})((2u\frac{\partial u}{\partial x} + v\frac{\partial u}{\partial y} + u\frac{\partial v}{\partial y} + w\frac{\partial u}{\partial z} + u\frac{\partial w}{\partial z}) + (\frac{\partial u}{\partial x} + 2\frac{\partial v}{\partial y} + \frac{\partial w}{\partial z})u) \\ S^*_{mom_y} &= (\rho_g - \rho_{eff})((u\frac{\partial v}{\partial x} + v\frac{\partial u}{\partial x} + 2v\frac{\partial v}{\partial y} + w\frac{\partial v}{\partial z} + v\frac{\partial w}{\partial z}) + (\frac{\partial u}{\partial x} + 2\frac{\partial v}{\partial y} + \frac{\partial w}{\partial z})v) \\ S^*_{mom_z} &= (\rho_g - \rho_{eff})((u\frac{\partial w}{\partial x} + w\frac{\partial u}{\partial x} + v\frac{\partial w}{\partial y} + w\frac{\partial v}{\partial y} + 2w\frac{\partial w}{\partial z}) + (\frac{\partial u}{\partial x} + \frac{\partial v}{\partial y} + 2\frac{\partial w}{\partial z})w) \end{aligned} \tag{A.14}$$

A.3 Effective wall thermal conductivity

The use of an effective wall thermal conductivity ($\lambda_{eff,wall}$) was derived since ANSYS Fluent® v19.5 does not allow for the modelling of multiple conduction layers when UDFs are utilised in a simulation. A thermal resistance analysis of the superheaters was conducted to incorporate the effects of fouling on the radiant superheaters. The transverse pitch between tubes for the SH2 and SH3 superheaters' tube banks results in a gap of 1 $[mm]$. Thus the tube banks can be modelled as flat plates. This assumption significantly reduces the complexity of the analysis. Figure A.1 illustrates the conduction heat transfer through a multi-layered material consisting of ash and steel.

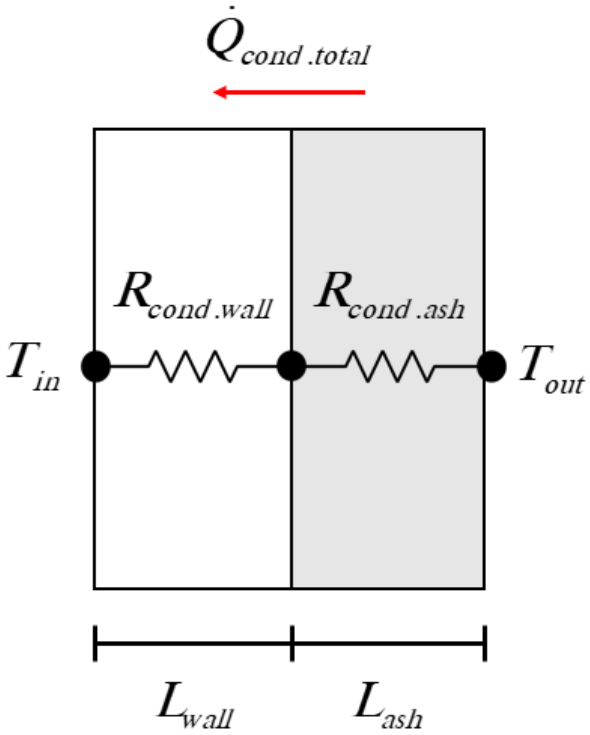

Figure A.1: Conduction thermal resistance network through a multi-layered material consisting of ash and steel.

The thermal resistance network of Figure A.1 allows for the total conduction heat transfer ($\dot{Q}_{cond.total}$) to be written as follows:

$$\dot{Q}_{cond.total} = \frac{(T_{out} - T_{in})}{R_{tot}} = \lambda_{eff.wall} A \frac{(T_{out} - T_{in})}{L} \tag{A.15}$$

The total thermal conductive resistance can be written in terms of the ash and steel walls' thermal conductivities, surface areas and thickness. The derived expression is shown in Equation (A.16).

$$\begin{aligned} R_{tot} &= R_{cond.ash} + R_{cond.wall} \\ &= \frac{L_{ash}}{\lambda_{ash} A_{ash}} + \frac{L_{wall}}{\lambda_{wall} A_{wall}} \\ &= \frac{\lambda_{wall} A_{wall} L_{ash} + \lambda_{ash} A_{ash} L_{wall}}{\lambda_{ash} \lambda_{wall}} \end{aligned} \tag{A.16}$$

With the flat plate assumption, the ash and steel wall areas are essentially the same, meaning $A_{ash} = A_{wall} = A$. The thickness of the ash layer is usually difficult to determine. The superheater components' fouling thermal resistance values typically range from $0.0047 - 0.015$ $[K/W]$. Making the thickness of the ash layer (L_{ash}) equal to the resistance value along with the ash conductivity (λ_{ash}) being equated to a value of 1 $[W/mK]$, the effect of an ash layer can be incorporated. Defining the ratio of the ash and steel wall thickness ($\eta_w = L_{ash}/L_{wall}$), the total resistance of Equation (A.16) can be written in terms of steel wall thickness as follows:

$$R_{tot} = \frac{L_{wall}}{A} \left(\frac{\lambda_{wall} \eta_w + \lambda_{ash}}{\lambda_{ash} \lambda_{wall}} \right) \tag{A.17}$$

Substituting Equation (A.17) into Equation (A.15), the effective conductivity can be written as follows:

$$\begin{aligned} \dot{Q}_{cond.total} &= \lambda_{eff.wall} A \frac{(T_{out} - T_{in})}{L_{wall}} = \left(\frac{\lambda_{ash} \lambda_{wall}}{\lambda_{wall} \eta_w + \lambda_{ash}} \right) \frac{A(T_{out} - T_{in})}{L_{wall}} \\ \therefore \lambda_{eff.wall} &= \frac{\lambda_{ash} \lambda_{wall}}{\lambda_{wall} \eta_w + \lambda_{ash}} \end{aligned} \tag{A.18}$$

Appendix B

Analytical calculations

In this section the boundary values and sample calculations for the CFD case studies discussed in chapter 5 are given. The results are used in conjunction with plant data as a verification guide for the developed CFD model. This section is therefore comprised of the following subsections:

1. Products of combustion calculations
2. Mass and energy balance calculations

B.1 Products of combustion

The following section illustrates the theoretical calculation procedure for determining the exit gas constituents for a solid fuel combustion reaction case. The procedure assumes infinitesimally fast reaction rates and complete global reactions. The results were used in the numerical case studies of chapter 6 to verify if complete combustion was successful.

B.1.1 Methods

On an as-received basis the ultimate analysis of the coal burnt for both case study configurations are given in Tables 4.2 and 5.2. These values are used in a stoichiometric combustion analysis to determine the theoretical amount of air that is required and the mass of the combustion products produced per kilogram of fuel burnt. A stoichiometric balanced global reaction consisting of reactants, oxidiser and product species can be written on a mass basis as follows:

$$\upsilon_R M_R + \upsilon_{OX} M_{OX} \rightarrow \upsilon_P M_P \tag{B.1}$$

Where M_R, M_{OX} and M_P are the molecular weights of the reactants, oxidiser and product species, and υ_R,υ_{OX} and υ_P are the stoichiometric balance coefficients respectively.

The ratio of oxygen and product species to the reactants/combustible matter is important to determine as it allows one to determine the mass of oxygen required and products species produced based on the mass fraction of combustible species present in the fuel. With combustible species being that of carbon C, hydrogen H and sulphur S for most solid fuel reactions. The ratio of oxygen/products to the reactant is written as:

$$S_{OX/P} = \frac{\upsilon_{OX,P} M_{OX,P}}{\upsilon_R M_R} \tag{B.2}$$

The reactions and subsequent $S_{OX/P}$ values for the solid fuel combustible species of carbon, hydrogen and sulphur are presented below:

$$\begin{aligned}
&C + S_{OX}O_2 \rightarrow S_P CO_2, && S_{OX} = 2.664\ kg_{O_2}/kg_{fuel} && S_P = 3.664\ kg_{CO_2}/kg_{fuel}\\
&H_2 + 0.5S_{OX}O_2 \rightarrow S_P H_2O, && S_{OX} = 7.936\ kg_{O_2}/kg_{fuel} && S_P = 8.936\ kg_{H_2O}/kg_{fuel}\\
&S + S_{OX}O_2 \rightarrow S_P SO_2, && S_{OX} = 0.998\ kg_{O_2}/kg_{fuel} && S_P = 1.998\ kg_{SO_2}/kg_{fuel}
\end{aligned} \tag{B.3}$$

The ratio of Equation (B.2) is used to determine the mass fraction, per kilogram of fuel, of the required oxygen and products produced by making use of the following expression:

$$m_{OX,P} = S_{OX,P} Y_{combustible} \tag{B.4}$$

From this the required amount of oxygen and products can be calculated. It follows that the exit flue gas constituents mass fractions can be calculated by considering the following definition:

$$Y_{i,fg} = \frac{m_{i,fg}}{m_{tot,fg}} \tag{B.5}$$

Where $Y_{i,fg}$ is the mass fraction of the i^{th} species present in the flue gas and m_i is the mass, per kilogram of fuel, of the i^{th} species present in the flue gas. With the mass fraction known the mole fractions can be computed using the following expression:

$$X_{i,fg} = \frac{\bar{M} Y_{i,fg}}{M_{i,fg}} \tag{B.6}$$

B.1.2 Sample calculation

A sample calculations for the utility boiler operating at 100% MCR are provided below with a summary of the final results given in Tables B.1.

Model inputs:

Air properties - (excess air ratio, specific humidity and air properties)

$\alpha = 1.155, \qquad \omega = 0.0016\, kg_{H_2O}/kg_{dry.air}, \qquad Y_{O_{2_{dry.air}}} = 0.232\, kg/kg,$

$Y_{N_{2_{dry.air}}} = 0.768\, kg/kg$

Fuel constituents based on an 'as received' ultimate analysis basis

$Y_C = 0.416\, kg/kg_{fuel}, \qquad Y_H = 0.022\, kg/kg_{fuel}, \qquad Y_N = 0.01\, kg/kg_{fuel},$

$Y_S = 0.009\, kg/kg_{fuel}, \qquad Y_O = 0.079\, kg/kg_{fuel}, \qquad Y_{H_2O} = 0.055\, kg/kg_{fuel},$

$Y_{ASH} = 0.409\, kg/kg_{fuel}, \qquad Y_{UC} = 0.045\, kg/kg_{fuel}$

$Y_C + Y_H + Y_N + Y_S + Y_O + Y_{H_2O} + Y_{ASH} + Y_{UC} = 1$

Step 1: Global oxidation reactions

Carbon oxidation reaction (R1)

$C + S_{OX}O_2 \rightarrow S_P CO_2$

$m_{O_{2_{R1}}} = S_{OX}Y_C = \frac{M_{O_2}}{M_C}Y_C = 1.107\, kg/kg_{fuel}$

$m_{CO_2} = S_P Y_C = \frac{M_{CO_2}}{M_C}Y_C = 1.523\, kg/kg_{fuel}$

Hydrogen oxidation reaction (R2)

$H_2 + 0.5S_{OX}O_2 \rightarrow S_P H_2O$

$m_{O_{2_{R2}}} = S_{OX}Y_H = 0.5\frac{M_{O_2}}{M_{H_2}}Y_H = 0.177\, kg/kg_{fuel}$

$m_{H_2O} = S_P Y_H = \frac{M_{H_2O}}{M_{H_2}}Y_H = 0.199\, kg/kg_{fuel}$

Sulphur oxidation reaction (R3)

$S + S_{OX}O_2 \rightarrow S_P SO_2$

$m_{O_{2_{R3}}} = S_{OX}Y_S = \frac{M_{O_2}}{M_S}Y_S = 0.009\, kg/kg_{fuel}$

$m_{SO_2} = S_P Y_S = \frac{M_{SO_2}}{M_S}Y_S = 0.019\, kg/kg_{fuel}$

Step 2: Theoretical amount of air

Calculate the required air, based on the amount oxygen required for the reactions R1-R3.

$m_{O_{2_{req}}} = m_{O_{2_{R1}}} + m_{O_{2_{R2}}} + m_{O_{2_{R3}}} - Y_O = 1.214\, kg/kg_{fuel}$

$m_{air.req} = \frac{m_{O_{2_{req}}}}{Y_{O_{2_{dry.air}}}} = 5.245\, kg/kg_{fuel}$

$m_{dry.air} = \alpha m_{air.req} = 6.058\, kg/kg_{fuel}$

$m_{moistair} = \omega m_{dry.air} = 0.055\, kg/kg_{fuel}$

Step 3: Mass of products per kilogram of fuel

The mass of the products per kilogram of fuel for each combustion product is calculated as:

$m_{CO_{2_{fg}}} = m_{CO_2} = 1.523\,kg/kg_{fuel}$

$m_{H_2O_{fg}} = m_{H_2O} + Y_{H_2O} + m_{moistair} = 0.309\,kg/kg_{fuel}$

$m_{SO_{2_{fg}}} = m_{SO_2} = 0.019\,kg/kg_{fuel}$

$m_{O_{2_{fg}}} = Y_{O_{2_{dry.air}}}(m_{dry.air} - m_{air.req}) = 0.188\,kg/kg_{fuel}$

$m_{N_{2_{fg}}} = Y_N + Y_{N_{2_{dry.air}}}(m_{dry.air}) = 4.665\,kg/kg_{fuel}$

Total mass of combustion products per kilogram of fuel:

$m_{tot_{fg}} = m_{CO_{2_{fg}}} + m_{H_2O_{fg}} + m_{SO_{2_{fg}}} + m_{O_{2_{fg}}} + m_{N_{2_{fg}}} = 6.704\,kg/kg_{fuel}$

Step 4: Mass fractions per kilogram gas of the combustion products

The mass fractions per kilogram gas can be calculated using Equation (B.5)

$Y_{CO_{2_{fg}}} = \frac{m_{CO_{2_{fg}}}}{m_{tot_{fg}}} = 0.227\,kg/kg$

$Y_{H_2O_{fg}} = \frac{m_{H_2O_{fg}}}{m_{tot_{fg}}} = 0.046\,kg/kg$

$Y_{SO_{2_{fg}}} = \frac{m_{SO_{2_{fg}}}}{m_{tot_{fg}}} = 0.003\,kg/kg$

$Y_{O_{2_{fg}}} = \frac{m_{O_{2_{fg}}}}{m_{tot_{fg}}} = 0.028\,kg/kg$

$Y_{N_{2_{fg}}} = \frac{m_{N_{2_{fg}}}}{m_{tot_{fg}}} = 0.696\,kg/kg$

$Y_{CO_{2_{fg}}} + Y_{H_2O_{fg}} + Y_{SO_{2_{fg}}} + Y_{O_{2_{fg}}} + Y_{N_{2_{fg}}} = 1$

Table B.1: Exit flue gas constituent mass fractions for the CFD case studies of Chapters 4 and 5

Load	$\mathbf{Y_{CO_2}}$	$\mathbf{Y_{H_2O}}$	$\mathbf{Y_{SO_2}}$	$\mathbf{Y_{O_2}}$	$\mathbf{Y_{N_2}}$
IFRF - 100% MCR	0.213	0.033	0.0012	0.038	0.0.713
IFRF - 60% MCR	0.197	0.031	0.0013	0.053	0.0.718
IFRF - 40% MCR	0.191	0.029	0.0011	0.059	0.720
Utility boiler - 100% MCR	0.227	0.046	0.0028	0.028	0.696
Utility boiler - 81% MCR	0.217	0.045	0.0027	0.036	0.699
Utility boiler - 60% MCR	0.209	0.043	0.0026	0.044	0.701
Utility boiler - 32% MCR	0.198	0.038	0.0024	0.052	0.712

The calculated exit mass fractions for all the CFD simulation load cases are presented in Table B.1. The exit mass fractions of Y_{O_2} and Y_{CO_2} were used as part of the convergence strategy to ensure combustion has stabilised during the simulations. Usually the excess air ratio is estimated from the X_{O_2} and X_{CO_2} molar concentration measurements.

B.2 Mass and energy balance calculations

Applying the principles of mass and energy conservation to the entire boiler, allows an engineer to determine and keep track of the total energy input and output to the boiler plant. Using an energy and mass balance the fuel and air mass flow rates can be determined. The energy balance for a boiler can be determined using the following equations:

$$\begin{aligned} E_{in} &= E_{out} \\ E_{in} &= \dot{Q}_{fuel,sensible} + \dot{Q}_{fuel,combustion} + \dot{Q}_{air,combustion} \\ E_{out} &= \dot{Q}_{steam} + \dot{Q}_{losses} + \dot{Q}_{fg,out} \end{aligned} \tag{B.7}$$

A schematic of a single control volume for the entire flue gas and water side of the system is given in Figure B.1. This accounts for both the mass and energy coming in and out of the boiler system.

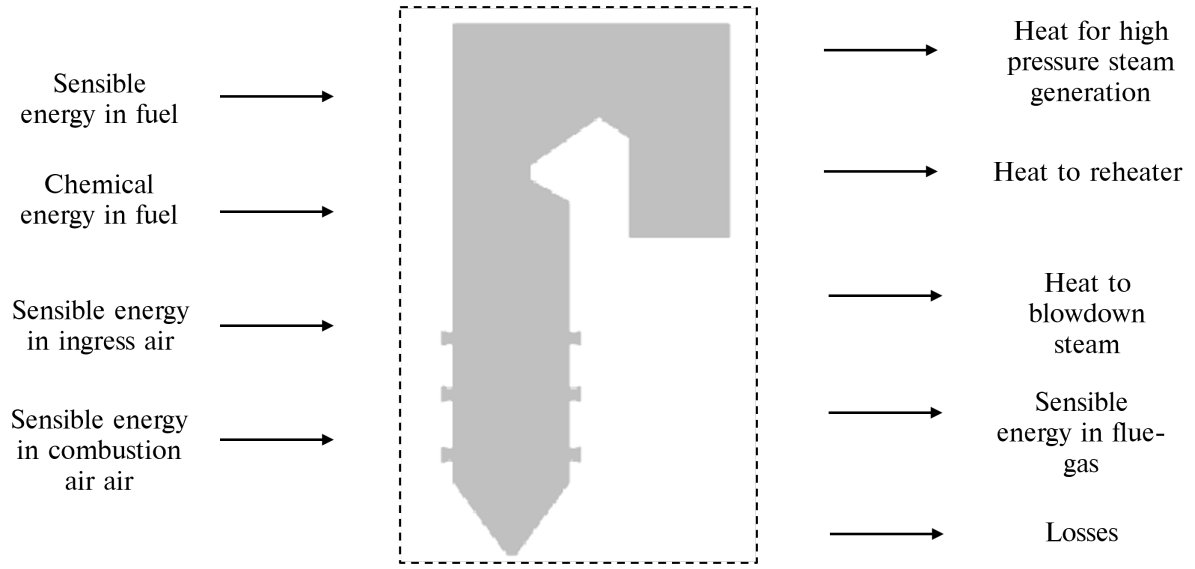

Figure B.1: Mass and energy balance for entire boiler system

B.2.1 Methods

The first step is to define all the energy components of Equation (B.7). The water/steam side heat load ($\dot{Q}_{steam}$) which comprises of all the heat transferred from the flue gas to generate steam at its final conditions can be calculated as:

$$\dot{Q}_{steam} = \dot{m}_{HP}(h_{HP_{out}} - h_{FW_{in}}) + \sum_{i=1}^{N} \dot{m}_{RH}(h_{RH_{out}} - h_{RH_{in}}) + \delta_{blowdown}\dot{m}_{HP}h_{drum} \quad \text{(B.8)}$$

The losses term ($\dot{Q}_{losses}$) of Equation (B.7) accounts for the radiation, unburned carbon, bottom ash, sensible energy of the fly-ash and sensible unburned carbon losses. The radiation losses accounts for the combination of the radiation and convective heat losses on the external surfaces of the boiler. A loss fraction (Rad_{loss}) is calculated from the ASME Power Test Code PTC 4.1-464 [142]. These losses are calculated as:

$$\dot{Q}_{rad} = \dot{m}_{fuel}HHV_{fuel}Rad_{loss} \quad \text{(B.9)}$$

Unburned carbon losses accounts for the carbon fraction not completely burnt in the furnace. The higher heating value of carbon is taken as 33820000 $[J/kg]$ with an assumed fraction of 1% of the fuel being unburned carbon. The loss can be calculated as:

$$\dot{Q}_{UC} = \dot{m}_{fuel}HHV_{carbon}Y_{UC} \quad \text{(B.10)}$$

Bottom ash losses is due to ash leaving the boiler through the hopper at elevated temperatures compared to the fuel feed temperature. A fly-ash fraction of 93% is used and a specific heat at constant pressure of 730 $[J/kgK]$ at a reference temperature of 298.15 $[K]$ [135]. The loss is calculated as:

$$\begin{aligned} \dot{Q}_{ash,bottom} &= \dot{m}_{fuel}Y_{ASH}(1 - Y_{flyash})c_{p_{ash,bottom}}(T_{ash,bottom} - 298.15K) \\ h_{ash,bottom} &= c_{p_{ash,bottom}}(T_{ash,bottom} - 298.15K) \end{aligned} \quad \text{(B.11)}$$

The sensible ash exit loss accounts for the energy of the fly-ash exiting the boiler system, and is determined as:

$$\begin{aligned} \dot{Q}_{flyash,sensible} &= \dot{m}_{fuel}Y_{ASH}Y_{flyash}c_{p_{flyash,out}}(T_{flyash,out} - 298.15K) \\ h_{flyash,out} &= c_{p_{flyash}}(T_{flyash,exit} - 298.15K) \end{aligned} \quad \text{(B.12)}$$

Similarly energy of the unburned carbon exiting the system is calculated, using a specific heat at constant pressure of 710 $[J/kgK]$, as:

$$\begin{aligned} \dot{Q}_{UC,sensible} &= \dot{m}_{fuel}Y_{UC}Y_{flyash}c_{p_{UC}}(T_{UC} - 298.15K) \\ h_{UC,sensible} &= c_{p_{UC}}(T_{UC} - 298.15K) \end{aligned} \quad \text{(B.13)}$$

It is common practise to include an additional loss term for unaccounted losses with typical loss fraction (C_{loss}) values between 0.2-0.5%. The unaccounted losses are incorporated into the energy balance as:

$$\dot{Q}_{unaccounted} = \dot{m}_{fuel}HHV_{fuel}C_{loss} \quad \text{(B.14)}$$

The energy losses due to the high temperature gases leaving the system ($\dot{Q}_{fg,out}$) can be defined as follows:

$$\dot{Q}_{fg,out} = \dot{m}_{fg,out} h_{fg,out} \tag{B.15}$$

where the enthalpy of the flue gas is calculated using Equation (3.9) of Chapter 3.

The energy entering the system is made up of the fuels sensible energy, chemical energy released and energy from combustion/transport air. The sensible energy of the fuel is calculated by assuming a specific heat at constant pressure value of 710 $[J/kgK]$.

$$\begin{aligned} \dot{Q}_{fuel,sensible} &= \dot{m}_{fuel} c_{p_{fuel}} (T_{fuel} - 298.15K) \\ h_{fuel,sensible} &= c_{p_{fuel,sensible}} (T_{fuel,sensible} - 298.15K) \end{aligned} \tag{B.16}$$

The chemical energy released into the system is the dominant input energy source and requires the higher heating value of the fuel to be known which is obtained from Table 5.2. The release of chemical energy is written as:

$$\dot{Q}_{fuel,combustion} = \dot{m}_{fuel} HHV_{fuel} \tag{B.17}$$

The energy from the combustion air fed into the boiler is determined using the inlet air compositions enthalpy and the required mass flow of air. This is calculated as:

$$\dot{Q}_{air,combustion} = \dot{m}_{air} h_{air,in} \tag{B.18}$$

It is important to note that the mass flow rate of the flue gas exiting ($\dot{m}_{fg,out}$) and the required combustion air ($\dot{m}_{air}$) can be written in terms of the fuel flow rate as:

$$\begin{aligned} \dot{m}_{fg,out} &= \dot{m}_{fuel}((1 - Y_{ash} - Y_{UC}) + m_{air}) \\ \dot{m}_{air} &= \dot{m}_{fuel} m_{air} \end{aligned} \tag{B.19}$$

where $m_{air}\,[kg_{air}/kg_{fuel}]$ is the total combustion air required which includes humidity ($m_{air} = m_{air,dry} + m_{air,moist}$). By substituting Equations (B.8) through (B.18) into Equation (B.7), the mass flow rate of fuel can be determined as follows:

$$\begin{aligned} \dot{m}_{fuel} =& (\dot{Q}_{steam})(HHV_{fuel} + (m_{air,dry} + m_{air,moist}) h_{air,in} + h_{fuel,sensible} \\ & - HHV_{carbon} Y_{UC} - HHV_{fuel} Rad_{loss} - Y_{ASH}(1 - Y_{flyash}) h_{ash,bottom} \\ & - HHV_{fuel} C_{loss} - (1 - Y_{ASH} - Y_{UC} + m_{air,dry} + m_{air,moist}) h_{fg,out} \\ & - Y_{ASH} Y_{flyash} h_{flyash,out} - Y_{UC} Y_{flyash} h_{UC,sensible})^{-1} \end{aligned} \tag{B.20}$$

B.2.2 Sample calculations

A sample calculation for the utility boiler operating at 100% MCR was conducted to determine the fuel and air mass flow rates. These form part of the CFD simulations inlet boundary conditions. The calculation procedure follows the same procedure for the other simulated loads.

Model inputs:

Air properties -
$\omega = 0.0016\,kg/kg, \qquad Y_{O_{2_{dry.air}}} = 0.232\,kg/kg, \qquad Y_{N_{2_{dry.air}}} = 0.763\,kg/kg$

Exit flue gas properties -

Utilise the flue gas mixture calculated in Section B.1.2, since calculation is based on a boiler load of 100% MCR.

Operating conditions -

$T_{ash,bottom} = 800°C, \qquad T_{air,ambient} = 38°C, \qquad T_{fg,out} = 127°C$

$Rad_{loss} \approx 0.4\%, \qquad C_{loss} = 0.005$

$Y_{flyash} = 0.95,$

Fuel properties -

$HHV_{fuel} = 15.07MJ/kg$

The same fuel is used as mentioned in Section B.1.2. Table B.2 lists the relevant information needed to determine the steam heat load.

Table B.2: Utility boiler steam mass flow rates and enthalpy values at 100% MCR

Mass flow rate	**Value**		
$\dot{m}_{HP_{exit}}$	$475.0\,kg/s$		
$\dot{m}_{RH_1}$	$446.2\,kg/s$		
$\dot{m}_{RH_2}$	$460.7\,kg/s$		
$\dot{m}_{attemperation}$	$\dot{m}_{RH_2} - \dot{m}_{RH_1}$		
Enthalpy	**P**	**T**	**h(P, T)**
$h_{HP_{out}}$	$16.42\,MPa$	$810.5\,K$	$3399.9\,kJ/kg$
$h_{FW_{in}}$	$17.35\,MPa$	$520.3\,K$	$1072.2\,kJ/kg$
$h_{RH_{1_{in}}}$	$3.74\,MPa$	$602.15\,K$	$3046.9\,kJ/kg$
$h_{RH_{2_{out}}}$	$3.71\,MPa$	$811.5\,K$	$3536.4\,kJ/kg$
h_{attemp}	$17.08\,MPa$	$431.1\,K$	$676.6\,J/kg$
$h_{blowdown}$	$17.08\,MPa$	$Sat.\,vapour$	$1693.3\,kJ/kg$

Using the values given in Table B.2 and a blowdown percentage ($\delta_{blowdown}$) of 1% of the required steam flow rate the heat transferred to the reheaters and subsequently the water/steam heat load are solved.

Step 1: Determine the total steam heat load

$\dot{Q}_{RH_{tot}} = \dot{m}_{RH_{1_{in}}}(h_{attemp} - h_{RH_{1_{in}}}) + (\dot{m}_{RH_{1_{in}}} + \dot{m}_{attemp})(h_{RH_{2_{out}}} - h_{attemp}) = 259.6\,MW$

$\dot{Q}_{steam} = \dot{m}_{HP_{out}}(h_{HP_{out}} - h_{FW_{in}}) + \dot{Q}_{RH_{tot}} + \delta_{blowdown}\dot{m}_{HP_{out}}h_{blowdown} = 1415.1\,MW$

Step 2: Determine losses due to operating conditions

$m_{air,dry} = 6.058\,kg/kg_{fuel}$ Refer to Section B.1.2

$m_{air,moist} = 0.055\,kg/kg_{fuel}$ Refer to Section B.1.2

$h_{air,in} = \sum_{k=1}^{N} Y_k h_k = 12.77\,kJ/kg$

$h_{fuel,sensible} = 710J/kgK(311.15K - 298.15K) = 9.23\,kJ/kg$

$h_{ash,bottom} = 730J/kgK(1073.15K - 298.15K) = 565.75\,kJ/kg$

$h_{fg,out} = \sum_{k=1}^{N} Y_k h_k = 209.51\,kJ/kg$

$h_{flyash,out} = 730J/kgK(400.15K - 298.15K) = 74.46\,kJ/kg$

$h_{UC,sensible} = 710J/kgK(400.15K - 298.15K) = 72.42\,kJ/kg$

Step 3: Solve for the mass flow rate of fuel

Substitute and solve for Equation (B.20)
$\dot{m}_{fuel} = 112.1\,kg/s$

Step 4: Solve for the mass flow rate of air

Substitute and solve for Equation (B.19)

$\dot{m}_{air} = 685.3\,kg/s$

Calculating the fuel and air mass flow rates provided all the CFD inlet boundary conditions for the case studies of Chapter 5 if site measured site data was not provided. A summary of the calculated results are provided in Table B.3.

Table B.3: Calculated total fuel, air and the flue gas flow rates required for the case studies of Chapter 5

Load	$\dot{\mathbf{m}}_{\mathbf{fuel,tot}}$	$\dot{\mathbf{m}}_{\mathbf{air,tot}}$	$\dot{\mathbf{m}}_{\mathbf{fg,tot}}$
Utility boiler - 100% MCR - $[kg/s]$	112.1	685.3	752.2
Utility boiler - 81% MCR - $[kg/s]$	90.7	577.8	630.6
Utility boiler - 60% MCR - $[kg/s]$	60.1	404.6	438.4
Utility boiler - 32% MCR - $[kg/s]$	37.2	305.3	328.1

Appendix C

NIST polynomials for fluid properties

All the fluid properties used in the CFD simulations utilised the National Institute of Standards and Technology (NIST) database to determine the polynomial coefficients a a function of temperature [70]. The properties of interest are the specific heat (c_p), thermal conductivity (λ) and viscosity (μ). The fluids of interest are the gases that make up the flue gas composition, which are primarily CO_2, N_2, O_2, CO, H_2O_g, and SO_2. The following equations can be used to calculate the mentioned fluid properties for the gases for the temperature range of 200 $[K]$ to 2200 $[K]$.

$$c_p(T) = a_0 + a_1T + a_2T^2 + a_3T^3 + a_4T^4$$
$$\lambda_g(T) = a_0 + a_1T + a_2T^2 + a_3T^3 + a_4T^4$$
$$\mu_g(T) = a_0 + a_1T + a_2T^2 + a_3T^3 + a_4T^4$$

The coefficients for the equations can be found in Table C.1.

Table C.1: NIST database polynomial coefficients

Species	$\mathbf{a_0}$	$\mathbf{a_1}$	$\mathbf{a_2}$	$\mathbf{a_3}$	$\mathbf{a_4}$
			Specific heat **-** $[c_p]$		
$c_{p_{CO_2}}$	5.295×10^{2}	1.349×10^{0}	-8.963×10^{-4}	2.882×10^{-7}	-3.618×10^{-11}
$c_{p_{N_2}}$	1.071×10^{3}	-2.750×10^{-1}	6.814×10^{-4}	-3.826×10^{-7}	6.843×10^{-11}
$c_{p_{O_2}}$	8.385×10^{2}	2.732×10^{-1}	5.982×10^{-5}	-1.131×10^{-7}	2.859×10^{-11}
$c_{p_{CO}}$	1.047×10^{3}	-1.568×10^{-1}	5.399×10^{-4}	-3.011×10^{-7}	5.050×10^{-11}
$c_{p_{H_2O}}$	2.338×10^{3}	-1.783×10^{0}	2.900×10^{-3}	-1.401×10^{-6}	2.295×10^{-10}
$c_{p_{SO_2}}$	5.798×10^{2}	2.608×10^{-1}	6.609×10^{-5}	0.000	0.000
			Thermal conductivity **-** $[\lambda_g]$		
λ_{CO_2}	-9.753×10^{-3}	1.022×10^{-4}	-3.876×10^{-8}	2.201×10^{-11}	-5.842×10^{-15}
λ_{N_2}	-2.246×10^{-3}	1.170×10^{-4}	-9.070×10^{-8}	5.201×10^{-11}	-1.111×10^{-14}
λ_{O_2}	-5.905×10^{-3}	1.289×10^{-4}	-9.779×10^{-8}	5.731×10^{-11}	-1.247×10^{-14}
λ_{CO}	5.971×10^{-3}	7.050×10^{-5}	-8.060×10^{-9}	3.609×10^{-13}	0.000
λ_{H_2O}	9.227×10^{-3}	4.277×10^{-5}	1.249×10^{-8}	4.754×10^{-11}	-1.834×10^{-14}
λ_{SO_2}	-3.371×10^{-3}	4.380×10^{-5}	3.123×10^{-9}	0.000	0.000
			Viscosity **-** $[\mu_g]$		
μ_{CO_2}	-1.686×10^{-6}	6.812×10^{-8}	-4.191×10^{-11}	2.084×10^{-14}	-4.357×10^{-18}
μ_{N_2}	-1.038×10^{-8}	7.424×10^{-8}	-5.745×10^{-11}	3.094×10^{-14}	-6.361×10^{-18}
μ_{O_2}	-9.671×10^{-7}	8.932×10^{-8}	-6.842×10^{-11}	3.644×10^{-14}	-7.468×10^{-18}
μ_{CO}	2.973×10^{-6}	5.589×10^{-8}	-2.514×10^{-11}	6.654×10^{-15}	0.000
μ_{H_2O}	6.700×10^{-6}	1.069×10^{-8}	2.876×10^{-11}	-9.138×10^{-15}	-1.282×10^{-20}
μ_{SO_2}	-1.357×10^{-6}	4.891×10^{-8}	-5.886×10^{-12}	0.000	0.000